Wrocław University of Technology
Centre of Advanced Materials and Nanotechnology

Materials Science
Poland

New Concepts and Materials for Molecular Electronics and Nanotechnology
CMME '04

Puszczykowo, Poland, 11-15 September 2004

Guest Editors:
Bogdan Bułka, Andrzej Graja and Roman Świetlik

Vol.22 • No. 4 • 2004

Oficyna Wydawnicza Politechniki Wrocławskiej

Materials Science is an interdisciplinary journal devoted to experimental and theoretical research into the synthesis, structure, properties and applications of materials.

Among the materials of interest are:

- glasses and ceramics
- sol-gel materials
- photoactive materials (including materials for nonlinear optics)
- laser materials
- photonic crystals
- semiconductor micro- and nanostructures
- piezo-, pyro- and ferroelectric materials
- high-T_c, superconductors
- magnetic materials
- molecular materials (including polymers) for use in electronics and photonics
- novel solid phases
- other novel and unconventional materials

The broad spectrum of the areas of interest reflects the interdisciplinary nature of materials research. Papers covering the modelling of materials, their synthesis and characterisation, physicochemical aspects of their fabrication, properties and applications are welcome. In addition to regular papers, the journal features issues containing conference papers, as well as special issues on key topics in materials science.

Materials Science is published under the auspices of the Centre of Advanced Materials and Nanotechnology of the Wrocław University of Technology, in collaboration with the Institute of Low Temperatures and Structural Research of the Polish Academy of Sciences and the Wroclaw University of Economics.

All accepted papers are placed on the Web page of the journal and are available at the address: http://MaterialsScience.pwr.wroc.pl

Editor-in-Chief

Juliusz Sworakowski

Institute of Physical and Theoretical Chemistry
Wrocław University of Technology
Wybrzeże Wyspiańskiego 27
50-370 Wrocław, Poland
sworakowski@pwr.wroc.pl

Associate Editors

Wiesław Stręk

Institute of Low Temperature
and Structure Research
Polish Academy of Sciences
P.O.Box 1410
50-950 Wrocław 2, Poland
strek@int.pan.wroc.pl

Jerzy Hanuza

Department of Bioorganic Chemistry
Faculty of Industry and Economics
Wrocław University of Economics
Komandorska 118/120
53-345 Wrocław, Poland
hanuza@credit.ae.wroc.pl

Scientific Secretary

Krzysztof Maruszewski
Intitute of Materials Science and Applied Mechanics
Wrocław University of Technology
Wybrzeże Wyspiańskiego 27
50-370 Wrocław, Poland
maruszewski@pwr.wroc.pl

Advisory Editorial Board

Michel A. Aegerter, Saarbrücken, Germany
Ludwig J. Balk, Wuppertal, Germany
Victor E. Borisenko, Minsk, Belarus
Mikhaylo S. Brodyn, Kyiv, Ukraine
Maciej Bugajski, Warszawa, Poland
Alexander Bulinski, Ottawa, Canada
Roberto M. Faria, São Carlos, Brazil
Reimund Gerhard-Multhaupt, Potsdam, Germany
Paweł Hawrylak, Ottawa, Canada
Jorma Hölsä, Turku, Finland
Alexander A. Kaminskii, Moscow, Russia
Wacław Kasprzak, Wrocław, Poland
Andrzej Kłonkowski, Gdańsk, Poland
Seiji Kojima, Tsukuba, Japan
Shin-ya Koshihara, Tokyo, Japan
Marian Kryszewski, Łódź, Poland
Krzysztof J. Kurzydłowski, Warsaw, Poland
Jerzy M. Langer, Warsaw, Poland
Janina Legendziewicz, Wrocław, Poland
Benedykt Licznerski, Wrocław, Poland
Tadeusz Luty, Wrocław, Poland
Joop H. van der Maas, Utrecht, The Netherlands
Bolesław Mazurek, Wrocław, Poland
Gerd Meyer, Cologne, Germany
Jan Misiewicz, Wrocław, Poland
Jerzy Mroziński, Wrocław, Poland
Robert W. Munn, Manchester, U.K.
Krzysztof Nauka, Palo Alto, CA, U.S.A.
Stanislav Nešpůrek, Prague, Czech Republic
Romek Nowak, Santa Clara, CA, U.S.A.
Tetsuo Ogawa, Osaka, Japan
Renata Reisfeld, Jerusalem, Israel
Marek Samoć, Canberra, Australia
Jan Stankowski, Poznań, Poland
Leszek Stoch, Cracow, Poland
Jan van Turnhout, Delft, The Netherlands
Jacek Ulański, Łódź, Poland
Walter Wojciechowski, Wrocław, Poland
Vladislav Zolin, Moscow, Russia

The Journal Is supported by the State Committee for Scientific Research

Editorial Office

Karol Langner
Łukasz Maciejewski

Printed in Poland

Drukarnia Oficyny Wydawniczej Politechniki Wrocławskiej
Zam. nr 56/2005.

CONTENTS

From the Guest Editors 283

E. Balthes, A. Nothardt, P. Wyder, D. Schweitzer, Electron-electron correlations in $(BEDT-TTF)_2$ I_3organic superconductors 285

A. Nothardt, E. Balthes, B. Salameh, W. Schmidt, D. Schweitzer, I Strempfer, B. Keimer, D. Maude, Quantum oscillation measurements on the organic superconductor Θ-$(BEDT-TTF)_2I_3$ 299

A. Girlando, M. Masino, A. Brillante, R.G. Della Valle, E. Venuti, Peierls phonons in organic molecular crystals and in charge transfer salts 307

A. Graja, M. Golub, Highly conducting organic composites obtained by charge transfer reaction in the solid state 317

M.Masino, A. Girlando, A. Brillante, R.G. Della Valle, E. Venuti, High-pressure optical study of the neutral-ionic phase transition in TTF-CA 333

B. Barszcz, A. Łapiński, A. Graja A.M. Flakina, R.N. Lyubovskaya, Spectral studies of new organic conductors based on TTF derivatives with polymeric isocyanuric acid anions 339

I, Olejniczak, B. Gromadziński, A. Graja, T. Devic, P. Batail, Optical properties of the one -dimensional organic conductors $\beta(EDT-TTF-I_2)_2$ $(Pb_{5/6} \bullet {}_{1/6}I_2)_3$ and $\beta(EDT-TTF-I_2)_2$ $(Pb_{2/3+x} Ag_{1/3-2x} \bullet {}_xI_2)_3$,x = 0.05 347

A. Kowalska, R. Wojciechowski, J. Ulanski, Phase transitions in ß-$(BEDT-TTF)_2XF_6$ (X = P, Sb or As) salts as seen by Raman Spectroscopy 353

M.G. Kaplunov, N.D. Kushch, S.S. Krasnikova, Reflectivity spectra of some conducting BETS salts 359

G. C. Papavassiliou, G.A. Mousdis, G.G. Anyfantis, K. Murata, T. Nakanishi, L. Li, H. Yoshino, H. Tajima, M. Inoue, T. Konoike, J.S. Brooks, E.S. Choi, D. Graf, Some new findings in τ-phase organic conductors 365

A. Boguta, D. Wróbel, Y.S. Avlasevich, R. Ries, A. Richter, Spectral and microscopic examinations of metalloporphyrin-labelled polymers on different substrates 373

J. Jaglarz, A. Kassiba, P. Armatys, M. Pokladko, E. Gondek, J. Sanetra, Polymeric photovoltaic devices 389

A. A. Apostoluk, L. Rocha, C. Fiorini-Debuisschert, C. Sentein, P. Raimond, L. Setti, A. Fraleoni-Morgera, J.-M. Nunzi, Semiconducting dye-functionalised poled polymers for photovoltaic applications 397

D. Wostek-Wojciechowska, J.K. Jeszka, P. Uznanski, C Amiens, B. Chaudret, P. Lecante, Synthesis of gold nanoparticles in solid state by thermal decomposition of an organometallic precursor 407

A. Tracz, T. Pakula, J.K. Jeszka, Zone casting - a universal method of preparing oriented anisotropic layers of organic materials 415

G. Paasch, S. Scheinert, Scaling organic transistors: materials and design 423

C. J. Lambert, S. Athanasopoulos, I.M. Grace, S.W. Bailey, Spin-dependent transport and interwall coupling in carbon nanotubes 435

B. Kramer, K. Dittmer, S. Debald, J. Ohe, F. Cavaliere, M. Sassetti, Spin transport through nanostructures 445

J. Wiśniewska, I. Weymann, J. Barnaś, Spin-dependent transport in ferromagnetic single-electron transistors with non-collinear magnetizations 461

O. Zaitsev, K. Richter, Weak antilocalization and spin relaxation in integrable quantum dots 469

D. Giuliano, P. Lucignano, A. Tagliacozzo, Manipulation of electron spin in a quantum dot using a magnetic field and voltage gates 481

T. Kostyrko, B.R. Bułka, Effects of Coulomb interactions in electron transport through short molecular chains 497

I. M. Grace, S.W. Bailey, J. Jefferson, C. J. Lambert, Electron transport through single molecular wires 507

S. Lipiński, B.R. Bułka, D. Krychowski, Spin-dependent transport through a double dot system... 513

W. Rudziński, Effective exchange interaction in tunnelling junctions based on a quantum dot with non-collinear magnetic moments of the leads 523
W.I. Babiaczyk, B.R. Bułka, Formation of the Kondo resonance in two-atom molecular systems for various interaction limits 529
M. Wawrzyniak, J. Barnaś, Influence of interface spin-flip processes on spin accumulation and spin currents in magnetic multilayers 537
M Wołoszyn, B.J. Spisak, On the localization of electrons in disordered molecular wires 545
D. Bercioux, M. Governale, V. Cataudella, V.M. Ramaglia, Quantum networks in the presence of the Rashba effect and a magnetic field 553
E. I. Zhilyaeva, G.V. Shilov, O.A. Bogdanova, R.N. Lyubovskaya, R.B. Lyubovskii, N.S. Ovanesyan, S.M. Aldoshin, C. Train, M. Graselle, A new organic metal with the dithiooxalato-bridged anion network, β''-$(ET)_2\{[NMe_3Ph]NaCr(C_2S_2O_2)_3(MeCN)\}$ 565
M. G. Kaplunov, S.S. Krasnikova, I.K. Yakushchenko, O.N. Ermakov, S.A. Stakhamy, New organic electroluminescent materials 571

From the Guest Editors

The Conference on *New Concepts and Materials for Molecular Electronics and Nanotechnology* (CMME '04), which took place in Puszczykowo near Poznań (Poland) on 11-15 September 2004, followed the series of international seminars on highly conducting organic materials for molecular electronics organised by the Institute of Molecular Physics of the Polish Academy of Sciences:

- Polish-French meetings (Czerniejewo, 1985, Nancy, 1987, Czerniejewo, 1989),
- Polish-Soviet meetings (Czerniejewo, 1988, Chernogolovka, 1990, Kiekrz, 1992),
- 4th International Seminar (Zajączkowo, 1994),
- 5th International Seminar (Puszczykowo, 1997),
- NATO Advanced Research Workshop (Poznań, 2001).

The detailed scope of these conferences evolved with time, but it was always focused on molecular electronics and its potential applications.

CMME '04 was planned to be an interdisciplinary meeting of scientists, both theoreticians and experimentalists. The main objective was to bring together scientists from the "old" European Union and new member countries working in the field of materials science, nanotechnology and processing of molecular devices. Training of young physicists, increasing their experience, knowledge and qualifications was an important aspect of the meeting. The programme focused on the following problems:

- fundamental scientific issues for molecular technology,
- experimental characterisation and probes of molecular structures,
- synthesis, assembly and processing of molecular systems,
- electron correlations in molecular conductors,
- quantum transport through nanostructures, magnetic and molecular systems,
- theory, modelling and simulations of molecular electronic devices,
- search for new molecular devices: wires, memories, diodes, laser, and others.

The conference gathered 68 registered participants from England, France, Germany, Greece, Italy, the Netherlands, Romania, Russia, Spain, USA and Poland. Altogether, 17 invited lectures, 12 oral contributions and 45 posters were presented.

CMME '04 was organised by the Centre of Excellence for Magnetic and Molecular Materials for Future Electronics affiliated in the Institute of Molecular Physics of the Polish Academy of Sciences within the European Union project. A general goal of the Centre is to orientate our research activity towards physics of magnetic and molecular (dielectric) nanostructured materials for future applications in novel electronics, all the envisaged measures are foresighted to build the scientific capacity of the Centre as a potent research partner for leading research institutions. With the growing competition and globalisation, new trends in modern physics and technology issue a challenge to us to intensify efforts in new priority areas, which we believe are the most promising.

Bogdan Bułka, Andrzej Graja and Roman Świetlik

Materials Science-Poland, Vol. 22, No. 4, 2004

Electron–electron correlations in (BEDT–TTF)$_2$I$_3$ organic superconductors

E. BALTHES[1], A. NOTHARDT[1, 2], P. WYDER[3], D. SCHWEITZER[1*]

[1]Physikalisches Institut, Universität Stuttgart, Pfaffenwaldring 57, 70569 Stuttgart, Germany

[2]Max Planck Institut für Festkörperforschung, Heisenbergstraße 1, 70569 Stuttgart, Germany

[3]Grenoble High Magnetic Field Laboratory, 25. Avenue des Martyrs,
B.P. 166, 38042 Grenoble, CEDEX 9, France

The detection of the fractional Landau level filling factor $\nu = 1/2$ and low integer filling factors in the two-dimensional multilayer organic metal κ-(BEDT–TTF)$_2$I$_3$ is presented, which shows the occurrence of electron localisation and electron–electron correlation in this bulk metallic two-dimensional system. These effects are found in the normal conducting state of the organic superconductor κ-(BEDT–TTF)$_2$I$_3$. In addition, quantum oscillation measurements are found to be a very promising tool for direct detection of the chemical potential and its variation with magnetic field, even under rather complex fermiological conditions.

Key words: *BEDT–TTF; organic metals; Shubnikov–de Haas; de Haas–van Alphen; effective mass; Fermi surface*

1. Introduction

Radical salts of the electron donor BEDT–TTF (i.e. bis(ethylenedithio)-tetrathiafulvalene) with I_3^- anions are of a special interest, since their syntheses reveal a variety of electronic systems with identical stoichiometry, i.e. (BEDT–TTF)$_2$I$_3$, but with different structures (the so-called α-, β-, κ-, θ-, … phases). The α-phase is an organic–metal between room temperature (RT) and 135 K, with a sharp metal–insulator transition at this temperature [1], whereas the β-phase has metallic properties between RT and about 1 K, at which it becomes superconducting [2]. The κ- and θ-phases are both organic metals down to about 4 K, at which they become superconducting as well [3, 4]. Within the I$_3$ salts, the highest superconducting transitions at

---

[*] Corresponding author, e-mail: d.schweitzer@physik.uni-stuttgart.de

T_c = 8 K and ambient pressure were observed in α_t-(BEDT–TTF)$_2$I$_3$ [5] and β_H-(BEDT–TTF)$_2$I$_3$ [6], which are obtained from the initial α- and β-phases, respectively, by a special treatment of these materials.

In principle, some electron–electron correlation exist in all these different structural phases of (BEDT–TTF)$_2$I$_3$, as can be seen, for example, from strongly enhanced susceptibilities or effective masses of the carriers. In this paper, we will concentrate on electron–electron correlation in κ- and θ-(BEDT–TTF)$_2$I$_3$. Both these phases are not easily obtained in typical electrochemical process [1], but their syntheses have been brought further since they are of a special interest, e.g. with respect to their electronic dimensionality: the former κ-phase is probably the most extreme two-dimensional (2D) organic metal [7, 8] in the class of BEDT–TTF radical salts (the ratio of transfer integrals perpendicular and parallel to the conducting (*b,c*) planes is $t_\perp/t_{\parallel} < 1{,}5\cdot 10^{-4}$). The latter θ-phase is electronically quasi-two-dimensional (Q2D) and is the only BEDT–TTF radical salt that has a very small 3-dimensional (3D) closed orbit on the Fermi surface [9]. Moreover, θ-(BEDT–TTF)$_2$I$_3$ shows a strong magnetic interaction at high magnetic fields [10].

2. Experimental

κ- and θ-(BEDT–TTF)$_2$I$_3$ single crystals were synthesised by the usual electrochemical procedure [1]. Quantum oscillation (QO) experiments were performed as both de Haas-van Alphen (dHvA) and Shubnikov-de Haas (SdH) measurements in superconducting magnets (up to 10 T), as well as in resistive magnets up to 28 T provided by the Grenoble High Magnetic Field Laboratory. Different sample-contacting methods were applied in order to avoid subtle contact effects. Annealed gold wires with a thickness of 15–25 μm where applied either directly to the samples or on evaporated gold contacts. The wires were attached by gold, platinum or carbon paints, respectively. Low metallic contact resistances of about 2–5 Ω (at room temperature) could be obtained, even if the evaporation of gold was refused. ac currents of frequencies between 90 Hz and 4 kHz were applied perpendicular and parallel to the conducting planes and were limited to 50–300 μA. Low temperatures down to 0.38 K were realised by pumping on both a ^{4}He bath cryostat and its ^{3}He insert, whereas temperatures down to 20 mK were realised in a ^{3}He/^{4}He dilution refrigerator. Angle-dependent QO experiments were carried out by mounting the samples on a rotatable sample-holder.

3. Results and discussion

3.1. κ-(BEDT–TTF)$_2$I$_3$

Highly conducting (*b,c*) planes of κ-(BEDT–TTF)$_2$I$_3$ are denoted as 2D planes in the following. It should be emphasised that a typical bulk single crystal contains about

10^5 successive conducting layers. This is a typical order of magnitude within these so-called organic charge-transfer (CT) salts. The investigations presented here concentrate on the normal conducting state of this compound.

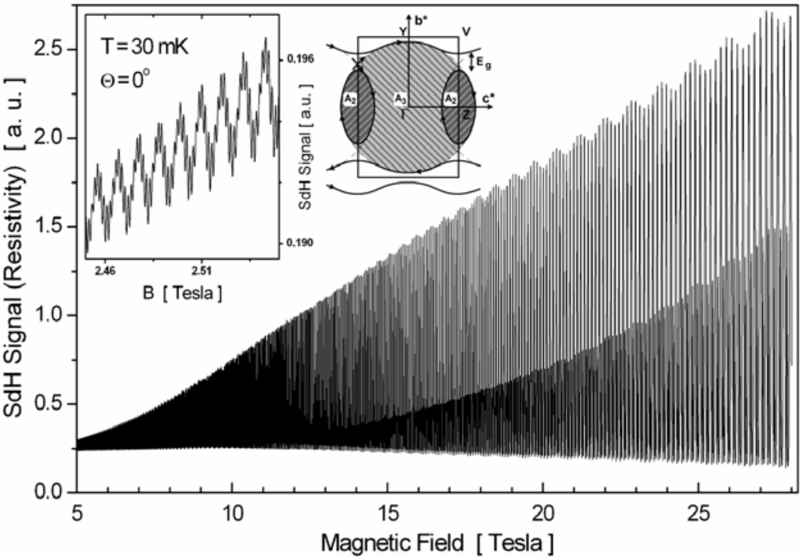

Fig. 1. Magneto-resistance and Fermi surface of κ-(BEDT–TTF)$_2$I$_3$. The inset shows the low-field part. For data evaluation, the SdH signal has to be divided by the non-oscillatory background magneto-resistance

Figure 1 shows typical SdH oscillations of κ-(BEDT–TTF)$_2$I$_3$ when the magnetic field is arranged perpendicular to the conducting planes ($\theta = 0°$) [7, 8, 11–15, 18]. A high-frequency oscillation (denoted as F_3 in the following) is observed with a strongly field-dependent amplitude (the double-peak structure of the F_3 oscillations is caused by Zeeman spin splitting). At low magnetic fields (see inset) as well as in the envelope of the signal at high magnetic fields, a lower-frequency oscillation can be recognized (called F_2 subsequently). For all κ-phase materials the Fermi surface (FS) is expected to consist of two extreme areas (see inset in Fig. 1). One of them is a closed lens-shaped orbit around Z, which encircles the extreme area A_2 and corresponds to the QO frequency $F_2 = 570$ T. The second one, a circular orbit covering A_3, corresponds very well to $F_3 = 3883$ T but is only closed as the gap ($E_g < 3$ meV) between V and Z is overcome by the so-called magnetic breakdown (MB) at sufficiently high magnetic fields (e.g., $B_{MB} \gtrsim 2$ T). For the carriers contributing to F_2 and F_3, respectively, the effective masses $m_2^* = 1.90 m_e$ and $m_3^* = 3.90 m_e$ (m_e = free electron mass) were obtained from the temperature dependence of the oscillation amplitudes [11, 12, 14–16, 18] by using the standard Lifshitz–Kosevich (LK) theory for QOs in metals [17].

During the investigations of κ-(BEDT–TTF)$_2$I$_3$ single crystals by QO experiments it turned out that regardless of the strong two-dimensionality of its electronic system, the standard LK description for QOs in 3D metals [17] applies very well. Minor deviations from the LK behaviour can be understood by considering oscillations of the chemical potential (μ) with the QO frequency F_3 [14, 18]. This quite normal LK behaviour has been observed in the entire field, temperature and angular ranges covered by the experiments, except for a set of very specific experimental conditions, namely high magnetic fields (> 12 T), low temperatures and the special field orientation $\mathbf{B} \parallel (b,c)$ (i.e., $\theta = 0°$). There, strong deviations from LK behaviour are observed, which manifest themselves as a dramatic reduction of the SdH amplitudes.

This strong departure from the LK behaviour is demonstrated in Fig. 2 which shows the temperature dependence of the SdH amplitudes of F_2 and F_3 at 25 T and $\theta = 0°$, as obtained by the Fourier transformation. The dashed lines recall the expected standard LK behaviour, whereas the full lines are a guide to the eye to illustrate the damping effects. These damping effects influence (or may even prohibit) an estimation of the effective masses m^* under these special conditions [7, 8, 11, 12, 14–16, 18]. It should be recalled here that in contrast to the results shown in Fig. 2, experiments done at $\theta > 1°$ result in quite normal LK behaviour. The damping effects at $\theta = 0°$ were attributed [7, 8, 12]* to a localisation of electrons as possible in 2D electronic systems at low filling factors ν [13], where $\nu \equiv 1$ is known as the quantum limit (QL).

Since even at 52 T, which is the highest field applied in the investigations described above, the filling factors of both F_2 and F_3 are far away from QL [19], we searched especially for low-frequency quantum oscillations, although no small orbit on the FS corresponding to such a frequency is known from extended Hückel band structure calculations [4]. The search for such low-frequency oscillations requires QO experiments the be extended to the lowest possible fields, since the widest possible field windows in [1/B] are needed for their identification. Such low-field experiments are enabled for κ-(BEDT–TTF)$_2$I$_3$ by its high crystal quality, and they were performed as SdH experiments, since at low B this method is by far more sensitive than the dHvA torque technique. Figure 3a shows a low-field SdH experiment at $\theta = 0°$ and 0.38 K, where the signal is plotted after division by the background resistivity. The variation in the depth of the oscillations suggests a main frequency, corresponding to $F_0 = 13.2$ T, and its spin-split oscillations. It was shown in Refs. [7, 14, 18] that the 00 with F_0 corresponds to a very small pocket in k-space, whose area A_{F0} represents only about 0.3% of the FS. In view of this, it is not very surprising that this small closed orbit might be beyond the resolution of standard band structure calculations.

F_0 is observed at 0.4 K, above about 1.25 T. At 2 T, the SdH amplitudes of F_0 reach about 0.04% of the background resistivity. Above about 2.4 T, the amplitudes of F_0 could not be observed directly, since the amplitudes of F_2 and F_3 increase strongly

---

*It is widely discussed in Refs. [7, 8, 12, 19] why $\theta = 0°$ is the exclusive field orientation in a metallic multilayer 2DES, where two-dimensionality (and its results) may take effect. Therefore, this discussion is not given here.

with field and dominate those of F_0 (see Fig. 3a). The *action* of F_0 onto the amplitudes of F_2 and F_3, however, can be unambiguously observed up to high fields. This is illustrated in Fig. 3b by means of the so-called “Dingle plots” (DPs), given by the implicit

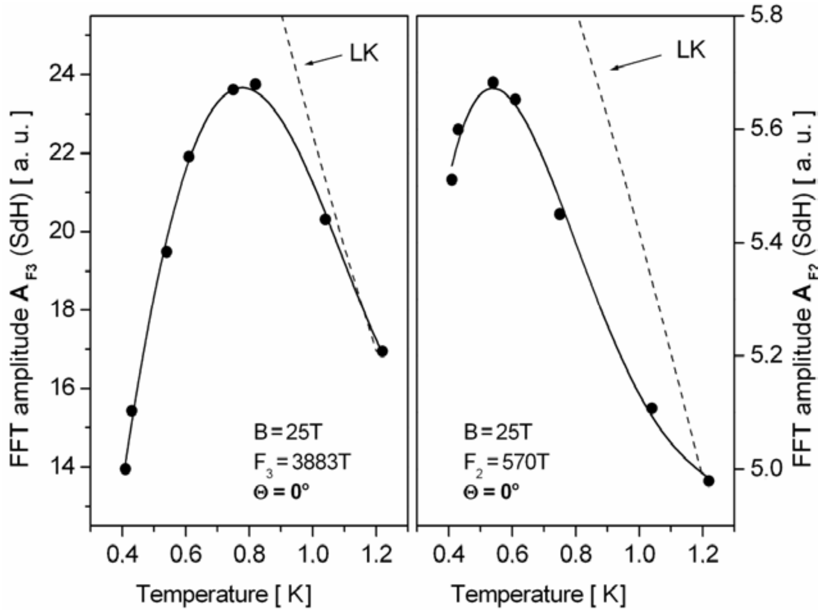

Fig. 2. Temperature dependence of the SdH amplitudes of F_2 and F_3 at 25 T and $\theta = 0°$ for κ-(BEDT–TTF)$_2$I$_3$. The dashed lines show the expected behaviour, according to the standard Lifshitz–Kosevich theory, whereas the full lines are guides to the eye

values of the FFT amplitudes of F_2 and F_3 (see left y-axis) versus $1/B$. In the standard LK theory, a DP should be linear and its slope is a measure for the Dingle temperature T_D and the corresponding scattering time τ. In the present case of magnetic breakdown (MB), the LK theory has to be extended by the so-called “coupled network description” (CND), in order to account for the magnetic field dependence of the MB probabilities. In this case, the Dingle plot of F_2 should be sublinear, while that of the MB orbit F_3 is expected to remain linear with a modified slope (both curves are determined by the Dingle temperatures (T_D) and by the magnetic breakdown field B_{MB}). Even though the low field region is least influenced by the anomalous damping effects, it can only hardly be fitted by taking an exaggerated B_{MB} ~ 4 T and a far too high T_D ~ 0.4 K (see the dotted curve in Fig. 3b for F_2 and the dashed line for F_3). This indicates that already at low fields the behaviour of the QO amplitudes can hardly be described by the LK theory and the CND. At higher fields, the discrepancy becomes much stronger. Above 2 T, the DP of F_2 strongly deviates from the estimated curve (note the logarithmic scale). The DP of F_3 shows strong deviations from linearity above about 4 T. At high fields, both DPs show strong damping effects (grey-shaded areas), which cannot be explained by MB.

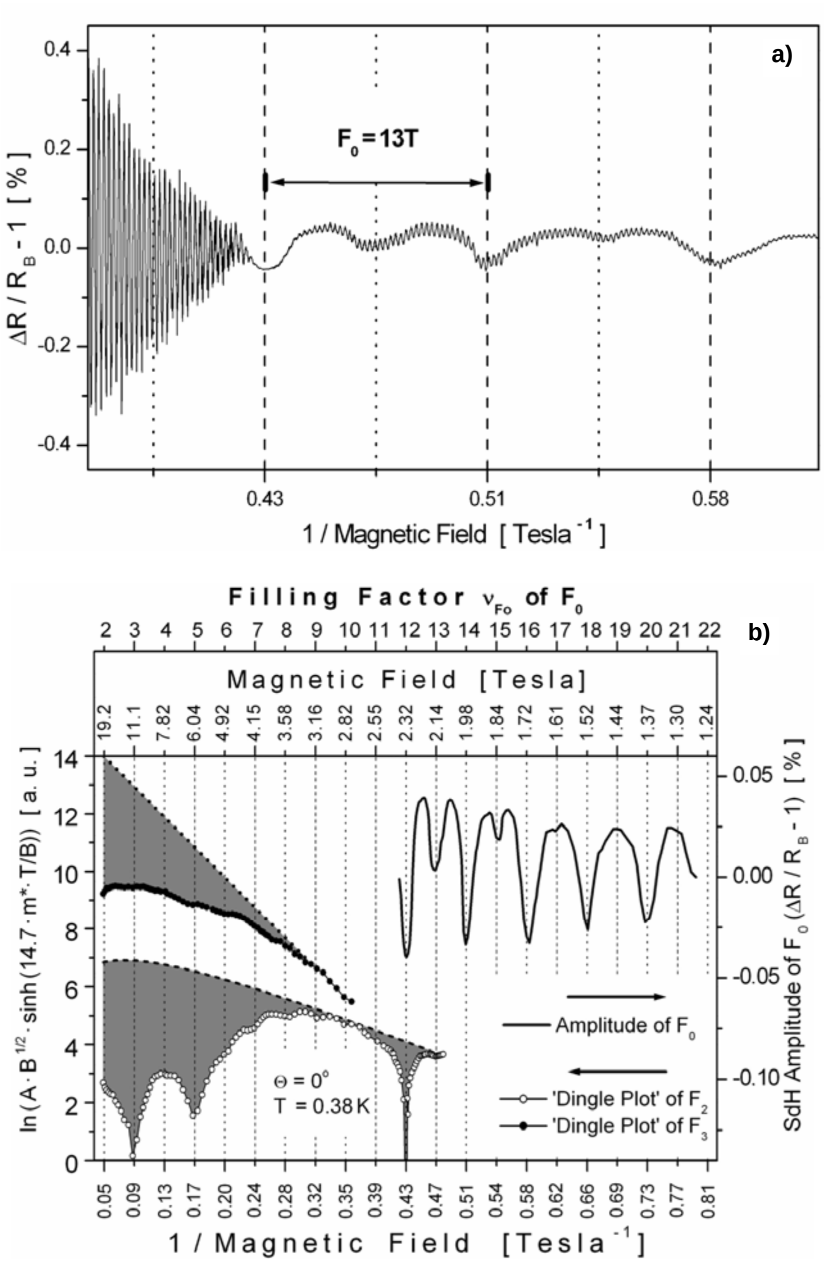

Fig. 3. Low-field SdH signal of a κ-(BEDT–TTF)$_2$I$_3$ single crystal versus $1/B$ at 0.38 K and $\theta = 0°$ after division by the background resistivity (a). SdH oscillations of F_0 in κ-(BEDT–TTF)$_2$I$_3$ single crystals at 0°. The filling factor ν of F_0 is indicated on the top axis (b), right). Dingle plots of F_2 and F_3 at 0° (see text) (b), left). The estimated dashed and dotted curves represent the expected amplitudes (accounting for magnetic breakdown). The grey-shaded areas represent the magnitude of the damping effects

The most important features in the DPs of both F_2 and F_3 are revealed by a “fine structure” of the DPs. These are discontinuities in their curvature at high fields. For understanding them, the field positions of the minima in the SdH signal of F_0 (where the Fermi energy E_F lies just between two successive spin-splitted Landau levels) are marked by grid lines and continued to high fields. The discontinuities and minima in the DP of F_2 show the same oscillatory structure as the oscillations with F_0. They occur just at the field values where the resistance minima of the F_0 oscillations are expected (i.e., where E_F lies between two adjacent spin levels of F_0, hence the corresponding ν is an integer; see top axis of Fig. 3b). The same behaviour (though weaker in magnitude) is present in the DP of F_3. Such an oscillatory structure with F_0 was observed in SdH experiments at $\theta = 0°$ on several crystals. By this, F_0 is identified to be directly involved in the damping of the amplitudes of F_2 and F_3. The filling factor ν_{F0} of F_0, as indicated on the top axis, turns out to be a controlling parameter for these effects [7]. While the amplitude of F_2 is already damped at $\nu_{F0} < 13$, that of F_3 is first demonstrably damped in the MB regime for $\nu_{F0} < 7$. The magnitude of the damping effects increases strongly with decreasing ν_{F0}. At the highest field applied, $\nu_{F0} = 2$ is reached with only two spin levels of the lowest Landau level of F_0 being occupied below the FS. While F_2 and F_3 are still at fairly high filling factors when the damping effects in their amplitudes occur, F_0 is at low ν already close to QL (the special situations at inverse field values $B^{-1} \sim 0.43$; 0.17 and 0.09 are discussed later). The observation illustrated with Fig. 3b – that the damping effects of the QO amplitudes of both F_2 and F_3 show an oscillatory pattern just with F_0 – proves that the electrons of all the corresponding “subsystems” (i.e., electronic bands) are strongly correlated. This correlation persists even though the involved bands are at very different filling factors ν. This established correlation means that the carriers contributing to F_2 and F_3 are themselves sensitive to the conditions introduced by F_0. This makes it easier to understand why the filling factor ν_{F0} of F_0 becomes a controlling parameter of the *entire* system and why at high fields it is able to force quantum limit conditions on the entire correlated electronic system.

Two-dimensionality and the obvious presence of electron correlation (EC) bring forth questions about their consequences, namely electron localisation around integer and noninteger low filling factors ν_{F0}. A correlation involving the electrons of all orbits proves that the resulting localisation effects may, accordingly, involve all carriers, not only those on the low-ν_{F0} orbit. Based on this, the damping effects of the QO amplitudes of F_2 and F_3 may be understood at this stage as a reduction of the number of mobile carriers contributing to these QOs. This reduction is caused by localisation effects, generated in turn by the low filling factors of F_0 [7, 16]. However, before going into detail with the discussion of this point, further decisive results are needed.

One of the fundamental differences between well-known semiconducting two-dimensional electron systems (2DESs) and the 2D organic metal κ-(BEDT–TTF)$_2$I$_3$ is the fact that in the former all electrons follow one single orbit, whereas in the latter they move on various orbits corresponding to very different QO frequencies. This condition can be excellently used to probe variations of the chemical potential μ with the successive QO frequencies [8]. The huge differences between the frequency values of F_0, F_2, and F_3 allow one to use the high-frequency QOs as a 'high-resolution' sensor, which probes the actual position of μ and its low-frequency variations, if present (see Refs. [8, 19] for details).

In order to investigate more thoroughly the behaviour of μ in κ-(BEDT–TTF)$_2$I$_3$, the successive field positions B_n were determined, at which the actually highest occupied n-th Landau cylinder (LC) of a certain frequency (here, e.g., F_3) passes the Fermi cylinder. The corresponding Landau level indices n_{F3} can be obtained from Landau quantisation [8, 19].

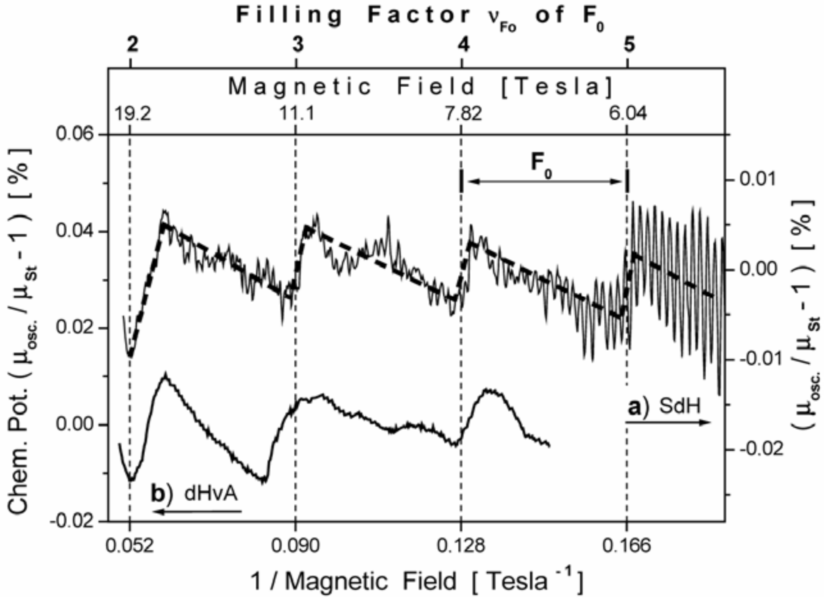

Fig. 4. Quantum oscillations of the chemical potential μ with F_0 at 0.38 K for κ-(BEDT–TTF)$_2$I$_3$. Curve a) was obtained from a SdH measurement at $\theta = 0°$ (see text), curve b) from a dHvA experiment at 9°, rescaled to 0° by the 1/cosθ law valid for 2EDSs ([8])

The result is plotted in Fig. 4. Curve a) is obtained from SdH measurements at $\theta = 0°$ and shows pronounced saw tooth oscillations of μ above c.a. 6 T, with an oscillatory sequence corresponding just to the low QO frequency $F_0 = 13$ T [16]. The filling factor ν_{Fo} and the corresponding magnetic field values are plotted on the top axes of Fig. 4. QOs with F_0 could not yet be detected above about 2.3 T (due to their low amplitude compared to the other QOs and background resistivity, see Fig. 3), whereas the μ oscillations with F_0, shown in Fig. 4, represent the detection of F_0 above 2.3 T up to high fields, where the concomitant damping effects in the SdH oscillations are prominent. This means that the μ oscillations with F_0 prove the presence of both a corresponding Landau cylinder structure and a corresponding closed orbit on the FS. The fact that "sensors" (such as F_2 and F_3 oscillations) are able to probe the influence of F_0 confirms that the electrons on the F_0, F_2, and F_3 orbits are correlated. The very different filling factors of the "sensors" F_2 and F_3 and the correlated "object", namely F_0, proves that EC bridges the very different ν and that EC is operative even at very high values of ν of F_2 and F_3.

Let us now discuss in more detail the special situations at inverse field values B^{-1} ~ 0.43, 0.17 and 0.09, which are shown in Fig. 3. In the left part of the figure the Dingle plot of F_2 shows strongest damping effects at $\nu_{F0} = 3$, 5 and 12. Even if they seem to be connected with the filling factor of F_0, they cannot be attributed in a conclusive way to this QO frequency, since they are far stronger than the damping effects at the neighbouring filling factors ν_{F0}. At first glance, the damping effects at $\nu_{F0} = 3$ and 5 might be attributed to a strong spin polarisation and the proximity of the QL, but the strong amplitude reduction at the even $\nu_{F0} = 12$ clearly contradicts both these possibilities. In Refs. [8, 19] it has been found that such effects cannot be explained by conventional damping mechanisms, even when going beyond those summarised in Ref. [17].

The strength of these special damping features in Fig. 3b gives rise to the question whether they may have a common origin beyond the existence of F_0. This in turn raises the question whether they are generated by a further low-frequency QO present in κ-(BEDT–TTF)$_2$I$_3$, whose lowest Landau level(s) only could be observed at high fields. The search for a further low-frequency oscillation in this material requires the SdH experiments to be extended further into the low-field range. This was enabled by decreasing T to dilution temperatures. It should be emphasised that this field region covers the magnetic breakdown between the closed F_2 orbit and open F_3 orbit. For this reason the oscillations of the F_3 orbit are a priori excluded in the investigations of the strong damping effects, since at these fields the F_3 orbit is not properly quantised and its investigation would be therefore influenced by MB effects.

Field sweeps were carried out on several κ-(BEDT–TTF)$_2$I$_3$ single crystals at 30 mK, with a very low sweeping rate and a field orientation perpendicular to the conducting planes (i.e., $\theta = 0°\pm0.04°$). The results of these SdH experiments are summarized in Fig. 5. The low-field part of the detected DPs of several crystals in Fig. 5b show a new oscillatory structure with a frequency of 3.8 (±0.3) T, henceforth called F_{new}. The corresponding frequency is confirmed in the FFTs of the SdH signals [19]. They clearly show that the strongest damping effects are governed by the oscillatory structure with F_{new} alone. A number of arguments have been given to show that neither $F_{\text{new}} = 3.8$ T nor $F_0 = 13$ T can be generated by an assumed warping of the FS [19] and that this new oscillatory structure, with $F_{\text{new}} = 3.8$ T, has to be attributed to a new quantum oscillation (just as F_0). The corresponding extreme area $A_{F\text{new}}$ is very small, representing merely 10^{-3} of the first Brillouin zone. In view of this, it is not surprising that the small pocket corresponding to F_{new} has not yet been found by band structure calculations. In order to verify the presence of a Landau level structure corresponding to F_{new} by a thermodynamic property, the position of the chemical potential μ and its variation was probed by the same method as before for the μ oscillations with F_0 [8, 19]. Due to the arguments discussed above, only the QOs with F_2 may be taken as "sensor" oscillations for probing μ. The results obtained on different crystals by SdH measurements at $\theta = 0°$ are depicted in Fig. 5a. The data show, with a very good agreement, an oscillatory structure with F_{new}. This confirms that F_{new} indeed corresponds to a thermodynamic quantity and confirms that F_{new} has to be identified with a quantised orbit on the FS and a Landau level structure.

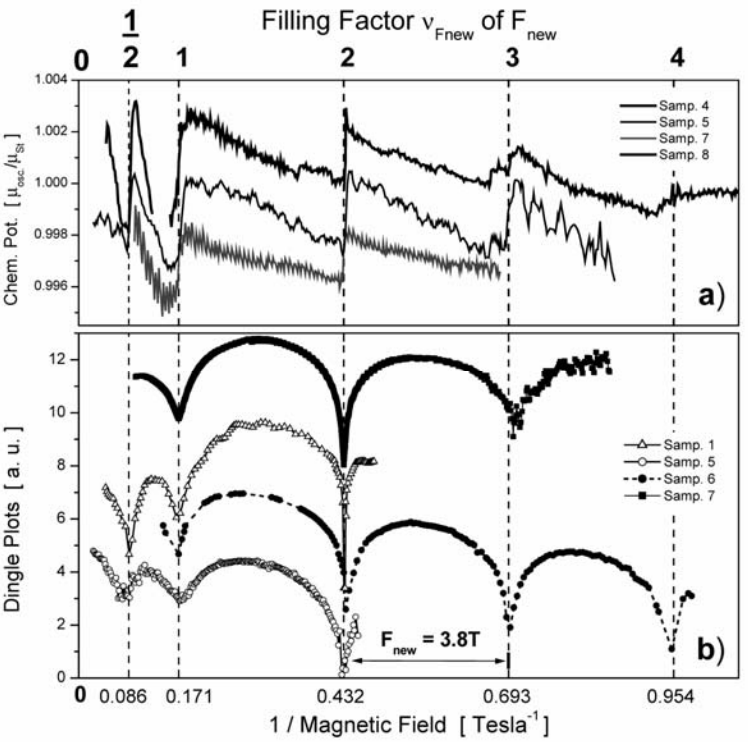

Fig. 5. Identification of the Landau level filling factors $\nu_{F\mathrm{new}}$ of F_{new} in the 2D multilayer organic metal κ-(BEDT–TTF)$_2$I$_3$ at $\theta = 0°$: a) chemical potential oscillations detected on several single crystals versus $\nu_{F\mathrm{new}}$, b) Dingle plots of the F_2 amplitudes from several single crystals as obtained by SdH measurements at 0°. Note that the *x*-axes end up at a infinite magnetic field, namely $\nu \equiv 0$

The top axis of Fig. 5 shows the attribution of the Landau level filling factors $\nu_{F\mathrm{new}}$ of F_{new} to corresponding chemical potential oscillations. Indeed, μ follows a saw tooth with its steep flank towards high fields and drops at integer values of ν, just as expected for an almost ideal 2DES. The quantum limit (QL), namely $\nu_{F\mathrm{new}} = 1$, is reached at about 0.17 T^{-1}, or 5.9 T. The equidistant saw tooth track of $\nu_{F\mathrm{new}}$ fits perfectly to the equidistant Landau level spacing of F_{new} between $\nu_{F\mathrm{new}} = 1$ and 4.

At higher fields, i.e., at $\nu_{F\mathrm{new}} < 1$, two fundamental conditions preset the interpretation of this extreme quantum limit region. First of all (as already mentioned),

$\nu_{F\mathrm{new}} = 1$ is unambiguously identified, since no further assumed Landau level can be placed equidistantly at higher fields (on the left-hand side of $\nu_{F\mathrm{new}} = 1$) in Fig. 5.

Secondly, the left margin of Fig. 5 is given by $1/B = 0$, i.e., an infinite field. This means that $\nu \sim 1/B \equiv 0$ at that point. These two definite conditions require that, within this extreme QL, the Landau level filling $\nu_{F\mathrm{new}}$ be defined in rational parts of the remaining field intercept between $\nu_{F\mathrm{new}} = 1$ and 0, which covers $\Delta[1/B] = [0\ \mathrm{T}^{-1}, 0.17\ \mathrm{T}^{-1}]$. This reveals that the additional saw tooth oscillation at about $1/B = 0.086\,\mathrm{T}^{-1}$ (i.e., $B = 11.6$ T) represents exactly $\nu_{F\mathrm{new}} = 1/2$ in the multilayer 2D system. The fact that the thermodynamic property μ oscillates at $\nu_{F\mathrm{new}} = 1/2$ proves the existence of a thermodynamically stable state. The presence of this state is also observed by strong damping effects in SdH oscillations at $\theta = 0°$ and $\nu_{F\mathrm{new}} = 1/2$, as illustrated by the Dingle plots in Fig. 5b. Likewise, the integer $\nu_{F\mathrm{new}} = 1$–4 can be identified in the Dingle plots as those field regions where the damping effects of SdH oscillations at 0° are strongest (note that strong damping effects are observed even at $\nu_{F\mathrm{new}} = 4$, which is at about 1 T).

All in all, the most recent SdH experiments on κ-(BEDT–TTF)$_2$I$_3$ presented here reveal that low integer ν and even $\nu_{F\mathrm{new}} = 1/2$ are present in this 2D multilayer organic metal. It is found that the values $\nu_{F\mathrm{new}} = 1/2; 1; 2; 3; 4$ coincide with the positions of the strongest damping effects in SdH oscillations (with the anomalous minima in the Dingle plots) at 0° in this 2DES. On the one hand, theoretical descriptions are still lacking for such 2D multilayer organic metals with correlated carriers close to the QL. On the other hand, the experimental results were found to be in remarkable agreement with theoretical descriptions and experiments for semiconducting 2DESs, where electron correlation and localisation is considered. This agreement concerns a number of fundamental aspects, especially the observation of $\nu_{F\mathrm{new}} = 1/2; 1; 2; 3; 4$ and their action onto the present correlated 2DES. It is straightforward that electron localisation in a 2DES around low ν may reduce the number of mobile carriers, thus leading to a damping of SdH amplitudes – a quantity which is only given by the (remaining) mobile carriers.

At a first glance, the observation of the $\nu = 1/2$ state in κ-(BEDT–TTF)$_2$I$_3$ is most exciting, especially since the originally expected single-layer fractional states of highest hierarchy [13], namely $\nu_{F\mathrm{new}} = 1/3; 2/3, \ldots$ are not observed here. On closer inspection, however, this is not too surprising in view of the fact that κ-(BEDT–TTF)$_2$I$_3$ is a *multilayer* 2DES. The present organic metal belongs undoubtedly to the category of coupled-multilayer systems with metallic[*], finite interlayer tunnelling. In semiconducting multilayer 2DESs, $\nu = 1/2$ is expected under such conditions [22], and this filling fraction is indeed observed here in κ-(BEDT–TTF)$_2$I$_3$. Furthermore, for finite tunnelling, both odd and even integer ν are expected by theory [22] and are indeed

---

[*] In Ref. [20] it has been shown that interlayer transport in κ-(BEDT–TTF)$_2$I$_3$ is metallic, later in Ref. [21] it was specified that it is even coherent.

observed in the present metallic 2DES*. These are very important aspects, in which the results on κ-(BEDT–TTF)$_2$I$_3$ agree remarkably with the behaviour expected for semiconducting multilayer 2DESs.

A further view on the results of the preceding sections points out that the values $\nu_{F\mathrm{new}}$ = 1/2; 1; 2; 3; 4 in the 2D multilayer organic metal κ-(BEDT–TTF)$_2$I$_3$ are brought into the system by 'subsystems'. These are the small pockets on the FS, which correspond to F_{new} and F_0, respectively, whereas the rest of the system, i.e., the orbits corresponding to F_2 and F_3, are still at fairly high ν. In view of this, the fact that low values of $\nu_{F\mathrm{new}}$ can be observed by their *action* on the electrons of the remaining system (i.e., those contributing to F_2 and F_3) proves the presence of sufficiently strong electron correlation to bridge over various bands with very different values of ν, thus involving even electrons with very high kinetic energy. Unfortunately, a theoretical description for such a complex situation in a correlated metallic multilayer 2DES is still lacking, and the electronic properties of κ-(BEDT–TTF)$_2$I$_3$ at high fields and low temperatures are still far from being understood.

3.2. Θ-(BEDT–TTF)$_2$I$_3$

Quantum oscillation experiments show two dominant oscillations with the frequencies F_α = 780 T and F_β = 4200 T [10], which correspond very well to the proposed FS of Θ-(BEDT–TTF)$_2$I$_3$ [3–5]. This agreement is confirmed by angular magnetoresistance oscillations, which additionally show that the quasi-two-dimensional FS is warped, or corrugated [10]. In addition to F_α and F_β, a further very-low-frequency oscillatory structure was observed in magnetotransport with a frequency value between 2 T and 12 T [23], which cannot be attributed to the results of any of the band structure calculations quoted above. This oscillation (henceforth called F_γ) is observed up to 10 T, at which the filling factor $\nu_{F\gamma}$ = 1 is reached [10]. A careful angular-dependent investigation showed that this oscillation is present not only for a field orientation perpendicular to the quasi-2D conducting planes, but even in a field orientation parallel to the planes. From these results it was concluded that the oscillatory structure can be attributed to a 3D pocket on the FS. Our SdH experiments clearly reproduce F_γ (comp. Ref. [10]). The presence of this very-low-frequency oscillation for fields orientated perpendicular and especially parallel to the conducting planes confirmed this 3D pocket on the FS. Attributing the F_γ oscillation to a real quantised orbit means that this Θ-phase salt indeed reaches the quantum limit at available fields. In view of this, and taking up the question of the strength of electronic two-dimensionality, we concentrated on the search for deviations in the temperature

---

[*] $\nu_{F\mathrm{new}}$ = 1/2 and all further ν_{Fj} represent *total* filling factors of the *bulk* electronic system, *not*, e.g., the filling of a single layer. This corresponds perfectly to the case of coupled 2D (multi-) layers with interlayer tunnelling as described in Ref. [22].

dependence of SdH amplitudes, especially at $\theta = 0°$. This was verified, in order to find out whether this (quasi-)2D material might show similarly strong effects of two-dimensionality (i.e., damping effects of the QO amplitudes) as those observed for the κ-phase of (BEDT–TTF)$_2$I$_3$. With SdH measurements it was found that the temperature dependence of the oscillation amplitudes of both F_α and F_β show the same behaviour at low (9 T) and high fields (23 T) [10]. Consequently, the values m^*_α(9 T) $=$ m^*_α (23 T) and m^*_β(9 T) $=$ m^*_β (23 T) were obtained for each of these frequencies. The same behaviour was found for other tilt angles between the field and conducting planes, namely $\theta \neq 0°$. Hence, contrary to the properties of the 2D κ-phase salt, in which this tilt angle plays a decisive role, no difference in the behaviour of the SdH oscillations in the Θ-phase were found for $\theta = 0°$ and $\theta \neq 0°$. This means that despite its presumably low filling factors, the SdH amplitudes of the Θ-phase of (BEDT–TTF)$_2$I$_3$ do not show strong field dependent damping effects, as does κ-(BEDT–TTF)$_2$I$_3$ at $\theta = 0°$. This, however, is not surprising in view of the fact that the small pocket on the FS of the Θ-phase salt is a 3D one. The presence of this 3D pocket on the FS certainly influences the (quasi-)2D electronic behaviour of this material.

Acknowledgements

This work was supported through the Human Potential Programme under contract N^o HPRI-1999-CT-00030 and the International Max-Planck Research School of the Max-Planck-Institutes Stuttgart, Germany.

References

[1] Bender K., Dietz K., Endres H., Helberg H.W., Hennig I., Keller H.J., Schäfer H.W., Schweitzer D., Mol. Cryst. Liq. Cryst., 107 (1984), 45; Bender K., Hennig I., Schweitzer D., Dietz K., Endres H., Keller H.J., Mol. Cryst. Liq. Cryst., 108 (1984), 359.

[2] Yagubskii E.B., Shegolev I.F., Laukhin V.N., Kononovich P.A., Kartsovnik M.V., Zvarykina A., Buravov L.I., Zh. Exp. Theor. Phys. Lett., 39 (1984), 12.

[3] Kajita K., Nishio Y., Moriyama S., Sasaki W., Kato R., Kobayashi H., Kobayashi A., Sol. State Commun., 64 (1987), 1279; Balthes E., Breining A., Kahlich S., Moldenhauer J., Schweitzer D., Bele P., Brunner H., Heinen I., Nuber B., Keller H.J., Synth. Metals, 56 (1993), 2859.

[4] Kobayashi H., Kato R., Kobayashi A., Moriyama S., Nishio Y., Kajita K., Sasaki W., Chem. Lett., 1986, 2017.

[5] Baram G.O., Buravov L.I., Degtariev L.C., Kozlow M.E., Laukhin V.N., Laukhin E.E., Orischenko V.G., Pokhodnia K.I., Scheinkman M.K., Shibaeva R.P., Yagubskii E.B., JETP Lett., 44 (1986), 293; Schweitzer D., Bele P., Brunner H., Gogu E., Haeberlen U., Hennig I., Klutz T., Swietlik R., Keller H. J., Z. Phys., B 67 (1987), 489.

[6] Creuzet F., Jerome D., Schweitzer D., Keller H.J., Europhys. Lett., 1 (1986), 461.

[7] Balthes E., Schiller M., Schweitzer D., Heinen I., Strunz W., Steep E., Jansen A.G.M., Wyder P., Europhys. Lett., 47 (1999), 70.

[8] Balthes E., Wyder P., Schweitzer D., Solid State Commun., 124 (2002), 141.

[9] Tokumoto M., Swanson A.G., Brooks J.S., Agosta C.C., Hannahs S.T., Kinoshita N., Anzai H., Tamura M., Tajima H., Kuroda H., Ugawa A., Yakushi K., Physica, B 184 (1993), 508.

[10] NOTHARDT A., BALTHES E., SALAMEH B., SCHMIDT W., SCHWEITZER D., STREMPFER J., KEIMER B., MAUDE D., Mat. Sci.-Poland, 22 (2004), 299.

[11] HEINECKE M., WINZER K., SCHWEITZER D., Z. Phys., B 93 (1993), 45; BALTHES E., SCHWEITZER D., HEINEN I., KELLER H.J., BIBERACHER W., JANSEN A.G.M., STEEP E., Synth. Metals, 70 (1995), 841; SCHWEITZER D., BALTHES E., KAHLICH S., HEINEN I., KELLER H.J., STRUNZ W., BIBERACHER W., JANSEN A.G.M., STEEP E., Synth. Metals, 70 (1995), 857; BALTHES E., SCHWEITZER D., HEINEN I., KELLER H.J., BIBERACHER W., JANSEN A.G.M., STEEP E., Acta Phys. Pol., 87 (1995), 767; HELM P., KRAAK W., SCHWEITZER D., KELLER H.J., Phys. Stat. Sol., (b) 189 (1995), 509.

[12] BALTHES E., SCHWEITZER D., HEINEN I., KELLER H.J., STRUNZ W., BIBERACHER W., JANSEN A.G.M., STEEP E., Z. Phys., B 99 (1996), 163.

[13] v. KLITZING K., DORDA G., PEPPER M., Phys. Rev. Lett. 45 (1980), 494; R.E. Prange, S.M. Girvin, (Eds.), *The Quantum Hall Effect*, 2nd Edition, Springer, Berlin, 1989; TSUI D.C., STÖRMER H.L., GOSSARD A.C., Phys. Rev. Lett., 48 (1982), 1559; LAUGHLIN R. B., Phys. Rev. Lett., 50 (1983), 1395; HALPERIN B. I., Helv. Phys. Acta 56 (1983), 75.

[14] HARRISON N., MIELKE C.H., RICKEL D.G., WOSNITZA J., QUALLS J.S., BROOKS J.S., BALTHES E., SCHWEITZER D., HEINEN I., STRUNZ W., Phys. Rev. B 58 (1998), 10248.

[15] BALTHES E., SCHILLER M., SCHWEITZER D., HEINEN I., STRUNZ W., STEEP E., JANSEN A.G.M., WYDER P., Physica, C 317-318 (1999), 108.

[16] BALTHES E., WYDER P., SCHWEITZER D., J. Phys. Chem. Sol., 63 (2002), 1249.

[17] LIFSHITZ I.M., KOSEVICH A.M., Zh. Eksp. Teor. Fiz., 29 (1955), 730; Sov. Phys. JETP, 2 (1956), 636; SHOENBERG D., *Magnetic oscillations in metals*, Cambridge Univ. Press, 1984.

[18] ITSKOVSKY M.A., ASKENAZY S., MANIV T., VAGNER I.D., BALTHES E., SCHWEITZER D., Phys. Rev., B 58 (1998), R 13347.

[19] BALTHES E., Habilitation Thesis, Universität Stuttgart, 2004.

[20] BALTHES E., BREINING A., KAHLICH S., MOLDENHAUER J., SCHWEITZER D., BELE P., BRUNNER H., HEINEN I., NUBER B., KELLER H.J., Synth. Met., 55–57 (1993), 2859.

[21] WOSNITZA J., HAGEL J., QUALLS J.S., BROOKS J.S., BALTHES E., SCHWEITZER D., SCHLUETER J.A., GEISER U., MOHTASHAM J., WINTER R.W., GARD G.L., Phys. Rev. B 65 (2002), R180506.

[22] REZAYI E.H., HALDANE F.D.M., Bull. Am. Phys. Soc., 32, 892 (1987); CAKRABORTY T., PIETILÄINEN P., Phys. Rev. Lett. 59, (1987) 2784; Cakraborty T., Pietiläinen P.[in:], *Recent Progress in Many-Body Theories*, A. Kallio, E. Pajane, R.F. Bishop (Eds.), Plenum, New York, 1988, p.113; HE S., XIE X.C., DAS SARMA S., ZHANG F.C., Phys. Rev., B 43 (1991), 9339; MURPHY S.Q., EISENSTEIN J.P., BOEBINGER G.S., PFEIFFER L.N., WEST K.W., Phys. Rev. Lett., 72 (1994), 728; EISENSTEIN J.P., BOEBINGER G.S., PFEIFFER L.N., WEST K.W., HE S., Phys. Rev. Lett. 68, (1992), 1383.

[23] TERASHIMA T., UJI S., AOKI H., TAMURA M., KINOSHITA M., TOKUMOTO M., Solid State Commun. 91 (1994), 595.

Received 14 September 2004
Revised 3 November 2004

Materials Science-Poland, Vol. 22, No. 4, 2004

Quantum oscillation measurements on the organic superconductor Θ-(BEDT–TTF)$_2$I$_3$

A. NOTHARDT[1, 2*], E. BALTHES[1], B. SALAMEH[1], W. SCHMIDT[1],
D. SCHWEITZER[1], J. STREMPFER[2], B. KEIMER[2], D. MAUDE[3]

[1]Physikalisches Institut, Universität Stuttgart, Pfaffenwaldring 57, 70569 Stuttgart, Germany

[2]Max-Planck Institute for Solid State Research, Heisenbergstraße 1, 70569 Stuttgart, Germany

[3]Grenoble High Magnetic Field Laboratory, 25 Avenue des Martyrs,
B.P. 166, 38042 Grenoble, Cedex 9, France

Quantum oscillation experiments were performed on high quality single crystals of Θ-(BEDT–TTF)$_2$I$_3$. Their electronic properties are similar to those of crystals of Θ-(BEDT–TTF)$_2$(I$_3$)$_{1-x}$(AuI$_2$)$_x$ ($x < 0.02$). Nevertheless, in the neat crystals used here, quantum oscillations for the α-orbit (F_α= 780 T) are observed already at a field of 2 T, and the magnetic breakdown of the β-orbit (F_β = 4200 T) occurs at 3 T. In the large magnetic field range, in which quantum oscillations are observed, the warping of the Fermi surface of the α-orbit and β-orbit could be determined to be ΔF_α = 6.6 T and ΔF_β = 16.6 T, respectively. At high magnetic fields, the de Haas–van Alphen signal consists of pronounced inverse saw-tooth oscillations, and the Shubnikov–de Haas signal has a peaked structure. This behaviour is interpreted in terms of magnetic interaction.

Key words: *quantum oscillation*; *magnetic field; organic superconductors; Fermi surface*

1. Introduction

The electrochemical synthesis of I_3^- anions with radical salts of the electron donor BEDT–TTF (i.e., bis(ethylenedithio)tetrathiafulvalene) results in a number of electronically quasi-two dimensional (Q2D) organic metals with identical stoichiometry, namely (BEDT–TTF)$_2$I$_3$, but different structures. The usual synthesis produces mainly crystals of the so-called α- or β-phases, but also single crystals of the κ- or even Θ-phase may grow. Here we present quantum oscillation experiments on neat single crystals of Θ-(BEDT–TTF)$_2$I$_3$. In earlier investigations on crystals with a similar stoichiometry, Θ-(BEDT–TTF)$_2$(I$_3$)$_{1-x}$(AuI$_2$)$_x$ ($x < 0.02$) [1–7] it has been shown that

---

[*] Corresponding author, e-mail: a.nothardt@physik.uni-stuttgart.de.

those crystals are metallic down to low temperatures [1]. It has also been demonstrated [1, 2] that a part of the Θ-$(BEDT–TTF)_2(I_3)_{1-x}(AuI_2)_x$ ($x < 0.02$) crystals indeed become superconducting at 3.6 K, while others do not show a superconducting transition. The origin for this behaviour is not clear yet. The Fermi surface was investigated by Shubnikov–de Haas (SdH) and de Haas–van Alphen (dHvA) measurements. In high magnetic fields, the dHvA oscillations became saw-toothed [3], which was ascribed to an oscillating chemical potential in connection with strong two-dimensional electronic properties ($\rho_\perp/\rho_\parallel = 1000$) [4]. Our investigations on neat Θ-$(BEDT–TTF)_2I_3$ single crystals yield somewhat different results. It will be shown that the Fermi surface is warped and that besides “inverse saw-tooth” dHvA oscillations in high magnetic fields, peaky SdH oscillations are also observed. Both results are discussed in terms of the so-called magnetic interaction effect [8].

2. Experimental

Θ-$(BEDT–TTF)_2I_3$ crystals were synthesised electrochemically, however without adding AuI_2^- anions during the preparation as mentioned in previous reports [1, 5]. Some single crystals used in the experiments showed a steep superconducting transition, while others did not (see above). Quantum oscillation experiments were made in a ^{3}He cryostat (0.4 K), using a rotatable sample-holder. High magnetic fields on the superconducting magnets (up to 10 T) as well as on the resistive magnets (up to 28 T) were provided by the Grenoble High Magnetic Field Laboratory. DHvA experiments were carried out by the torque method [8], whereas for SdH measurements the single crystals were contacted by the “standard four probe method” using 25 μm gold wires and carbon paint. The current was applied normal to the highly conducting (a, b) plane*. In order to verify the reproducibility of the results, the SdH measurements were carried out simultaneously for several crystals on completely separated electronic setups.

3. Results

The crystal structure of neat Θ-$(BEDT–TTF)_2I_3$ crystals belongs to the monoclinic space group with $P2(1)/c$ symmetry. The lattice parameters are: $a = 9.926$ Å, $b = 10.074$ Å, $c = 34.201$ Å, $\beta = 98.27°$. The packing motive of the molecules and the structure data are very similar to those of Θ-$(BEDT–TTF)_2(I_3)_{1-x}(AuI_2)_x$ ($x < 0.02$) crystals [1], whereby most of the Θ-$(BEDT–TTF)_2(I_3)_{1-x}(AuI_2)_x$ ($x < 0.02$) crystals are twinned to form a pseudo-orthorhombic lattice with half of the length in the a-direction as compared to the monoclinic cell. Since most of the present neat

---

*The structure data of the monoclinic cell were used.

Θ-(BEDT–TTF)$_2$(I$_3$) crystals are not twinned, the frequencies of quantum oscillations as well as the warping of the Fermi surface could be determined very accurately.

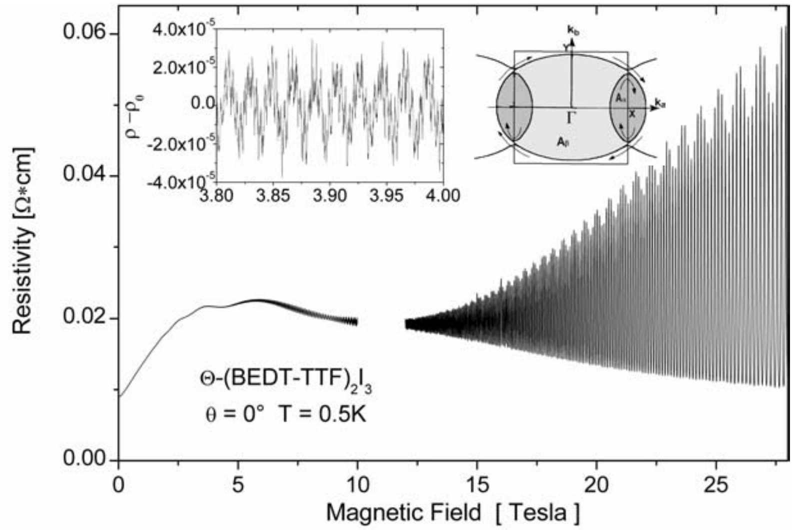

Fig. 1. Fermi surface and magneto-resistance of Θ-(BEDT–TTF)$_2$I$_3$ (see text). The inset shows the low-field part after subtracting the nonoscillatory background magneto-resistance

From the huge SdH oscillations shown in Fig. 1, the frequencies F_α = 780±10 T of the small α-orbit, F_β = 4200±20 T of the larger β-orbit (see the Fermi surface in Fig. 1), as well as F_γ = 7.8±0.2 T of the small three-dimensional (3D) orbit [3, 6] were determined (the orbit corresponding to F_γ is not shown on the Fermi surface). The inset in Fig. 1 shows the low-field SdH signal after subtracting the nonoscillatory background magnetoresistance. The angular dependences of the frequencies and the effective carrier masses ($m_\alpha = 1.8m_0$ and $m_\beta = 3.5m_0$ at an angle of 0°; m_0 is a free electron mass) are obtained by declining the conducting planes out of the position perpendicular to the magnetic field (where $B \perp (a, b) \equiv \theta = 0°$). These properties show a $1/\cos\theta$ behaviour as expected from a Q2D electronic system.

Figure 2a, b shows the so-called Dingle plots of the α- as well as the β-orbit versus the inverse magnetic field, as well as the SdH oscillations after filtering the experimental data by a band-pass filter (for 780 T in Fig. 2a and 4200 T in Fig. 2b). Figure 2c shows the field range from 4 to 10 T and compares the raw data of the SdH experiment after subtracting the background (bottom) with the composed curve obtained from the filtered signals of Figs. 2a and b (top). The minima in the Dingle plots in Fig. 2a and b correspond to the minima (i.e., “beating nodes”) of the oscillation amplitudes. Therefore, a Dingle plot is a good way to determine these beating nodes. The beating nodes, however, can be observed in the oscillation curves as well, which were band-pass filtered. Figures 2a–c show the 1st and 2nd beating nodes of the α-frequency and the 2nd and 3rd nodes of the β-frequency. From the beating frequencies, $\Delta F_\alpha = 6.6$ T and $\Delta F_\beta = 16.6$ T, the warping (i.e., corrugation) of the Fermi surface is estimated to be 0.8% for the α-orbit and 0.4% for the β-orbit. The beating nodes of the β-frequency are at the theoretically predicted positions for beating in consequence of warping [9], whereas the beating nodes of the α-frequency are shifted, so that they occur at the positions: $B_n = \Delta F/(n + 1/4)$. A similar shift for beating nodes in SdH measurements was observed in (BEDT–TTF)$_4$[Ni(dto)$_2$] crystals by Schiller et al. [10]. As soon as the crystal is declined to the magnetic field by an angle of 15° (which represents the first Yamaji angle, measured by Kajita et al. [2]), the beating of the β-frequency disappears. This confirms that the beating is created by a warping of the Fermi surface, but not by the assumed twinned structure of the crystal.

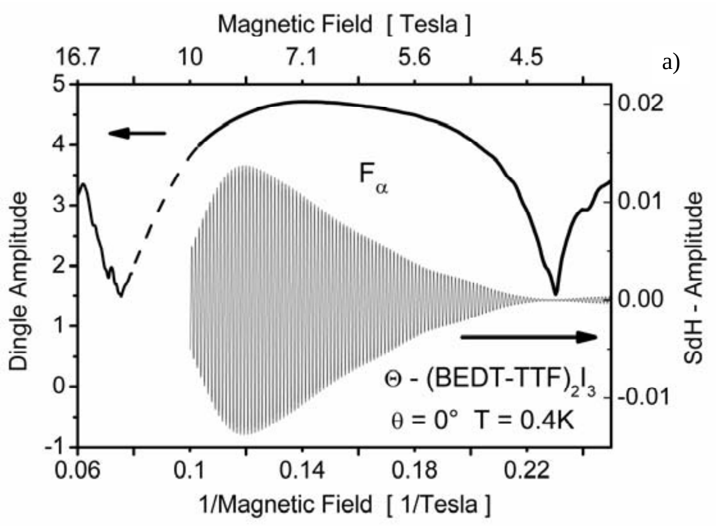

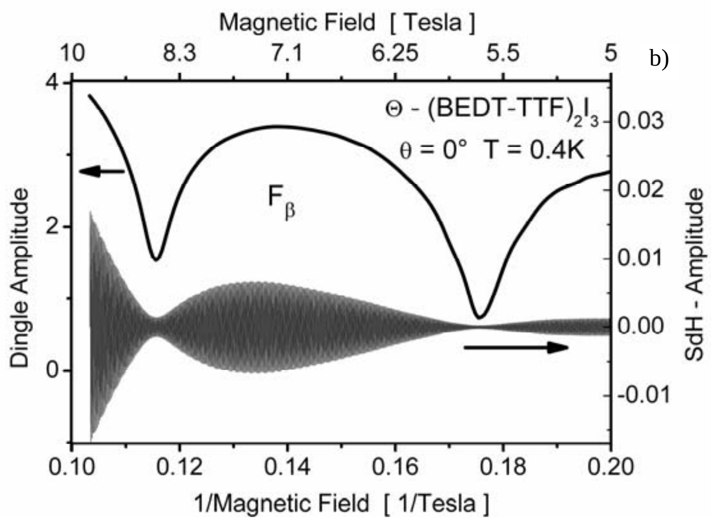

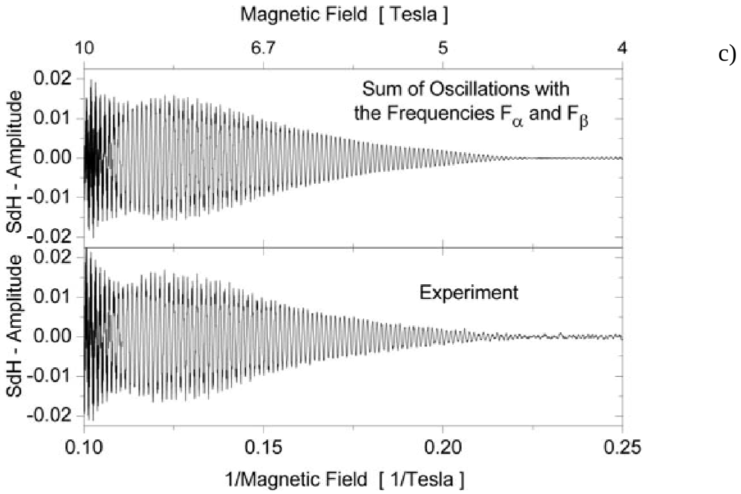

Fig. 2. Dingle plots of F_α (a) and F_β (b), and the detected SdH oscillations versus 1/*B*, after passing them through a band-pass filter, for 780 T (a) and 4200 T (b). Detected SdH oscillations versus 1/*B* (for 4 T ≤ *B* ≤ 10 T) after subtracting the background (c). For comparison (top): The composed signal, obtained from the filtered signals of (a) and (b)

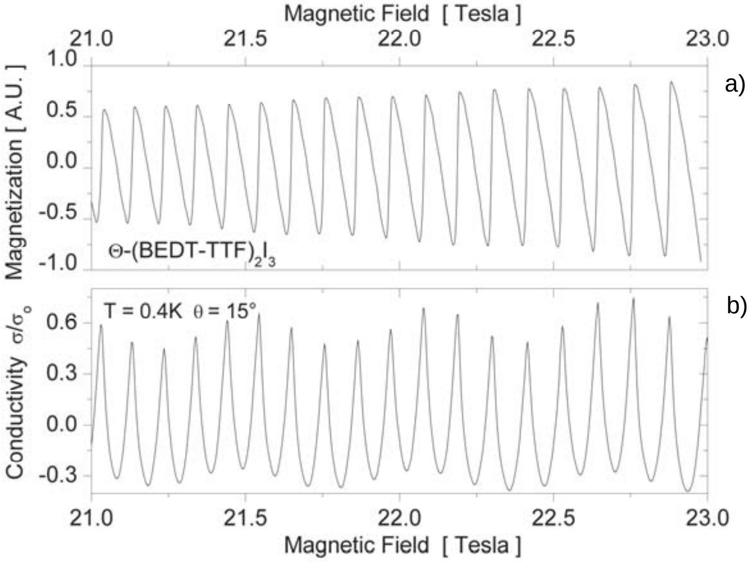

Fig. 3. Comparison of the shape of the oscillations in magnetization (a) and conductivity (b) at $T = 0.4$ K, $\theta = 15°$, and high magnetic fields (see text for details)

Concerning the 3D γ-orbit ($F_\gamma = 7.8$ T) [6], it can be estimated from Fig. 1 that the last Landau cylinder passes the γ-orbit at a field of about 10 T (to be seen as a minimum in resistivity). The 3D γ-orbit has the shape of a cigar. The cross-section normal to the *b*-direction has a size of 0.018 nm^{-2} (1.9 T).

At high magnetic fields, the oscillations in magnetization (i.e., dHvA) show a so-called inverse saw-tooth shape for angles 15° ≤ $\Theta \leq$ 60°, which means that the sheer flank is on its low-field side (see Fig. 3, top). Corresponding to this sharp saw-tooth signal, the fast Fourier transform (FFT) shows 18 harmonics of F_β (not shown here). A similar behaviour is observed in the SdH signal, where the conductivity should be identical to the derivative of the dHvA signal. In fact the magnetic field dependence of conductivity at high fields shows a peaky structure (shown in the bottom of Fig. 3), and the FFT also shows a rich harmonic content of F_β. Considering the above-mentioned relation between SdH and dHvA signals, it is important that the peaks in the SdH signal point *upwards*. This fact confirms that the shape of the dHvA signal is indeed an 'inverse' saw-tooth, instead of a 'normal' saw-tooth, which might be shifted by 180^{o} within the dHvA data detection process. The orientation of the saw-tooth is decisive for its interpretation (see below).

4. Discussion

The observed huge quantum oscillation amplitudes (see Fig. 1) indicate a high quality of the neat Θ-$(BEDT–TTF)_2I_3$ crystals. The observed frequencies are similar to those detected in Θ-$(BEDT–TTF)_2(I_3)_{1–x}(AuI_2)_x$ (x < 0.02). The so-called magnetic breakdown between the small α-orbit (F_α = 780 T) and β-orbit (F_β = 4200 T) was observed at a magnetic field of only 3 T at 0.4 K (and not at 15 T, as mentioned in the literature for Θ-$(BEDT–TTF)_2(I_3)_{1–x}(AuI_2)_x$ (x < 0.02) crystals [3]).

As pointed out above, the oscillations in magnetization (dHvA) show an inverse saw-tooth (see Fig. 3 top) at high magnetic fields. One origin of saw-tooth variations in the magnetization may be an oscillation of the chemical potential μ in a strong two-dimensional electronic system as a function of the magnetic field. For such a situation, two cases can be distinguished. At first, the 2D closed orbit in *k*-space (here corresponding to F_β) may be coupled to a further trajectory on the FS, to which the carrier tunnelling is possible. In this case, the latter trajectory would represent a reservoir for F_β, and in conclusion the orientation of the saw-tooth would be "inverse" as described above. In the second case (not given here), i.e. in the absence of such a reservoir, the orientation of the saw-tooth would be "normal", i.e. with its sheer flank on its high-field side [7, 8]. At a first glance, the orientation of the observed saw-tooth should hint the realisation of the former case, with the 3D γ-orbit as a candidate for such a reservoir. F_γ can probably be excluded as an electron reservoir, however, since F_γ is already present at low fields (1 T) and a magnetic breakdown between F_β and F_γ is not observed up to 10 T. This means that the energy gap(s) between the F_γ-orbit and the other 2D orbits (i.e., F_α and F_β) is (are) too large to enable carrier tunnelling. This excludes F_γ from being a reservoir. Therefore, the observed "inverse" saw-tooth dHvA oscillations must have a different explanation.

If the dHvA signal is so huge that the oscillatory magnetization itself modifies the effective internal field, the shape of oscillations may be turned to an inverse saw-tooth with its sheer flank on its low-field side [8]. Considering this, we assume that magnetic interaction is the dominant reason for the inverse saw-tooth signal at high magnetic fields in the dHvA-experiment for Θ-$(BEDT–TTF)_2I_3$, rather than the above-mentioned presence of a reservoir. The observed strong temperature dependence of the saw-tooth supports the interpretation proposed above. In addition, a paramagnetic behaviour was observed in this material at temperatures below 20 K and fields above 0.05 T by SQUID and ESR measurements [11], whereas the material showed poor metallic behaviour (and even diamagnetic behaviour due to superconductivity below 3.5 K) at lower fields. This feature might be a further indication of the presence of magnetic interaction in Θ-$(BEDT–TTF)_2I_3$ at high fields.

Acknowledgements

This work has been supported by the Human Potential Programme under contract N° HPRI-1999-CT-00030 and the International Max-Planck Research School of the Max-Planck-Institutes Stuttgart, Germany.

References

[1] KOBAYASHI H., KATO R., KOBAYASHI A., MORIYAMA S., NISHIO Y., KAJITA K., SASAKI W., Chem. Lett., 1986, 2017.

[2] KAJITA K., NISHIO Y., TAKAHASHI T., SASAKI W., KATO R., KOBAYASHI H., KOBAYASHI A., Solid State Commun., 70 (1989), 1181.

[3] TOKUMOTO M., SWANSON A.G., BROOKS J.S., TAMURA M., TAJIMA H., KURODA H., Solid State Commun., 75 (1990), 439.

[4] KAJITA K., NISHIO Y., MORIYAMA S., SASAKI W., KATO R., KOBAYASHI H., KOBAYASHI A., Solid State Commun., 64 (1987), 1279.

[5] KOBAYASHI H., KATO R., KOBAYASHI A., NISHIO Y., KAJITA K., SASAKI W., Chem. Lett., 1986, 789.

[6] TERASHIMA T., UJI S., AOKI H., TAMURA M., KINOSHITA M., TOKUMOTO M., Solid State Commun. 91 (1994), 595.

[7] TOKUMOTO M., SWANSON A.G., BROOKS J.S., AGOSTA C.C., HANNAHS S.T., KINOSHITA N., ANZAI H., TAMURA M., TAJIMA H., KURODA H., UGAWA A., YAKUSHI K., Physica B, 184 (1993), 508.

[8] SHOENBERG D., *Magnetic oscillations in metals,* Cambridge University Press, Cambridge, 1984.

[9] YAMAJI K., J. Phys. Soc. Jpn., 58 (1989) 1520.

[10] SCHILLER M., SCHMIDT W., BALTHES E., SCHWEITZER D., KOO H.-J., WHANGBO M.H., HEINEN I., KLAUSA T., KIRCHER P., STRUNZ W., Europhys. Lett., 51 (2000), 82.

[11] SALAMEH B., NOTHARDT A., MUCH A., SCHWEITZER D., Conference on New Concepts and Materials for Molecular Electronics and Nanotechnology, Poznań 2004, Conf. Abstracts, p. 59.

Received 14 September 2004
Revised 29 September 2004

Materials Science-Poland, Vol. 22, No. 4, 2004

Peierls phonons in organic molecular crystals and in charge transfer salts

ALBERTO GIRLANDO[1*], MATTEO MASINO[1], ALDO BRILLANTE[2],
RAFFAELE G. DELLA VALLE[2], ELISABETTA VENUTI[2]

[1] Dip. Chimica G.I.A.F. and INSTM-UdR Parma, Parma University, Parma, Italy

[2] Dip. Chimica Fisica ed Inorg. and INSTM-UdR Bologna, Bologna University, Italy

We review the Quasi-Harmonic Lattice Dynamic (QHLD) method, which we have recently implemented and adopted to carefully reproduce the crystal structure and lattice phonon dynamics of molecular crystals as a function of temperature and pressure. Association with mean field electronic structure calculations allows us to characterize the Peierls coupling, namely the coupling between electrons and lattice phonons. We apply this method to organic superconductors based on bis-ethylene-dithio-tetrathiafulvalene (BEDT-TTF), showing that many experimental findings related to superconducting properties are rationalized in terms of the Peierls coupling. Electron–intramolecular phonon coupling and electron –electron interactions, however, have to be taken into account for a full characterization. We also present results concerning another class of molecular crystals, the acenes. In this case, the focus is on the understanding of the temperature dependences of mobilities. First and foremost, however, we emphasize the possibility of accurately predicting both the crystal structure and lattice phonon spectral signatures. We analyse pentacene and tetracene, showing that both systems can crystallize into two different polymorphs. The two polymorphs have comparable stabilities, and can coexist in the same crystallite. Raman spectroscopy in the lattice phonon region is used as a convenient tool to identify the two phases. The Peierls coupling strength of pentacene is evaluated.

Key words: *electron-phonon coupling; lattice phonons; organic superconductors; acenes*

1. Introduction

The coupling between electrons and intermolecular (lattice) phonons, or the Peierls coupling, is at the heart of many fundamental phenomena in low-dimensional molecular crystals. Yet the role of Peierls phonons in basic properties such as charge transport has to be clarified. We have recently implemented [1, 2] a method (Quasi

---

[*] Corresponding author, e-mail: alberto.girlando@unipr.it.

Harmonic Lattice Dynamics – QHLD) able to accurately reproduce the crystal structure and lattice phonon dynamics of complex molecular crystals, also as a function of temperature and pressure. Association with Raman measurements and mean field electronic structure calculations allows one to characterize the phonon structure and the corresponding Peierls coupling. Here, we describe the successful application of the model to two rather different classes of molecular crystals, bis-ethylene-dithio-tetrathiafulvalene (BEDT-TTF) superconductors and acene semiconductors.

2. The QHLD method

In our approach, we start from the isolated molecule, using standard DFT methods (6-31G(d) basis, B3LYP hybrid functional) to calculate the molecular geometry, atomic charges, vibrational frequencies and Cartesian eigenvectors of the normal modes. These data are used to deal with molecular degrees of freedom when considering the molecular crystal. The intermolecular potential energy Φ_{inter} in the molecular crystal is expressed in terms of an atom–atom Buckingham model, combined with an electrostatic contribution represented by the set of DFT (ESP) atomic charges q_m calculated for the isolated molecule [1, 2]:

$$\Phi_{\text{inter}} = \frac{1}{2}\sum_{mn}\left[A_{mn}\exp\left(-B_{mn}r_{mn}\right) - \frac{C_{mn}}{r_{mn}^{6}} + \frac{q_m q_n}{r_{mn}}\right] \tag{1}$$

where the sum extends over all distances r_{mn} between pairs m, n of atoms in *different* molecules. The Ewald method is used to accelerate the convergence of the Coulomb interaction $q_m q_n / r_{mn}$. A_{mn}, B_{mn}, and C_{mn} in the Buckingam part of the potential are empirical atomic parameters – there is one triad for each different pair of atoms involved. The Buckingam parameters should be, in principle, universal parameters, transferable among different crystals containing the same atoms. In practice, they are transferable only within the class of molecular crystals they have been tuned for.

Given the above atom–atom potential, the effect of temperature T and pressure p are accounted for by computing the structure that has minimum Gibbs energy $G(p,T)$ with the QHLD method. In this method, where the vibrational Gibbs energy of the phonons is estimated in the harmonic approximation, the Gibbs energy of the system is expressed as:

$$G(p,T) = \Phi_{\text{inter}} + pV + \sum_{\mathbf{q},j}\left\{\left(\frac{h\nu_{q,j}}{2}\right) + k_B T \ln\left[1 - \exp\left(-h\nu_{q,j}/k_B T\right)\right]\right\} \tag{2}$$

where V is the molar volume, $\sum_{\mathbf{q},j}(h\nu_{q,j}/2)$ is the zero-point energy, and the last term is the entropic contribution of the lattice phonons. The sums extend over all j phonon branches of frequency $\nu_{\mathbf{q},j}$ and wave vector $\mathbf{q}$. Given an initial lattice structure, one computes Φ_{inter} and its derivatives with respect to the molecular coordinates. The second derivatives form the dynamical matrix, which is diagonalised to yield the lattice phonon frequencies and eigenvectors. The structure as a function of T and p is then obtained by minimizing $G(T,p)$ with respect to the lattice parameters, molecular positions and orientations.

In the above expressions, the lattice phonons are considered separately from molecular vibrations. This is the so-called rigid molecule approximation, but in crystals made up of large molecules the approximation is no longer valid, and there is a certain amount of coupling between lattice and low-frequency intramolecular phonons. To account for such a coupling, we adopt an exciton-like approach [3], where the interaction between different molecular coordinates is mediated by the intermolecular potential depending on atomic displacements. These correspond to the Cartesian eigenvectors of the isolated molecule normal modes calculated by DFT.

3. The Peierls coupling strength

The QHLD method provides a rather accurate description of the lattice phonon frequencies and eigenvectors, independent of the crystal electronic structure. In order to evaluate the strength of the Peierls coupling, we also need a proper description of the electronic degrees of freedom, which is not a trivial problem in the case of molecular crystals, as they are characterized by narrow bands and strong electronic correlations. Coherently with the QHLD scheme, we adopt a semi-empirical approach, which is less computer demanding and gives a better insight into the type of lattice phonons involved in the Peierls coupling. We define the Peierls, or electron–lattice phonon (e–LP), coupling constants $g(KL;\,\mathbf{q},j)$ as:

$$g\left(KL;\mathbf{q},j\right)=\left(\frac{\partial t_{KL}}{\partial Q_{\mathbf{q}j}}\right)_0 \tag{3}$$

where t_{KL} is the hopping or charge-transfer (CT) integral between neighbouring pairs of molecules KL and $Q_{\mathbf{q}j}$ is the dimensionless normal coordinate for the jth phonon with the wave vector $\mathbf{q}$. In this definition, the electronic part is dealt with in real space, being relevant to a pair of molecules: the CT integrals are indeed calculated as the variation of the HOMO (LUMO) energy in going from an isolated molecule to the KL pair. The HOMO (LUMO) energy and its $Q_{\mathbf{q}j}$ modulation is computed by an appropriate semi-empirical method, such as the extended Hückel (EH) [4] or the ZINDO methods [5]. Even then, the computational effort is considerable, given the high number of vibrational degrees of freedom. On the other hand, the coupling constants of optical phonons depend weakly on the phonon wave vector, so we evaluate them only at $\mathbf{q} = 0$. The coupling constants of acoustic phonons are zero by symmetry at the zone centre; therefore, we calculate them at several representative zone-border points and assume a linear dependence of $g^2(j)/\nu_j$ on $|\mathbf{q}|$. An appropriate tight binding scheme is adopted to compute the band structure starting from the value t for the nearest neighbours, and to evaluate the dependence of the coupling constants from the electronic wave vector **k** [2].

4. Raman measurements

Raman spectra have been collected with a Jobin Yvon T64000 spectrometer, coupled to an Olympus microscope, with a spatial resolution between 2 and 1 mμ, yielding the possibility of spatially mapping the crystals under investigation. Exciting lines were from a Krypton ion laser. Micro-Raman measurements at low temperatures (down to 80 K) and high pressures (up to 6 GPa) have been performed with a liquid Nitrogen Linkam HFS 91 cryostat and with a LOTO diamond anvil cell, respectively. Both were mounted on the microscope stage.

5. BEDT-TTF superconductors

The nature of the pairing mechanism in superconducting BEDT-TTF salts has been the subject of extensive discussions [6]. The superconducting state is adjacent to magnetically or charge ordered states, showing evidence of important electron-electron interactions. On the other hand, the crystal and phonon structures of these salts are very complex, so the possible role of phonons in the superconductivity mechanism is difficult to assess. We have applied the QHLD method to $(BEDT\text{-}TTF)_2I_3$ salts [7, 8], which have several non-superconducting and superconducting phases. We have verified that the various phases indeed correspond to minima of the Gibbs energy. The available experimental data (Raman, specific heat) connected to the lattice phonons of the superconducting β^*- and κ-phases are properly reproduced. The Peierls coupling constants have been evaluated by the EH tight-binding scheme, within the framework of the dimer model [2].

By expressing the Peierls coupling constants in the reciprocal space, we evaluate the Eliashberg function, which turns out to be in a qualitative agreement with available β^*- and κ-$(BEDT\text{-}TTF)_2I_3$ experimental data. From the Eliashberg function, we derive the dimensionless coupling constant λ and the logarithmic average phonon frequency ω_{ln}. When these quantities are substituted in the Allen-McMillan equation for the superconducting T_c [9], we find values well below the experimental ones. The values of T_c depend critically on the electronic density of states at the Fermi energy $N(E_F)$, which is difficult to evaluate. In any case, the Peierls coupling does not account for β^*- and κ-$(BEDT\text{-}TTF)_2I_3$ values of T_c. The above scenario changes substantially when we include the Holstein (electron–intramolecular) coupling when evaluating λ and ω_{ln}. Indeed, Holstein coupling contributes to λ in only about 25%, but ω_{ln} is more than doubled. Then, even before trying to estimate the superconducting critical temperature, it is instructive to see if the new value of ω_{ln} including the Holstein (intramolecular) contribution accounts for other experimental observables related to superconductivity. Indeed, some years ago Marsiglio and Carbotte [10] proposed empirical relations directly connecting ω_{ln} to the superconducting gap Δ_0 and to the specific heat jump at T_c. Table 1 shows that there is an excellent agreement between experiment and the values estimated trough the Marsiglio and Carbotte relations. Finally, by assuming plausible values for $N(E_F)$, the Allen–McMillan equation gives the values of T_c in agreement with experiment and properly scaled for the two salts [7, 8].

Table 1. Calculated and experimental superconducting gap, $2\Delta_0$, and specific heat jump, $\Delta C_p/\gamma T_c$, of two superconducting $(BEDT–TTF)_2I_3$ salts

Superconducting phase	$2\Delta_{0CALC}$ (cm^{-1})	$2\Delta_{0EXP}$ (cm^{-1})	$(\Delta C_p/\gamma T_c)_{CALC}$	$(\Delta C_p/\gamma T_c)_{EXP}$
$\beta^*(BEDT\text{-}TTF)_2I_3$	22	25^a	–	–
$\kappa\text{-}(BEDT\text{-}TTF)_2I_3$	9	12^b	1.7	1.6^c

[a] from Ref. [11].
[b] From Ref. [12].
[c] From Ref. [13].

As a further test of our approach, we have considered the effect of pressure on T_c. In BEDT-TTF salts, the decrease of T_c with p is large, up to ~ 3 K/kbar [14]. This unusual pressure effect has been sometimes taken as the evidence of a non-conventional pairing mechanism [15]. We have calculated the crystal and lattice phonon structure of β^*-$(BEDT\text{-}TTF)_2I_3$ at 8 K, under 0 and 6 kbars. The pressure effect on the Holstein coupling is very small, and has been disregarded. Preliminary results show that the calculated decrease in T_c is smaller than that measured (about 1 K vs. almost 5 K). Even keeping in mind all the approximations of the calculations, which are currently being refined and checked, we underline that the Peierls variation with p is at least as important as the variation in $N(E_F)$. From the data presented above, we conclude that the phonon contribution cannot be disregarded in a proper description of the coupling mechanism in organic superconductors.

6. Acene semiconductors

Acene crystals exhibit the highest mobilities among organic semiconductors [16], and the Peierls coupling is thought to be important in explaining the temperature dependence and anisotropy of the mobilities [17]. On the other hand, for practical applications at room temperature, it is much more important to assess the acene crystal structures and the corresponding lattice phonon spectral signatures. Indeed, the polymorphism of pentacene has been the subject of intense experimental and theoretical studies [18].

By applying our computational method, we have first aimed to identify the genuinely different polymorphs among the various reported single-crystal X-ray structures. We have obtained two local minima of the potential energy Φ_{inter}, i.e., two different "inherent structures" [19]. This behaviour clearly indicates that there are at least two different single crystal polymorphs of pentacene. One of them (polymorph C) corresponds to the structure reported in 1962 by Campbell and Robertson [20]. The other (polymorph H) corresponds to the structure found in all more recent measurements [21]. We have also obtained information on the global stability of the minima by systematically sampling the potential energy surface, and have found that the two polymorphs correspond to the two deepest minima [22]. The calculations also predict significant differences between the corresponding Raman spectra that we have checked experimentally, confirming the existence of two polymorphs [23]. Micro-Raman measurements have also shown that the two polymorphs can coexist as micro-domains in the same crystal. Application of pressures beyond 0.6 GPa irreversibly transforms polymorph C into the thermodynamically more stable H phase [24].

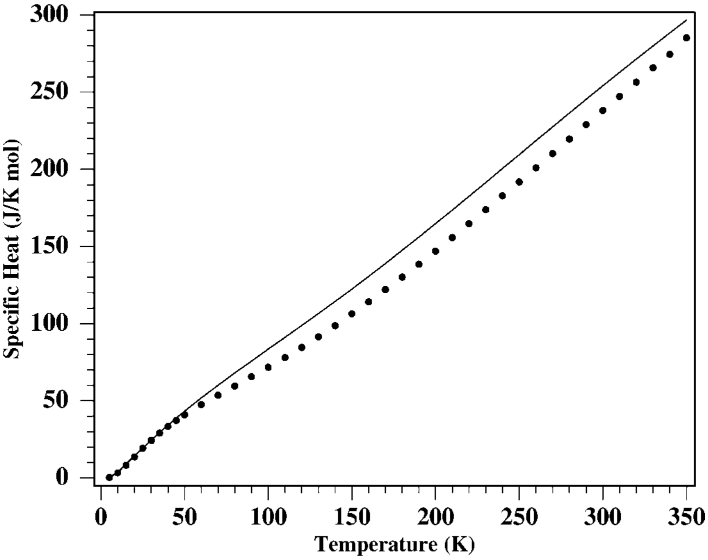

Fig. 1. Temperature dependence of tetracene specific heat.
Dots: experiment (from Ref. [26]); continuous line: QHLD calculations

Only one complete X-ray crystal structure has been reported for tetracene [20], which is known to undergo a phase transition both when lowering *T* and increasing *p* [25]. No clear indications exist about the low *T* and high *p* structures, partly because the crystal is damaged upon the phase transition. Our combination of theoretical and spectroscopic approaches is the key in elucidating this case. First, we have explored the potential energy surface of tetracene, finding that, similarly to pentacene, there are two minima very close in energy, one of which corresponds to the room temperature experimental crystal structure. The calculated thermodynamic properties of the two polymorphs are very similar – the experimental temperature dependence of the specific heat [26], which is calculated very well by our model (Fig. 1), indeed does not show evidence of phase transitions. On the other hand, the QHLD method predicts that Raman lattice mode frequencies should be different for the two polymorphs. Raman spectra as a function of *T* gave evidence for a phase transition from one polymorph to the other below 135 K. We have shown that the same low-temperature polymorph can also be obtained by applying pressure [25].

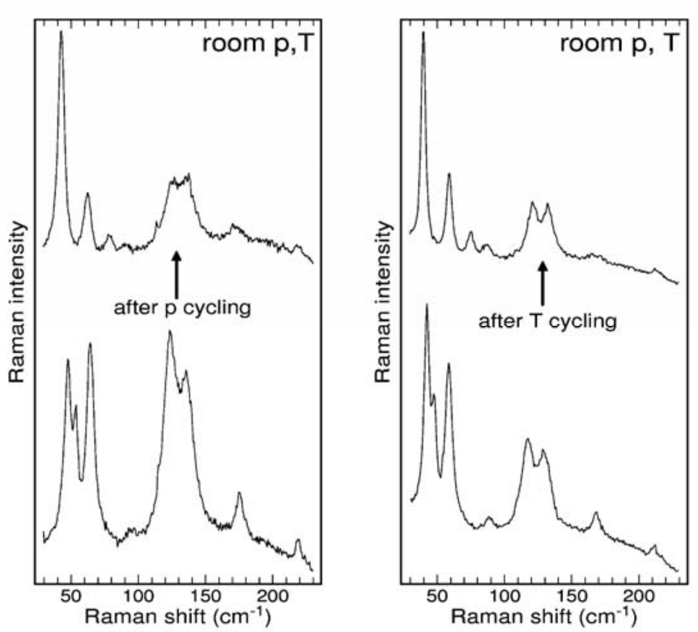

Fig. 2. Raman spectra of tetracene in the lattice phonon frequency region at ambient conditions. Bottom spectra: as grown crystals. Top spectra: after undergoing the *T*-induced (left) and the *p*-induced (right) phase transitions

As shown in Fig. 2, transitions induced by both *T* and *p* show large hysteresis or even irreversibility, so that the initial phase is not recovered when the sample is brought back to ambient conditions. The ambient tetracene polymorph has a crystal structure very similar to the C phase of pentacene, whereas the low *T*, high *p* phase is similar to the denser phase H. As in the case of pentacene, micro-Raman spectroscopy reveals phase inhomogeneities that might affect tetracene mobilities. The lattice phonon Raman spectroscopy therefore represents a convenient and reliable tool for checking crystal quality, providing a way to improve the performance of acene-based devices.

In the case of pentacene, we have also started to evaluate the strength of the Peierls coupling. The Peierls coupling constants for $\mathbf{q} = 0$ optical phonons of pentacene have been computed as described above. Since pentacene has a simpler molecular structure than BEDT-TTF, we preferred the ZINDO to the EH method to evaluate the hopping integrals in this case. Table 2 reports the Valence (VB) and Conduction Band (CB) lattice relaxation energy, $E_{\mathrm{LR}}(j)$, for the low-frequency lattice optical phonons of the pentacene H phase at 0 K. The lattice relaxation energy directly expresses the strength of the Peierls coupling and is defined as $E_{\mathrm{LR}}(j) = G^2_j/2\pi\nu_j$, where G_j is the total Peierls coupling constant of mode j, a sum of the modulations of the four main hopping integrals in the *ab* crystal plane. By symmetry, only totally symmetric (A_g) phonons can be coupled to electrons. Table 2 shows that several phonons are appreciably coupled to the charge carriers, and that some difference exists between coupling in the VB and CB. Phonons above 203 cm^{-1} are not appreciably coupled, and the largest contribution (~ 70%) to the total lattice relaxation energy comes from the two lowest frequency modes, which are described as librations around the two short molecular axes approximately parallel to the conducting *ab* crystal plane. Given the low frequency of these librations, they are likely to affect the mobilities even at low temperatures. A more detailed analysis of pentacene and tetracene mobilities and their temperature dependences is in progress.

Table 2. Low-frequency A_g phonons and lattice relaxation energy E_{LR} of pentacene (H phase) at 0 K

ν (cm^{-1})	Valence band E_{LR} (meV)	Conduction band E_{LR} (meV)
27	20.1	15.5
61	6.7	3.2
70	~0	1.1
96	1.2	2.5
132	~ 0	~ 0
148	2.6	~ 0
156	0.8	1.8
162	~ 0	~ 0
203	2.1	1.2

6. Conclusions

We have shown that the QHLD method can be employed to characterize the structure and lattice phonon dynamics of complex molecular crystals. The method is very simple, and its semi-empirical nature requires careful tuning over the class of molecular crystals of interest. In this way, a proper choice of parameters may compensate for the inherent approximations and shortcomings. The QHLD approach allows one to exploit the molecular nature of the crystals, dealing separately with the inter- and intramolecular phonon dynamics, the latter being solved through conventional *ab initio* methods. Association with mean-field electronic structure calculations has allowed us to characterize the Peierls coupling in two rather different classes of molecular crystals, BEDT-TTF organic superconductors and acene semiconductors. We have shown that the Peierls coupling plays a fundamental role in the superconducting pairing mechanism. In acene semiconductors, on the other hand, the QHLD method has provided important clues about the obtainable crystal phases, revealing the possible influence of crystal phase purity on the observed mobilities.

Acknowledgements

Work supported by the Consorzio Interuniversitario per la Scienza e Tecnologia dei Materiali (I.N.S.T.M. - PRISMA 2002 project) and by the Italian Ministry of University and Research (M.I.U.R. – FIRB 2003 project).

References

[1] DELLA VALLE R.G., VENUTI E., FARINA L., BRILLANTE A., Chem. Phys., 273 (2001), 197.

[2] GIRLANDO A., MASINO M., VISENTINI G., DELLA VALLE R.G., BRILLANTE A., VENUTI E., Phys. Rev., B62 (2000) 14476.

[3] CALIFANO S., SCHETTINO V., NETO N., *Lattice Dynamics of Molecular Crystals*, Springer-Verlag, Berlin, 1981.

[4] HOFFMANN R., J. Chem. Phys. 39 (1965), 1397.

[5] ZERNER M.C., LOEW G.H., KIRCHNER R.F., MUELLER-WESTERHOFF U.T., J. Am. Chem. Soc., 102 (1980), 589.

[6] LANG M., MUELLER J., [in:] K.H. Bennemann, J.B. Ketterson (Eds.), *The Physics of Superconductors*, Vol. 2, Springer-Velag, Heidelberg, 2003.

[7] GIRLANDO A., MASINO M., BRILLANTE A., DELLA VALLE R.G., VENUTI E., Phys. Rev., B66 (2002), 100507 (R).

[8] GIRLANDO A., MASINO M., BRILLANTE A., DELLA VALLE R.G., VENUTI E., [in:] R.W. Stevens (Ed.), *New Developments in Superconductivity Research*, Nova Science Publishers, Hauppauge, 2003, p. 15.

[9] ALLEN P.B., DYNES R.C., Phys. Rev., B12 (1975), 905.

[10] MARSIGLIO F., CARBOTTE J.P., Phys. Rev., B 33 (1986), 6141.

[11] DRICHKO N., HAAS P., GORSHUNOV B., SCHWEITZER D., DRESSEL M., Europhys. Lett., 59 (2002), 774.

[12] LUDWIG T., SCHWEITZER D., KELLER H.J., Synth. Metals, 85 (1985), 1587.

[13] WOSNITZA J., LIU X., SCHWEITZER D., KELLER H., Phys. Rev., B 50 (1994), 12747.

[14] SADEWASSER S., LOONEY C., SCHILLING J.S., SCHLUETER J.A., WILLIAMS J.M., NIXON P.G., WINTER R.W., GARD G.L., Solid State Comm. 104 (1997), 571.

[15] CAUFIELD J., LUBCZYNSKI W., PRATT F.L., SINGLETON J., KO. D.J.K., HAYES W., KURMOO M., DAY P., J. Phys. C : Condens. Matter 6 (1994), 2911.

[16] DIMITRAKOPOULOS C.D., MASCARO D.J., IBM Res. & Dev., 45 (2001), 11.

[17] HANNEWALD K., BOBBERT P.A., Phys. Rev., B69 (2004), 075212.

[18] DELLA VALLE R.G., VENUTI E., FARINA L., BRILLANTE A., MASINO M., GIRLANDO A., J. Phys. Chem., B 108 (2004), 1822, and references therein.

[19] VENUTI E., DELLA VALLE R.G., BRILLANTE A., MASINO M., GIRLANDO A., J. Amer. Chem. Soc., 124 (2002), 2128.

[20] CAMPBELL R.B., ROBERTSON J.M., Acta Cryst., 15 (1962), 289.

[21] HOLMES D., KUMARASWAMY S., MATZGER A.J., VOLLHARDT K.P., Chem.Eur.J., 5 (1999), 3399; SIEGRIST T., KLOC CH., SCHOEN J.H., BATTLOGG B., HADDON R.C., BERG S., THOMAS G.A., Angew. Chem. Int. Ed. Engl., 40 (2001), 1732; MATTHEUS C.C., DROS A.B., BAAS J., MEETSMA A., DEBOER J.L., PALSTRA T.T.M., Acta Cryst., C 57 (2001), 1732.

[22] DELLA VALLE R.G., VENUTI E., BRILLANTE A., GIRLANDO A., J. Chem. Phys. 118 (2003), 807.
[23] BRILLANTE A., DELLA VALLE R.G., FARINA L., GIRLANDO A., MASINO M., VENUTI E., Chem. Phys. Lett. 357 (2002), 32.
[24] FARINA L., BRILLANTE A., DELLA VALLE R.G., VENUTI E., AMBOAGE M., SYASSEN K., Chem. Phys. Lett. 375 (2003), 490.
[25] VENUTI E., DELLA VALLE R.G., FARINA L., BRILLANTE A., MASINO M., GIRLANDO A.Phys. Rev. B 70 (2004), 104106.
[26] WONG W.K., WESTRUM JR.E.F., Mol. Cryst. Liq. Cryst. 61 (1980), 207.

Received 14 September 2004
Revised 2 November 2004

Materials Science-Poland, Vol. 22, No. 4, 2004

Highly conducting organic composites obtained by charge transfer reaction in the solid state

ANDRZEJ GRAJA[*], MYKOLA GOLUB

Institute of Molecular Physics, Polish Academy of Sciences, 60-179 Poznań, Poland

In this paper, we shortly present and discuss structural, electrical and spectral properties of organic composites with the general formulae (BEDT-TTF)$_x$/A and (BEDO-TTF)$_x$/A, where A denotes an electron-acceptor species such as iodine, AuI, or AuI_3. Electron transfer between large conducting grains restricts electrical conductivity of the composites; the most probable mechanism being fluctuation -induced tunnelling conduction. Extensive spectral properties of organic composites are presented. It is shown that spectral studies can provide specific information about charge localization, electron-electron and electron-molecular vibration interactions, and about changes in the properties of highly conducting organic composites with ageing or annealing.

Key words: *organic composites; BEDT-TTF; BEDO-TTF; electrical transport; optical spectroscopy*

1. Introduction

Charge transfer (CT) complexes with the tetrathiafulvalene (TTF) organic donor or its derivatives possess very interesting physical properties such as high anisotropy and two-dimensional metal-like electron transport; some of them also show superconductivity and charge or spin ordering. However, these materials usually crystallize in the form of tiny and brittle crystals, which are difficult to handle and utilize. One of the possibilities of obtaining organic material in a form convenient for applications and with good physical properties is to prepare conducting organic composites directly in the solid state. As was shown by Brau and Farges [1, 2], charge-transfer reactions between suitable electron donor and acceptor moieties occur in the solid state in the course of grinding them together. Such a mechano-chemical method has been employed for the preparation of highly conducting composites of tetrathiafulvalene (TTF), *bis*(ethylenedithio)tetrathiafulvalene (BEDT-TTF), and *bis*(ethylenedioxy)-tetrathiafulvalene (BEDO-TTF) [3–5], with various electron acceptors, e.g. iodine,

---

[*] Corresponding author, e-mail: graja@ifmpan.poznan.pl.

AuI, AuI_3, and $AuBr_3$. The main advantage of this method is an unlimited size and shape of the composite samples. Physical properties of such composites roughly resemble the properties of their crystalline analogues obtained by traditional ways. Grains forming the composite sample, however, are anisotropic and exhibit all the properties typical of single crystals. We have already widely exploited the method of Brau and Farges [1, 2], and some of our observations will be reviewed here.

2. Organic composites – preparation and structural properties

One of the methods of preparation of organic composites is to produce the conductive material by a CT reaction, which occurs directly in the solid state between organic electron donor and acceptor parent substances. The reaction is evidenced by a significant darkening of the mixture, prepared quite simply by crushing both donor and acceptor in an agate mortar. An appropriate molar proportion of substrates is ground for a defined time, then compacted and annealed (for details see [2–6]).

The morphology of the composites depends on their composition, and on the conditions of the synthesis and annealing procedure [7]. Usually, the morphology of the composite resembles the texture of a sponge. It has been suggested from X-ray diffractograms and Raman spectra that the composites are built mainly of grains, whose composition corresponds to the stoichiometry of the corresponding crystalline complexes, e.g. $(BEDT\text{-}TTF)_2I_3$, $(BEDT\text{-}TTF)_2AuI_2$, or $(BEDO\text{-}TTF)_2I_3$ [8]. The conducting grains are separated by amorphous matter of various composition and electrical properties; in some cases, neutral grains of metallic gold also occur. This composition has been confirmed and described in detail by SEM imaging and energy dispersive X-ray analysis (EDX) [7, 9, 10]. From the SEM and EDX investigations, it was also stated that annealing the composite leads to the development and completion of the CT reaction, as well as to chemical exchange between components [5, 7, 9, 10].

3. Electrical transport properties – basic remarks

The electrical properties of BEDT-TTF- and BEDO-TTF-based composites have been recently reviewed [5, 11]; this is why the discussion of transport properties in this presentation will be limited to the most important problems.

BEDT-TTF-based composites exhibit a variety of electrical properties depending on their preparation conditions [5, 11, 12]. Samples of $(BEDT\text{-}TTF)_x/I$, where x defines the molar proportions of solid donor and acceptor, show semiconducting behaviour before annealing. Appropriate thermal treatment, however, changes these properties from metal-like at high temperatures and semiconductor-like at low temperatures to metal-like behaviour over the entire temperature range (for properly annealed samples). Composites obtained by grinding BEDT-TTF with gold iodides (AuI or AuI_3)

present similar properties, although in this case it is more difficult to obtain samples that display metallic conductivity in the whole temperature range [12].

The transport properties of BEDO-TTF-derived composites are completely different. The electrical conductivity of these materials reaches 15 $S\cdot cm^{-1}$ at room temperature (RT) and is even higher when the temperature is lowered [4]. The prominent feature of $(BEDO\text{-}TTF)_x/I$ composites is their metal-like behaviour observed down to about 150 K for non-annealed samples (Fig. 1). On the other hand, ageing and annealing of BEDO-TTF composites causes the degradation of their transport properties.

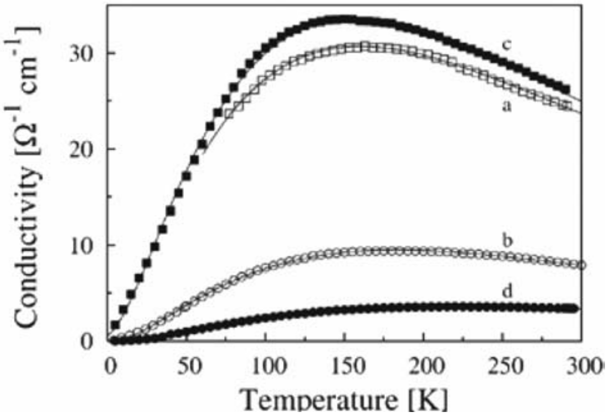

Fig. 1. Temperature dependence of the d.c. conductivity of: fresh (a) and 2-month (b) samples of $(BEDO\text{-}TTF)_{1.1}/I$ composite, a sample of $(BEDO\text{-}TTF)_{1.1}/I$ before (c) and after (d) annealing. Solid lines are fits with Eq. (1)

For the production of composites with desired electrical properties, it is very important to understand what mechanisms are responsible for temperature variations of the conductivity and to identify factors influencing electrical properties of the composites. Two mechanisms seem to be the most probable reasons for the semiconducting behaviour of non-annealed composite samples: charge carrier localization due to material defects and intergrain effects (poor contacts between grains). SEM investigations have shown that in BEDT-TTF-based composites during annealing both grain recrystallization and contact improvement between them take place. The first process can lead to a defect reduction and electron delocalization in grains, while the second improves the electrical transport between the grains. The crossover in annealed samples to semiconducting behaviour at low temperatures points out that one or both of the processes mentioned previously are not suppressed enough for metallic properties to be achieved at all temperatures.

From an analysis of the experimental data [13] it appears that fluctuation-induced tunnelling of the electrons (FIT) between grains is the most probable mechanism of composite conductivity at low temperatures [14]. Thermal fluctuations give rise to a decrease in intergrain resistances with increasing temperature, and the conductivity shows $T^{-\alpha}$ behaviour typical of the contribution of metallic intragrain conductivity. To fit experimental data at all temperatures, one can introduce the simplest model of the composite as a system of arrays with various resistances; one resistance represents the contribution of intergrain junctions and another one represents the grains themselves. In this case, the temperature dependence of composite conductivity can be approximated with the formula

$$\sigma(T) = \left[B \exp\left(\frac{T_1}{T + T_0} \right) + C T^{\alpha} \right]^{-1} \tag{1}$$

where *B* and *C* are geometrical factors depending on the fraction of the sample length and cross-section area which correspond to the intergrain regions and conducting grains, respectively; the parameters T_0 and T_1 depend on the properties of contacts between grains [15]. The above equation can be fitted to experimental values of electrical conductivity. A good agreement between experimental data and fits allows one to suggest that the annealing of composites makes the influence of electron localization negligible and inhibits (but does not eliminate entirely) the undesirable effect of intergrain tunnelling. Using relations between T_0, T_1, and the contact parameters (contact width, area, and barrier height) [15], one can find out, for example, how contact characteristics change with *x*, annealing conditions, grinding time, and other composite preparation parameters. This information is required to understand the processes of composite formation.

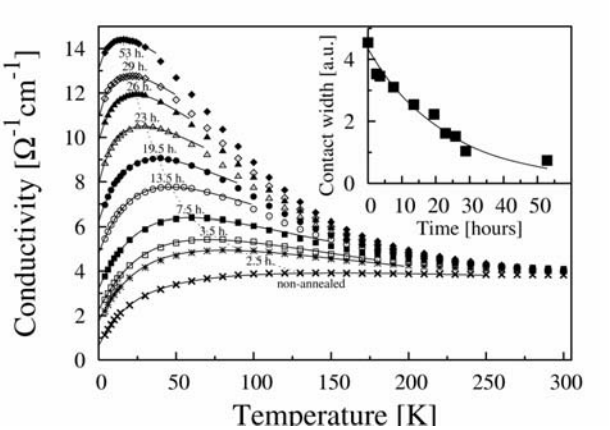

Fig. 2. Temperature dependence of the $(BEDT\text{-}TTF)_{2.17}/(AuI_3)$ composite as a function of annealing time. Solid lines are fits by Eq. (1). In the insert, the changes of intergrain contact width on annealing, deduced from the fit parameters, are shown

The electrical properties of annealed BEDT-TTF composites almost do not change in time. On the other hand, the properties of non-annealed samples change with composite ageing [13]. Analysis of the experimental data shows that the ageing of non-annealed samples can be considered as non-effective annealing. The temperature dependence of the conductivity of aged samples as a function of annealing time is shown in Fig. 2. Aged samples need to be annealed for tens of hours to achieve the same effect as fresh samples annealed for 1–2 hours. The conductivity of the (BEDT-TTF)$_{2.17}$/(AuI$_3$) composite has been analysed in terms of the FIT model in order to obtain information on how annealing influences intergrain contacts. The dependence of contact width on annealing time is shown in the insert of Fig. 2. Contact width decreases with annealing (contacts improve), which is in agreement with SEM observations.

An analysis of the temperature dependence of the conductivity of BEDO-TTF-derived composites (Fig. 1) shows that, as in the case of BEDT-TTF composites, the conductivity of these materials is determined mainly by two factors: 1) the metal-like conductivity of (BEDO-TTF)$_{2.4}$I$_3$ grains and 2) fluctuation-induced tunnelling of carriers between grains. The *T*-dependence of BEDO-TTF composite conductivity can thus also be approximated by Eq. (1). As the conductivity of single crystals at high temperatures is proportional to T^{-2} [16], the parameter α was taken to be equal 2.

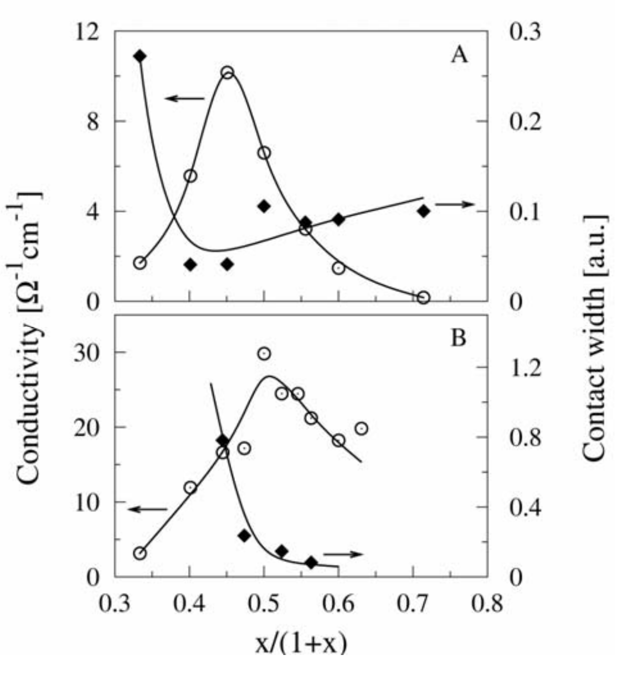

Fig. 3. Dependence of intergrain contacts on *x* for (BEDT-TTF)$_x$/(AuI) (A) and (BEDO-TTF)$_x$/I (B) composites. For comparison, the *x*-dependence of RT conductivity is presented. The solid curves are only to guide the eye

Changes in intergrain distances with *x* for (BEDO-TTF)$_x$/I composites are shown in Fig. 3. Contrary to similar parameter variations for (BEDT-TTF)$_x$/(AuI), no minimum of the contact width at $x \approx x_{\text{opt}}$ is found in this case. These differences in the transport properties of both types of composites reflect the differences in their structures. In (BEDT-TTF)$_x$/(AuI), conducting grains of (BEDT-TTF)$_2$I$_3$ and (BEDT -TTF)$_2$AuI$_2$ are formed. Grain concentration is the largest for $x = x_{\text{opt}}$, hence intergrain distance (contact width) is minimal. In (BEDO-TTF)$_x$/I, an insulating phase of (BEDO -TTF)I$_3$ is formed together with conducting grains of (BEDO-TTF)$_2$. This phase forms a layer between (BEDO-TTF)$_{2.4}$I$_3$ grains and unreacted iodine. The thickness of the (BEDO-TTF)I$_3$ shell decreases with increasing x due to the deficit of iodine, which also leads to a monotonic decrease in the contact width.

Suggestions resulting from analysing the temperature dependence of conductivity should be confirmed by other methods. IR investigations, discussed below, give additional information about conduction electrons and appear to be in agreement with the conclusions made here. Thermoelectric power measurements can also be used to confirm these suggestions [13, 17]. As shown by us, the same effect is observed for all types of annealed composites: although d.c. conductivity shows a strong x-dependence, the x-sensitivity of thermoelectric power is weak in the region of optimal composition (x_{opt}) and above it. Not only RT thermoelectric power but also its temperature dependence do not depend on x when it is close to x_{opt} [13, 17]. In contrast to the conductivity, both thermoelectric power and its T-dependence change weakly with the annealing of composites for $x \approx x_{\text{opt}}$. Conducting microcrystals give the main contribution to the thermoelectric power of the composites [13, 17]. Weak sensitivity of the composites to thermal treatment means that the annealing influences mainly the non-conducting intergrain layers and weakly changes the thermoelectric properties of conducting grains. On the other hand, the thermoelectric properties of these microcrystals are almost the same as those of corresponding single crystals.

The interpretation of the electrical properties of BEDT-TTF and BEDO-TTF composites presented here allows one to make suggestions about ways to control and improve the electrical transport properties of composites obtained by direct CT reaction in the solid state. As intergrain conduction plays the most important role in BEDT-TTF composites, first of all one should try to improve the contacts between grains. One of the ways, proposed by us, is to apply the hot pressing method for organic composite production [13]. With this method, composites with better electrical transport characteristics have been obtained. Better intergrain contacts in composites prepared by hot pressing are responsible for improvement in their electrical properties. In BEDO-TTF-derived composites, mainly the insulating (BEDO-TTF)I$_3$ shell affects the electrical properties of the composites and their changes on ageing. Therefore, to improve the transport properties and stability of composites one should suppress (BEDO-TTF)I$_3$ phase formation or use some procedure to remove this phase after the composite has been prepared.

4. Spectral properties of organic composites

Optical spectral studies play an important role in the investigation of organic conductors, including not only crystalline but also polymeric and other unconventional forms, such as highly conducting organic composites obtained by direct CT reaction in the solid state. Properties of organic conductors are determined by various interactions and instabilities. The optical properties of these materials can be roughly described by the simplest model, assuming non-interacting electrons (the one -electron model). In this approximation, the infrared (IR) properties may be derived in the self-consistent approximation. Assuming a frequency-independent relaxation rate γ and a background electric permeability ε_0 arising from high-frequency transitions, the result takes the Drude form [18]:

$$\varepsilon^*(\omega) = \varepsilon_0 - \frac{\omega_p^2}{\omega^2 - i\omega\gamma} \tag{2}$$

where ω_p is the plasma frequency. This expression is frequently used to describe the optical properties of organic metal-like conductors in the IR region and to estimate some of their electron parameters. On the other hand, electron-molecular vibration (e-mv) coupling plays a fundamental role in organic conductors. In general, the interaction of electrons with intramolecular vibrations can be written in the form given by Rice [19]:

$$H = H_e + H_v + \sum_{\alpha,i} g_\alpha n_i Q_{\alpha i} \tag{3}$$

The first two terms describe radical electrons and molecular vibrations in the absence of vibronic coupling. A linear e-mv coupling is expressed explicitly by the third term. The set $\{g_\alpha\}$ of constants denotes linear π-electron-molecular vibration constants.

Vibrational spectroscopy plays an important role in the characterization of highly conducting organic composites. Major spectroscopic interest is centred in the following areas: 1) differentiation and identification of various phases in composites and the evaluation of the charge distribution on their grains; 2) determining the extent of charge transfer from a donor to an acceptor moiety as a result of the CT reaction in the solid state; 3) determining of optical anisotropy, electronic structure, plasma frequencies, optical band gap, optical conductivity, and other parameters characterising electronic properties of the composite grains; 4) evaluating surface homogeneity of composite samples; 5) assignment of vibrational features. As will be shown below, the data mentioned above are helpful in offering a model of composite structure.

It is known from SEM and EDX investigations [7, 9, 10] that composites obtained by CT reaction in the solid state have a complex heterogeneous structure, containing grains of various compositions and properties, as well as intergrain matter. These observations of composite morphology, however, cannot give more exact information, maybe beyond confirming the existence of free gold grains in BEDT-TTF composites with gold iodides. As a microscopic tool, vibrational spectroscopy can differentiate between grains that exhibit metallic conductivity, e.g. (BEDT-TTF)$_2$I$_3$, (BEDT-TTF)$_2$AuI$_2$, and (BEDO-TTF)$_{2.4}$I$_3$, and those that are semiconducting or insulating.

The IR spectra of the complexes show characteristic features, such as interband transitions (usually in the range of 1000–4000 cm^{-1}), accompanied by very strong and broad vibronic bands originating from a coupling of electronic excitations with the totally symmetric (A_g) intramolecular vibrations of the organic donor molecules (such as BEDT-TTF or BEDO-TTF). The latter features are localized between 100 and 1500 cm^{-1}, with a characteristic strong absorption near 1250 cm^{-1} [20]. The spectra of semiconducting composites, complexes, or ion-radical salts show distinct CT bands with an onset between 1500 and 2500 cm^{-1} and a well developed set of vibronic bands corresponding to A_g modes of the donor molecule. The spectra of metal-like composites or other organic conductors are, oppositely, dominated by the broad and strong absorption given by conduction electrons. The strongest vibronic band or bands are usually detectable as sub-maxima on the broad electronic absorption [20]. Such qualitative information can be restated precisely by Raman scattering investigations.

Raman scattering spectra of selected BEDT-TTF-derived composites, namely (BEDT-TTF)$_{0.67}$/I, (BEDT-TTF)$_2$/AuI$_3$, and (BEDT-TTF)$_{0.82}$/I, are shown in Fig. 4 [8]. The maximum at 30 cm^{-1} is attributed to bending and the one at 120 cm^{-1} to stretching vibrations of the I_3^- anion. In the spectra of (BEDT-TTF)$_2$/AuI$_3$ and (BEDT-TTF)$_{0.82}$/I, one can also see the I_3^- line, and an additional band at 160 cm^{-1}, which can be assigned to stretching vibration of the AuI_2^- anion [21]. This suggests that there are also (BEDT-TTF)$_2$AuI$_2$ grains in the two latter composites, except in (BEDT-TTF)$_2$I$_3$. This is corroborated by an analysis of the range 20–60 cm^{-1}, corresponding to bending vibrations, where a distinct evolution with the appearance of a new band below 60 cm^{-1} is observed.

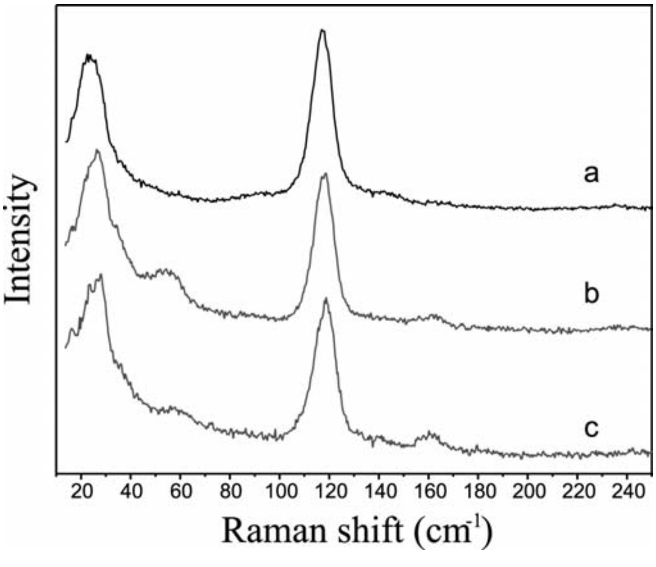

Fig. 4. Resonant Raman scattering spectra of (BEDT-TTF)$_{0.67}$/I (a), (BEDT-TTF)$_{0.82}$/AuI (b), and (BEDT-TTF)$_2$/AuI$_3$ (c) composites

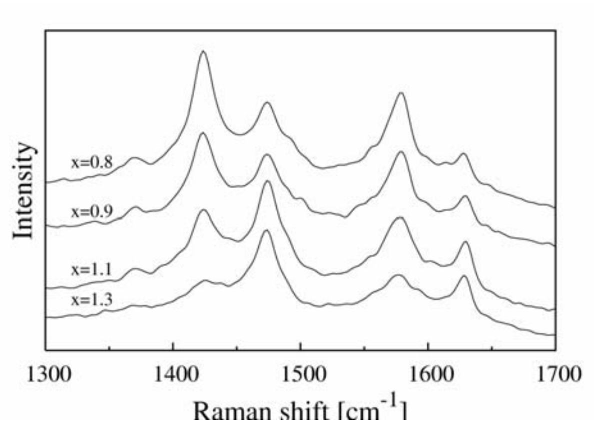

Fig. 5. Raman spectra of (BEDO-TTF)$_x$/I composites
in the frequency range of C=C stretching vibrations

Phase identification and evaluation of charge on the donor moieties can be performed with IR or Raman spectroscopy. The latter is more accurate, since Raman lines are better separated than IR bands. Raman spectra of (BEDO-TTF)$_x$/I composites in the most interesting range, between 1300 and 1700 cm^{-1}, are shown in Fig. 5. These spectra, independent of sample composition (described by the parameter x), consist of four lines at 1424, 1474, 1578, and 1630 cm^{-1}. These lines are assigned to A_g stretching vibrations of the central and ring C=C bonds, respectively, downshifted according to the value of charge on the BEDO-TTF cations in the composites [22, 23]. A similar effect, a linear correlation between vibrational band localization and charge on the considered bond has been observed some time ago by Farges et al. [1] in their studies on the IR absorption of the TEA(TCNQ)$_2$ organic conductor. The presence of four lines in the Raman spectra of (BEDO-TTF)$_x$/I composites suggests that two kinds of microstructures (grains) co-exist in the composites [24]. The doublet at 1474 and 1630 cm^{-1} is characteristic of one grain type and the doublet at 1424 and 1578 cm^{-1} of the other. Ionisation shifts are approximately 53 and 27 cm^{-1} in the former case, and 104 and 79 cm^{-1} in the latter case [25]. In order to evaluate the CT degree (ρ) on the cation, a linear dependence between the frequencies of the two totally symmetric C=C modes and the charge on the BEDO-TTF was assumed. Using the formulae of Drozdova et al. [23]:

$$\rho = \frac{1524.9 - \nu_{3,\text{obs}}}{109.0}, \qquad \rho = \frac{1660.8 - \nu_{2,\text{obs}}}{74.1} \tag{4}$$

where $\nu_{3,\text{obs}}$ and $\nu_{2,\text{obs}}$ are the observed wave numbers of the bands, one can evaluate the degrees $\rho' = 0.42$ and $\rho'' = 1.0$ of each expected microstructure type for (BEDO-TTF)$_x$/I composites [24, 25]. The former one corresponds to the crystal stoichiometry of 2.4:3 and the latter to 1:3. This indicates that the composite contains two phases, (BEDO-TTF)$_{2.4}$I$_3$ and (BEDO-TTF)I$_3$.

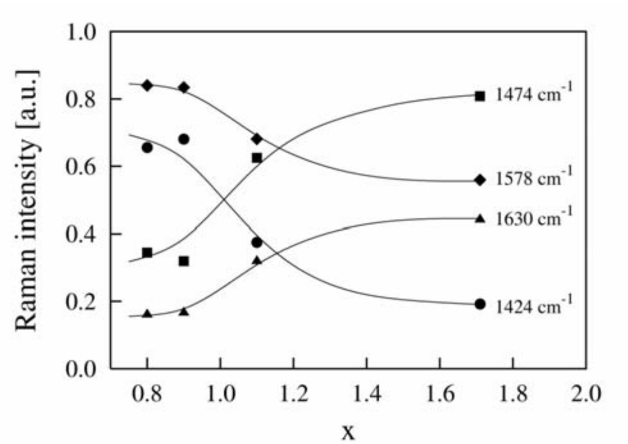

Fig. 6. Raman intensity of the C=C Raman lines as a function of *x* for (BEDO-TTF)$_x$/I composites. The solid curves are only to guide the eye

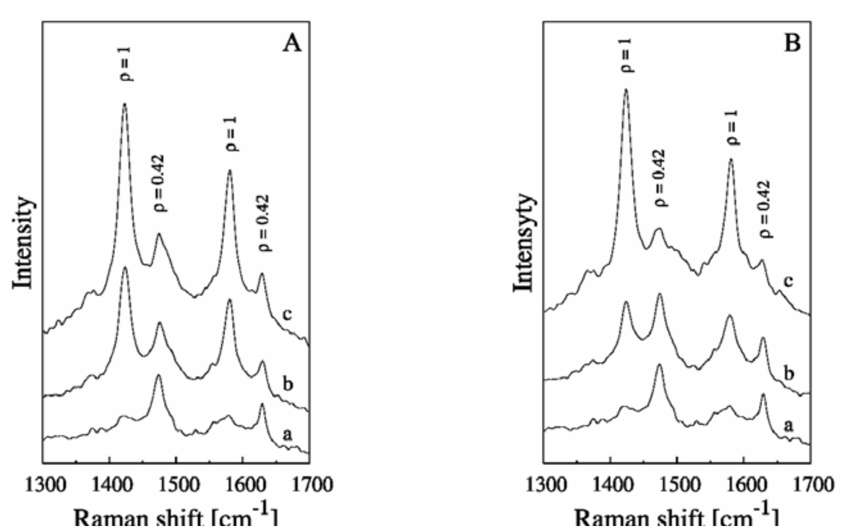

Fig. 7. Raman spectra of (BEDO-TTF)$_{1.0}$/I composites: A) spectra of : 9- (a), 15- (b), and 38- (c) day old samples; B) spectra of non-annealed (a) and annealed (b, c) samples; the latter were annealed for 1 h (b) and 2 h (c) at a temperature of 80° C

The contents of grains of both types strongly depend on the sample composition (Fig. 6), its age, and thermal treatment (Fig. 7) [25]. The intensity of Raman lines (Fig. 6), characteristic of (BEDO-TTF)$_{2.4}$I$_3$, decreases in the region of optimal composition ($x \approx 1$). The intensity of the lines assigned to (BEDO-TTF)I$_3$, however, increases in the same region. This means that for $x < 1$ and $x > 1$ the relative amounts of (BEDO-TTF)I$_3$ and (BEDO-TTF)$_{2.4}$I$_3$ phase are different. The ageing process for the (BEDO-TTF)$_{1.0}$/I composite is illustrated in Fig. 7A. The Raman spectrum of a relatively fresh sample is dominated by the lines at 1474 and 1630 cm^{-1}. These components decrease slightly during the ageing of the sample; at the same time, the components at 1424 and 1578 cm^{-1} increase distinctly and become dominant after about 40 days. This evolution shows that the phase with the stoichiometry of 2.4:3 dominates in the beginning, but during ageing the contents of the 1:3 phase prevails. This process can be enhanced if the sample is annealed, as is shown in Fig. 7B. These spectral results show that annealing causes an evolution of the sample towards increased content of the (BEDO-TTF)I_3 phase. This is a low-conducting phase, therefore the electrical conductivity of the BEDO-TTF composite decreases strongly with annealing.

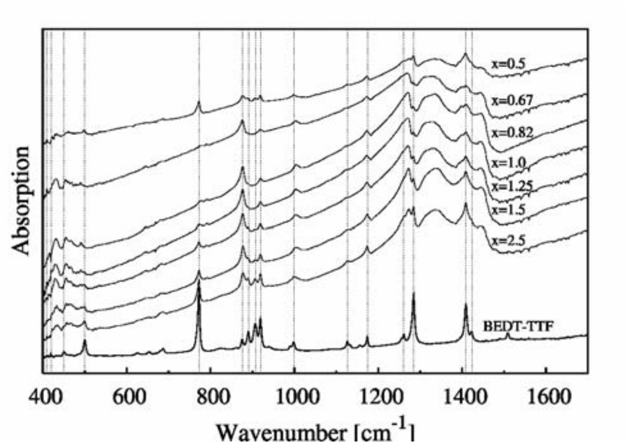

Fig. 8. Absorption spectra of (BEDT-TTF)$_x$/(AuI) composites for various sample compositions, recorded in a KBr matrix; the spectrum of neutral BEDT-TTF, taken in the same conditions, is shown for comparison

The IR spectra of the composites also give important information on the samples [20, 24–28]. Absorption spectra of (BEDT-TTF)$_x$/(AuI) composites in the most interesting spectral region, for various sample compositions, recorded in a KBr matrix, are shown in Fig. 8. For comparison, the spectrum of neutral BEDT-TTF, taken in the same conditions, is also shown. The spectra are typical of conducting BEDT-TTF materials [3, 26, 27] and are similar to those of BEDO-TTF composites [24, 25]. They can be roughly divided into two parts: 1) from 7000 cm^{-1} to the sharp absorption increase at about 1600 cm^{-1} (not shown here) and 2) from 1600 to 600 cm^{-1}. In the first part, quite a broad absorption band is observed with a maximum between 3200 and 2900 cm^{-1}, depending on the sample composition. This band is generally assigned to an electronic interband transition between split bands. The splitting is caused by strong intermolecular interactions between electron donor and acceptor molecules. This feature can be viewed as the plasma part of the spectrum. The second, most informative part of the IR spectra of the composites, shows a very rich vibrational structure. The majority of the observed bands can be assigned to the normal vibrations of BEDT-TTF$^+$ (or BEDO-TTF$^+$) cations. These bands are down-shifted with respect to the corresponding bands of the neutral donor. The shifts are independent of the sample molar composition and are influenced by the average electron charge on the donor and by a modified charge distribution on the donor moieties after composite formation. A broadening of these bands is observed with increasing donor concentration in the mixture, which is characteristic of the formation of highly conducting composites as well as crystalline complexes [3, 25–27]. There are two particularly interesting bands in the IR spectra of BEDT-TTF and BEDO-TTF composites: in BEDT-TTF composites, a broad band centred at about 1320 cm^{-1} and a structure at about 1400 cm^{-1}, and in BEDO-TTF-derived materials at about 1340 cm^{-1} and 1600 cm^{-1}. The coupling of totally symmetric normal vibrations (A_g modes) in a donor molecule with appropriate electronic excitations [27, 28] is the origin of the activation of these bands. The A_g modes mentioned above are attributed to the stretching of the central and ring C=C bonds, respectively [22, 27].

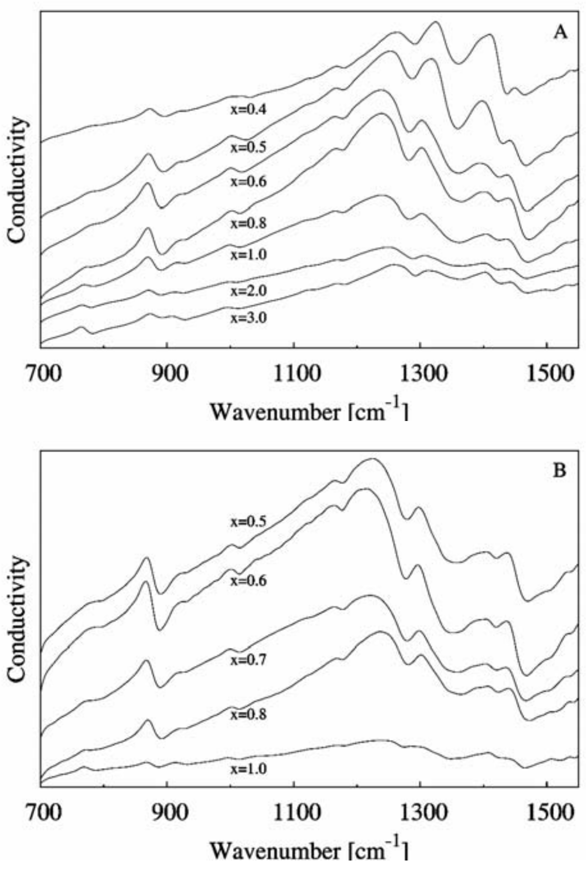

Fig. 9. Optical conductivity spectra of (BEDT-TTF)$_x$/I composites before (A) and after (B) annealing, for various *x*, recorded in a KBr matrix

As was shown before, BEDT-TTF composite conductivity, which is semiconductor-like just after preparation (before annealing), becomes metallic after appropriate thermal treatment. Such a drastic change in physical properties can also be observed by IR spectral methods. For example, the optical conductivity spectra, which are equivalent to absorption spectra of $(BEDT\text{-}TTF)_x/I$ composites before and after annealing, for various x, are shown in Fig. 9. After annealing, the bands become broader, are down-shifted and overlap with the broad and strong electronic absorption caused by conducting electrons. The conducting electrons are responsible for plasma-edge-like dispersion, which appears in the near IR region both for highly conducting crystalline synthetic metals and for metal-like organic composites. The IR reflectivity spectrum of the $(BEDO\text{-}TTF)_{1.0}/I$ composite and a least-square fit to the reflectance calculated from the Drude model [18] (dashed line) are shown as an example in Fig. 10. From the best fit one can evaluate fitting parameters such as ω_p, γ, ε_0, relaxation time τ, mean free path of charge carriers Λ, and optical conductivity at zero frequency $\sigma_{\mathrm{opt}}(0)$. It is difficult to directly compare such evaluated transport parameters with the parameters for corresponding crystalline complexes due to their anisotropy and to the scattering of data from various papers, even for the same material. The plasma frequency and dielectric constant evaluated for composites are usually reasonable when compared with data for related single crystals, but the damping rate of the composites is significantly higher than that of single crystals with the same composition [24]. The transport of charge carriers is strongly damped in composites due to their granular structure and grain defects. Consequently, the mean free path is relatively short.

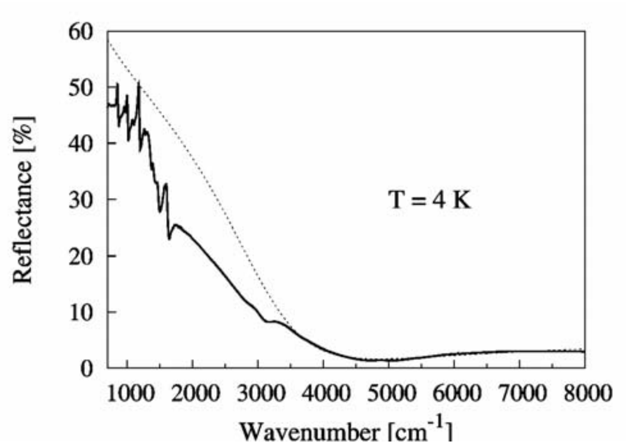

Fig. 10. Reflectance spectrum of the $(BEDO\text{-}TTF)_{1.0}/I$ composite. Least-square fit to the reflectance, calculated from the Drude model, is shown by the dashed line

Microreflectance studies of composites suggest that the organic conductors obtained by CT reaction in the solid state are macroscopically homogeneous [26, 27]. This observation is conformable to SEM and EDX investigations. Besides, spectral methods are appropriate for characterizing materials and confirming the appearance of particular molecular groups. Various IR spectral methods (absorption of composites dispersed in KBr pellets, absorption of very thin composite samples, reflectance from the composite surface, optical conductivity evaluated from composite reflectance), supplemented by Raman scattering studies, give extensive information on the spectral properties of the investigated materials.

As mentioned in this chapter, optical studies of organic composites are crucial for understanding their macroscopic structure, electronic interactions, and electronic structure. Information comes from studies in the wide spectral region, from far IR to vacuum ultraviolet. Spectral studies of organic composites can provide specific information about the localization of charges, electron-electron and electron-molecular vibration interactions, vibronic activations of the modes, phase transitions, and changes in the properties of highly conducting organic composites with ageing or annealing.

5. Concluding remarks

The synthesis of non-traditional organic materials that display good physical properties, in particular high electrical conductivity, optical transparency or nonlinearity, and good stability, is an important aspect of contemporary molecular engineering. Organic conductors are precursors of such momentous species as nano-materials. At present, it is possible to fabricate various organic conductors not only as crystals but also in the form of thin conducting films, conducting reticulate doped polymeric films, or polycrystalline samples. Although these materials are of great practical importance, they exhibit some shortcomings. One of them is the rather difficult and expensive technology associated with them. This is why we present a relatively simple mechano-chemical way of preparing conducting organic composites.

We have given a discussion of the basic problems concerning the physical properties of BEDT-TTF- and BEDO-TTF-derived composites, especially their spectral properties. It seems that a better understanding and description of the phenomena occurring in these type of new organic materials are necessary to both develop their technology and to discover their applications in molecular electronic devices.

Acknowledgement

The authors are grateful to Dr. Iwona Olejniczak for her critical reading of the manuscript.

References

[1] FARGES J.P., BRAU A., DUPUIS P., Solid State Commun., 54 (1985), 531.

[2] FARGES J.P., BRAU A., [in:] H.S. Nalwa (Ed.), *Handbook of Advanced Electronic and Photonic Materials and Devices*, Academic Press, San Diego, 2001, p. 329–369.

[3] SEMKIN V.N., GRAJA A., SMIRANI I., BRAU A., FARGES J.P., J. Mol. Struct., 511/512 (1999), 49.

[4] GRAJA A., BRAU A., FARGES J.P., Synth. Met., 122 (2001), 233.

[5] GRAJA A., GOLUB M., Compt. Rend. Chimie, 6 (2003), 367.

[6] BRAU A., SMIRANI I., FARGES J.P., LIPIEC R., GRAJA A., Synth. Met., 108 (2000), 75.
[7] GOLUB M., SZCZEŚNIAK L., GRAJA A., BRAU A., FARGES J.P., J. Mater. Sci., 36 (2001), 5543.
[8] GRAJA A., BRAU A., FARGES J.P., GOLUB M., TRACZ A., JESZKA J.K., Synth. Met., 120 (2001), 753.
[9] GOLUB M., GRAJA A., BRAU A., FARGES J.P., Synth. Met., 125 (2002), 337.
[10] GOLUB M., GRAJA A., JÓŹWIAK K., Synth. Met., 144 (2004), 201.
[11] GRAJA A., GOLUB M., Nonlinear Optics Quantum Optics, 32 (2004), 21.
[12] GOLUB M., GRAJA A., BRAU A., FARGES J.P., Synth. Met., 125 (2002), 301.
[13] GOLUB M., Ph.D. Thesis, Institute of Molecular Physics, Polish Academy of Sciences, Poznań, 2003.
[14] SHENG P., Phys. Rev. B, 21 (1980), 2180.
[15] PAASCH G., LEHMANN G., WUCKEL L., Synth. Met., 37 (1990), 23.
[16] WUDL F., YAMOCHI H., SUZUKI T., ISOTALO H., FITE C., KASMAI H., LIOU K., SRDANOV G., J. Am. Chem. Soc., 112 (1990), 2461.
[17] GOLUB M., GRAJA A., J. Physics D: Appl. Phys., 36 (2003), 3064.
[18] BORN M., WOLF E., *Principles of Optics*, Pergamon Press, New York, 1959.
[19] RICE M.J., Solid State Commun., 31 (1979), 93.
[20] GRAJA A., *Low-Dimensional Organic Conductors*, World Scientific, Singapore, 1992.
[21] OHTSUKA I., NAKAYAMA H., ISHI. K., J. Raman Spectr., 20 (1989), 489.
[22] POKHODNIA K.I., KOZLOV M.E., ONISCHENKO V.G., SCHWEITZER D., MOLDENHAUER J., ZAMBONI R., Synth. Met., 56 (1993), 2364.
[23] DROZDOVA O., YAMOCHI H., YAKUSHI K., URUICHI M., HORIUCHI S., SAITO G., J. Am. Chem. Soc., 122 (2000), 4436.
[24] GRAJA A., ŚWIETLIK R., POŁOMSKA M., BRAU A., FARGES J.P., Synth. Met., 125 (2002), 319.
[25] GOLUB M., GRAJA A., POŁOMSKA M., phys. status solidi (a), 194 (2002), 226.
[26] SMIRANI I., SEMKIN V.N., GRAJA A., BRAU A., FARGES J.-P., Synth. Met., 102 (1999), 1263.
[27] GRAJA A., *Optical properties* [in:] J.-P. Farges (Ed.), *Organic Conductors*, Marcel Dekker, Inc., New York, 1994, p. 229.
[28] RICE M.J., LIPARI N.O., STRÄSSLER S., Phys. Rev. Lett., 39 (1977), 1359.

Received 14 September 2004
Revised 29 October 2004

Materials Science-Poland, Vol. 22, No. 4, 2004

High-pressure optical study of the neutral–ionic phase transition in TTF-CA

MATTEO MASINO[1,*], ALBERTO GIRLANDO[1], ALDO BRILLANTE[2],
RAFFAELE G. DELLA VALLE[2], ELISABETTA VENUTI[2]

[1] Dip. Chimica G.I.A.F. and INSTM-UdR Parma, Parma University, Parma, Italy

[2]Dip. Chimica Fisica ed Inorg. and INSTM-UdR Bologna, Bologna University, Italy

We have studied the pressure-induced neutral–ionic phase transition of tetrathiafulvalene-chloranil (TTF-CA) with polarized infrared absorption spectra of single crystals inside a diamond anvil cell (DAC). The evolution of the phase transition is complex, implying at least two steps. The nature of the intermediate regime is briefly discussed.

Key words: *charge transfer crystals; phase transitions; organic semiconductors; high-pressure optical spectroscopy*

1. Introduction

Neutral–ionic phase transitions (NIT) in mixed stack charge-transfer (CT) crystals were discovered nearly 25 years ago [1, 2], but continue to attract considerable attention [3] in view of the intriguing properties exhibited at the transition, such as unusual dielectric responses [4] or negative resistance effects [5]. NITs are characterized by a change in the degree of ionicity, ρ, the average charge on the electron-donor (D) and electron-acceptor (A) molecules that alternate along the stack. In the ionic phase ($\rho \geq 0.5$), the stack dimerises due to Peierl instability [3]. Therefore, there is a complex interplay between electronic valence instability (order parameter – ρ) and the structural phase transition (order parameter – the extent of dimerisation δ).

Among CT salts undergoing NIT, the prototype tetrathiafulvalene-chloranil (TTF -CA) occupies a special place, because it is almost unique in undergoing both temperature- [2] and pressure-induced [1] neutral–ionic phase transitions. On the other hand, most experimental studies have been devoted to the *T*-induced phase transitions.

---

[*] Corresponding author, e-mail: matteo.masino@unipr.it.

Studies on the p-induced transitions [6–10] showed that it occurs through some sort of “intermediate phase”, whose nature has remained elusive. The issue is important for a proper construction of the TTF-CA pressure–temperature (p–T) phase diagram [11, 12] and for the understanding of the NIT mechanism in general.

2. Experimental

TTF-CA single crystals were prepared by vacuum sublimation (75° C) of crystals obtained by mixing saturated acetonitrile solutions of commercial grade TTF and CA. In this way, very thin single crystals, suitable for absorption spectroscopy, were grown. The crystals exhibit significant dichroism in white light transmission: they appear green when the light is polarized parallel to the stack axis a, and yellow when polarized perpendicular to the stack.

The infrared (IR) absorption spectra were measured with a Bruker FTIR spectrometer (model IFS66), equipped with an A590 microscope. The spectral resolution was 2 cm^{-1}. High-pressure measurements up to 3.2 GPa were performed with a custom designed gasketed diamond anvil cell (DAC), able to fit under the IR microscope. Nujol or perfluorocarbon oil was used as the pressure-transmitting medium. Nujol oil, which is hydrostatic up to 5 GPa, gave good results in terms of pressure homogeneity inside the DAC. On the other hand, the pressure appeared to be inhomogeneous throughout the sample when perfluorocarbon oil was used, so these measurements were disregarded. Pressure calibrations were done with the ruby luminescence technique [13]. Error bars in pressure readings were ± 0.05 GPa.

3. Results

Figure 1 shows a portion of the absorption spectra polarized perpendicular to the stack axis (i.e. roughly parallel to the molecular planes) as a function of pressure. The reported spectral region (1525–1685 cm^{-1}) shows the pressure evolution of the CA b_{1u} ν_{10} normal mode, corresponding to carbonyl antisymmetric stretching. The frequency of this mode is generally used to estimate ρ by assuming a linear frequency dependence: $\nu(\rho) = \nu(0) - \Delta_{\mathrm{ion}}\rho$, where $\Delta_{\mathrm{ion}} = 160\ \mathrm{cm}^{-1}$ is the ionicity frequency shift from the fully neutral (CA^0, 1685 cm^{-1}) to the fully ionic molecule (CA^{-1}, 1525 cm^{-1}).

Figure 2 compares the pressure evolution of ionicity, as estimated from the frequency of the CA b_{1u} ν_{10} mode, with the corresponding temperature evolution [14]. In the temperature induced NIT, ρ jumps discontinuously from 0.3 to 0.5 at $T_{N\text{-}I} = 81$ K, evidencing the first-order character of the phase transition. The evolution of the pressure-induced phase transition is much more complex. The ionicity increases smoothly on increasing pressure up to $\rho \approx 0.45$ at 0.85 GPa. Above this pressure, *two bands* corresponding to the CA b_{1u} ν_{10} mode are clearly seen, which indicates the coexis-

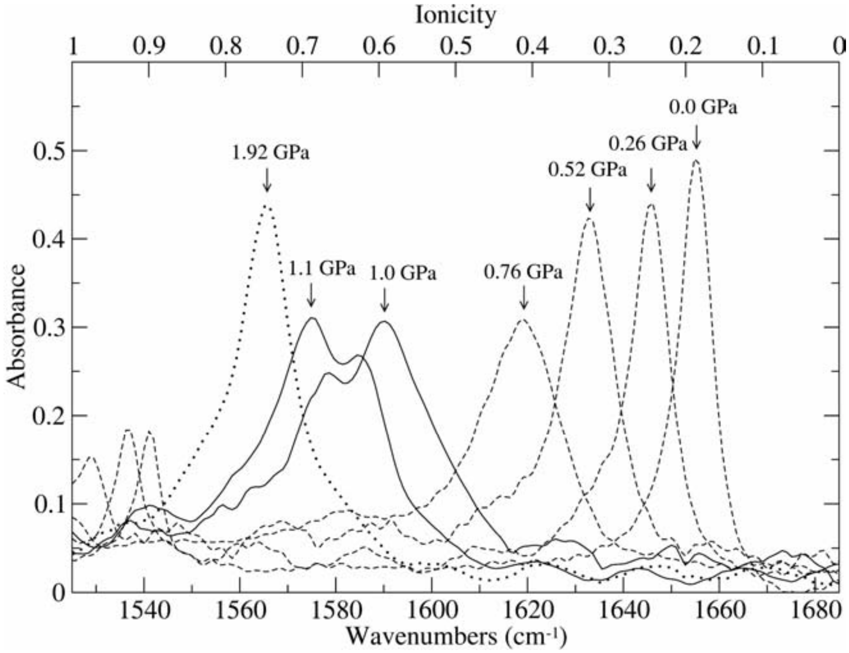

Fig.1. Pressure dependence of the TTF-CA absorption spectra polarized perpendicular to the stack axis in the 1525–1685 cm^{-1} spectral region. Continuous-line spectra refer to the intermediate phase

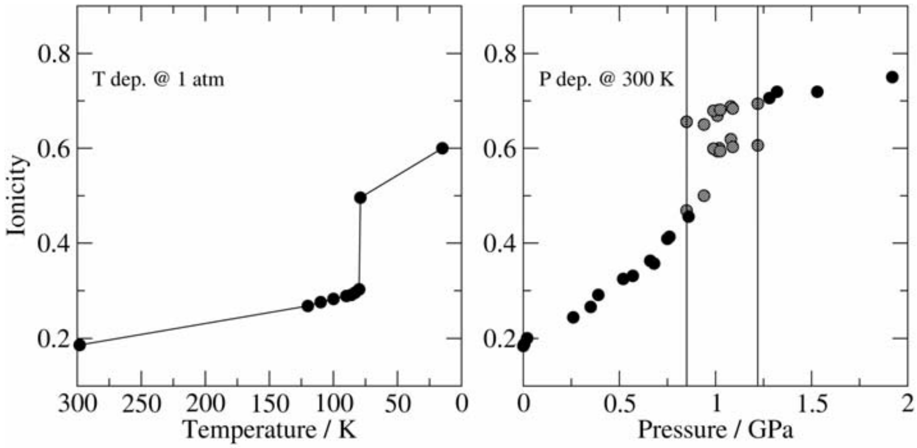

Fig. 2. Temperature (left panel) [14] and pressure (right panel) evolution of the ionicity ρ, as estimated from the CA b_{1u} mode (see text). The vertical lines indicate the pressure range stability of the intermediate phase

tence of two CA species of different ionicities, namely $\rho_1 \approx 0.5$–0.6 and $\rho_2 \approx 0.7$. The relative amount of the two species varies with pressure: The band corresponding to the more ionic ρ_2 species, present in the 0.9 GPa IR spectra only as a shoulder, gradually gains intensity and dominates over the ρ_1 band above 1.1 GPa (Fig. 1). In addition, while the ionicity of the ρ_2 species is nearly constant around 0.7, the ionicity of the ρ_1 species slightly increases from 0.5 to 0.6 on increasing the pressure (right panel of Fig. 2). We point out that the doublet structure in the IR spectra is hardly due to any macroscopic inhomogeneity, such as a non-uniform strain in the crystal, as we have checked for pressure homogeneity by means of micro-Raman mapping of the crystal sample. Moreover, the spectral changes are well reproducible for various cycles on different crystal samples. The doublet structure disappears above 1.2 GPa, and we observe a single CA b_{1u} ν_{10} band. Above this pressure, the ionicity is unique again, and increases from $\rho \approx 0.70$ to $\rho \approx 0.78$ at 2 GPa.

4. Discussion

We will now review previous studies on the pressure-induced NIT of TTF-CA and compare them with the data presented above. A generally accepted picture emerging from previous spectroscopic studies is that the *p*-induced NIT in TTF-CA occurs through some sort of intermediate state, in which quasi-ionic and quasi-neutral molecular species ($I + N$) coexist. Indeed, evidence of a doublet structure for bands mostly sensitive to ionicity has been found in vibrational IR [6, 8], Raman spectra [9], and in UV-VIS optical reflectivity measurements [7]. At room temperature, this intermediate mixed ($I + N$) state starts at a pressure around 0.7 GPa and ends up at 1.1 GPa, when the system undergoes the transition towards a single ionicity ionic phase [6, 8].

More recently, the *p*-*T* phase diagram of TTF-CA has been investigated by means of neutron diffraction and nuclear quadrupole resonance in a remarkable work by Lemée-Cailleau et al. [11]. They postulate the existence of a triple point, located approximately at 0.5 GPa and 205 K, above which the *N*-*I* first order phase transition line splits into two. Such an observation agrees with the picture described above, implying an intermediate phase in the *p*-induced NIT above 205 K. The nature of this unusual solid-state *p*-*T* phase diagram has been described in terms of the condensation and ordering of CT excitations [11, 12]. In other words, at relatively high temperatures, the neutral phase should be considered to be composed of neutral and ionic *dynamic* domains, thermally fluctuating in time and space. When the concentration of the ionic domains is high enough, a first order phase transition occurs: the ionic domains condense in 1-D strings, forming the intermediate phase. The first order line ends up at a critical point, when the difference between the neutral and intermediate phases disappears. By further increasing pressure, a 3-D ordering phase transition of the 1-D ionic strings drives the intermediate phase to the ionic phase.

Our data (Fig. 1) confirm the presence of an intermediate phase, which now appears well established even at room temperature. As a consequence, the neutral phase -to-intermediate phase transition line should be extended up to at least 300 K, shifting the critical point, if any, to a higher temperature. At variance with previous studies, we observe the starting of the intermediate state at a pressure around 0.85 GPa, slightly higher than the previously reported values. Both species (ρ_1 + ρ_2) seem to be already on the ionic side. We remark, however, that the IR spectra polarized parallel to the stack axis, which are not reported here and currently under analysis, show significant changes already at 0.7 GPa. In addition, we point out that the neutral–ionic borderline changes with the stack structure: if the stack is regular, theory puts the crossover at $\rho \approx 0.68$ [15], whereas for a chain of DA dimers the crossover is at $\rho \approx 0.5$. Further studies, both experimental and theoretical, are therefore needed, and are in progress, to understand the complex nature of the pressure-induced NIT in TTF-CA.

Acknowledgements

Work supported by INSTM (Prisma 2002 project) and by the MIUR.

References

[1] TORRANCE J.B., VAZQUEZ J.E., MAYERLE J.J., LEE V. Y., Phys. Rev. Lett., 46 (1981), 253.
[2] TORRANCE J.B., GIRLANDO A., MAYERLE J.J., CROWLEY J.I., LEE V. Y., BATAIL P., LAPLACA S.J., Phys. Rev. Lett., 47 (1981), 1747.
[3] GIRLANDO A., PAINELLI A., BEWICK S.A., SOOS Z.G., Synth. Metals, 141 (2004), 129.
[4] OKAMOTO H., MITANI T., TOKURA Y., KOSHIHARA S., KOMATSU T., IWASA Y., KODA T., SAITO G., Phys. Rev. B, 43 (1991), 8224.
[5] TOKURA Y., OKAMOTO H., KODA T., MITANI T., SAITO G., Phys. Rev. B, 38 (1988), 2215.
[6] TOKURA Y., OKAMOTO H., KODA T., MITANI T., SAITO G., Solid State Comm., 57 (1986), 607.
[7] KANEKO Y., TANUMA S., TOKURA Y., KODA T., MITANI T., SAITO G., Phys. Rev. B, 35 (1987), 8024.
[8] TAKAOKA K., KANEKO Y., OKAMOTO H., TOKURA Y., KODA T., MITANI T., SAITO G., Phys. Rev. B, 36 (1987), 3884.
[9] HANFLAND M., BRILLANTE A., GIRLANDO A., SYASSEN K., Phys. Rev. B, 38 (1988), 1456.
[10] MORÉAC A., GIRARD A., DELUGEARD Y., J. Phys. Condens. Matter, 8 (1996), 3569.
[11] LEMÉE-CAILLEAU M.H., LE COINTE M., CAILLEAU H., LUTY T., MOUSSA F., ROOS J., BRINKMANN D. TOUDIC B., AYACHE C., KARL N., Phys. Rev Lett., 79 (1997), 1690.
[12] LUTY T., CAILLEAU H. KOSHIARA S., COLLET E., TAKESADA M., LEMÉE-CAILLEAU M.H., BURON-LE COINTE M., NAGAOSA N., TOKURA Y, ZIENKIEWICZ E., OULADDIAF B., Europhys. Lett., 59 (2002), 619.
[13] PIERMARINI G.J., BLOCK S., BARRETT J.D., FORMAN R.A., J. Appl. Phys., 46 (1975), 2744.
[14] MASINO M., GIRLANDO A., SOOS Z.G., Chem. Phys. Lett., 369 (2003), 428.
[15] ANUSOOYA-PATI Y., SOOS Z.G., PAINELLI A., Phys. Rev. B, 63 (2001), 205118.

Received 20 September 2004
Revised 6 October 2004

Materials Science-Poland, Vol. 22, No. 4, 2004

Spectral studies of new organic conductors based on TTF derivatives with polymeric isocyanuric acid anions

BOLESŁAW BARSZCZ[1*], ANDRZEJ ŁAPIŃSKI[1], ANDRZEJ GRAJA[1]
ALEXANDRA M. FLAKINA[2], RIMMA N. LYUBOVSKAYA[2]

[1]Institute of Molecular Physics, Polish Academy of Sciences,
ul. M. Smoluchowskiego 17, 60-179 Poznań, Poland

[2]Institute of Problems of Chemical Physics, RAS, Ac. Semenov Prospect 5,
142432 Chernogolovka, Moscow Region, Russia

Spectral investigations of new organic conductors (BEDO-TTF)$_2$($C_3H_2N_3O_3$) and (DB-TTF) ($C_3H_2N_3O_3$) were performed. Optical absorption spectra in the range of 400–40 000 cm^{-1} of the powdered salts dispersed in KBr pellets were recorded and analysed. The spectra of (BEDO-TTF)$_2$($C_3H_2N_3O_3$) are characteristic of organic metals and show small anisotropy, which is typical of quasi-two-dimensional materials. On the other hand, the spectra of (DB-TTF)($C_3H_2N_3O_3$) are typical of semiconducting materials. The (BEDO-TTF)$_2$($C_3H_2N_3O_3$) salt undergoes a phase transition at about 120 K. The polarized reflectance spectra of single crystals of (BEDO-TTF)$_2$($C_3H_2N_3O_3$) were recorded in the range of 600–7000 cm^{-1}, down to 4 K. The frequency dependences of reflectivity were fitted with a Drude model and the transport parameters were evaluated and investigated vs. temperature. An assignment of some vibrational bands in the IR spectra was proposed.

Key words: *BEDO-TTF salt; DB-TTF salt; TTF derivatives; organic conductors; IR spectroscopy; transport properties*

1. Introduction

Most of the research concerning organic conductors has been focused on the synthesis and studies of cation radical salts based mainly on the bis(ethylenedithio)-tetrathiafulvalene (BEDT-TTF or ET) molecule and its numerous structural modifications. For our spectral investigations we chose new salts formed by bis(ethylenedioxy)tetrathiafulvalene (BEDO-TTF) and dibenzotetrathiafulvalene (DB-TTF) donors, with a monosubstituted anion of isocyanuric acid $(C_3H_2N_3O_3)^-$ (Scheme 1).

---

[*] Corresponding author, e-mail: barszcz@ifmpan.poznan.pl.

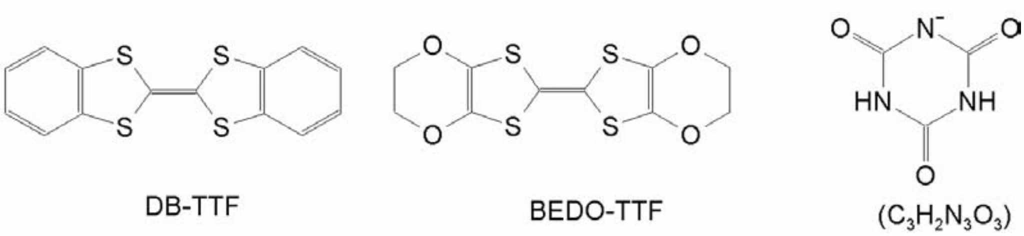

Scheme 1. The DB-TTF molecule, BEDO-TTF molecule and $(C_3H_2N_3O_3)^-$ isocyanuric acid anion

BEDO-TTF and DB-TTF are modifications of the BEDT-TTF molecule; the difference between these molecules lies in their outer rings. The BEDO-TTF molecule, with four sulphur atoms in the outer rings substituted by oxygen atoms, is a well-known donor molecule that has been successfully used for the synthesis of many ion-radical salts exhibiting metallic conductivity and superconductivity [1–4]. The DB-TTF molecule is less commonly used; instead of two outer rings with ethylenedithio fragments, it contains two outer benzene rings. The carbon atoms in the benzene rings are smaller than sulphur (in BEDT-TTF) or oxygen atoms (in BEDO-TTF), which strongly influences physical properties of DB-TTF salt compared to the salts of BEDT-TTF and BEDO -TTF.

Similar to $(BEDT\text{-}TTF)_2(C_3H_2N_3O_3)$ [5], the crystal structure of $(BEDO\text{-}TTF)_2\text{-}(C_3H_2N_3O_3)$ has a layered arrangement; the BEDO-TTF layers alternate with $(C_3H_2N_3O_3)^-$ anions. In DB-TTF salt, one can observe one-dimensional stacks. As in $(BEDT\text{-}TTF)_2(C_3H_2N_3O_3)$ [5], the anions in $(BEDO\text{-}TTF)_2(C_3H_2N_3O_3)$ and $(DB\text{-}TTF)(C_3H_2N_3O_3)$ are also linked by hydrogen bonds in one-dimensional polymer chains, which do not interact with each other. $(BEDO\text{-}TTF)_2(C_3H_2N_3O_3)$ is a 2D metal-like conductor down to 120 K (σ_{RT} =3.34 S/cm); at this temperature the salt undergoes a phase transition. $(DB\text{-}TTF)(C_3H_2N_3O_3)$ salt, on the other hand, exhibits semiconducting properties with a room temperature conductivity of $\sigma_{RT} = 10^{-1}$ S/cm [5].

In this communication, we report the first spectral studies of $(BEDO\text{-}TTF)_2(C_3H_2N_3O_3)$ and $(DB\text{-}TTF)(C_3H_2N_3O_3)$ salt. The aim of these investigations is to obtain information on the physical properties of these salts over broad spectral and temperature ranges.

2. Experimental

Crystal preparation by electrocrystallization has been described elsewhere [5]. The typical dimensions of the single crystals selected for spectral investigations were about 0.02 × 0.5 × 1.0 mm^3 for BEDO-TTF salt and 0.02 × 0.1 × 2.0 mm^3 for DB-TTF salt. Samples of $(BEDO\text{-}TTF)_2(C_3H_2N_3O_3)$ crystallize in the form of elongated plates with flat and reflecting faces, whereas $(DB\text{-}TTF)(C_3H_2N_3O_3)$ crystallizes in the form of needles. The DC conductivity of $(BEDO\text{-}TTF)_2(C_3H_2N_3O_3)$ was measured by a standard DC four-probe technique down to the helium temperature.

The near normal polarized reflectance spectra of (BEDO-TTF)$_2$($C_3H_2N_3O_3$) salt for frequencies in the range of 600–7000 cm^{-1} were investigated as a function of temperature (4–300 K). The spectra were recorded from the best-developed crystal face, parallel to the conducting layers, using a FT-IR Perkin Elmer 1725X spectrometer equipped with a suitable IR microscope and cryostat. The spectra were measured for two mutually perpendicular polarizations of the incident IR beam, corresponding to the maximum ($E_{\max}$) and minimum ($E_{\min}$) of the reflected energy. For low-temperature measurements, the samples were mounted in an Oxford Instruments helium cryostat, connected to a temperature controller. The plasma-edge-like dispersion in the reflectance spectra was fitted with a Drude dielectric function. Temperature dependences of optical transport parameters (plasma frequency – ω_p, relaxation rate – Γ, and all higher frequency contributions to the dielectric function – ε_∞) were investigated. Additionally, we studied the absorption spectra of powdered samples of both BEDO-TTF and DB-TTF salts dispersed in KBr pellets in the frequency range of 400–40 000 cm^{-1}, at room temperature. These investigations were performed with two spectrometers: a Bruker Equinox 55 and a UV/Vis/NIR Perkin Elmer Lambda 19.

3. Results and discussion

3.1. Electronic structure

The electronic and vibrational absorption spectra of (BEDO-TTF)$_2$($C_3H_2N_3O_3$) and (DB-TTF)($C_3H_2N_3O_3$) salts are shown in Fig. 1.

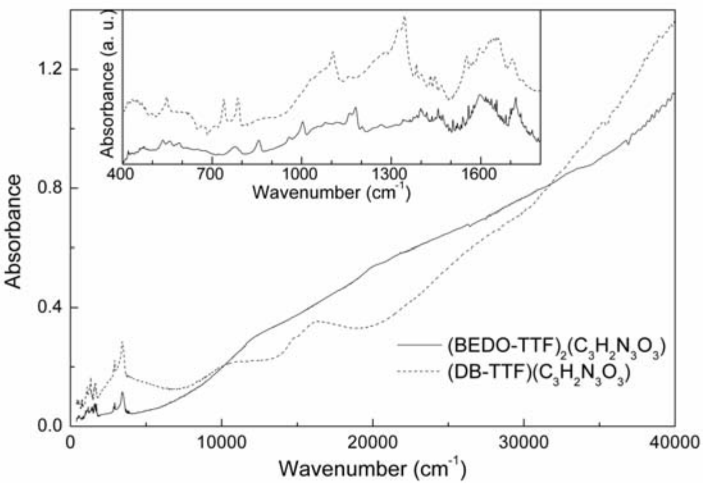

Fig. 1. Electronic absorption spectra of (BEDO-TTF)$_2$($C_3H_2N_3O_3$) and (DB-TTF)($C_3H_2N_3O_3$) powders dispersed in KBr pellets (weight concentration 1:2000). The inset shows the vibrational part of the absorption spectrum

The spectrum of (BEDO-TTF)$_2$($C_3H_2N_3O_3$) consists of intermolecular charge transfer bands at about 3000 cm^{-1} and 12 200 cm^{-1}, and a band related to intramolecular excitations at about 20 000 cm^{-1}. The band at 3000 cm^{-1} corresponds to the charge transfer process BEDO-TTF^0 + BEDO-TTF$^+$ → BEDO-TTF$^+$ + BEDO-TTF^0 [6]; its position depends on the hopping integrals and the Coulomb repulsion energy between two electrons on adjacent molecules. The band at 12 200 cm^{-1} is attributed to the charge transfer process BEDO-TTF$^+$ + BEDO-TTF$^+$ → BEDO-TTF^{2+} + BEDO-TTF^0 [7]. The position of this band can be described approximately by the value of the effective Coulomb interaction, which is given by $U = U_0 - V_1$, where U_0 is the intramolecular Coulomb repulsion energy between two electrons on the same site. The most important difference between the electronic spectra of BEDT-TTF and BEDO-TTF reveals itself in the position of the mentioned intermolecular band at about 12 000 cm^{-1}; it is observed in BEDT-TTF salt at a lower frequency, namely around 10 000 cm^{-1}. It results from calculations of valence force constants that the rigidity of the outer rings of BEDO-TTF is larger than that of BEDT-TTF [8]. This can lead to a less effective screening of Coulomb interactions and an increase in both U_0 and the frequency of this charge transfer band. The spectrum of (DB-TTF)($C_3H_2N_3O_3$) consists of bands at about 3400 cm^{-1}, 11 000 cm^{-1}, 16 500 cm^{-1}, and 28 000 cm^{-1}. By analogy to BEDT-TTF compounds (see e.g. [7]), we relate the first two bands to intersite charge transfer excitations, whereas the bands at 16 500 cm^{-1} and 28 000 cm^{-1} to the intramolecular excitation of the DB-TTF molecule.

The reflectance spectra of (BEDO-TTF)$_2$($C_3H_2N_3O_3$) salt at 300 K and 40 K, for two perpendicular polarizations, are displayed in Figs. 2 and 3.

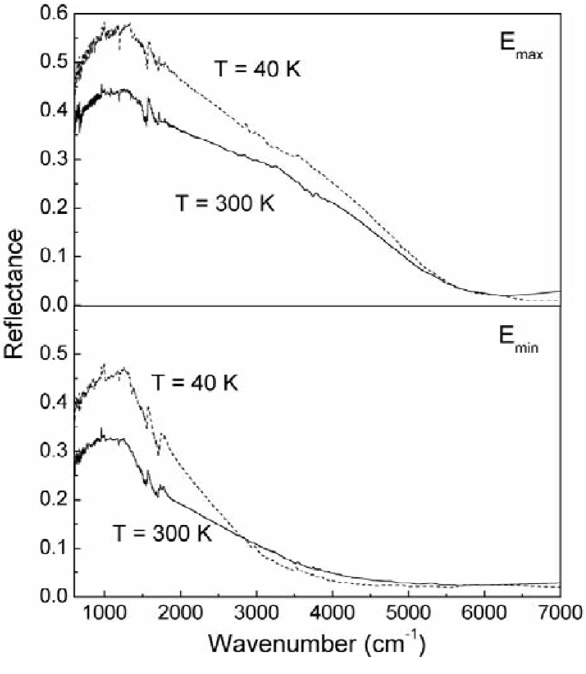

Fig. 2. Polarized reflectance spectra of (BEDO-TTF)$_2$($C_3H_2N_3O_3$) single crystals at 300 K and 40 K for two perpendicular polarizations, E_{max} (upper panel) and E_{min} (lower panel)

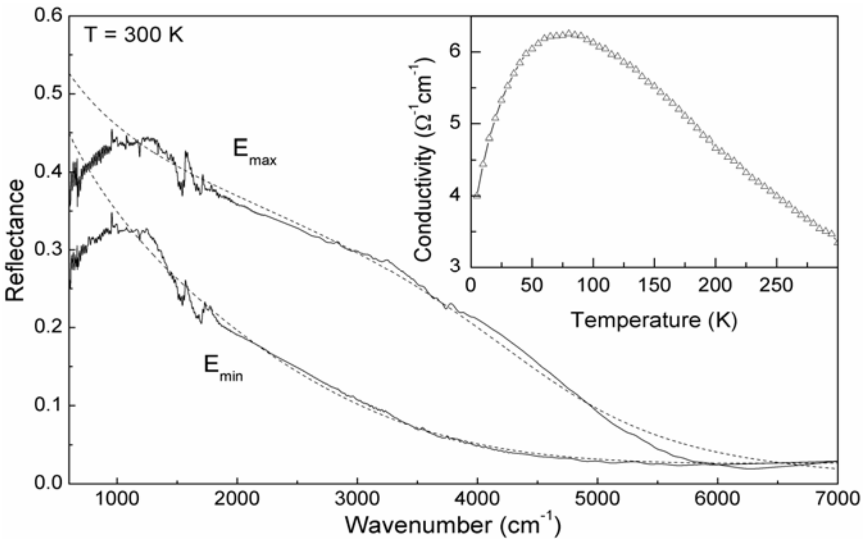

Fig. 3. Polarized reflectance spectra of (BEDO-TTF)$_2$(C$_3$H$_2$N$_3$O$_3$) single crystals at room temperature for two perpendicular polarizations, E_{max} and E_{min}, of the IR beam (dotted lines represent the Drude fits). The inset shows the temperature dependence of electrical conductivity for (BEDO-TTF)$_2$(C$_3$H$_2$N$_3$O$_3$)

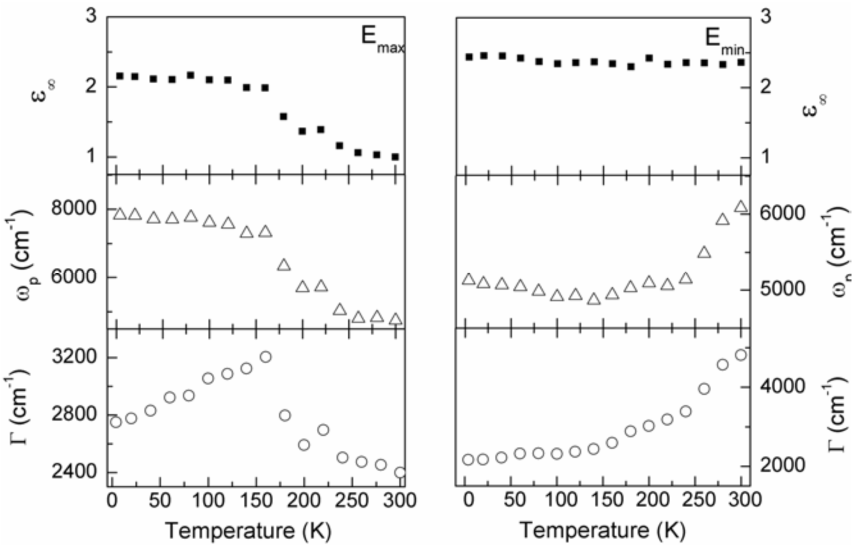

Fig. 4. Temperature dependences of the Drude parameters, extracted from fitting the reflectance data of (BEDO-TTF)$_2$(C$_3$H$_2$N$_3$O$_3$) crystals for two perpendicular polarizations, E_{max} and E_{min}, of the IR beam; ω_{p} is the plasma frequency, ε_∞ represents all higher frequency contributions to the dielectric function, and Γ is the damping constant, which is related to the relaxation time of carriers τ ($\Gamma = 1/c\tau$, c is the speed of light)

The electronic dispersion observed below about 6000 cm^{-1} is characteristic of compounds showing metallic properties; it is in agreement with electrical conductivity measurements (see the inset in Fig. 3). The observed plasma-like dispersion authorized us to use the Drude model for calculating the plasma frequency ω_p and relaxation rate Γ. Least squares fits to the experimental reflectance in the range of 2000–7000 cm^{-1} (not taking into account the region of vibrational bands, which could perturb the fit parameters) were made for reflectance calculated from the Drude dielectric function $\varepsilon(\omega)=\varepsilon_\infty-\omega_p^2/\omega(\omega+i\Gamma)$. The results of the fitting procedure at room temperature, for the two perpendicular polarizations of the IR beam E_{max} and E_{min}, are shown in Fig. 3. The temperature dependences of the transport parameters, determined by the Drude analysis, are presented in Fig. 4.

The phase transition in (BEDO-TTF)$_2$($C_3H_2N_3O_3$) considerably influences the band structure parameters. When decreasing the temperature down to about 140 K, the relaxation rate Γ and plasma frequency ω_p grow for a polarization of E_{max} and decrease for a polarization of E_{min}. Below 140 K, the plasma frequency ω_p slightly grows with decreasing temperature, whereas the relaxation rate Γ decreases. Such a behaviour of the transport parameters can be related to an increase in transfer integrals, in turn resulting from a reduction of the unit cell volume at lower temperatures. It should be emphasized that the phase transition in (BEDO-TTF)$_2$($C_3H_2N_3O_3$) is smeared over a broad temperature range in electrical conductivity measurements, and is observed at temperatures lower than the phase transition temperature determined from spectroscopic data. The modification of the transport parameters in this salt can be explained by a redistribution of charge density, and by an increase of the fraction of localized charges due to a decrease in the interactions between the BEDO-TTF molecules of neighbouring stacks.

3.2. Vibrational structure

Compared to the vibrations of the BEDT-TTF molecule [9], a normal coordinate analysis of BEDO-TTF [8] shows that the substitution of sulphur by oxygen in the outer rings leads to a markedly different charge distribution. The charge densities on the central C_2S_4 fragments of both molecules are practically the same but important differences are observed in the outer rings; the strongly electro-negative oxygen almost completely gathers the electron density of the carbon atoms. Many bands, especially those related to C-O-C fragments, therefore appear at shifted frequencies. The presence of the oxygen atoms also leads to a sharp increase in electron-molecular vibration (EMV) coupling for totally symmetric A_g modes related to the outer rings [8].

The infrared spectrum is useful for evaluating the ionicity of the ground state of CT complexes, and the degree of CT from donor to acceptor molecules. It can be estimated by utilizing specific vibrational frequencies which are sensitive to the ionicity of the molecule [10]. Moldenhauer et al. [11] have reported that the four absorption bands of BEDO-TTF^0 (864, 963, 1011, and 1082 cm^{-1}) display distinct ionisation frequency shifts on CT complex formation. According to the normal coordinate analysis of the neutral BEDO-TTF molecule, the above four bands involve vibrations of C-O bonds [8]. In this work concerning (BEDO-TTF)$_2$($C_3H_2N_3O_3$) single crystals, the appropriate bands are observed at 856, 956, 1000, and 1078 cm^{-1}. Taking into account this result [11], we estimate that the average charge per donor molecule in the salt is +0.5e.

The most characteristic feature of the IR spectra of BEDO-TTF salt is the large red shift of the ring C=C stretching band upon oxidation which appears between 1646 cm^{-1} (neutral BEDO-TTF) and 1456 cm^{-1} (BEDO-TTF^{2+}). These peaks may be assigned to BEDO-TTF in a partly oxidized state, especially the peak appearing at 1527 cm^{-1} (Fig. 1) was assigned to the C=C stretching in BEDO-TTF^{+} [12]. The IR spectra of (BEDO-TTF)$_2$($C_3H_2N_3O_3$) salt are much richer than those of BEDO-TTF; Shinohara et al. [6] have observed a similar effect. Different absorption wavenumbers from that of BEDO-TTF also imply that new electronic states appear, different from those of neutral BEDO-TTF.

4. Conclusions

In this paper, the spectra of two new salts, namely (BEDO-TTF)$_2$($C_3H_2N_3O_3$) and (DB-TTF)($C_3H_2N_3O_3$), were presented and preliminarily discussed for the first time. An analysis of the spectra allowed us to obtain information about their electronic and vibrational properties. The spectral data confirm the presence of a phase transition in (BEDO-TTF)$_2$($C_3H_2N_3O_3$) at about 120 K. Subsequent investigations of the salts will be published soon.

Acknowledgements

This project was supported by the Polish Committee for Scientific Research as a research project in the years 2004–2007, by the Centre of Excellence for Magnetic and Molecular Materials for Future Electronics within the European Commission (G5MA-CT-2002-04049), and partially by the Russian Foundation of Basic Research, grant 04-03-32296.

References

[1] Drichko N., Vlasova R.M., Semkin V.N., Bogdanova O.A., Zhilyaeva E.I., Lyubovskaya R.N., Lyubovskii R.B., Graja A., Phys. Stat. Sol. (b), 236 (2003), 668.

[2] Drichko N., Vlasova R., Semkin V., Graja A., Bogdanova O.A., Zhilyaeva E., Lyubovskaya R.N., Synth. Metals, 109 (2000), 123.

[3] Horiuchi S., Yamochi H., Saito G., Sakaguchi K., Kusunoki M., J. Amer. Chem. Soc., 118 (1996), 8604.

[4] Tanatar M.A., Świetlik R., Kushch N.D., Yagubskii E.B., J. Phys. Condens. Matter, 9 (1997), 6383.

[5] Flakina A.M., Chekhlov A.N., Luybovskaya R.N., J. Phys. IV France, 114 (2004), 501.

[6] Shinohara E., Ishimaru S., Kitagawa H., Ikeda R., Yamochi H., Saito G., Solid State Commun., 127 (2003), 407.

[7] Świetlik R., Garrigou-Lagrange C., Sourisseau C., Pages G., Delhaes P., J. Mater. Chem., 2 (1992), 857.¶

[8] POKHODNIA K.I., KOZLOV M.E., ONISCHENKO V.G., SCHWEITZER D., MOLDENHAUER J., ZAMBONI R., Synth. Metals, 55/57 (1993), 2364.
[9] KOZLOV M.E., POKHODNIA K.I., YURCHENKO A.A., Spectrochimica Acta, 45A (1989), 437.
[10] CHAPPELL J.S., BLOCH A.N., BRYDEN W.A., MAXFIELD M., POEHLER T.O., COWAN D.O., J. Am. Chem. Soc., 103 (1981), 2442.
[11] MOLDENHAUER J., POKHODNIA K.I., SCHWEITZER D., HEINEN I., KELLER H.J., Synth. Metals, 55–57 (1993), 2548.
[12] HORIUCHI S., YAMOCHI H., SAITO G., MATSUMOTO K., Mol. Cryst. Liq. Cryst., 284 (1996), 357.

Received 5 October 2004
Revised 28 October 2004

Materials Science-Poland, Vol. 22, No. 4, 2004

Optical properties of the one-dimensional organic conductors β-(EDT-TTF-I$_2$)$_2$(Pb$_{5/6}$ $_{1/6}$I$_2$)$_3$ and β-(EDT-TTF-I$_2$)$_2$(Pb$_{2/3+x}$Ag$_{1/3-2x}$ $_x$I$_2$)$_3$, $x = 0.05$

IWONA OLEJNICZAK[1*], BARTŁOMIEJ GROMADZIŃSKI[1,2], ANDRZEJ GRAJA[1],
THOMAS DEVIC[3], PATRICK BATAIL[3]

[1]Institute of Molecular Physics, Polish Academy of Sciences, Poznań, Poland

[2]Institute of Physics, Poznan University of Technology, Poznań, Poland

[3]Laboratoire de Chimie Inorganique, Matériaux et Interfaces,
CNRS FRE 2447, Université d’Angers, France

We report the room-temperature polarized infrared reflectance spectra of two radical cation salts based on halogenated TTF and two-dimensional polymeric iodoplumbate or Ag-doped iodoplumbate anions. These salts were β-(EDT-TTF-I$_2$)$_2$(Pb$_{5/6}\square_{1/6}$I$_2$)$_3$ and β-(EDT-TTF-I$_2$)$_2$(Pb$_{2/3+x}$Ag$_{1/3-2x}\square_x$I$_2$)$_3$, where $x = 0.05$ and $\square$ is a vacancy. Both materials display a metallic response, characteristic of quasi-one-dimensional organic conductors. The β-(EDT-TTF-I$_2$)$_2$(Pb$_{2/3+x}$Ag$_{1/3-2x}\square_x$I$_2$)$_3$ salt, with $x = 0.05$ is partly transparent along the lowest conductivity direction in the infrared frequency range. The single-crystal polarized absorption spectrum recorded in this direction displays a number of vibrational features related to the intramolecular modes of the EDT-TTF-I$_2$ molecule, which are assigned using available normal mode calculations. In addition, the absorption spectrum of the β-(EDT-TTF-I$_2$)$_2$(Pb$_{2/3+x}$Ag$_{1/3-2x}\square_x$I$_2$)$_3$ material dispersed in a KBr pellet is reported and discussed.

Key words: *EDT-TTF-I$_2$; iodoplumbate anion; organic conductors; reflectance spectrum; absorption spectrum*

1. Introduction

The manipulation of weak noncovalent intermolecular interactions for designing new low-dimensional solids has received increasing attention (see [1, 2] and refer-

---

[*] Corresponding author, e-mail: ywy@ifmpan.poznan.pl.

ences herein). Recently, two metallic radical cation salts based on two-dimensional polymeric iodoplumbate anions and halogenated TTF, namely β-(EDT-TTF-I$_2$)$_2$(Pb$_{5/6}\square_{1/6}$I$_2$)$_3$ and β-(EDT-TTF-I$_2$)$_2$(Pb$_{2/3+x}$Ag$_{1/3-2x}\square_x$I$_2$)$_3$, where $x = 0.05$ and $\square$ is a vacancy, have been synthesized (EDT-TTF-I$_2$ is a shortcut for ethylenedithio-1,2-diiodo-tetrathiafulvalene) [1]. In these materials, organic–halogen$\cdots$inorganic–halogen (I$\cdots$I) van der Waals interactions help stabilise the organic–inorganic interface.

Both β-(EDT-TTF-I$_2$)$_2$(Pb$_{5/6}\square_{1/6}$I$_2$)$_3$ and β-(EDT-TTF-I$_2$)$_2$(Pb$_{2/3+x}$Ag$_{1/3-2x}\square_x$I$_2$)$_3$, with $x = 0.05$, have a similar triclinic layered structure with the space group $P\bar{1}$ [1]. A conducting layer parallel to the *ab*-plane is formed by EDT-TTF-I$_2$ molecules, which are arranged in the well-known β-motif with loose stacks of one-electron-oxidized dimers along the *b*-direction. In the charge compensating inorganic Pb$_x$Ag$_y$I$_2$ slab, the edge-sharing octahedra form a polymer of the CdI$_2$-type [1]. Unlike the two-dimensional electronic structure typical of the β-(BEDT-TTF)$_2$X family [3], the intermolecular interactions within a conducting donor layer are characterized by weak interchain interactions, accompanied by significantly stronger uniform interactions along the EDT-TTF-I$_2$ chains. The specific one-dimensional-like electronic band structure [1] is related to the head-to-tail arrangement of asymmetric donor molecules in the stack. In spite of the close similarities between β-(EDT-TTF-I$_2$)$_2$(Pb$_{5/6}\square_{1/6}$I$_2$)$_3$ and β-(EDT-TTF-I$_2$)$_2$(Pb$_{2/3+x}$Ag$_{1/3-2x}\square_x$I$_2$)$_3$, with $x = 0.05$, both in their crystal and electronic structures, there is a significant difference between their room temperature d.c. conductivities, which are 2.5 $\Omega^{-1}\cdot\mathrm{cm}^{-1}$ and 110 $\Omega^{-1}\cdot\mathrm{cm}^{-1}$, respectively.

In order to characterize the optical properties of β-(EDT-TTF-I$_2$)$_2$(Pb$_{5/6}\square_{1/6}$I$_2$)$_3$ and β-(EDT-TTF-I$_2$)$_2$(Pb$_{2/3+x}$Ag$_{1/3-2x}\square_x$I$_2$)$_3$, with $x = 0.05$, we have measured the room temperature polarized reflectance and absorption spectra of single crystalline samples. Our overall goal is to investigate the structure–property relationships in this class of low-dimensional solids.

2. Experimental

Single crystals of both materials were prepared by the electrochemical method as described elsewhere [1]. Samples of β-(EDT-TTF-I$_2$)$_2$(Pb$_{5/6}\square_{1/6}$I$_2$)$_3$ were square-shaped shiny platelets with a typical size of about $0.2 \times 0.2 \times 0.05$ cm^3. On the other hand, β-(EDT-TTF-I$_2$)$_2$(Pb$_{2/3+x}$Ag$_{1/3-2x}\square_x$I$_2$)$_3$, with $x = 0.05$, crystallizes in very thin, flat, and partly transparent brown needles; the lengths of the largest samples used for measurements were about 1.3 mm. Samples were oriented based on the polarized infrared reflectance spectra and calculated interaction energies [1]. Near-normal incidence polarized reflectance and absorption spectra in the conducting *ab*-plane were measured using a Perkin-Elmer 1725 X Fourier-transform infrared spectrometer, equipped with an infrared microscope (650–7000 cm^{-1}, resolution 2 cm^{-1}) and a gold wire grid polariser. The absorption spectra of the KBr pellets were recorded using a Bruker

Equinox 55 Fourier-transform infrared spectrometer (400–7000 cm^{-1}, resolution 2 cm^{-1}) and a Perkin Elmer Lambda 19 spectrophotometer (5000–40 000 cm^{-1}). Optical conductivity spectra were calculated by the Kramers–Kronig analysis, based on the extrapolation of infrared reflectance to low frequencies with a metallic Hagen–Rubens equation; standard extrapolations were used for higher frequencies.

3. Results and discussion

Figure 1 shows the reflectance (upper panel) and optical conductivity spectra (lower panel) of β-(EDT-TTF-I$_2$)$_2$(Pb$_{5/6}\square_{1/6}$I$_2$)$_3$ and β-(EDT-TTF-I$_2$)$_2$(Pb$_{2/3+x}$Ag$_{1/3-2x}\square_x$I$_2$)$_3$, with

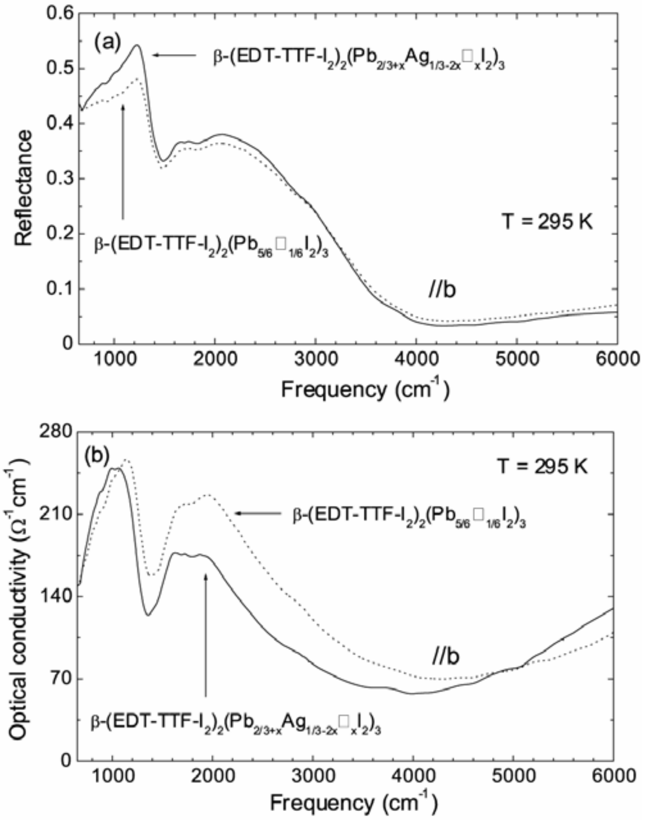

Fig. 1. Infrared reflectance (a) and optical conductivity (b) spectra of β-(EDT-TTF-I$_2$)$_2$(Pb$_{5/6}\square_{1/6}$I$_2$)$_3$ (dotted line) and β-(EDT-TTF-I$_2$)$_2$(Pb$_{2/3+x}$Ag$_{1/3-2x}\square_x$I$_2$)$_3$, with $x = 0.05$ (solid line), polarized along the *b* direction

$x = 0.05$, polarized in the *b*-direction. Both materials display similar behaviour, characteristic of one-dimensional organic conductor [4, 5]. In the *b*-direction which is parallel to the stacks of EDT-TTF-I$_2$ molecules, reflectance is high and metallic in character, with a plasma edge about 4000 cm^{-1}. The $\perp b$ spectra (not shown) are flat and generally structureless but influenced by interference fringes (weakly in the case of $\beta\text{-(EDT-TTF-I}_2)_2(\text{Pb}_{5/6}\square_{1/6}\text{I}_2)_3$, and very strongly in the case of $\beta\text{-(EDT-TTF-I}_2)_2(\text{Pb}_{2/3+x}\text{Ag}_{1/3-2x}\square_x\text{I}_2)_3$, with $x = 0.05$), which appear because both materials are partially transparent to infrared light. In the $\|b$ optical conductivity spectra (lower panel), two distinct low-energy electronic bands are observed in the frequency range of 1000–2000 cm^{-1}. They are possibly related to charge transfer excitations along the EDT-TTF-I$_2$ stack. The Drude peak, which is expected in a metallic material, does not appear in the two spectra due to the limited frequency range (above 650 cm^{-1}); the Drude feature can be very narrow for organic conductors [4].

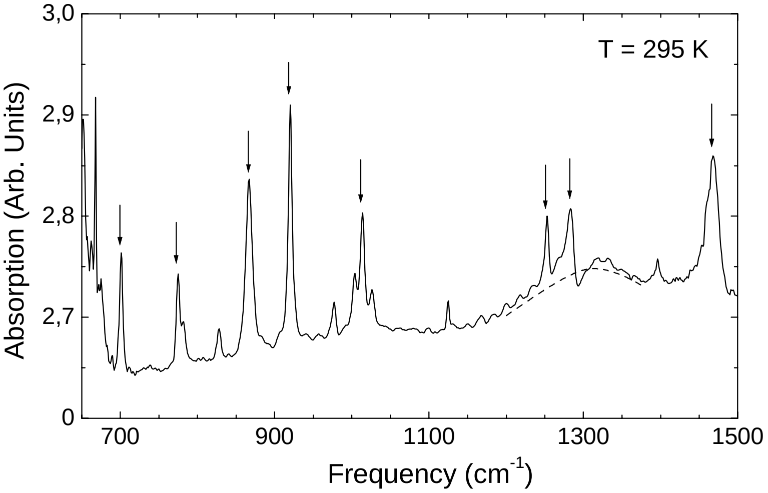

Fig. 2. Absorption spectrum of $\beta\text{-(EDT-TTF-I}_2)_2(\text{Pb}_{2/3+x}\text{Ag}_{1/3-2x}\square_x\text{I}_2)_3$, with $x = 0.05$, polarized along the $\perp b$ direction, in the frequency range of intramolecular modes; the bands discussed are shown by arrows

The $\perp b$ absorption of $\beta\text{-(EDT-TTF-I}_2)_2(\text{Pb}_{2/3+x}\text{Ag}_{1/3-2x}\square_x\text{I}_2)_3$, with $x = 0.05$, measured in the transmission mode in the frequency range of the vibrational features, is displayed in Fig. 2. The spectrum is polarized approximately parallel to the short EDT-TTF-I$_2$ axis in the crystal structure. Here, a number of vibrational bands are shown, and we assign them as intramolecular modes of the EDT-TTF-I$_2$ molecule. In addition, a weak electronic excitation is observed about 1300 cm^{-1}; another weak and very broad electronic band appears about 3000 cm^{-1} (not shown). Due to the low symmetry of $\beta\text{-(EDT-TTF-I}_2)_2(\text{Pb}_{2/3+x}\text{Ag}_{1/3-2x}\square_x\text{I}_2)_3$ with $x = 0.05$, which results from an asymmetric donor molecule, all intramolecular modes can appear both in Raman and infrared spectra. Using normal mode calculations, infrared spectra, and Raman spectra for neutral EDT-TTF-I$_2$ [6], we attribute the 1468 cm^{-1} feature as a stretching C=C mode, whose frequency is downshifted from 1516 cm^{-1} (the Raman mode in neutral molecule) due to oxidation and also possibly to electron-molecular vibration (EMV) coupling with low-lying electronic excitations [7, 8]. In the case of an asymmetric donor molecule, only weak coupling is expected, but basically all intramolecular vibrations are allowed for coupling[*]. In fact, the C=C stretching vibration is barely seen in the infrared spectra of neutral EDT-TTF-I_2 [6], and it is the strongest band in the infrared spectrum of β-(EDT-TTF-$I_2)_2(Pb_{2/3+x}Ag_{1/3-2x}\square_xI_2)_3$ with $x = 0.05$. This can serve as a proof that the band is activated by EMV coupling. Other relatively strong and broad features that are possibly EMV-activated include the mode at 1283 cm^{-1} related to C–H wagging, 1253 cm^{-1} (C–H wagging), 1014 cm^{-1} (C–H rocking, C–C stretching), 920 cm^{-1} (C–S stretching, C–I stretching), 867 cm^{-1} (C–H rocking), 775 cm^{-1} (C–H rocking, C–S stretching), and 701 cm^{-1} (C–S stretching, C–I stretching).

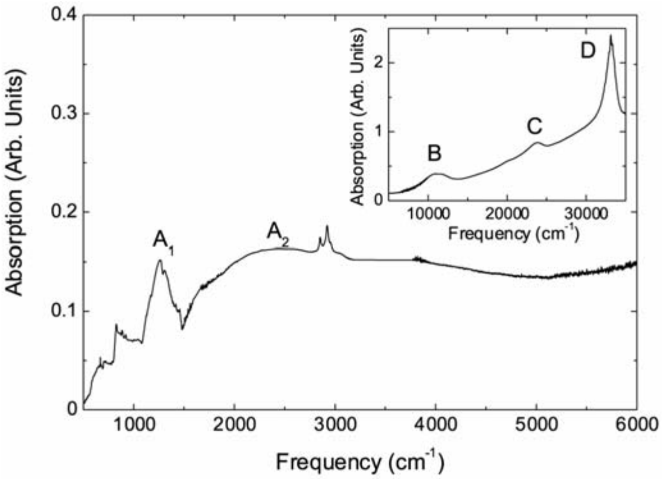

Fig. 3. Infrared and optical (inset) absorption spectra of β-(EDT-TTF-$I_2)_2(Pb_{2/3+x}Ag_{1/3-2x}\square_xI_2)_3$, with $x = 0.05$, dispersed in a KBr pellet (unpolarised)

Figure 3 shows the unpolarised absorption spectrum of β-(EDT-TTF-$I_2)_2(Pb_{2/3+x}Ag_{1/3-2x}\square_xI_2)_3$, with $x = 0.05$, dispersed in a KBr pellet. We relate most of the bands in the spectrum to electronic excitations. In the infrared frequency range, we observe features polarized in both the $\parallel b$- and $\perp b$ directions. The A_1 band is probably related to the lowest energy excitation in the *b* direction (Fig. 1b), and to the $\perp b$ excitation (the dashed line in Fig. 2). A very broad A_2 band is probably connected to both the 2000 cm^{-1} excitation polarized in the *b* direction (Fig. 1b) and the 3000 cm^{-1} excitation in $\perp b$-direction. The sequence of higher energy excitations (the inset in Fig. 3) is somehow reminiscent of the classification developed by Torrance et al. for one-dimensional TCNQ-based compounds (TCNQ – tetracyanoquinodimethane) [9]. In this picture, A and B bands both involve charge transfer between donor molecules (B excitation

---

[*] In the case of the lowest symmetry (C_1), all intramolecular modes are of the *A*-type and can be coupled with the electronic states.

leads to a double-charged donor molecule, so its energy can serve as a rough estimation of the electron Coulomb interaction U); C and D bands correspond to intramolecular excitations. On the other hand, EDT-TTF-I_2 is substantially different than TCNQ, and it is well known that iodoplumbate compounds can have excitations in the visible frequency range, which is where C and D bands are located [10].

4. Conclusions

We investigated the room temperature polarized response of the organic conductors $\beta\text{-(EDT-TTF-I}_2)_2(\text{Pb}_{5/6}\square_{1/6}\text{I}_2)_3$ and $\beta\text{-(EDT-TTF-I}_2)_2(\text{Pb}_{2/3+x}\text{Ag}_{1/3-2x}\square_x\text{I}_2)_3$, with $x = 0.05$, in the infrared frequency range. These materials exhibit similar one-dimensional metallic behaviour, as expected from electronic band structure calculations [1]. In the vibrational frequency range, signatures of EMV coupling are found. The strongest bands, arising from intramolecular modes, are assigned. Further studies are on the way to give more information on the complicated picture of charge transfer excitations and EMV coupling in both materials.

Acknowledgements

This work was supported by the Polish Committee for Scientific Research as the research project in the years 2004–2007.

References

[1] Devic T., Evain M., Moëlo Y., Canadell E., Auban-Senzier P., Fourmigue M., Batail P., J. Am. Chem. Soc., 125 (2003), 3295.

[2] Devic T., Canadell E., Auban-Senzier P., Batail P., J. Mater. Chem., 14 (2004), 135.

[3] Whangbo M.-H., Williams J.M., Leung W.P.C., Beno M.A., Emge T.J., Wang H.H., Carlson K.D., Crabtree G.W., J. Am. Chem. Soc., 107 (1985), 5815.

[4] Jacobsen C.S., *Infrared Properties of Organic Conductors*, [in:] D. Jérome and L.G. Caron (Eds.), *Low-Dimensional Conductors and Superconductors*, Plenum Press, New York, 1987, p. 253.

[5] Kawamoto T., Ashizawa M., Aragaki M., Mori T., Yamamoto T., Tajima H., Kitagawa H., Mitani T., Misaki Y., Tanaka K., Phys. Rev. B, 60 (1999), 4635.

[6] Łapiński A., Świetlik R., unpublished results.

[7] Rice M.J., Phys. Rev. Lett., 37 (1976), 36.

[8] Yartsev V.M., Graja A., Int. J. Mod. Phys. B, 12 (1998), 1643.

[9] Torrance J.B., Scott B.A., Kaufman F.B., Solid State Commun., 17 (1975), 1369.

[10] Ishihara T., *Optical Properties of Pb-Based Inorganic–Organic Perovskites*, [in:] T. Ogawa and Y. Kanemitsu (Eds.), *Optical Properties of Low-Dimensional Materials*, World Scientific, Singapore, 1995, p. 286.

Received 30 October 2004
Revised 3 November 2004

Materials Science-Poland, Vol. 22, No. 4, 2004

Phase transitions in β-(BEDT-TTF)$_2$XF$_6$ (X = P, Sb or As) salts as seen by Raman Spectroscopy

A. KOWALSKA[*], R. WOJCIECHOWSKI, J. ULANSKI

Department of Molecular Physics, Technical University of Łódź, 90-924 Łódź, Poland

Raman spectra of three charge-transfer salts, β-(BEDT-TTF)$_2$XF$_6$ (where X = P, Sb, As), were measured in the temperature range of 300–80 K. The salts exhibit fluctuations in charge ordering, indicating the formation of Wigner-like crystals.

Key words: *Raman spectroscopy; charge ordering; Wigner crystal*

1. Introduction

The nature of phase transitions in low-dimensional organic metals has attracted a lot of interest for many years. In some organic conductors, phase transitions generate a charge ordered (CO) state in the form of charge-rich and charge-poor sites. Such a phase transition is connected with charge localisation on molecules, and a possible explanation of these phenomena is electron correlation effects. In the presence of a strong dimerisation, on-site Coulomb interactions can give rise to a dimer Mott insulating state, while the inter-site Coulomb interactions can stabilize the CO as a Wigner crystal, even in the presence of some weak dimerisation [1].

In the present study, we have investigated vibrational spectra for three salts of the bis(ethylenedithio)tetrathiafulvalene (BEDT-TTF) donor molecule: β-(BEDT-TTF)$_2$PF$_6$, β-(BEDT-TTF)$_2$SbF$_6$, and β-(BEDT-TTF)$_2$AsF$_6$. These salts show a metal–insulator phase transition at 293 K (X = PF$_6$), 273 K (X = SbF$_6$), and 264 K (X = AsF$_6$) [2– 4], respectively. In crystals of the β-(BEDT-TTF)$_2$PF$_6$ salt, the donor molecules are strongly dimerised [5]. The two other salts, β-(BEDT-TTF)$_2$SbF$_6$ and β-(BEDT-TTF)$_2$AsF$_6$, show only weak dimerisation [3, 5]. It was therefore of interest to check which of the effects (Mott insulator or Wigner crystal) is responsible for the phase transitions.

---

[*] Corresponding author, e-mail: chwiejcz@p.lodz.pl.

Vibrational spectroscopy is an effective method of investigating electron correlation effects and phase transitions in BEDT-TTF salts. The frequencies of some C=C stretching modes in the donor molecule carry information on the charge localised on the molecule making possible the determination of charge spatial distribution in the crystal's unit cell [6]. Charge ordering can be observed in the Raman spectrum as a splitting of the Raman bands sensitive to the charge on the donor molecules. It is well known that for the BEDT-TTF molecule two in-phase ring C=C stretching modes, ν_2 and ν_3, show large charge-dependent frequency shifts. There is also one antiphase ring C=C stretching mode sensitive to the charge, ν_{27}, which can be observed in infrared spectroscopy. Nevertheless, the antiphase vibration of molecules forming a dimer can become Raman active and in such a case the mode ν_{27} will be visible in the Raman spectrum [6].

2. Experimental

Single crystals of the charge transfer salts (BEDT-TTF)$_2$XF$_6$ (where X = P, Sb, As) were synthesized by electro-crystallisation according to the known procedure [4]. Crystallographic X-ray investigations have shown that all the crystals obtained are in the β-phase. The salt β-(BEDT-TTF)$_2$PF$_6$ belongs to the orthorhombic crystal system, with the P_{nna} space group at room temperature [2]. The salts β-(BEDT-TTF)$_2$SbF$_6$ and β-(BEDT-TTF)$_2$AsF$_6$ belong to the monoclinic crystal system, with a $C_{2/c}$ space group at room temperature [4].

Raman spectra in the temperature range of 300–80 K were recorded using a Micro-Raman Spectrometer (Jobin-Yvon T64000) and 514.5 nm laser light. Single crystals were mounted with silicon grease on a cold stage in a homemade helium cryostat. The spectra were collected upon cooling in ca. 20 K intervals; the crystals were thermostated at each temperature for ca. 20 minutes. The Raman bands in the characteristic frequency range of the C=C stretching modes (1200–1700 cm^{-1}) were recorded for the incident light polarised along and perpendicular to the long axis of the BEDT-TTF molecules.

3. Results and discussion

The Raman spectra obtained for all the investigated BEDT-TTF salts show an abrupt change in the C=C stretching band, from a broad band at high temperatures to multiple peaks below the metal-isolator transition temperature. The spectra for all three salts are very similar at room temperature, i.e., in the metal states. Therefore, in Fig. 1 and Fig. 2 we show the spectra at different temperatures only for the salt β-(BEDT-TTF)$_2$AsF$_6$. For the two other salts, only the spectra obtained at 80 K (i.e., well below their phase transition temperatures) are presented in the insets.

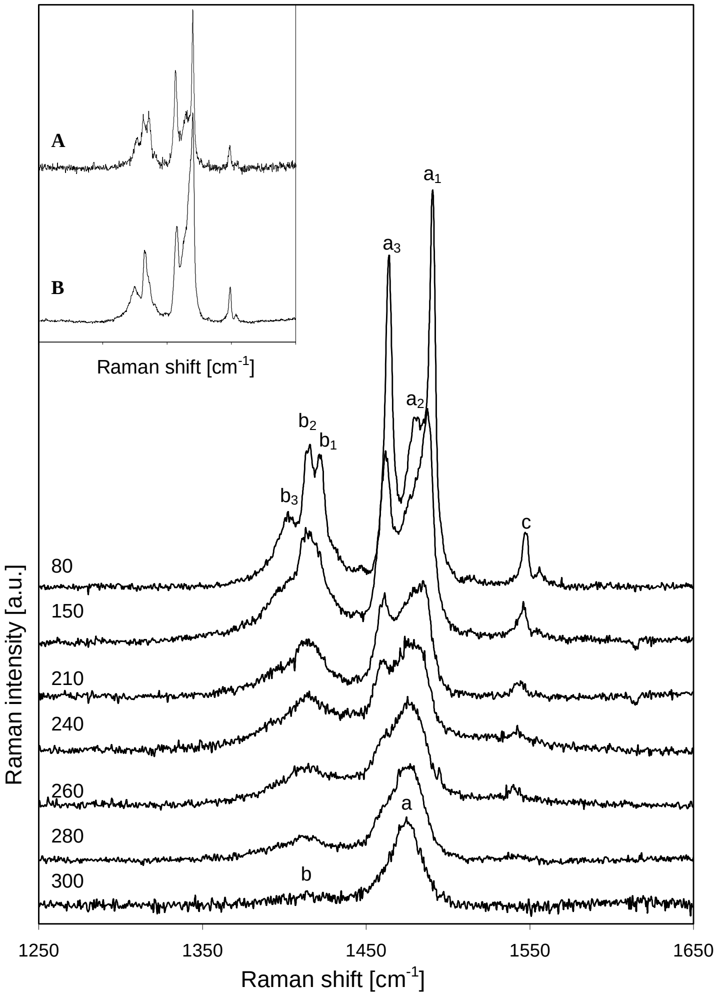

Fig. 1. Temperature dependences of the Raman active C=C stretching modes for β- (BEDT-TTF)$_2$AsF$_6$ salt, with the laser light polarisation plane parallel to the long axis of the donor molecules. The inset shows spectra for β-(BEDT-TTF)$_2$PF$_6$ (A) and β-(BEDT-TTF)$_2$SbF$_6$ (B) salts at 80 K and the same polarisation

Figure 1 shows the spectra obtained for the incident light polarised along the long axis of the BEDT-TTF molecules. The bands marked as *a* and *b*, observed at 300 K, undergo a splitting at 260 K, i.e. at the metal–insulator transition temperature for β-(BEDT-TTF)$_2$AsF$_6$, observed in resistivity and EPR measurements [4]. Among the multiple peaks observed at 80 K, we can attribute the peaks *c* (1547 cm^{-1}) and a_1 (1489 cm^{-1}) to ν_2, the peak a_2 (1482 cm^{-1}) to ν_{27}, and the peak a_3 (1463 cm^{-1}) to ν_3. Since the frequencies of the ν_2 mode are sensitive to charge, the observed position of the bands after splitting indicates that peak *c* corresponds to the charge-poor site, while peak a_1 corresponds to the charge-rich one. Basing only on the frequency of the ν_2 mode, we estimated the deviation of the charge on the donor molecules to be 0.16 and 0.84.

An unequivocal assignment of three peaks at lower frequencies (b_1 at 1422 cm^{-1}, b_2 at 1415 cm^{-1}, and b_3 at 1403 cm^{-1}) is difficult. One of them should be assigned to the ν_3 mode, the others probably to bending ones.

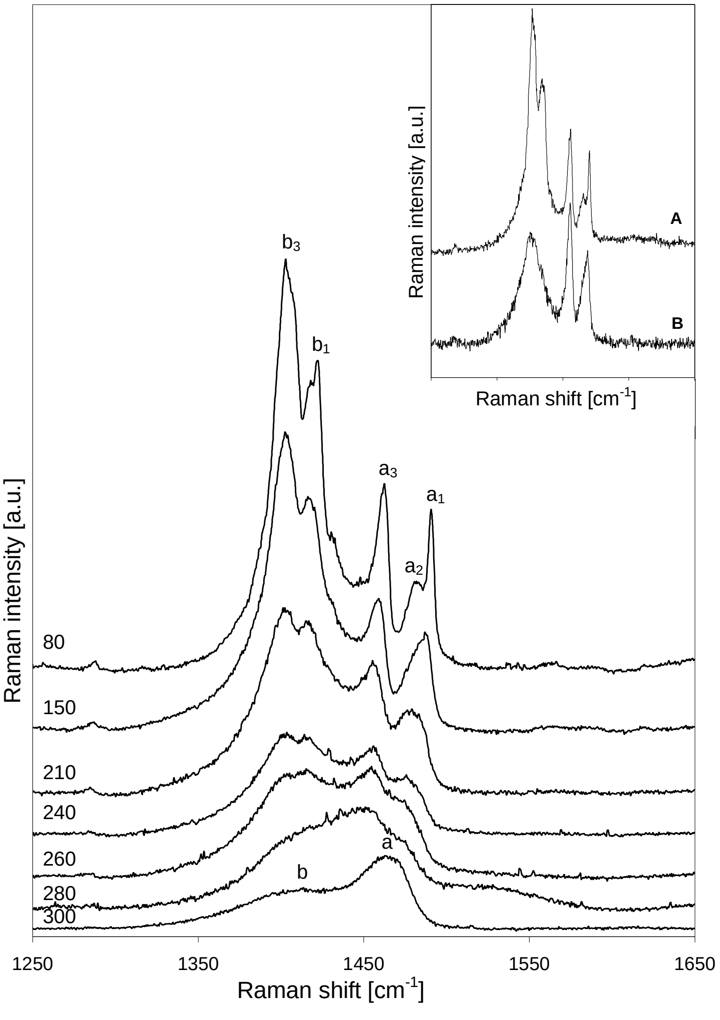

Fig. 2. Temperature dependences of the Raman active C=C stretching modes for the β-(BEDT-TTF)$_2$AsF$_6$ salt, with the laser light polarisation plane perpendicular to the long axis of the donor molecules. The inset shows spectra for β-(BEDT-TTF)$_2$PF$_6$ (A) and β-(BEDT-TTF)$_2$SbF$_6$ (B) salts at 80 K and the same polarisation

For the β-(BEDT-TTF)$_2$PF$_6$ salt, the splitting of the observed *a* and *b* bands starts at room temperature. This is due to the fact that the metal–insulator phase transition occurs at 293 K in this salt. In β-(BEDT-TTF)$_2$SbF$_6$, analogous changes were observed at 270 K (the phase transition occurs at 273 K). Comparing the spectra recorded for these two salts at 80 K (see the inset in Fig. 1), one can notice that both are very similar to the spectrum of the salt β-(BEDT-TTF)$_2$AsF$_6$ taken at the same temperatures. The most important difference relates to the a_2 band (ν_{27}), which is considerably weaker in the spectrum of (BEDT-TT)$_2$SbF$_6$ than in that of the two other salts (see inset B in Fig. 1).

Figure 2 shows the temperature dependence of the Raman spectrum for the β-(BEDT-TTF)$_2$AsF$_6$ salt, taken with a laser light polarisation plane perpendicular to the long axis of BEDT-TTF molecule. The broad bands, marked *a* and *b*, split at low temperatures, and at 80 K five main bands, a_1, a_2, a_3, b_1, and b_3 (1489 cm^{-1}, 1482 cm^{-1}, 1463 cm^{-1}, 1422 cm^{-1}, and 1403 cm^{-1}, respectively), can be distinguished. We can attribute the peak a_1 to ν_2, a_2 to ν_{27}, and a_3 to ν_3. The a_1 band, assigned to the ν_2 mode, corresponds to the charge-rich site (analogous to the a_1 band in Fig.1.). The assignments of the b_1 (1422 cm^{-1}) and b_3 (1402 cm^{-1}) bands are not certain, as discussed above in relation to the spectra in Fig.1. Note that the same bands are observed for both light polarisations - only their relative intensities are different.

The spectra for the two other salts for perpendicular incident light polarisation are also similar to the spectrum of the β-(BEDT-TTF)$_2$AsF$_6$ salt – see the inset in Fig. 2. Also in this case, the β-(BEDT-TTF)$_2$SbF$_6$ salt exhibits only a weak a_2 (ν_{27}) band, which is shown in inset B.

The results published by Laversanne et al. [4] and Mori et al. [5] indicate that among the three investigated BEDT-TTF salts, β-(BEDTTTF)$_2$PF$_6$ exhibits the strongest dimerisation of the donor molecules, and the two other salts show rather weak dimerisation. Taking into account the relative intensities of the ν_{27} bands, we can conclude from our studies that strong dimerisation occurs also in β-(BEDT -TTF)$_2$AsF$_6$.

The temperature dependence of the Raman spectra for the β-(BEDT-TTF)$_2$PF$_6$ salt has already been published by Ding and Tajima [7]. In contrast to the results obtained by us, they did not observe any splitting of the *b* band. In fact, this band disappears in their spectra at low temperatures. As discussed above, one should expect the second ν_3 mode in this region, which can appear at low energies due to the *e-mv* interaction.

4. Conclusions

The results obtained show that the dimerisation occurs in all three investigated salts, (BEDT-TTF)$_2$XF$_6$ (where X = P, Sb, As), upon cooling below their M–I phase transition temperatures. On the other hand, the splitting of the C=C stretching bands ν_2 and ν_3 clearly demonstrates that charge ordering occurs in the insulating state, indicating formation of a Wigner-like crystal. The splitting of the ν_2 mode indicates an irregular charge distribution in the unit cell. Therefore, we conclude that the phase transitions in the (BEDT-TTF)$_2$XF$_6$ salts are caused by charge localizations. To verify these conclusions derived from Raman studies, X-ray diffraction investigations at different temperatures are in progress.

Acknowledgments

We wish to thank Prof. Janina Karolak-Wojciechowska from Technical University of Lodz for the help in performing the X-ray diffractions.

References

[1] SEO H., FAKUYAMA H., Synthetic Metals, 133–134 (2003), 257.
[2] KOBAYASHI H., MORI T., KOBAYASHI A., SASAKI Y., SAITO G., INOKUCHI H., Chemistry Lett. (1983), 581.
[3] LAVERSANNE R., AMIELL J., DELHAES P., CHASSEAU D., HAUW C., Mol. Cryst. Liq. Cryst., 119 (1985), 405.
[4] LAVERSANNE R., AMIELL J., DELHAES P., CHASSEAU D., HAUW C., Solid State Commun., 52 (1984), 177.
[5] MORI T., KOBAYASHI A., SASAKI Y., KATO R., KOBAYASHI H., Solid State Commun., 53 (1985), 627.
[6] YAMAMOTO K., YAKUSHI K., MIYAGAWA K., KANODA K., KAWAMOTO A., Phys. Rev. B, 085110 (2002), 65.
[7] DING Y., TAJIMA H., Synth. Metals, 135–136 (2003), 599.

Received 14 October 2004
Revised 10 November 2004

Materials Science-Poland, Vol. 22, No. 4, 2004

Reflectivity spectra of some conducting BETS salts

M.G. KAPLUNOV[*], N.D. KUSHCH, S.S. KRASNIKOVA

Institute of Problems of Chemical Physics, Russian Academy of Sciences,
142432, Chernogolovka, Moscow Region, Russia

We have measured the polarized reflectivity spectra of three BETS-based organic metals with the α-phase structure: α-$(BETS)_2NH_4Hg(SCN)_4$ (I), α-$(BETS)_2TlHg(SeCN)_4$ (II), and α-$(BETS)_2Cu_5I_6$ (III) in the range of 600–6500 cm^{-1}. The spectra exhibit a metallic-type reflection with the plasma edge about 4000–5000 cm^{-1} and high reflectivity at low frequencies. The electron-vibrational bands observed in the range of 1200–1400 cm^{-1} are due to the interaction of the intramolecular vibrational modes of BETS with conduction electrons.

Key words: *organic conductors; optical properties*

1. Introduction

Radical-cation salts of bis(ethylenedithio)tetraselenafulvalene (BETS) attract considerable attention due to unique properties (such as superconductivity or the Shubnikov–de Haas effect) of some of them ([1, 2] and refs. therein). We have studied the optical properties of three BETS-based organic metals of the α-phase structure: α-$(BETS)_2NH_4Hg(SCN)_4$ (I), α-$(BETS)_2TlHg(SeCN)_4$ (II) [1], and α-$(BETS)_2$ -Cu_5I_6 (III) [2] in the range of 600–6500 cm^{-1}.

2. Experimental

Reflectivity spectra of the compounds studied were recorded at room temperature in the range of 600–6500 cm^{-1} in polarized light by means of a Perkin-Elmer 1600 and Perkin-Elmer Spectrum BX Fourier transform spectrometers. The samples were made of one or two single crystals (of typical dimensions 1×2 mm^2 each). The spectra were taken from the plane of conducting BETS layers.

---

[*] Corresponding author, e-mail: kaplunov@icp.ac.ru.

Optical conductivity spectra were obtained from the reflectivity spectra by means of the Kramers–Kronig analysis. The result of the analysis in the range of 600–5000 cm^{-1} does not qualitatively depend on the kind of extrapolation to low and high frequencies. We suppose that the reflectivity approaches unity at low frequencies (which is typical of metals) and that it is constant at high frequencies.

3. Results and discussion

3.1. Electronic spectra

Figure 1a shows the polarized reflectivity spectra of $(BETS)_2NH_4Hg(SCN)_4$ in the range of 600–6500 cm^{-1} for the two main optical directions, x and y, for which the maximal differences in reflectivity are observed. Figure 1b shows the spectra of optical conductivity for the same main optical directions. Figure 2 shows the reflectivity and conductivity spectra of $(BETS)_2TlHg(SeCN)_4$, belonging to the same isostructural family [1]. The spectra resemble those of the analogous isostructural ET compounds $(ET)_2TlHg(SeCN)_4$ [3] and $(ET)_2NH_4Hg(SCN)_4$ [4]. Figure 3 shows the spectra of the $(BETS)_2Cu_5I_6$ salt.

The α-phase structure is characterized by the presence of stacks of BETS molecules with strong intermolecular interactions in the direction perpendicular to the stacks. The directions x and y correspond to polarizations with the electric vector perpendicular and parallel to the direction of BETS stacks [1, 3]. This means that the electronic reflectivity is greater for the polarization perpendicular to BETS stacks for all three salts studied. This fact is due to a large amount of shortened contacts between S(Se) atoms in the BETS molecules of adjacent stacks. The spectra of $(BETS)_2NH_4Hg(SCN)_4$ exhibit a pronounced plasma edge in the x direction, while in the y direction and in the spectra of $(BETS)_2TlHg(SeCN)_4$ the plasma edge is much less pronounced. The conductivity spectra of $(BETS)_2NH_4Hg(SCN)_4$, similar to those of $(BETS)_2TlHg(SeCN)_4$ and $(ET)_2TlHg(SeCN)_4$ [1, 3], do not exhibit a maximum in conductivity at about 3000 cm^{-1}, which is usual for many ET and BETS salts [3–6]. This may be an evidence of the absence of an energy gap in the spectrum of electronic states of these salts. On the contrary, the optical conductivity spectra of $(BETS)_2Cu_5I_6$ exhibit such a maximum at ca. 2300 cm^{-1}, which may be taken as an evidence of an energy gap (or pseudo-gap) in the electronic spectra of this salt.

The reflectivity spectra of the salts studied may be described in terms of the Drude–Lorentz model used for α-$(ET)_2I_3$ [5]. The obtained parameters (dielectric constant at high frequencies ε_∞, plasma frequency ω_p, electron energy gap 2Δ, electronic damping Γ) are shown in Table 1.

Carrier effective masses m_x and m_y were obtained from the equation $\varepsilon_\infty \omega_p^2 = 4\pi n e^2/m$ (e is electron charge, n is the concentration of carriers taken as *n* =1×10^{21} cm^{-3} from the structure data, supposing one electron charge per two BETS molecules in analogy with [1]) and the transfer integrals t_x = 0.14 eV and t_y = 0.12 eV were calculated from the effective masses by numerical integration in analogy with [6] (intermolecular distances were accepted as half periods along *x* and *y* directions, a_x = 0.5 nm and a_y = 0.5 nm, in analogy with [1]).

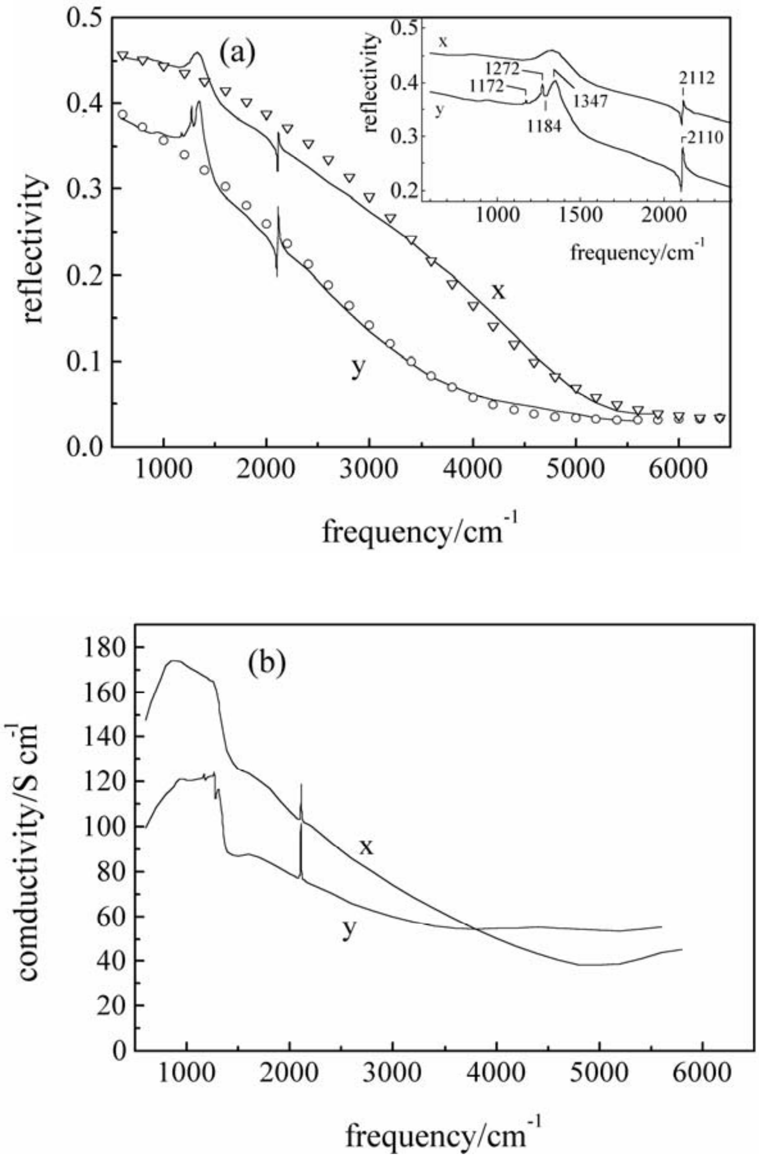

Fig. 1. Reflectivity (a) and optical conductivity (b) spectra of α-$(BETS)_2NH_4Hg(SCN)_4$ for the two main optical directions *x* and *y*. The circles and triangles show the Drude–Lorentz fit

The parameters obtained are summarized in Table 1. In all cases, the effective masses are higher and the transfer integrals lower in the *y* direction (parallel to molecular stacks). In comparison with other salts, $(BETS)_2NH_4Hg(SCN)_4$ is characterized by much lower effective masses and much larger transfer integrals (i.e., wider conduction bands).

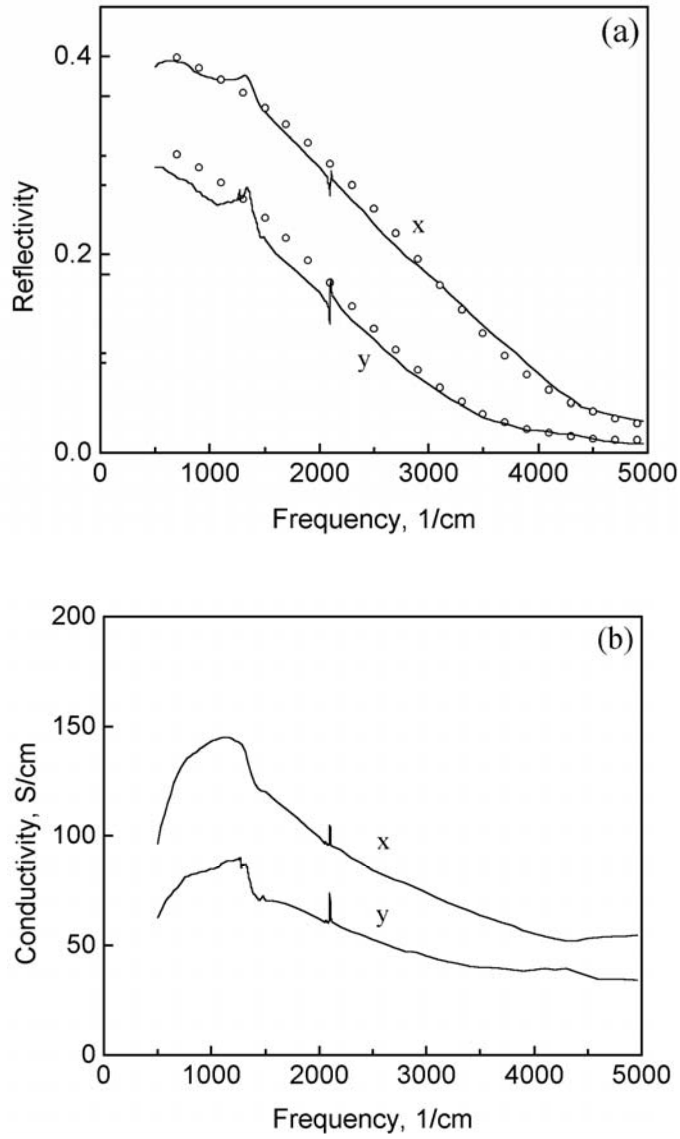

Fig. 2. Reflectivity (a) and optical conductivity (b) spectra of α-$(BETS)_2TlHg(SeCN)_4$ for the two main optical directions *x* and *y*. The circles show the Drude–Lorentz fit

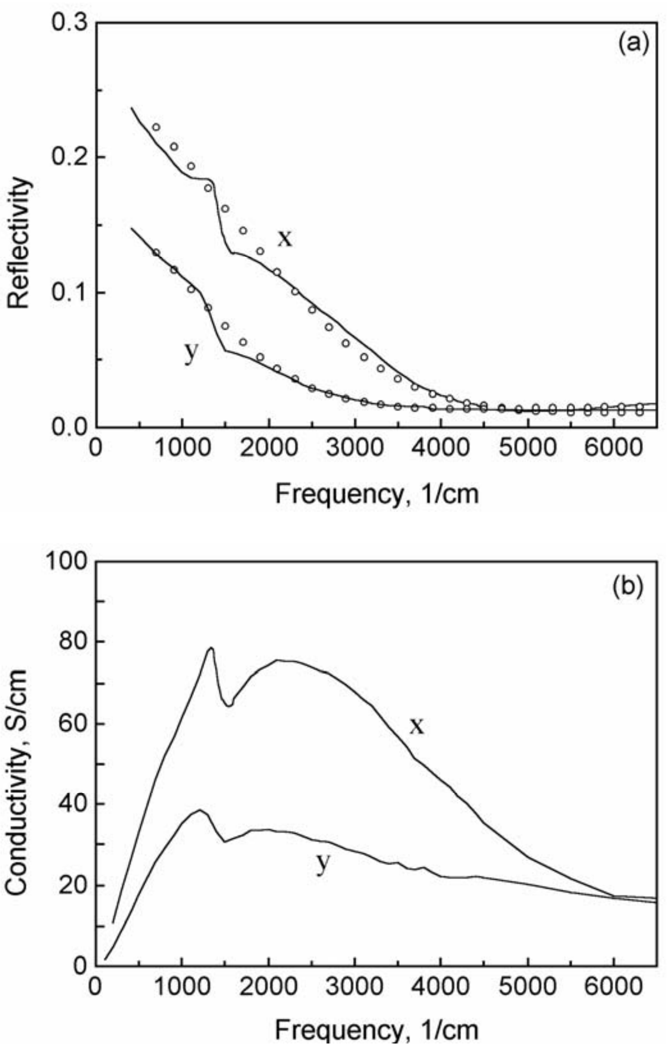

Fig. 3. Reflectivity (a) and optical conductivity (b) spectra of α-$(BETS)_2Cu_5I_6$ for the two main optical directions *x* and *y*. The circles show the Drude–Lorentz fit

Table 1. Parameters of the Drude–Lorentz fit

Parameter	α-$(BETS)_2NH_4Hg(SCN)_4$		α-$(BETS)_2TlHg(SeCN)_4$ [1]		α-$(BETS)_2Cu_5I_6$ [2]	
	x	*y*	*x*	*y*	*x*	*y*
ε_∞	3.0	2.7	2.5	2.0	1.8	1.8
ω_p, cm^{-1},	4600	3600	3850	3100	3200	2100
2Δ, cm^{-1},	1600	1400	1400	1300	1600	1500
Γ, cm^{-1}	3300	3300	3000	2850	4000	3500
m, m_e	1.4	2.6	2.4	4.7	4.8	11.3
t, eV	0.14	0.12	0.09	0.06	0.033	0.031

3.2. Vibrational spectra

The insert in Fig.1a shows the spectral range of molecular vibrations. Similar to (BETS)2TlHg(SeCN)$_4$ and (ET)2TlHg(SeCN)$_4$ [1, 3], the doublet electron-vibrational band (with a slight reflectivity minimum at 1284 cm^{-1}) is observed in the polarization parallel to BETS stacks (*y* direction), while the electron reflectivity is more intensive in the polarization perpendicular to the stacks. The maxima of this doublet are slightly shifted to higher frequencies: 1272 and 1347 cm^{-1}, vs. 1270 and 1340 cm^{-1}for (BETS)$_2$TlHg(SeCN)$_4$ and 1258 and 1316 cm^{-1} for the ET salt. For comparison, an analogous doublet in the κ-phase salt (BETS)$_2$FeCl$_4$ was observed at 1280 and 1320 cm^{-1} [7]. These bands are due to the interaction of the conduction electrons with the symmetric vibrational modes of BETS molecules [4–6], apparently including C–C stretching modes (taking into account relatively small shift between BETS and ET containing salts). For the *x* direction, only a weak, broad maximum is observed in the electron-vibrational range of 1000–1400 cm^{-1}, similar to that of (BETS)$_2$TlHg(SeCN)$_4$ and (ET)$_2$TlHg(SeCN)$_4$.

An interesting peculiarity of (BETS)$_2$Cu$_5$I$_6$ is the absence of the minimum of reflectivity at 1280–1290 cm^{-1}, observed in other salts. This may be due to the absence of centrosymmetric BETS molecules in the crystal stucture of this salt [2].

Narrow bands near 2100 cm^{-1} are due to vibrations of CN fragments in the anionic layer. The maxima of these bands are slightly shifted to higher frequencies compared with that of analogous salts: 2112 and 2110 cm^{-1} for *x* and *y* directions cf. 2110 and 2105 for (BETS)$_2$TlHg(SeCN)$_4$ and 2104 and 2102 cm^{-1} for (ET)$_2$TlHg(SeCN)$_4$ [1].

Acknowledgements

This work was supported by RFBR-DFG grant N 03-02-04023.

References

[1] KUSHCH N.D., BURAVOV L.I., PESOTSKII S.I., LYUBOVSKII R.B., KAPLUNOV M.G., GOLUBEV E.V., NARYMBETOV B.Z., KHASANOV S.S., ZORINA L.V., ROSENBERG L.P., SHIBAEVA R.P., KOBAYASHI A., KOBAYASHI H., J. Mater. Chem., 8 (1988), 897.

[2] KUSHCH N.D., DYACHENKO O.A., GRITSENKO V.V., BURAVOV L.I., TKACHEVA V.A., YAGUBSKII E.B., KAPLUNOV M.G., GOLUBEV E.V., TOGONIDZE T.G., KOBAYASHI A., KOBAYASHI H., J. Mater. Chem., 9 (1999), 687.

[3] KAPLUNOV M.G., KUSHCH N.D., LYUBOVSKAYA R.N., Adv. Mater. Opt. Electron., 7 (1997), 19.

[4] DRESSEL M., DRICHCO N., SCHLUETER J., MERINO J., Phys. Rev. Lett., 90 (2003), 176002.

[5] KAPLUNOV M.G., YAGUBSKII E.B., ROSENBERG L.P., BORODKO YU.G., Phys. Stat. Sol. (a) 89 (1985), 509.

[6] KAPLUNOV M.G., LYUBOVSKAYA R.N., ALDOSHINA M.Z., BORODKO YU.G., Phys. Stat. Sol., (a) 104 (1987), 833.

[7] OLEJNICZAK I., GRAJA A., KUSHCH N.D., CASSOUX P., KOBAYASHI H., Synth. Metals, 86 (1997), 2155.

Received 14 October 2004
Revised 15 November 2004

Materials Science-Poland, Vol. 22, No. 4, 2004

Some new findings in τ-phase organic conductors

G. C. PAPAVASSILIOU[1*], G. A. MOUSDIS[1], G. C. ANYFANTIS[1], K. MURATA[2],
T. NAKANISHI[2], L. LI[2], H. YOSHINO[2], H. TAJIMA[3], M. INOUE[3], T. KONOIKE[4],
J. S. BROOKS[5], E. S. CHOI[5], D. GRAF[5]

[1]Theoretical and Physical Chemistry Institute, NHRF, 48,
Vassileos Constantinou Ave., Athens 116-35, Greece

[2]Graduate School of Science, Osaka City University, Sumiyoshi-ku, Osaka 558-8585, Japan

[3]Institute for Solid State Physics, University of Tokyo,
Kashiwanoha, Kashiwa-shi, Chiba 277-8581, Japan

[4]National Institute for Material Science, 3-13 Sakura, Tsukuba, Ibaraki 305-0003, Japan

[5]National High Magnetic Field Laboratory and Physics Department,
Florida State University, Tallahassee, Florida 32310, USA

Some new findings concerning the structural, optical, transport, and magnetotransport properties of τ-phase organic conductors, based on the donor molecules ethylenedioxy-*S*,*S*-dimethylethylenedithio-tetrathiafulvalene, ethylenedioxy-*R*,*R*-dimethylethylenedithio-tetrathiafulvalene, pyrazino-*S*,*S*-dimethyl-ethylenedithio-tetrathiafulvalene, pyrazino-*R*,*R*-dimethylethylenedithio-tetrathiafulvalene, pyrazino-*r*-dimethylethylenedithio-tetrathiafulvalene, pyrazino-*S*,*S*-dimethylethyledithio-diselenadithiafulvalene, pyrazino-*r*-methylethylenedithio-tetrathiafulvalene, and pyrazino-*r*-methylethylenediseleno-tetrathiafulvalene are described. Some similarities and differences in their properties are discussed.

Key words: *organic conductors; structure; optical properties; transport properties*

1. Introduction

During the last ten years, a number of τ-phase conductors have been prepared and studied [1–13]. They were based mainly on the following unsymmetrical π-donor molecules:

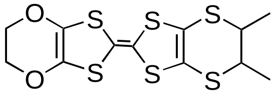

(EDO-*X*-DMEDT-TTF): *X* = *S*, *S*; *R*, *R*; r (= *S*, *S* + *R*, *R*)

---

[*] Corresponding author, e-mail: pseria@eie.gr.

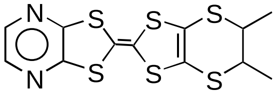

(P-*X*-DMEDT-TTF): *X* = *S*, *S*; *R*, *R*; r (= *S*, *S* + *R*, *R*)

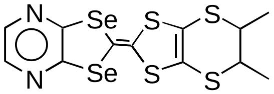

(P-*X*-DMEDT-DSDTF): *X* = *S*, *S*; *R*, *R*

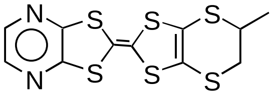

(P-*X*-MEDT-TTF): *X* = r (= *S* + *R*)

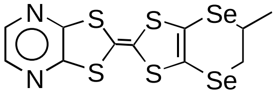

(P-*X*-MEDS-TTF): *X* = *r* (= *S* + *R*)

and also on linear anions such as AuI_2^-, AuBr_2^- and I_3^- . Most of work has been done on τ-(P-*S*,*S*-DMEDT-TTF)$_2$(AuBr$_2$)$_{1+y}$ and τ-(EDO-*S*,*S*-DMED-TTF)$_2$(AuBr$_2$)$_{1+y}$ ($y \approx 0.75$). Recent investigations of the optical absorption spectra of polycrystalline samples of these two salts in the spectral region from UV to far IR showed some differences in their optical behaviours, attributed to differences in the relative concentrations of the neutral and charged species (i.e., D^0, $D^{\bullet+}$, D^{2+}) in the corresponding salts [1, 2]. Considerable changes in the properties have been observed after heat treatment of the crystals [2, 10]. The changes have a similar origin, since during heat treatment some portion of the anion escapes, leaving the material with various compositions. Also, the redox potentials of the corresponding donor molecules in solution indicate that the preparation and stabilization of (P-*X*-DMEDT-TTF)$^{2+}$ is more difficult than that of (EDO-*X*-DMEDT-TTF)$^{2+}$ [2]. Moreover, it has been found from magnetic measurements that τ-(P-*S*,*S*-DMEDT-TTF)$_2$(AuBr$_2$)$_{1+y}$ undergoes an antiferromagnetic transition at ca. 11 K, while τ-(EDO-*S*,*S*-DMEDT-TTF)$_2$(AuBr$_2$)$_{1+y}$ does not exhibit any long-range magnetic order (see [7, 8] and refs. therein). In the last salt, the angular-dependent magnetoresistance oscillations have a peak as the field direction approaches the layers, which indicates interlayer coherency [7, 8]. Also, magnetotransport properties related to the quantum Hall effect and chiral surface states, rather than to other effects [14], have been reported [1].

In this paper, some new findings concerning the properties of the compounds

- τ-(EDO-*S*,*S*-DMEDT-TTF)$_2$(AuBr$_2$)$_{1+y}$, τ-(P-*S*,*S*-DMEDT-TTF)$_2$(AuBr$_2$)$_{1+y}$,
- τ-(EDO-*R*,*R*-DMEDT-TTF)$_2$(AuBr$_2$)$_{1+y}$, τ-(EDO-*R*,*R*-DMEDT-TTF)$_2$(AuI$_2$)$_{1+y}$,
- τ-(P-*R*,*R*-DMEDT-TTF)$_2$(AuBr$_2$)$_{1+y}$, τ-(P-*S*,*S*-DMEDT-DSDTF)$_2$(AuBr$_2$)$_{1+y}$,
- τ-(P-*r*-DMEDT-TTF)$_2$(AuBr$_2$)$_{1+y}$, τ-(EDO-*S*,*S*-DMEDT-TTF)$_2$[Ag(CN)$_2$]$_{1+y}$,
- τ-(P-*r*-MEDT-TTF)$_2$(AuBr$_2$)$_{1+y}$, and τ-(P-*r*-MEDS-TTF)$_2$(AuBr$_2$)$_{1+y}$

are described. Some similarities and differences in the properties of these compounds are discussed.

2. Results and discussion

The compounds of τ-phase are crystallized in the form of platelets showing several habits. Typical examples of the morphology of crystals and their schematic presentations are shown in Fig. 1. In all cases, the largest surface of each crystal is parallel to the (highly conducting) *ab*-plane, i.e., perpendicular to the *c*-axis.

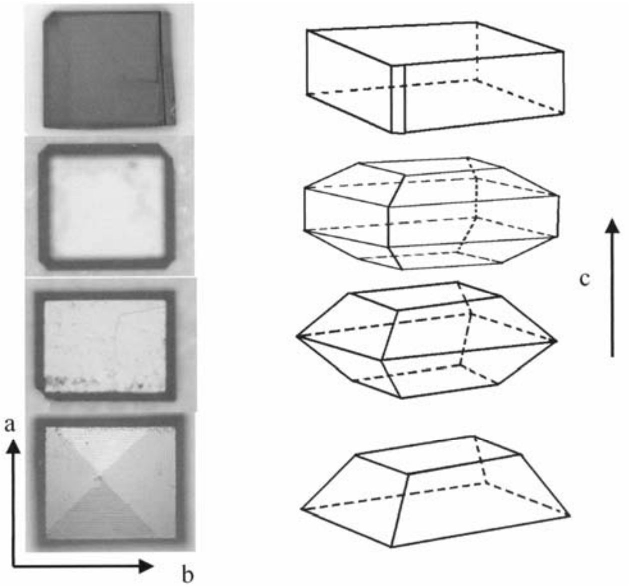

Fig. 1. Morphology of crystals of τ-phase conductors
(four typical habits: A, B, C and D) and corresponding schematic presentations

Room-temperature X-ray diffraction data led to the following results for the crystal structures. The compounds τ-(EDO-*S*,*S*-DMEDT-TTF)$_2$(AuBr$_2$)$_{1+y}$, τ-(P-*S*,*S*-DMEDT-TTF)$_2$(AuBr$_2$)$_{1+y}$, τ-(P-*R*,*R*-DMEDT-TTF)$_2$(AuBr$_2$)$_{1+y}$, and τ-(EDO-*S*,*S*-DMEDT-TTF)$_2$ [Ag(CN)$_2$]$_{1+y}$ are crystallized with the noncentrosymmetric space group $I4_122$ (see [6] and refs. therein). τ-(P-*r*-DMEDT-TTF)$_2$(AuBr$_2$)$_{1+y}$, τ-(P-*r*-MEDT-TTF)$_2$(AuBr$_2$)$_{1+y}$ and τ-(P-*r*-MEDS-TTF)$_2$(AuBr$_2$)$_{1+y}$ are crystallized with the centrosymmetric space group $I4_1/amd$ [3, 6]. Also, we found that τ-(EDO-*R*,*R*-DMEDT-TTF)$_2$(AuBr$_2$)$_{1+y}$ and τ-(P-*S*,*S*-DMEDT-DSDTF)$_2$(AuBr$_2$)$_{1+y}$ are crystallized with the centrosymmetric space group $I4_1/amd$. In the last two cases, diffraction data do not provide a clear choice between the centrosymmetric and a noncentrosymmetric space groups (see [3] and ref. [6] cited therein). An uncertainty concerning crystal structures has also been noticed in some other compounds, such as 4,5-dimethylethylenedithio-1,3-dithiole-2-thione (see [3] and ref.[6] cited therein) and (TMET)$_3$(ClO$_4$)$_2$ (see [11] and ref.[4] cited therein). The crystal structure of the compound τ-(EDO-*R*,*R*-DMEDT-TTF)$_2$(AuI$_2$)$_{1+y}$ has not yet been definitely determined. In the compounds τ-(EDO-*S*,*S*-DMEDT-TTF)$_2$(AuBr$_2$)$_{1+y}$ and τ-(P-*S*,*S*-DMEDT-TTF)$_2$(AuBr$_2$)$_{1+y}$, no considerable differences in the crystal structures among the several habits have been found.

The reflectance spectra, with the wave vector of light parallel to the conducting plane, and optical absorption spectra of τ-phase crystals exhibit a broad band at ca. 5500 cm^{-1}. Figure 2. shows the observed [4, 9] and calculated spectra, based on the mean-field Hubbard model, assuming anti-ferromagnetic order [7, 9, 15]. One can see that there is a good agreement between experiment and theory.

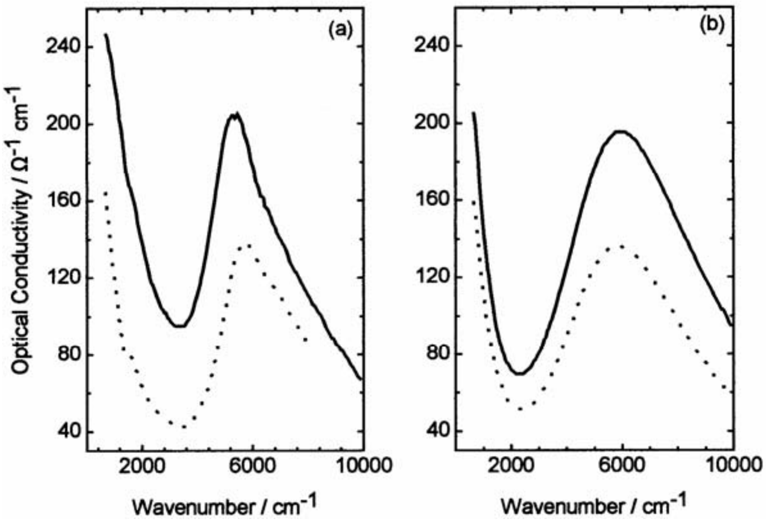

Fig. 2. Observed (a) and calculated (b) optical conductivity spectra of τ-(EDO-*S*,*S*-DMEDT-TTF)$_2$(AuBr$_2$)$_{1+y}$ (solid lines) and τ-(P-*S*,*S*-DMEDT-TTF)$_2$(AuBr$_2$)$_{1+y}$ (dotted lines), using transfer integral values of t_1 = 0.184 and 0.138 eV, respectively, t_2 = 16 meV, a filling factor of ρ = 0.9375, and Δ = 0.31 eV

The in-plane resistivity (ρ_{ab}) of τ-(P-*S*,*S*-DMEDT-TTF)$_2$(AuBr$_2$)$_{1+y}$ shows a metallic temperature dependence down to low temperatures, with an upturn at ca. 10 K and a weak crossover at ca. 120 K. The out-of-plane resistivity (ρ_c) shows a semiconducting behaviour down to low temperatures, a crossover at ca. 20 K, and an upturn in resistivity at ca. 5 K. The resistivity anisotropy ρ_c/ρ_{ab} is of the order 10^3 at room temperature and much higher at low temperatures (see [5, 7, 8] and refs. therein). The compounds τ-(P-*R*,*R*-DMEDT-TTF)$_2$(AuBr$_2$)$_{1+y}$ and τ-(P-*r*-DMEDT-TTF)$_2$(AuBr$_2$)$_{1+y}$ exhibit similar behaviour [6]. The resistivity anisotropy for these compounds was found to be 310–1250 at room temperature. The in-plane resistivity of τ-(EDO-*S*,*S* -DMEDT-TTF)$_2$(AuBr$_2$)$_{1+y}$ shows a metallic temperature dependence, with an upturn at 30–50 K. The out-of-plane resistivity varies from crystal to crystal. Some crystals exhibit weak metallic behaviour down to very low temperatures (ca. 0.4 K), while other crystals exhibit an upturn in resistivity at ca. 30–40 K. The resistivity anisotropy is of the order 10^3–10^4 (see [1, 7, 8, 10] and refs. therein). Interlayer transport is coherent in τ-(EDO-*S*,*S*-DMEDT-TTF)$_2$(AuBr$_2$)$_{1+y}$ and incoherent in τ-(P-*S*,*S*-DMEDT

-TTF)$_2$(AuBr$_2$)$_{1+y}$ [7, 8]. The results are similar in τ-(EDO-*R*,*R*-DMEDT-TTF)$_2$(AuBr$_2$)$_{1+y}$, as shown in Fig. 3. In the crystal (#0209), the temperature dependence of in-plane resistivity shows a metallic behaviour down to low temperatures, while the temperature dependence of the out-of-plane resistivity shows weak metallic behaviour and an upturn at ca. 50 K. There is no crossover in ρ_c at high temperatures. Also, as in other compounds, resistivity anisotropy is large. Similar results have been obtained for τ-(P-*S*,*S*-DMEDT-DSDTF)$_2$(AuBr$_2$)$_{1+y}$, except that ρ_c shows a weak crossover at ca. 270 K [3]. The behaviour of ρ_{ab} and ρ_c for one crystal (#0302) of this compound is similar to that observed in [3] for two other separate crystals. Also, another crystal of τ-(EDO-*R*,*R*-DMEDT-TTF)$_2$(AuBr$_2$)$_{1+y}$ (#0213) exhibited metallic behaviour in ρ_{ab}, and weak metallic behaviour in ρ_c down to ca. 5 K (Fig. 3). Details will be reported elsewhere [12]. The results are much different in τ-(EDO-*R*,*R*-DMEDT-TTF)$_2$(AuI$_2$)$_{1+y}$, as shown in Fig. 4. This compound exhibits metallic behaviour in both directions, with resistivity anisotropy of the order 10^3. A weak crossover is observed in ρ_c at ca. 250 K. At 7K, a sudden drop in ρ_{ab} was observed, which is not associated with superconductivity. As in the case of other τ-phase compounds, several significant features are observed in the temperature dependence of resistivity at low temperatures (e.g., a weak upturn in resistivity is observed at ca. 5 K). These are more pronounced under pressure, as shown in Fig. 5. One can see that when the pressure is increased from 0 to 1.23 GPa, the compound becomes more metallic. As the pressure increases above 1.65 and 2.02 GPa, however, the compound becomes semiconducting, showing upturns in resistivity at ca. 18.3–20.5 and 24.8–26.5 K, respectively. The results are similar to those observed for τ-(EDT-*S*,*S*-DMEDT-TTF)$_2$(AuI$_2$)$_{1+y}$ [2, 11], where EDT-*S*,*S*-DMEDT-TTF is ethylenedi-

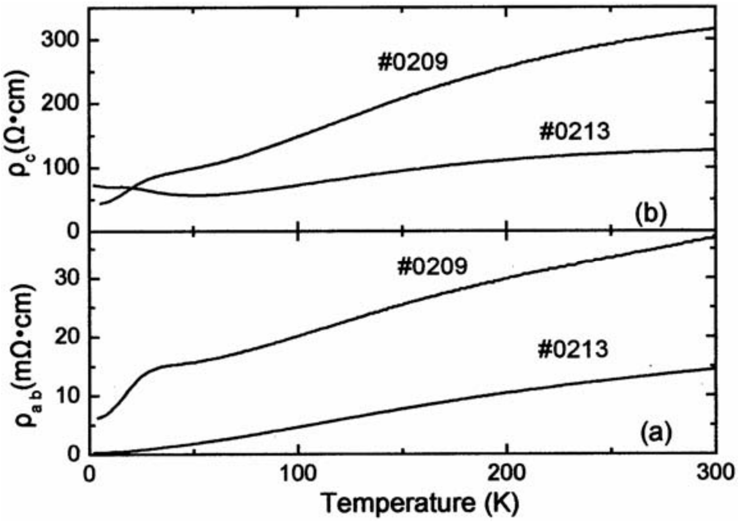

Fig. 3. Temperature dependences of the in-plane resistivity (a) and out-of-plane resistivity (b) for two crystals of τ-(EDO-*R*,*R*-DMEDT-TTF)$_2$(AuBr$_2$)$_{1+y}$

thio-*S*,*S*-dimethylethylenedithio-tetrathiafulvalene, abbreviated as *S*,*S*-DMBEDT-TTF in [11]. The behaviour is different in τ-(EDO-*S*,*S*-DMEDT-TTF)$_2$[Ag(CN)$_2$]$_{1+y}$, τ-(P-r -MEDT-TTF)2(AuBr2)$_{1+y}$, and τ-(P-r-MEDS-TTF)$_2$(AuBr$_2$)$_{1+y}$.

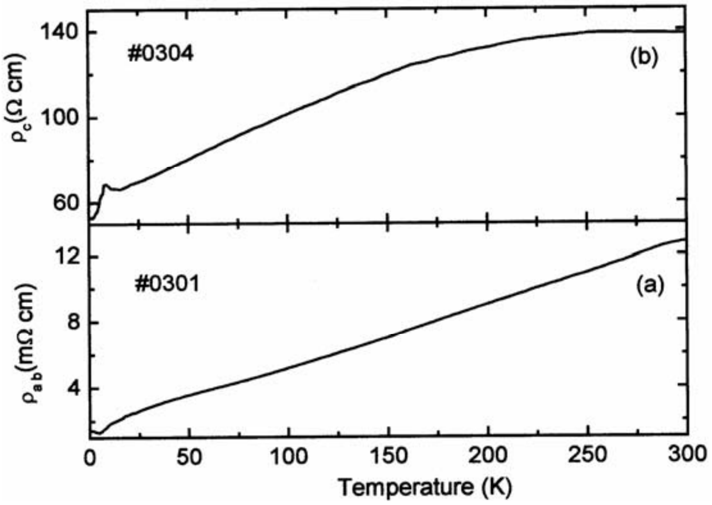

Fig. 4. Temperature dependences of in-plane (a) and out-of-plane (b) resistivity for τ-(EDO-*R*,*R*-DMEDT-TTF)$_2$(AuI$_2$)$_{1+y}$ (under ambient pressure)

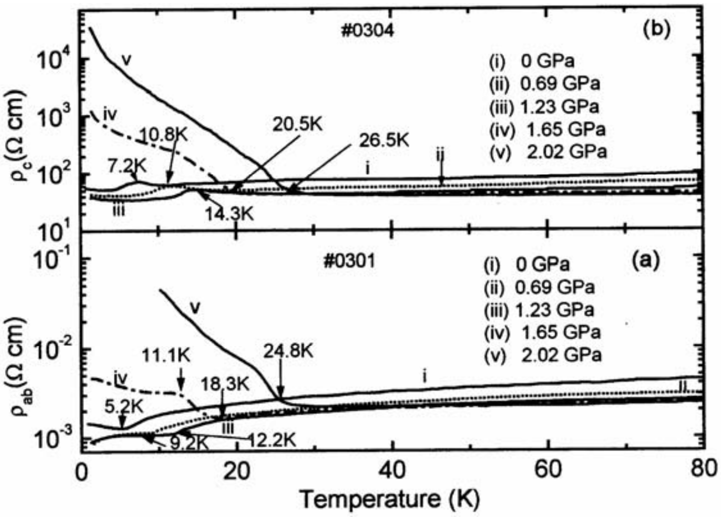

Fig. 5. Temperature dependences of in-plane (a) and out-of-plane (b) resistivity for τ-(EDO-*R*,*R*-DMEDT-TTF)$_2$(AuI$_2$)$_{1+y}$ under ambient and high pressure

In these compounds, both ρ_{ab} and ρ_c exhibit a semiconducting behaviour from room temperature down to very low temperatures. The anisotropy ρ_c/ρ_{ab} for the first compound is c.a. 10^3, while for the latter two it is small, i.e., 27 and 3–15, respectively.

Some similarities and differences concerning magnetotransport properties of τ-(EDO-*S*,*S*-DMEDT-TTF)$_2$(AuBr$_2$)$_{1+y}$ and τ-(P-*S*,*S*-DMEDT-TTF)$_2$(AuBr$_2$)$_{1+y}$ have been reported in [1, 6, 7]. Crystals of τ-(P-*S*,*S*-DMEDT-TTF)$_2$(AuBr$_2$)$_{1+y}$, τ-(P-*R*,*R*-DMEDT-TTF)$_2$(AuBr$_2$)$_{1+y}$, and τ-(P-*r*-DMEDT-TTF)$_2$(AuBr$_2$)$_{1+y}$ exhibit a negative magnetoresistance at low fields and fast Shubnikov–de Haas (SdH) oscillations at higher fields (see also [5–8]), with frequencies close to those of τ-(EDO-*S*,*S* -DMEDT-TTF)$_2$(AuBr$_2$)$_{1+y}$, as well as weak slow oscillations of frequency ca. 180 T [7, 8]. The compounds exhibit an upturn in magnetoresistance near ca. 35 T. Semiconducting and metallic crystals of τ-(EDO-*R*,*R*-DMEDT-TTF)$_2$(AuBr$_2$)$_{1+y}$ exhibit two kinds of SdH oscillations at high fields, with frequencies of 42.1–44.5 T and 487–500 T. In other words, the Fermi surface area shows some dependence on the sample. The details of SdH oscillations in metallic and semiconducting crystals of this compound will be reported elsewhere [12]. Also, the compound τ-(EDO-*R*,*R*-DMEDT-TTF)$_2$(AuI$_2$)$_{1+y}$ exhibits negative magnetoresistance at low fields. At high fields, the compound exhibits SdH oscillations with frequencies << 40 T and ca. 586 T [13].

Finally, the magnetoresistance was measured for virgin and heated samples from the same crystal of τ-(EDO-*S*,*S*-DMEDT-TTF)$_2$(AuBr$_2$)$_{1+y}$ at 0.5 K and up to 45 T. Both samples showed two series of SdH oscillations corresponding to the smaller and larger Fermi surfaces. It was found that the SdH frequency corresponding to the smaller Fermi surface decreases by about 20% after heating the sample up to 400 K, while the faster frequency remains unchanged. No difference was found with X-ray studies in the crystal structures of another sample before and after heating up to 420 K. This means that band filling can be controlled by simply heating the crystal in vacuum.

In conclusion, we found that the properties of τ-phase compounds exhibit small differences from crystal to crystal of the same compound, and large differences from compound to compound, the origin of which being not understood yet. Also, external conditions play an important role in the properties of these materials. Under ambient pressure, EDO-containing conductors exhibit similar transport properties (see Figs. 3, 4 and refs. [1, 5, 12]). It is expected that these compounds will also exhibit quantum Hall plateaus and chiral surface effects in their magnetotransport properties, as in the case of τ-(EDO-*S*,*S*-DMEDT-TTF)$_2$(AuBr$_2$)$_{1+y}$ [1].

Acknowledgements

The work was carried out as a part of the *Research for the Future* project grant JSPS-RFTF 97P00105, supported by Japan Society for the Promotion of Science, as well as a part of the *Excellence in Research Institutes* project grant 64769, supported by GSRT/Ministry of Development in Greece.

References

[1] Papavassiliou G.C., Mousdis G.A., Anyfantis G.C., Murata K., Li L., Yoshino H., Tajima H., Konoike T., Brooks J.S., Graf D., Choi E.S., Z. Naturforsch. A., 59a (2004), 952.

[2] Papavassiliou G.C., *Tetrachalcogenafulvalenes with Four Additional Heteroatoms*, [in:] J. Yamada and T. Sugimoto (Eds.), *TTF Chemistry*, Kodansha and Springer, Tokyo, 2004, p.35.

[3] PAPAVASSILIOU G.C., MOUSDIS G.A., TERZIS A., MURATA K., LI L., YOSHINO H., J. Phys. IV France, 114 (2004), 569.
[4] LAPINSKI A., GRAJA A., PAPAVASSILIOU G.C., MOUSDIS G.A., Synth. Metals,139 (2003), 405.
[5] GRAF D., CHOI E.S., BROOKS J.S., HARRISON N., MURATA K. KONOIKE T., MOUSDIS G.A., PAPAVASSILIOU G.C., Phys. Rev. B, in press.
[6] PAPAVASSILIOU G.C., MOUSDIS G.A., TERZIS A., RAPTOPOULOU C., MURATA K., KONOIKE T., YOSHINO H., GRAJA A., LAPINSKI A., Synth. Metals, 135–136 (2003), 651.
[7] KONOIKE T., PhD Thesis, Osaka State Univ. (2003).
[8] KONOIKE T., IWASHITA K., YOSHINO H., MURATA K., SASAKI T., PAPAVASSILIOU G.C., Phys. Rev., B 66 (2002), 245308.
[9] OLEJNICZAK I., MUSFELDT J.L., PAPAVASSILIOU G.C., MOUSDIS G.A., Phys. Rev., B 62 (2000), 15634; H. TAJIMA, private communication.
[10] MURATA K., SHIRAKAWA N., YOSHINO H., TSUBAKI Y., PAPAVASSILIOU G.C., TERZIS A., ZAMBOUNIS J.S., Synth. Met., 86 (1997), 2021; YOSHINO H., [in:] Proc. ICSM ‘04, Wollongong, Australia (2004).
[11] ZAMBOUNIS J.S., MAYER C.W., HAUENSTEIN K., HILTI B., HOFHERR W., PFEIFFER J., BURKLE M., RIHS G., Mat. Res. Soc. Symp. Proc., 247 (1992), 509.
[12] NAKANISHI T., [in:] Proc. ICSM 2004, Wollongong, Australia (2004).
[13] LI L., [in:] Proc. ICSM ‘04, Wollongong, Australia (2004).
[14] CHAMPEL T., MINEEV V.P., Physica, B 346-347 (2004), 392 and refs. therein.
[15] DING Y., TAJIMA H., Phys. Rev., B 69 (2004), 115121 and refs. therein.

Received 14 September 2004
Revised 8 November 2004

Materials Science-*Poland, Vol. 22, No. 4, 2004*

Spectral and microscopic examinations of metalloporphyrin-labelled polymers on different substrates

ANDRZEJ BOGUTA[1*], DANUTA WRÓBEL[1], YURI S. AVLASEVICH[2],
RONALD RIES[3], ASTA RICHTER[3]

[1]Institute of Physics, Poznan University of Technology, Nieszawska 13A, 60965 Poznań, Poland

[2]Institute of Molecular and Atomic Physics, National Academy of Sciences of Belarus,
70 F. Skaryna Ave., 220072 Minsk, Belarus

[3]Laboratory of Surface Science, University of Applied Sciences Wildau,
Bahnhofstr. 1, 15745 Wildau, Germany

The topography of quartz and semiconducting (In_2O_3 and SnO_2) surfaces coated with a dye–polymer layer was investigated with optical microscopy and scanning force microscopy. The following macromolecular systems were used in the experiments: copper or zinc porphyrins covalently linked to polyethylene glycol (PEG) or polyisopropylacrylamide (PNIPAM) polymers. It was shown that images of the surface topography are closely connected with the relation between the magnitude of substrate grains and geometrical size of the dye–polymers. The dye–polymer layer, based on the PNIPAM polymer, shows a ring-like structure, whereas the sample based on the PEG polymer is characterized by a longitudinal dendritic topography. When the dye–polymer layer was deposited on the surface, absorption spectroscopy in polarized light was used to determine dye orientation with respect to the substrate surface. The tilt angle between the dye layer and substrate was estimated. A correlation between the substrate surface topography and the molecular arrangement of dyes is also discussed.

Key words: *light microscopy; electronic spectroscopy; scanning force microscopy; “smart” polymers; surface image*

1. Introduction

Organic dye-labelled polymers are perfect molecular systems which find a wide range of applications in science, technology and medicine [1, 2].The family of por-

---

[*] Corresponding author, e-mail: bogan@phys.put.poznan.pl.

phyrins and phthalocyanines constitutes a group of dyes that are very good agents as photoconverters in solar devices and as photosensitisers in photodynamic therapy and cancerous tissue diagnostics. They can also be used as molecular systems modelling biological objects (e.g. in photosynthesis) [3, 4]. On the other hand, “smart” polymers are also the subject of extensive investigations due to their particular physical properties (e.g. a wide range of electrical conductivity), and they can also serve as models of biomimetic systems (proteins, lipid–protein complexes) [5, 6]. Since porphyrin dyes and polymers are interesting objects for investigations, and they can be quite easily chemically modified to provide a wide variety in their molecular structure (and thus modifications in their physical, photophysical, and photochemical properties), a system of porphyrin macrocycles bound with polymer chains could potentially be very useful in photovoltaics and optoelectronics. Therefore, copper and zinc porphyrins covalently linked to a polymer chain are the subject of our present investigations.

In a recent study, it has been stated that only the dye layer that is in close contact with the semiconducting electrode is involved in photoelectric processes [7]. Some photophysical processes, such as charge separation upon light illumination, electron injection, etc., can occur at the dye layer–semiconductor interface, and it has been shown that the dye effectiveness in photoconversion also depends on the kind of substrate and its roughness [8, 9].

Therefore, in this paper, we focus our attention on the topography of porphyrin -labelled polymer layers on solid substrates. Some photophysical properties of dye –polymer thin layers were also investigated. As far as we know, the topography of such polymer–dye species has never been investigated by optical microscopy or scanning force microscopy (SFM). These methods are especially useful techniques for studying the topography of solid substrates, the sizes of their grains, the formation of islands, and surface roughness.

The results presented in this paper could be essential in the study of the electronic processes occurring in dye–sensitised solar cells and in optoelectronics.

2. Materials and methods

The molecular systems under investigation are copper (CuTPP) and zinc (ZnTPP) complexes of 5-(4-pyridyl)-10,15,20-tri(4-methoxy-phenyl)porphyrin, covalently bound to polymers: CuTPP connected with poly(N-isopropylacrylamide (PNIPAM copolymer) (samples **1** and **2**), and ZnTPP linked to polyethylene glycol 6600 (PEG polymer) (sample **3**). The synthetic procedure for the samples **1** and **2** was similar to that described in Refs. [10, 11], and the molecular structures of the investigated macromolecules are shown in Fig. 1. Systems **1** and **2** differ in the distance between the porphyrin dyes and length of the polymer chains, and thus also in the average distances between dyes linked to the polymer chains. The x/y ratios in polymers **1** and **2** are 330 and 2678, respectively (Fig. 1). Sample **3** was synthesised as described below.

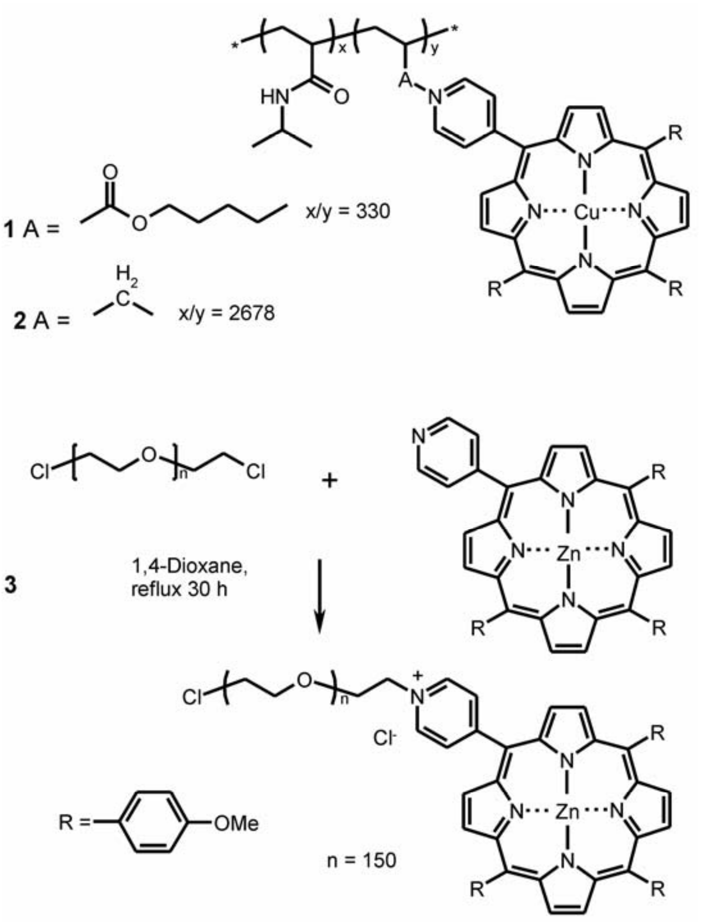

Fig. 1. Molecular structures of the investigated samples

Commercial PEG-6600 was purchased from Serva Co. 5-(4-Pyridyl)-10,15,20-tri(4-methoxyphenyl)porphyrin and synthesized as described previously [11]. It exhibits satisfactory ^{1}H NMR data [11]. Thionyl chloride was purchased from Aldrich Chemical Co. For the synthesis, reagent-grade solvents were used without further purification, except for tetrahydrofuran (THF), 1,4-dioxane, and pyridine, which were distilled from calcium hydride.

2.1. Preparation of Cl-Modified PEG-6600

0.21 ml (3 mmol) of thionyl chloride was added under stirring at room temperature to 6.6 g (1 mmol) of PEG-4000 and 0.22 ml (3 mmol) of pyridine dissolved in 30 ml of THF. After 24 h, the solution was refluxed for 1 h and treated with active carbon (1 g). Carbon was filtered off and washed with hot dioxane (2×10 ml). The combined filtrates were evaporated to 10 ml and cooled to room temperature. Hexane (100 ml) was added to the solution and well mixed. The obtained precipitate was filtered off, washed with hexane (2×20 ml), and dried *in vacuo* at room temperature. Yield 6.16 g (93.3%). Anal. $(C_2H_4O)_{148.6}C_2H_4Cl_2$ $(44)_{148.6}+99$: Calcd. C 54.10, H 9.01, O 35.82; Found C 54.11, H 8.74, O 35.67. IR (KBr, cm^{-1}) 735 (νC–Cl).

2.2. Preparation of porphyrin-labelled PEG-6600

Cl2-PEG-6600 (66 mg, 10-5 mol) and Zn-5-(4-pyridyl)-10,15,20-tri(4-methoxyphenyl)porphyrin (7.6 mg, 10-5 mol) were dissolved in 1,4-dioxane (8 ml). The reaction flask was shielded from ambient light and the resulting solution was magnetically stirred under reflux for 30 h. It was cooled to room temperature and then hexane (50 ml) was added. The purple suspension was filtered, washed with hexane (2×10 ml) and dried in vacuo at room temperature. Yield 49.2 mg (66,6%). It was dissolved in a minimal volume of dioxane and then precipitated by hexane to purify the labelled PEG from the porphyrin traces.

Elementary microanalysis was performed using a Vario ELIII device. The porphyrin units content in the samples (Fig. 1) was calculated from the absorption of polymers solution in dioxane, with the use of Cu-TPP and Zn-TPP extinction coefficients [12] (absorption spectra were taken with a Varian UV-Vis-NIR Cary 500 Scan spectrophotometer, and IR spectra were recorded with a Specord 75 IR spectrophotometer). The relationships between dye and polymer absorption band intensities depend on the average amount of dye molecules per unit polymer chain (x/y).

In our experiments, the following substrates were used: a quartz plate and two semiconductors (In_2O_3 and SnO_2) deposited on a quartz plate. The semiconducting (In_2O_3 or SnO_2) substrates were deposited by evaporation onto a quartz plate. Since the investigated dye-containing polymers have a high solubility (e.g. in water), it is impossible to prepare Langmuir and Langmuir–Blodgett films of such compounds. Therefore, the modified dynamic deposition method was applied for preparing thin organic films on the quartz or semiconducting substrates [13–15]. In our experiments, chloroform was used for the dynamic deposition on solid substrates. In sample preparation, 100 μl of the dye solution in chloroform (c = 1 mM) was deposited on the cleaned substrate. The solution was spread over the solid substrate, which was set at 25 degrees with respect to the ground. The solid film was obtained as a result of chloroform evaporation during the lamellar flow of the solution. The thickness of the deposited dye layer was about 20 nm (estimated on the basis of the SFM studies).

Polarized absorption spectra for the dye layer were measured in the range of 400–900 nm with a Specord M40 UV-Vis spectrophotometer. The reference sample was a proper substrate without dyes. The dye concentration was 1 mM for sample preparation. The accuracy of the absolute absorbance intensity was 0.001. Two absorption components were measured: $A_{\parallel}$ and $A_{\perp}$ ($A_{\parallel}$ and $A_{\perp}$ are the absorbance components measured for the light electric vector parallel and perpendicular to the deposition direction of the layer, respectively). $A_{\parallel}$ and $A_{\perp}$ were measured in two geometrical arrangements:

- with the light beam perpendicular to the sample surface ($\beta = 0°$),
- with the light beam inciding at $\beta = 10°$.

Such an experimental approach allows the molecular arrangement to be determined with respect to the substrate surface, according to the method of Yoneyama et al. [16], using the following equation

$$\left\langle \cos^2\theta \right\rangle = \frac{D_0 - \left(1 + D_0 \sin^2\beta\right) D_\beta}{\left(1 - 2\sin^2\beta\right) D_\beta - \left(1 + D_\beta \sin^2\beta\right) D_0} \tag{1}$$

where i = 0° or β, and θ is the angle between the molecular skeleton (assuming that the absorption transient moment lies in the dye molecular scaffold) and substrate surface; $D = A_{\parallel}/A_{\perp}$.

The linear dichroism was defined as [17]

$$LD = \frac{A_{\parallel} - A_{\perp}}{A_{\parallel} + 2A_{\perp}} \tag{2}$$

The fluorescence spectra of the investigated polymers were measured with a steady-state spectrofluorometer Hitachi F4500. The experimental arrangement of such measurements for the dye layers on the solid plates was as described in [18].

The optical microscopy images were obtained using a micro-optical 3D measuring device (GFM, Teltow, Germany). SFM measurements were performed with a Nanoscope IV in air at room temperature. The images were obtained using a standard Si_3N_4 microtip with a force constant of 0.38 $N \cdot m^{-1}$. An applied force of about 10 nN was estimated from the signal of the feedback set point. This is only an approximate measure, since the capillary condensation contributions between the tip and the surface layer are unknown. All images were obtained at the scanning rate of 2.54 Hz. None of the features in the micrographs were changed when the scan rate was varied around this value. The best results were obtained in the SFM contact mode. No damage in the molecular coating was observed after several scans.

Investigations with SFM give two types of micrographs: a deflection and height picture. Deflection images were obtained from the data that came from the differential signal of the SFM photodiode pair. The z (height) piezo voltage set by the feedback calculation in the digital signal processor was used to produce the height image. This image was thus caused by a signal of the difference between the loop error and point set control. The image, therefore, showed the edges clearly. The height picture was used to analyse the roughness of the samples. However, topographical features can be seen best from the deflection pictures, and these are given in this paper [19, 20].

The roughness parameter R_a was determined as an average value in a sample area of 1×1 μm^2. R_a is the arithmetical mean line deviation or the so-called centre line average. It is defined as the arithmetic average over all absolute values of height h_i with respect to a reference line [20, 21] and can be measured automatically within SFM.

3. Results

3.1. Electronic spectroscopy

Figure 2 shows the polarized absorption spectra ($A_{||}$ and $A_{\perp}$) of dye–polymer films on a quartz plate as an example. The bands that range between 400 and 900 nm are assigned to the dye moieties, whereas polymers are responsible for absorption in the range of 200–300 nm (not shown). The absorption spectra of the dyes on solid substrates are more or less changed with respect to dye–polymers dissolved in water [1, 11, 22]. Slight shifts of the Soret bands (2 nm for samples **1** and **2**, 5 nm for the polymer **3**) are assigned to the interaction of the dye–polymer with the solid surfaces. For the polymer **3**, the splitting of the Soret band is observed – the band intensity (the ratio of the band at 425 nm and 449 nm) changes as compared to that in aqueous solution [1, 22]. This band splitting could be assigned to a strong interaction between dye moieties, which are close to one another, as observed for strongly interacting molecules. The shapes of the spectra for the remaining substrates (In_2O_3 and SnO_2) are

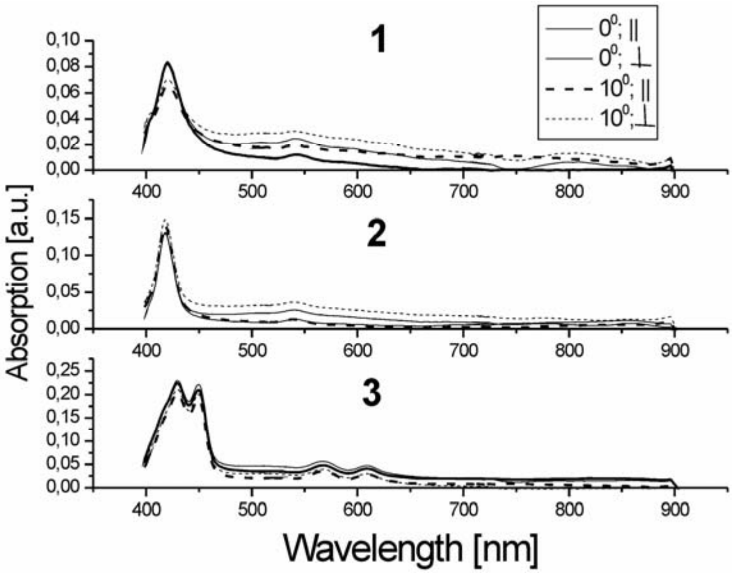

Fig. 2. Polarized absorption spectra of the dye–polymer films on quartz plates. The absorption components $A_{||}$ and $A_{\perp}$ were measured with a light beam perpendicular to the sample surface (0°) and with the light beam inciding at 10°

essentially unchanged (not shown). The relative intensities of these bands, however, are altered when thin films are deposited on quartz, In_2O_3, or SnO_2 plates. This indicates that the interaction between the dye molecules and polymer chains is disturbed in different ways by various solid substrates. It can also be due to a different dye orientation with respect to the solid surface.

On the basis of polarized absorption measurements, the orientation of dye molecules on the solid surface can be evaluated. We begin with a description of the orientation of sample **3** on quartz, In_2O_3 and SnO_2. The first interesting feature is that the perpendicular component ($A_\perp$) is a little higher in intensity than the parallel one ($A_{||}$). This indicates that the dye molecules are oriented rather perpendicular to the substrate surface. Such an arrangement of the porphyrin dyes is supported by the values of the linear dichroism (LD) parameters. The corresponding tilt angles and LD parameters are given in Table 1. We realize that our estimation is rather rough due to small difference between $A_{||}$ and $A_\perp$ and due to the low absorbance of dyes in the thin films. Nevertheless, the data in Table 1 show a tendency of the dye molecules to be arranged in an out-of-plane orientation. In our previous paper, we have also investigated the orientation of porphyrin dyes in a form of the Langmuir or Langmuir –Blodgett layers [9]. A flat arrangement of the LB dye layer (without polymer) on solid In_2O_3 and SnO_2 was shown [9]. The estimated angles were from 24° to 33° in the Langmuir–Blodgett layer [9], whereas in this paper the angles lie between 56° and 68°. For a similar porphyrin, the variation in the tilt angles on the same substrates could be assigned to the large influence of the polymer skeleton **3** on the orientational behaviour of the dye molecules.

Table 1. Linear dichroism (LD)[1] values of dyes on different substrates and the angles θ between the dye molecular skeleton and substrate surface

Sample	LD			θ, deg		
	Substrate					
	Quartz	In_2O_3	SnO_2	Quartz	In_2O_3	SnO_2
1	0.030	0.050	0.020	26	9	13
2	-0.010	0.030	0.110	68	7	32
3	-0.010	-0.010	-0.010	68	56	61

[1] LD estimated at the maximal dye absorbance. $\Delta LD = \pm 0.005$, $\Delta\theta = 3°$.

On the other hand, the dye molecules are rather in-plane oriented when linked to the other polymer chains (samples **1** and **2**). The estimated tilt angles range between 70 and 320 (except for polymer **2** on the quartz plate). In comparison with our previous LD observation for porphyrin molecules in the LB film on In_2O_3 and SnO_2 substrates [9], the arrangement of the dye molecules is also disturbed by the presence of the polymers. This conclusion is supported by the data presented in our previous paper for the porphyrin molecule in the absence of polymers (**1** and **2**) [9].

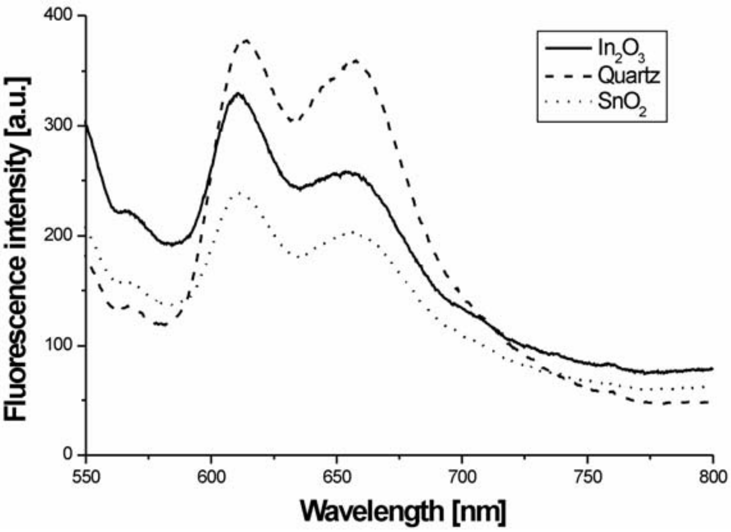

Fig. 3. The fluorescence spectra of dye–polymer **3** on various substrates

The dye–polymer species studied do not show any fluorescence in aqueous solution (or it is extremely low; data not shown). The fluorescence features are dramatically changed after depositing the dye layers on the solid substrates. Figure 3 shows examples of the dye–polymer **3** on quartz, In_2O_3 and SnO_2. Two bands, typical of porphyrin dyes, are observed. One band is located around 610 nm and the other at about 650 nm. The band locations are different from those obtained for the dyes in, e.g. DMSO [9]. Also, the bands are much broader than those observed for these dyes dissolved in organic solvents [9, 23]. This means that the interaction of the dye–polymers with the solid surface affects their fluorescence behaviour. In the previous work [24], the infrared spectroscopy showed the charge redistribution in the dye macrocycles after dye Langmuir–Blodgett layer formation. We can thus suppose that electronic interaction between π electrons in the dye skeleton and the solid is the reason for the enhanced dye fluorescence observed in this paper.

Summarizing, we conclude that the dye arrangement in thin films on the solid substrates depends crucially on the substrate material. The most important observation is that the dye orientation is altered in the presence of the polymer chains. A marked variation in dye arrangement is shown for the ZnTPP dye linked to the polymer system (**3**). We thus suggest that the molecular arrangement and electronic interactions in the dye–polymer systems could affect the final topography of the thin film.

3.2. Microscopic studies

In our experiments, we use three solid substrates: a quartz plate, and In_2O_3 or SnO_2 deposited on the quartz plates. Previously, the differences in their topographies were shown and they were characterized by a different size of grains [9]. The quartz plate had a very smooth surface with the lowest roughness parameter (R_a = 0.1 nm), In_2O_3 on quartz was characterized by low surface granularity (R_a = 0.4 nm), and the SnO_2 layer exhibited the highest value of the roughness parameter (R_a = 2.2 nm). The same substrates were used in this paper, and their images are comparable with those presented in the previous paper [9].

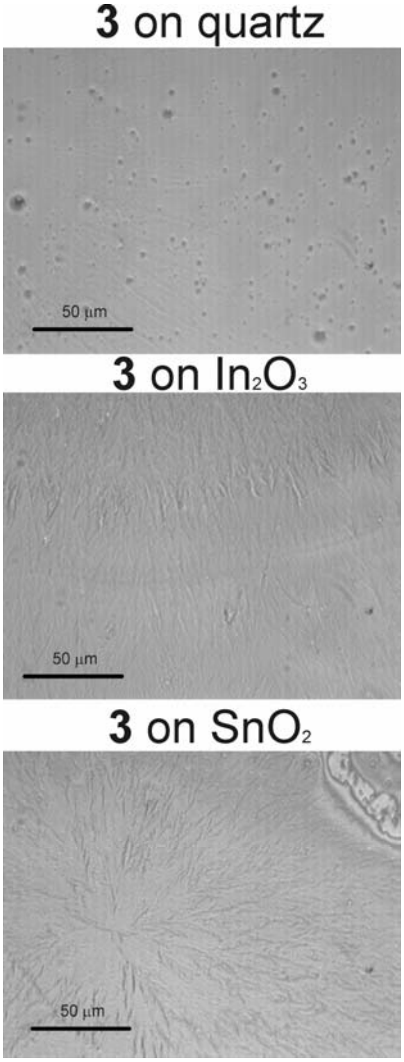

Fig. 4. Optical microscopy images of **3** on quartz, In_2O_3 and SnO_2

Deposition of sample **3** on the quartz plate and on In_2O_3 and SnO_2 (Fig. 4) leads to differences in the macroscopic images. A marked variation in the topography of the dye–polymer system **3** is observed as compared to the images of the substrates [9].

A dendritic structure of the polymer film, with crystallization centres, can be seen (on In_2O_3 and SnO_2 substrates). Its character depends on the granularity of the original surfaces. The higher the roughness parameter, the larger are the visualised dendritics and crystallization grains.

For samples **1** and **2**, rather smooth homogeneous surfaces are observed, and the differences between the surface structures of these samples on quartz and SnO_2 are due to variations in the grain sizes of these two solid substrates (data not shown).

In summary, we conclude from this part of the paper that the dye–polymer systems **1** and **2** present rather homogeneous topographies, while the dye–polymer **3** exhibits a dendritic topography and its final image depends on the granularity of the solid surface.

A deeper insight into the topography of dye–polymer systems can be obtained from SFM experiments, since SFM visualization gives much more details than optical microscopy. The SFM images of samples **1**, **2**, and **3** on SnO_2 give very similar images (not shown). For each dye–polymer on SnO_2, an image of the substrate is observed rather than the individual character of the polymer layer owing to the large granularity of SnO_2. Detailed SFM images of the film are thus impossible to obtain due to the high roughness of the SnO_2 substrate.

Much more interesting results were obtained for dye–polymer films deposited on substrates of low granularity – on quartz and In_2O_3. Figures 5–8 show the results for samples **1** and **3**, respectively, on quartz or In_2O_3. A comparison of these figures evidently shows that the final SFM images depend strongly on the dye–polymer and the granularity of the solid substrate. For sample **1**, a ring-like topography is observed (Fig. 5). The sequences of the rings are repeated along the whole sample. In the panel in Fig. 5, a cross-section analysis of this structure is presented. The size of the polymer could be estimated basing on the evaluation of the roughness parameters for the bare substrates. The height of the polymer is about 9–11 nm. The diameter was estimated to be about 450 nm.

Small changes can be observed in the SFM images when the porphyrin–polymer **1** covers the In_2O_3 surface. Figure 6 shows the SFM image of this sample on In_2O_3, with the section analysis of the image also shown. Again, a ring-like structure could be recognized, but it is not as clear as for the same dye–polymer on quartz. Cross-section analysis gives the height values 12 and 17 nm. These values could be described as follows. On the basis of our previous results concerning SFM images of the In_2O_3 substrate, the height of In_2O_3 grains was estimated to be about 5–7 nm. The first cross section value (12 nm) can thus be assigned to the thickness of polymer layer that is in contact with the In_2O_3 grain pit. The higher value (17 nm) reflects the height of the polymer layer on top of an In_2O_3 grain. This value is higher than that for the same sample on quartz, as expected. The variations in the SFM images of sample **1** on In_2O_3 and quartz and the differences in height could be caused by either a difference in grain size between the two substrates or by a different dye orientation with respect to the substrates.

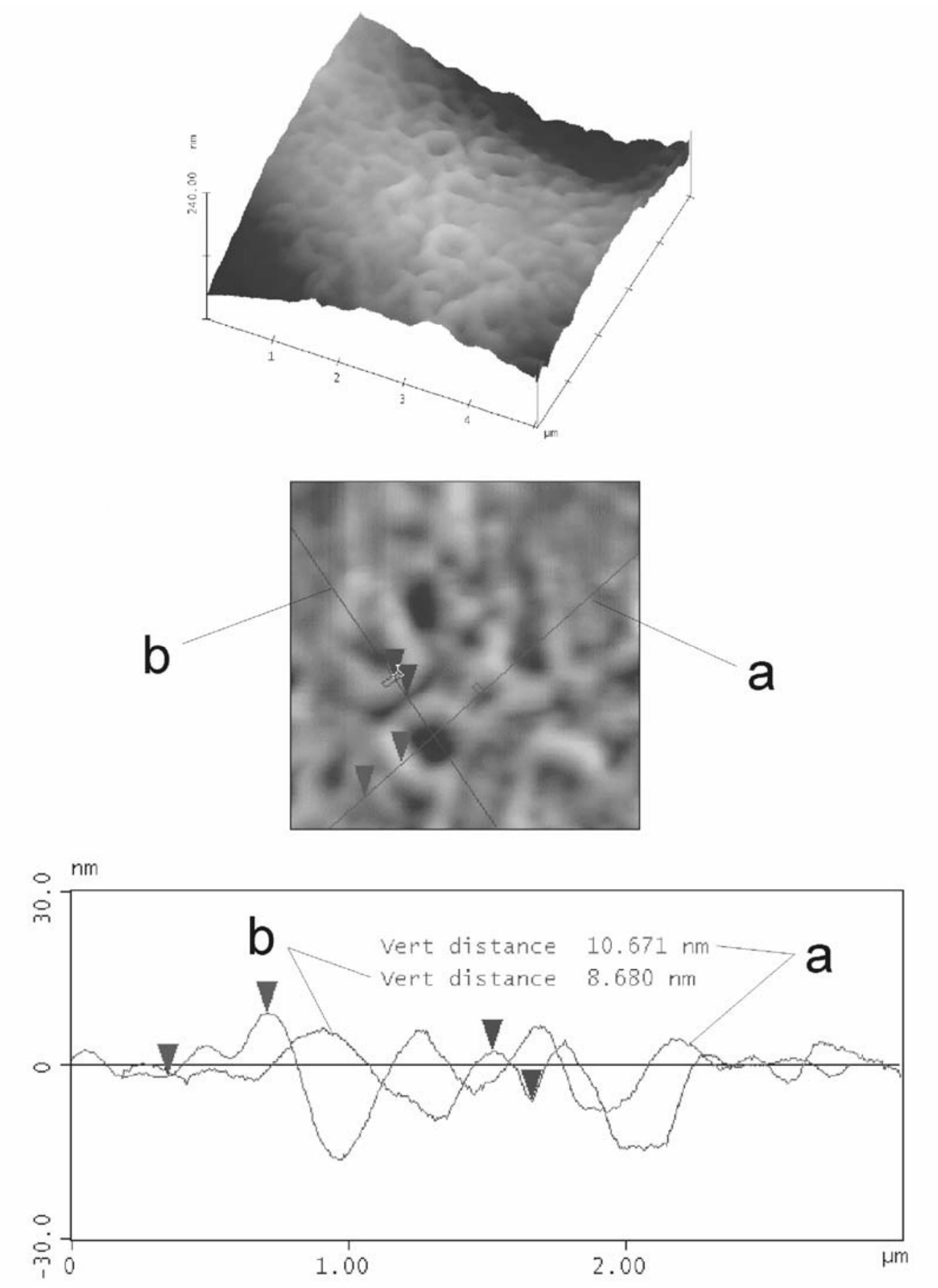

Fig. 5. SFM images of **1** on quartz: an overview, and cross-section analysis (the straight lines represent the directions in the sample taken into consideration in the profile analysis)

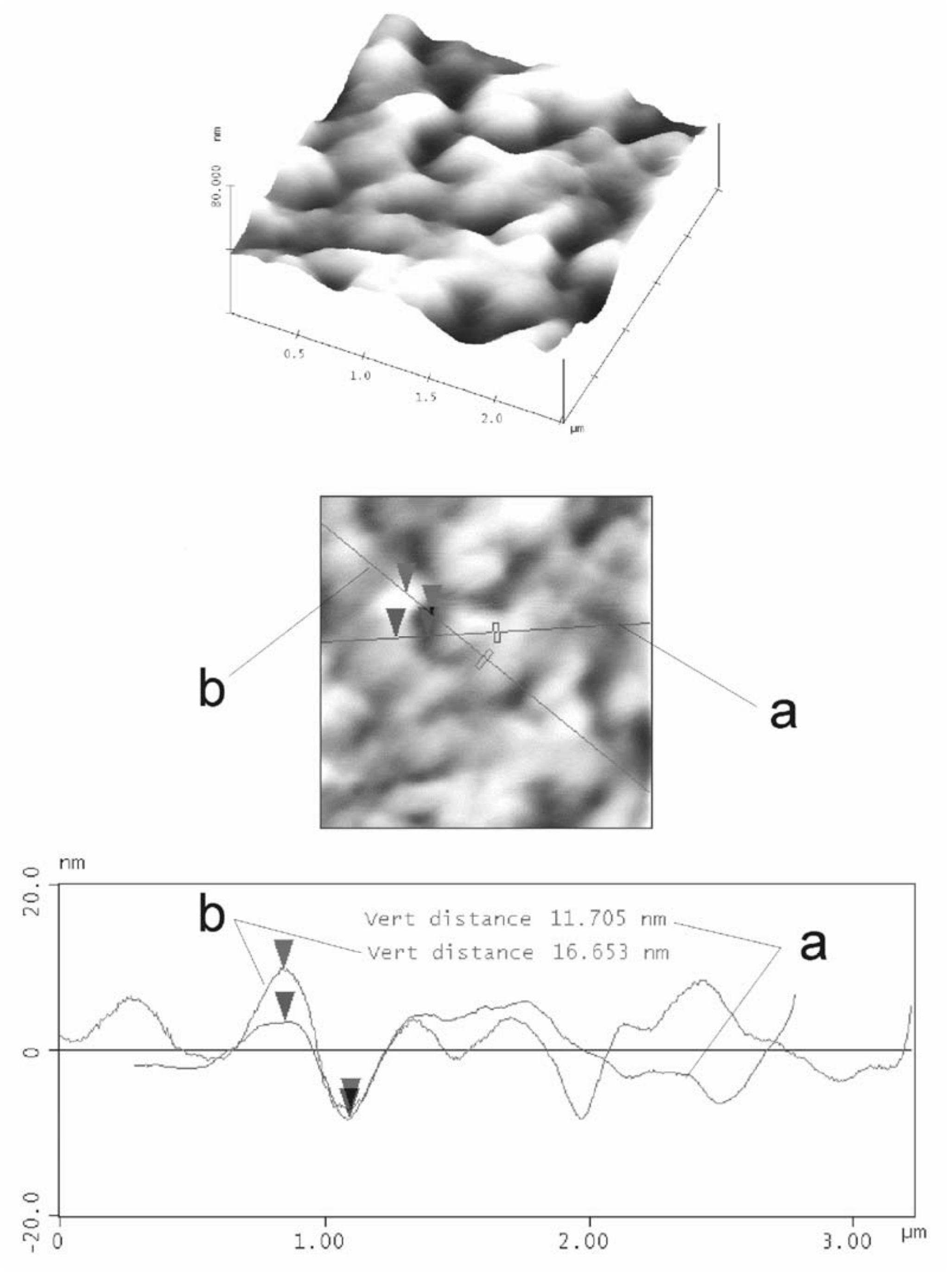

Fig. 6. SFM images of **1** on In_2O_3: an overview, and cross-section analysis (the straight lines represent the directions in the sample taken into consideration in the profile analysis)

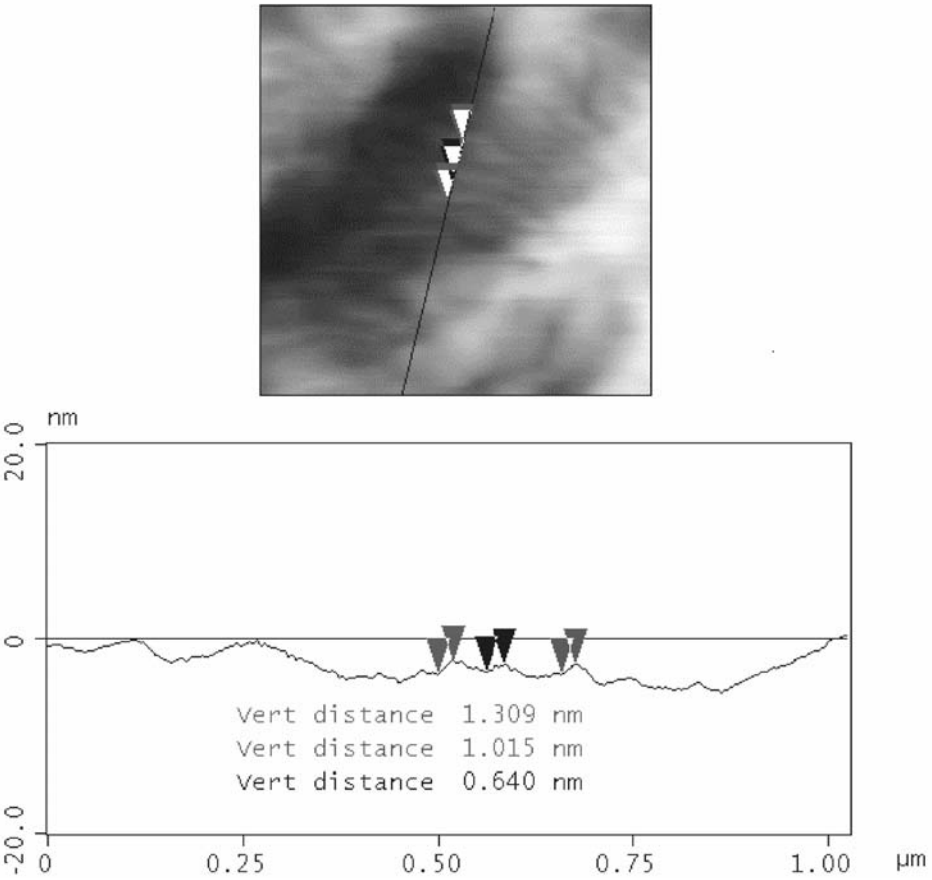

Fig. 7. The cross-section analysis of SFM images of **3** on quartz. The straight lines represent the directions in the sample taken into consideration in the profile analysis

The surface of the dye–polymer system **3** can be seen in Fig. 7, which presents the SFM image of this sample on a quartz plate. The sample is characterized by a longitudinal topography, in which the dye–polymer chains are observed. Basing on the cross-section analysis of surface **3**, we find that the average value of polymer chain height is about 1.1 nm. Figure 8 confirms again the longitudinal structure of sample **3** on the In_2O_3 surface. The section analysis is also shown. A complex profile of the surface topography indicates a multicomponent structure of the dye–polymer with the thickness of about 12 nm with respect to a pit of the In_2O_3 grain. The values of 2.5 nm and 5 nm could describe the layer-by-layer thickness jumps of the polymer on the substrate. These values could be correlated with the van der Waals radius of the PEG chain, being about 3.5 nm [25].

The cross-section results indicate that the final morphologies of the thin films in the dye–polymer systems are affected by the kind of the sample and by the original topography of the substrate.

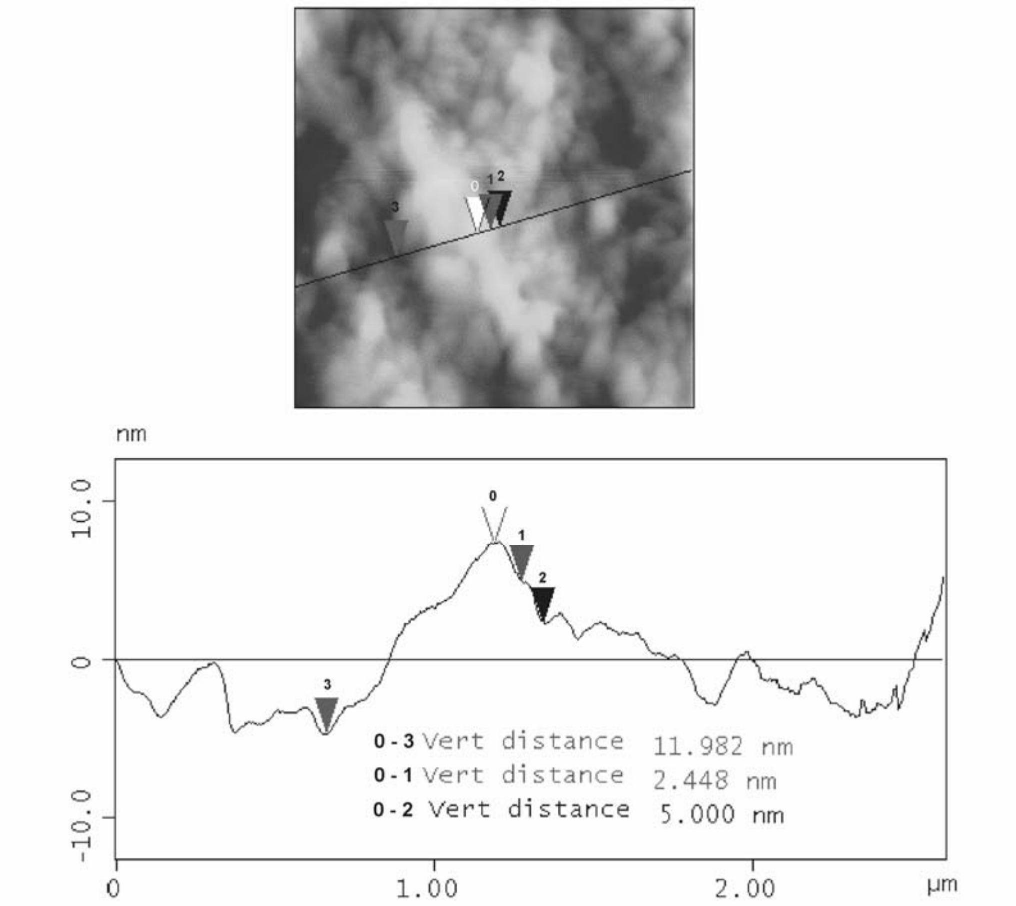

Fig. 8. The cross-section analysis of SFM images of **3** on In_2O_3. The straight lines represent the directions in the sample taken into consideration in the profile analysis

4. Discussion

A general idea of this paper was to show that the optical microscopy and SFM images of polymeric samples are affected by their molecular structure, by polymer length, and by the population of dye molecules covalently linked to the polymeric chain. To find a correlation between the variation of the final images of dye–polymer systems and the granularity of the substrates, one has to consider several effects and factors:

- the relation between the granularity of the substrate and the size of the dye –polymeric systems,
- differences between molecular structures of various dye–polymeric systems; samples **1**, **2**, and **3** differ in their polymer chain structure, polymer chain length, and in their population of dye molecules along the chain,

- differentiation of the orientation of dye–polymer samples with respect to the substrate surface.

Samples **1** and **2** are characterized by a rather homogeneous topography when deposited on a quartz plate or In_2O_3. This effect could be discussed in terms of the dye dimensions and dye orientation with respect to the substrate. The size of these polymeric samples are suitable for quartz and In_2O_3 granulites. Every dye–polymer system exhibits different topography when deposited on solid surfaces: the dye–polymer **1** shows a ring-like structure, whereas the dye–polymer **3** presents a dendritic surface structure with well observed crystallized grains. In the case of the dye–polymer **1**, the ring–like structure lies almost flatly on the quartz and In_2O_3 substrates (the tilt angles are 90 and 130, respectively), owing to the rather low granularity of In_2O_3. On the other hand, although the polymer **3** has a dendritic structure, its chains also lie flatly on the In_2O_3 surface due to low In_2O_3 granularity. Similar results were also observed for much smaller molecular materials (phthalocyanines) [9, 15], and these new results confirm our previous observation.

We have also shown that the substrate with large grains (SnO_2) exhibited a tendency to preserve its own topography. Although the investigated dye–polymer systems differ essentially in their molecular structures and sizes, the image of the SnO_2 surface is rather weakly changed after coating it with the macromolecular materials due to the original large grains. It is evidently seen for the dye–polymer **3**; the original topography is still preserved, and this could be interpreted to be caused by filling the troughs between SnO_2 grains by perpendicularly oriented dyes and dendritic polymers. This polymer is thus not seen on the surface of large grains upon SFM examination. Studying dye–polymers deposited on SnO_2, however, is difficult due to a high roughness of the substrate. Small changes in the SFM image of SnO_2 were also observed after the surface was coated by some porphyrin and phthalocyanine dyes. These changes are discussed in terms of the large grain of SnO_2 and out-of -plane orientation of the dyes with respect to the semiconducting surface [9].

Summarizing, we have shown that the final topography of the dye–polymer layer covering the solid substrate depends predominantly on the molecular structure of the polymer. Also, the granularity of the substrate has a great influence on the final image of the dye–polymer layer. The effect of sample orientation cannot be excluded. In the case of the substrate with large grains (SnO_2), the space between grains is sufficiently large to be filled and covered by the polymer chain. Otherwise, when the substrate has a more homogeneous topography, the polymer is rather flatly deposited on the substrate surface (quartz, In_2O_3).

Acknowledgements

The paper is supported by the Poznan University of Technology, grant BW 62-195/04. The study was also supported by the DAAD/ZIP (grant no. 214/IQN, UAS Wildau, Germany). A. Boguta thanks the Foundation of Polish Science for a Fellowship for Young Scientists. Yu.S. Avlasevich thanks the INTAS for a YSF 2002-362 Fellowship.

References

[1] KNYUKSHTO V.N., AVLASEVICH Y.S., KULINKOVICH O.G., SOLOVYOV K.N., J. Fluorescence, 9 (1999), 371.

[2] GUST D., MOORE T.A., MOORE A.L., IEEE Eng. in Med. Biol., 2 (1994), 58.

[3] ROSENTHAL I., Photochem. Photobiol., 53 (1991), 859.

[4] MOAN J., Photochem. Photobiol., 43 (1986), 681.

[5] SAIKAI Y., SADAOKA Y., MATSUGUCHI M., YOKOUCHI H., TAMAI K., Mat. Chem. Phys., 42 (1995), 73.

[6] GALAEV I.Y., MATTIASSON B., Trends Biotechn., 17 (1999), 335.

[7] PTAK A., DER A., TOTH-BOCONADI R., NASER N.S., FRĄCKOWIAK D., J. Photochem. Photobiol. A, 104 (1997), 133.

[8] WRÓBEL D., BOGUTA A., MAZURKIEWICZ P., Spectrochim. Acta A, 59 (2003), 2841.

[9] BOGUTA A., WRÓBEL D., BARTCZAK A., ION R.M., RIES R., RICHTER A., Surface Sci., 513 (2002), 295.

[10] AVLASEVICH YU.S., KULINKOVICH O.G., KNYUKSHTO V.N., SOLOVYOV K.N., J. Appl. Spectr., 66 (1999), 597.

[11] AVLASEVICH YU.S., CHEVTCHOUK T.A., KULINKOVICH O.G., KNYUKSHTO V.N., SOLOVYOV K.N., J. Porphyrins Phthalocyanines, 4 (2000), 579.

[12] SMITH K.M., *Porphyrins and metalloporphyrins*, Elsevier, Amsterdam, 1975.

[13] SALTER G.J., KELL D.B., ASH L.A., ADAMS J.M., BROWN A.J., JAMES R., Enzyme Microb. Technol., 12 (1990), 419.

[14] GREGORY FOREST M., WANG Q., BECHTEL S.E., J. Rheology, 41 (1997), 821.

[15] CHEN S.B., JIANG L., Phys. Fluids, 11 (1999), 2878.

[16] YONEYAMA M., SUGI M., SAITO M., IKEGAMI K., KURODA S., IZIMA S., Jap. J. Appl. Phys., 25 (1986), 961.

[17] NORDEN B., Appl. Spectr. Rev., 14 (1978), 157.

[18] ŁUKASIEWICZ J., HARA M., NAKAMURA C., MIYAKE J., WRÓBEL D., FRĄCKOWIAK D., J. Photochem. Photobiol. A, 138 (2001), 235.

[19] RICHTER A., RIES R., Mol. Phys. Rep., 21 (1998), 11.

[20] RICHTER A., RIES R., SZULZEWSKY K., PIETZAK B., SMITH R., Surface Sci., 394 (1997), 201.

[21] WEINGRABER H., ABOU-ALY M., *Handbook of Technical Surfaces* (in German), Vieweg&Son, Braunschweig, 1989.

[22] WÓJCIK A., BOGUTA A., AVLASEVICH Y.S., WRÓBEL D., Int. J. Photoenergy, submitted.

[23] WRÓBEL D., ŁUKASIEWICZ J.AND MANIKOWSKI H., Dyes and Pigments, 58 (2003), 7.

[24] BOGUTA A., WRÓBEL D., BARTCZAK A., ŚWIETLIK R., STACHOWIAK Z., ION R.M., Mat. Sci. Eng. B, 113 (2004), 99.

[25] TANAKA S., ATAKA M., ONUMA K., KUBOTA T., Biophys. J., 84 (2003), 3299.

Received 20 October 2004
Revised 4 November 2004

Materials Science-Poland, Vol. 22, No. 4, 2004

Polymeric photovoltaic devices

JANUSZ JAGLARZ[1], ADI KASSIBA[2], PAWEŁ ARMATYS[3],
MONIKA POKLADKO[1], EWA GONDEK[1], JERZY SANETRA[1*]

[1]Institute of Physics, Cracow University of Technology, 30-084 Cracow, Poland

[2]Laboratoire de Physique de l'Etat Condensé, Universite du Maine, 72085 Le Mans, France

[3]Faculty of Physics and Applied Computer Science,
AGH University of Science and Technology, 30-059 Cracow, Poland

We present a study on photovoltaic devices based on polypyrrole (PP) and SiC nanoparticles (~30 nm) in the matrix of poly(N-vinylcarbazole) (PVK). The photovoltaic cell structure was ITO/(polymer with SiC)/Ca/Al. The photophysics of such photoactive devices is based on photoinduced charge transfer from donor-type semiconducting conjugated polymers to acceptor-type SiC nanoparticles. The process mimics early photo effects in natural photosynthesis. In the general context of organic photovoltaics, polymeric materials have a cutting edge since they combine the photoelectrical properties of semiconductors with the large scale/low cost technology of polymeric materials.

Key words: *photovoltaic effects; polymer; photovoltaic cell*

1. Introduction

Organic photovoltaics, one of the first organic double layers reported in 1986 by Tang [1], only recently have become of broader interest. Organic materials, especially conducting polymers have been studied extensively owing to their potential application in active electronic devices [2, 3].

Polymer photovoltaics offer great technological potential as a renewable, alternative source of electrical energy. The potential advantages of an all-polymer heterojunction solar cell include: low cost (large scale production using the existing polymer processing technology), large area (plastic thin films can be produced with macroscopic dimensions), flexibility (the mechanical properties of polymers). The materials used are hydrocarbon-based non-toxic molecules, and the production of these thin film solar cells is done at room temperature without any dangerous exhausts. Since the band gap of polymeric semiconductors can be manipulated, it is possible to tune

---

[*] Corresponding author, e-mail: pusanetr@cyf-kr.edu.pl.

the colour of the solar cells, which in return is uniquely important for architecture. Furthermore, this approach allows unused large areas other than roofs to be accessed for photovoltaic energy conversion, by fabricating semitransparent photoactive thin films. These potential advantages bring a legitimate relevance for industrial interest to this approach.

Most of the development in polymer electronics has been done in the production of either p-n junctions or Schottky and metal-insulator-semiconductor diodes [4–6].

In spite of the intensively investigated photophysics of conjugated organic materials, the mechanism of charge carrier photogeneration is still under debate. The primary photoexcitations can be considered to be excitons that have a certain probability to dissociate into free charge carriers (polarons) (Fig. 1) if the binding energy of the exciton can be compensated [7]. There is a fast photoinduced charge transfer reaction in these polymer photovoltaic cells at the donor acceptor interface, which results in a metastable charge-separated state [8].

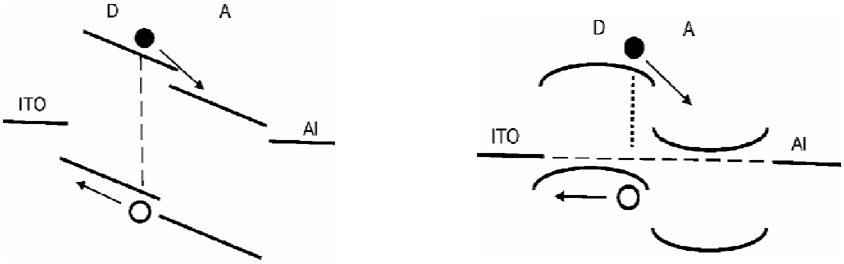

Fig. 1. Band energy diagrams for a D/A double layer device in the short circuit mode. Left: the built-in field, due to ΔW_f between the electrodes, leads to tilted bands if only a few free charge carriers are present. Right: at higher charge carrier concentrations, the bands can remain flat in the bulk, and blocking contacts may be formed [1]

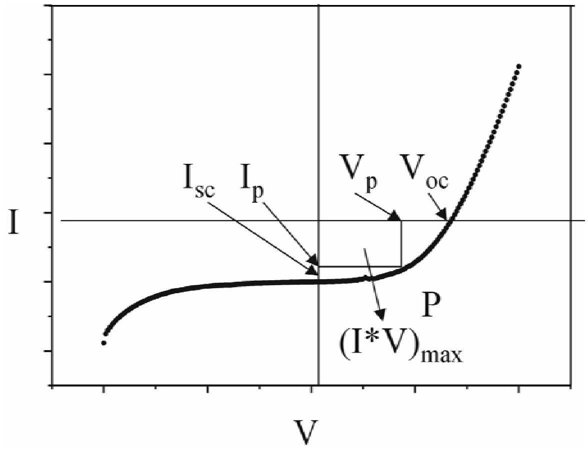

Fig. 2. The current versus applied voltage of a solar cell. The extracted current is negative. The fourth quadrant represents the voltage and current generated by the cell. An externally applied voltage is necessary to obtain data points in the first and third quadrant

The left figure in Fig. 1, shows a simplified band energy diagram for a double layer device with a low concentration of free charge carriers. The difference between the work functions of the electrodes ΔW_f can cause the bands to tilt, as shown, which creates a constant field across the bulk. The right figure in Fig. 1 shows the situation for a device with a free charge carrier concentration high enough to compensate the built in field within a fraction of the layer thickness. According to this picture, the driving force, i.e., V_{oc} is mainly determined by the offset at the D/A junction, although the increased built in field can help transport charges through the bulk.

The overall efficiency η_{eff} of a solar cell is calculated by the following formula:

$$\eta_{\mathrm{eff}} = \frac{V_{oc} I_{sc} (FF)}{I_{\mathrm{light}}} \tag{1}$$

where V_{oc} is the open circuit voltage, I_{sc} is the short circuit current in A/m^2, FF is the fill factor, and I_{light} is the incident solar radiation in W/m^2. The fill factor of solar cells, which reflects their diode properties, is determined by

$$FF = \frac{I_{mpp} V_{mpp}}{I_{sc} V_{oc}} \tag{2}$$

with I_{mpp} and V_{mpp} being the current and voltage at the maximum power point in the 4th quadrant of the I/V curve (Fig. 2).

2. Experimental

Semiconducting polymers can be used as electron donors in combination with SiC nanoparticles as electron acceptors to construct polymer photovoltaic cells.

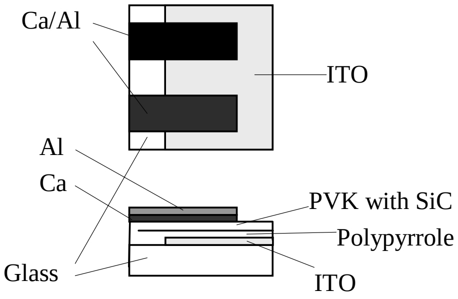

Fig. 3. Structure of the photodiode

Commercial poly(ethylene oxide)(poly(oxy-1,2-ethanedienyl), PEO, type Polyox WSRN 750, produced by Union Carbide, was used without further purification. Anhydrous iron(III) chloride ($FeCl_3$, Merck) was purified by sublimation. The PEO-

$FeCl_3$ (7:3) complex was prepared as described in [9]. Complex films were obtained by spin coating from solutions in nitromethane (10 wt. %). The polymerisation of pyrrole was carried out in the saturated monomer vapour at room temperature (21±2 °C). Thin polypyrrole composite films were prepared on the surface of the glass covered with ITO. Next, the tetrahydrofuran solution of PVK, used as a matrix of SiC nanoparticles (20–40 nm), was spin-coated on the polypyrrole layer (Fig. 3).

The chemical structure of the compounds is shown in Fig. 4. Calcium and subsequently aluminium as an electrode were evaporated on the surface.

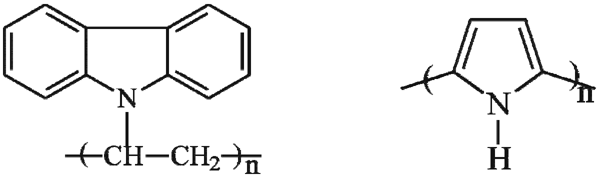

Fig. 4. Structures of poly(N-vinylcarbazole) (PVK) and polypyrrole (PP)

The photovoltaic cell had an active area of 0.3×0.5 cm^2. The structure of the cell, obtained this way, was ready to measure.

3. Results and discussion

First, an *I*–*V* characteristic of the structure was determined (Fig. 5), then the current in short circuit mode under light and voltage in open circuit were measured. Figure 5a shows the curves *I* vs. *V* of ITO/polypyrrole-PVK with SiC/Ca/Al structure in the dark, which exhibits a clear current rectification. Under illumination, the device exhibits a short-circuit current and an open-circuit voltage (Fig. 5b), which makes this structure a photovoltaic cell. Although it presents a very low current intensity, it is promising from the materials research point of view.

Figure 6 shows a schematic energy diagram of a PP and PVK with SiC heterojunction photovoltaic cell. The ionisation potentials of PP and PVK with SiC films were evaluated by photoelectron spectroscopy to be about 5.5 and 5.6 eV, respectively. The band gaps of PP and PVK with SiC were evaluated from the absorption edge to be about 3.2 and 3.0 eV, respectively. The work function of ITO [10] and Ca [11] were 4.6 and 3.2 eV, respectively. Since the conduction band of PVK with SiC is located about 0.2 eV below the conduction band of PP, electrons should be injected into PVK with SiC from PP at the PP/PVK interface by the dissociation of photoexcited excitons or exciton-polarons in PP.

It was assumed that the top of the valence band of PP is located at a higher energy than that of PVK with SiC by about 0.1 eV. This should make it possible to photoinduce hole transfer from PVK with SiC to PP in the same manner. That is, the photoinduced charge transfer by the dissociation of excitons and exciton-polarons results in

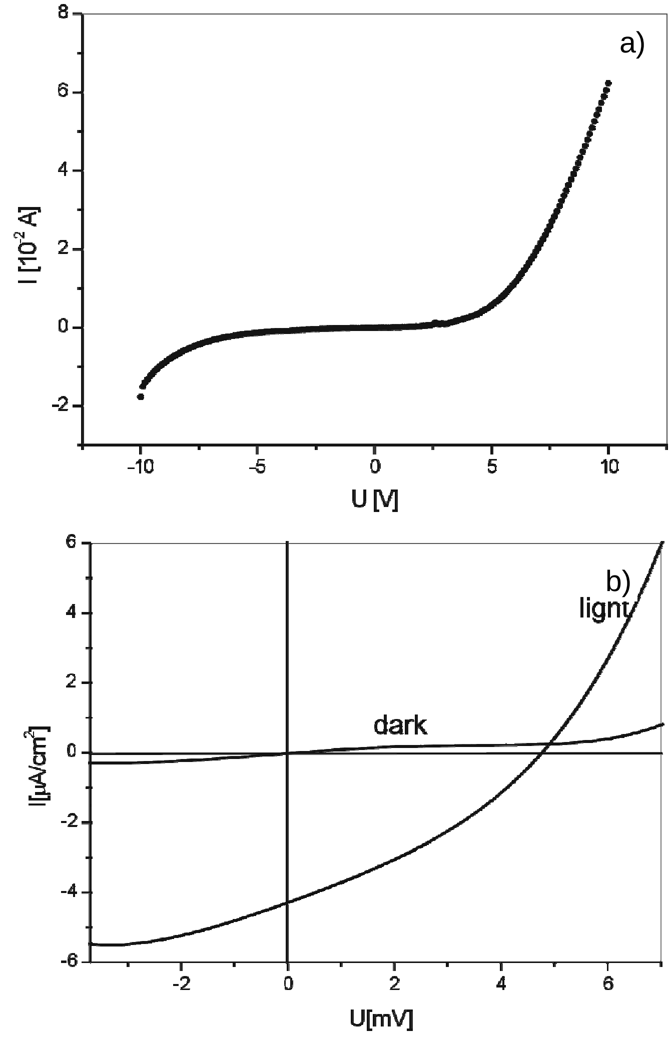

Fig. 5. Current density–voltage characteristics of an ITO/polypyrrole/PVK with SiC/CaAl cell: a) in the dark, b) in the dark and under 12 mW/cm^2 light irradiation

Table 1. Photovoltaic parameters for a sequence of layers

Sequence of layers	Short-circuit current density [µA/cm^2]	Open-circuit voltage [mV]	Power conversion efficiencies	Fill factor FF [%]
A) ITO/polypyrrole/PVK with SiC /Ca/Al	4.3	48	0.8 %	28
B) ITO/PVK with SiC-polypyrrole/Ca/Al	3.25	33	0.6 %	26
C) ITO/blend of polypyrrole and SiC/Ca/Al	0.25	167	0.2 %	17

the presence of positive carriers in PP and negative carriers in PVK with SiC. When the structure of the photovoltaic cell changes (ITO/PVK with SiC/PP/Ca/Al), the properties of the solar cell also change (Table 1). All characteristic photovoltaic parameters are smaller. The differences are not so large, because there is a small difference between the energy levels (Fig. 6) of the CB bands of PP and PVK with SiC. The same is true for VB bands, and is also caused of small values of V_{oc} for the investigated materials. In the case of structure C (Table 1), solar cells were built from a blend PP with SiC; their properties are different. The short circuit current is smaller than that for multilayer solar cells by one order of magnitude, but the open circuit voltage is higher.

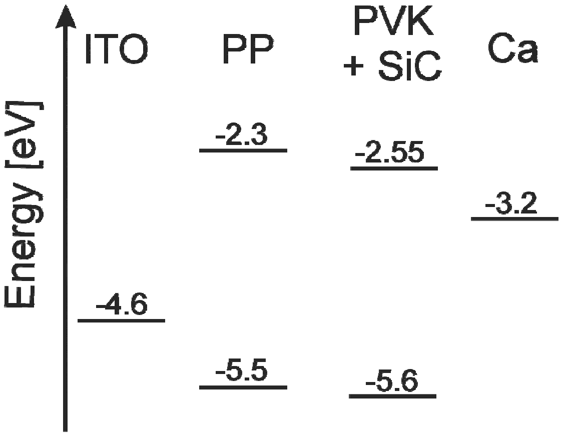

Fig. 6. Schematic energy band diagram of the ITO/PP/PVK with SiC/Ca/Al heterojunction photovoltaic cell

This effect is probably a result of the recombination of charge carriers and excitons in the bulk blend. Recombinations are caused by the migration of both negative and positive charges in the same material. This effect decreases the number of charges on the electrodes and sometimes increases the temperature of the cell.

4. Conclusions

Further optimisation of device performance can be achieved by optimising its physics:

- Optimising the choice of the D/A pair (energetics determine the open circuit potential). In addition, the band gap of the semiconducting polymer should be chosen for efficient harvesting of the solar spectrum.
- Optimising the network morphology of the phase-separated composite material for enhanced transport and carrier generation. The absorption of light and mobility of

the charge carriers within the components of the bulk heterojunction have to be maximized.

The photocurrent of the B) system photovoltaic cell (Table 1) is larger than that of the C) system photovoltaic cell by more than one order of magnitude.

The observed photoirradiation effects in the heterojunction photovoltaic cell can be explained in terms of photoinduced interfacial charge transfer between PP and PVK with SiC by taking into account the difference between the electronic states of PP and PVK with SiC.

Acknowledgements

This work has been partly supported by the State Committee of Scientific Research (KBN) in the years 2002–2005.

References

[1] TANG C.E., Appl. Phys. Lett., 48 (1986), 183.
[2] AKHMEDOV KH.M., KARIMOV KH.S., FIODOROV M.I., Appl. Sol. Energy, 31 (1995), 63.
[3] CHAMBERLAIN G.A., Sol. Cells., 8 (1983), 47.
[4] WORHLE D., MEISSNER D., Adv. Mater., 3 (1991), 129.
[5] CURRAN S., CALLAGHAN J., WLDON D., BOURDIN E., CAZINI K., BLAU W., WALDRON E., MCGOVERAN D., DALMESIERE M., SARAZIN Y., HOGREL C., Electron. Prop. Fullerenes, 117 (1993), 427.
[6] HAYASHI S., KOZARU K., YAMAMOTO K., Solid State Commun., 79 (1991), 63.
[7] ARKHIPOV V.I., EMELLIANOVA E.V., BASSLER H., Phys. Rev. Lett., 82 (1999), 1321.
[8] KRAABEL B., HUMMELEN J.C., VACAR D., MOSES D., SARICIFTCI N.S., HEEGER A.J., J. Chem. Phys., 84 (1996), 4267.
[9] RABEK J.F., LINDEN L.A., ADAMCZAK E., SANETRA J., STARZYK F., PIELICHOWSKI J., Mater. Sci. Forum, 191 (1995), 225.
[10] PARK Y., CHOONG V., GAO Y., HSHIEC B.R., TANG C.W., Appl. Phys. Lett., 68 (1996), 2699.
[11] MICHAELSON H.B., J. Appl. Phys., 48 (1977), 4729.

Received 14 September 2004
Revised 8 November 2004

Materials Science-Poland, Vol. 22, No. 4, 2004

Semiconducting dye-functionalised poled polymers for photovoltaic applications

ALEKSANDRA A. APOSTOLUK[1*], LICINIO ROCHA[1]
CÉLINE FIORINI-DEBUISSCHERT[1], CAROLE SENTEIN[1], PAUL RAIMOND[1],
LEONARDO SETTI[2], ALESSANDRO FRALEONI-MORGERA[2], JEAN-MICHEL NUNZI[3]

[1]Commissariat à l'Energie Atomique, CEA-Saclay, CEA-DRT-LITEN, DSEN/GENEC/L2C, bât. 451,
Laboratoire Cellules et Composants, 91191 Gif-sur-Yvette Cedex, France

[2]University of Bologna, Dept. of Industrial and Materials Chemistry, Faculty of Industrial Chemistry,
Viale Risorgimento 4, 40136 Bologna, Italy

[3]Université d'Angers, UFR: Sciences, Laboratoire de Propriétés Optiques des Matériaux et Applications
(POMA), UMR CNRS 6136, 2 Boulevard Lavoisier, 49045 Angers Cedex 01, France

In order to build efficient single-layer polymer photovoltaic devices, the realization of an equivalent distributed p-n junction is proposed. Orientation in the initially centrosymmetric material is obtained by ordering polar molecules contained in a polymer matrix with a DC field. The molecular rectification effect induced in an oriented polymer film improves the efficiency of polymeric semiconducting devices like solar cells. The first experiments were conducted with a poly(methylmethacrylate) (PMMA) matrix containing azo-dye compounds (such as the Disperse Red 1, DR1) as the polar molecules, grafted onto the chains of the polymer backbones. Although this material allows for high orientation efficiencies, it is not adapted for photovoltaic applications, since DR1-MMA has very poor semiconducting properties due to the dielectric nature of PMMA. Organic semiconductors are uncommon and it is difficult to find an appropriate polymer system. We present preliminary results obtained for two intrinsically semiconducting and dye-functionalised polymer systems which may be found applicable in the fabrication of organic photovoltaic solar cells using the concept of polar molecular ordering. We use polymer systems with a covalent bond between the dye molecule and conjugated backbone to obtain a high dye content and to avoid phase separation problems. To achieve the largest stable molecular polar orientation possible and to optimise the electric field stored in an oriented structure, we studied the orientation parameters of samples, i.e., the orientation field, temperature, poling duration, and cooling conditions.

Key words: *organic semiconductors; polymer semiconducting film; molecular diode; organic photovoltaic cell*

---

[*] Corresponding author, e-mail: AA206034@ortolan.cea.fr.

1. Introduction

Semiconducting polymers are receiving growing attention in view of the fabrication of flexible and low-cost organic photovoltaic cells, with standard coating and printing processes taking advantage of their easy processability [1, 2]. In order to create efficient solar cells, building a rectifying junction is mandatory. The structure leads to the existence of an internal field allowing a charge separation after exciton generation [3]. Such a junction can be of the Schottky-type, between an organic semiconductor and a metal, or it can be a p-n junction, between p- and n-type organic semiconductors. p-n type junctions, in which the metal to polymer contacts are ohmic, turn out to be the most efficient in the realization of optoelectronic devices. They also permit to avoid degradation problems, characteristic of the Schottky junctions and resulting from electrochemical potential differences at the rectifying contacts that induce the diffusion of the electrode material into a polymer film. This is corrected in p-n junctions by the ohmic nature of their metal-polymer contacts. The realization of a standard p-n junction requires the use of two polymer layers bearing wet-processing compatibility. Moreover, n-type organic semiconductors are less common than p-type ones, due to their lower stability under oxygen in consequence of their reductive behaviour. A further limitation of this approach concerns a weak extension of the depletion zone (between 10 nm and 50 nm), where the majority of the exciton dissociation occurs. This limits the maximum thickness of the devices, making it very difficult to efficiently harvest the visible light.

To increase the efficiency of a photovoltaic polymeric device, we propose an alternative to the classical p-n junction: induction of an internal field over the whole thickness of a photovoltaic layer through orientation of polar molecules, obtained by the application of a static electric field. Oriented molecules (push-pull type) induce a rectifying effect, behaving as a distributed homojunction in an initially centrosymmetric material [4]. The junction is distributed throughout the entire thickness of the device. All photogenerated excitons are likely to find a junction and split before recombination, thus avoiding recombination channels (radiative and non-radiative).

It has also been demonstrated that molecular-induced orientation in a polymer device increases the charge mobility in the material [5] and that the barrier height between the electrode material and the polymer decreases with growing polar order [6]. The improvement of the efficiency of photovoltaic cells based on a polymeric single layer bearing oriented polar chromophores has also been clearly evidenced [5]. In fact, it is known that the photogenerated excited states in organic molecules, termed excitons, which are exploited in organic photovoltaic devices, split themselves into electrons and holes in presence of strong electric fields, such as those provided by physical interfaces between different materials. In view of this, it is interesting to investigate if the proposed poling method, which is capable of providing molecularly distributed homojunctions, may be of help in enhancing the photovoltaic performance of organic solar cells when applied to the appropriate polymer systems. Organic solar cells are seriously affected by the recombination of relatively long-living excitons.

A polymer fulfilling the basic requirements for application in oriented photovoltaic solar cells should possess the following characteristics:

- It should be intrinsically semiconducting and produced with high purity and low defect concentration, in order to prevent trapping, and possess ordered regions in the 100 nm scale to guarantee efficient transport channels of charges.
- It should be grafted with dye molecules possessing high dipolar moments; moreover, these molecules should have good photochemical stability.
- It should possess a high T_g (typically higher than 80 °C). Another solution would be a crosslinkable system, in order to ensure a higher stability of the induced molecular polar order. Indeed, crosslinkable polymers permit the polar molecular orientation to be frozen by the induction of covalent bonds between the chromophore and conjugated backbone after the orientation process.
- It should be easily soluble in common organic solvents, to permit an easy fabrication of thin films of good optical quality and low roughness, avoiding short circuits during electrode deposition. If the surface of a polymer layer is not smooth, the surface of an evaporated electrode will consequently be rough. A rough polymer surface means that there are zones where the thickness of the film is lower than in neighbouring ones. These low-thickness zones may be destroyed during electrode evaporation, which results in short circuits.

Further, as the molecular polar orientation is directly related to the number of oriented molecules, it will also be necessary to optimise the grafting ratio of the polymer matrix in order to obtain the optimal molecular concentration, at which the dipolar interactions (intermolecular interactions) do not hinder the orientation of molecules; typically, a 30% molar concentration in chromophores is chosen. Additionally, its synthesis must exhibit high yields, in order to test the reproducibility of the results in the long term. Furthermore, grafted dye polar molecules should possess very little or no photoinduced molecular movements. This avoids any disorientation following illumination with solar light. The polymer systems described above are uncommon and till now few materials have been investigated in view of their potential applications in ordered photovoltaic devices [5].

In this work, we report the results for two polymer systems grafted with the Disperse Red 1 (DR1) molecules that are intrinsically semiconducting. The optimisation procedure of the induced molecular orientation is presented in view of the potential application of the studied polymers in the fabrication of photovoltaic organic solar cells.

2. Experimental

In previous studies, the DR1-MMA copolymer system has been used [4]. The PMMA polymer matrix is optically inactive and transparent in the visible and near-infrared ranges. DR1-MMA was tested, as the orientation process is very effective in this material. PMMA is not appropriate for photovoltaic applications due to its poor semiconducting properties (very weak currents, in the range of several nA/cm^2). In order to optimise the polymer system and to obtain a maximal photovoltaic device efficiency, we performed preliminary studies on two intrinsically semiconducting polymers grafted with dye polar molecules, namely poly(1-methoxy-4-(*O*-disperse red 1))-2,5-phenylenevinylene) and (poly((3-hexyl)-co-(3-(2-(4-(4'-Nitrophenyl-azo)phenoxy)-ethyl))thiophene. Polar molecular order is induced in the studied materials through the electric field poling method (Corona poling).

We have identified two polymer materials that may be employed in the preparation of plastic photovoltaic devices. The first is the commercially available poly-(1-methoxy-4-(*O*-disperse red 1))-2,5-phenylenevinylene) (DR1-PPV), purchased from Aldrich and tested without any additional purification procedure. Disperse Red 1 (4-(N-(2-hydroxyethyl)-N-ethyl)-amino-4'-nitroazobenzene, or DR1 (with the dipole moment of 7 D), grafted to a polyphenylenevinylene (PPV) matrix, was used as the active polar molecule. DR1-PPV, shown in Fig. 1, is grafted at a 100% molar ratio. Its glass transition temperature T_g, measured by Differential Scanning Calorimetry (Mettler DSC 20 TC 11), was found to be 65 °C. A solution of DR1-PPV in 1,1,2-trichloroethane (15 g/1 l) was first filtered through 0.45 μm and then 0.2 μm PTFE Teflon Millipore filters in order to remove any insoluble parts of the polymer. The solution was then spin-coated onto ITO-coated glass substrates. The thickness of the obtained samples was determined with a Dektak profilometer to be about 48 nm (± 2%). The resulting films were baked in an oven at 60 °C for 30 minutes to remove any residual solvent.

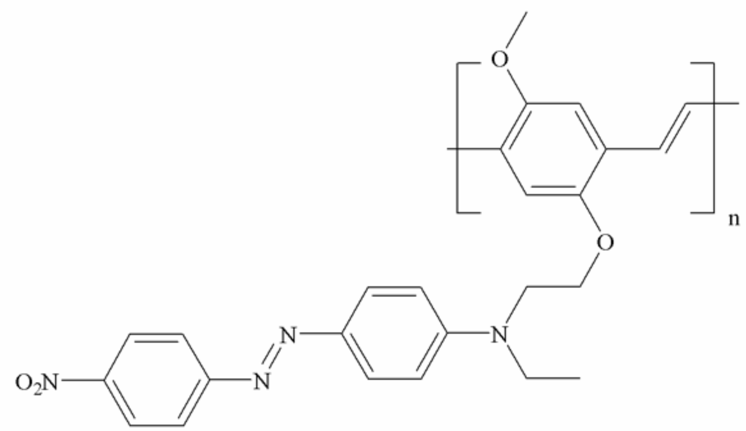

Fig. 1. Chemical structure of poly(1-methoxy-4-(*O*-disperse red 1))-2,5-phenylenevinylene) (DR1-PPV). The polymer matrix is grafted at 100% with the chromophore molecule

The thin films of DR1-PPV were oriented without an upper semitransparent metal electrode. The polymer thin films were oriented under 10 kV (positive charge) for 10 minutes at 60 °C, after which the samples were cooled down to room temperature with the tension still applied in order to freeze the molecular order.

The second polymer system was an azo dye-substituted, solution-processable polythiophene, namely poly((3-hexyl)-co-(3-(2-(4-(4′-Nitrophenyl-azo)phenoxy)ethyl))-thiophene, or PEAHT. The synthesis of the polymer and its characteristics are described elsewhere [7, 8]. The structure of the polythiophene-based copolymer, functionalised with NLO-active chromophoric units, is presented in Fig. 2. The molecular weight of the polymer (M_w) was 44 000, as determined by GPC measurement vs. polystyrene standards. The amount of dye incorporated in the copolymer was equal to the 33% molar ratio. This polymer is easily soluble in common organic solvent due to the presence of flexible alkylic side chains.

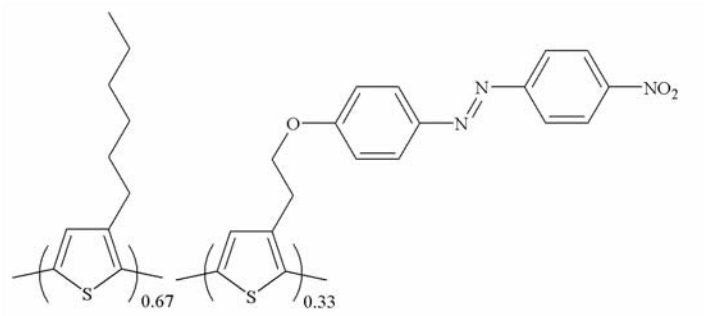

Fig. 2. Chemical structure of the polythiophene copolymer with alkyl side chains, partially functionalised with chromophore groups (PEAHT). The chromophore molar concentration is 33%

T_g of this polymer was estimated to be around 100 °C upon poling evidences, while DSC measurements delivered a value of about 80 °C. This difference may be ascribed to the partial crosslinking occurring during polymer storage (several months), as the tests on this polymer were not performed directly after its synthesis. For the preparation of the device, 33 mg of the PEAHT were dissolved in 1 ml of chloroform ($CHCl_3$). The solution was then filtered through a 0.45 μm filter and spin-coated onto clean ITO substrates. The film thickness, measured with the Dektak profilometer, was 130 nm. The sample was oriented under 6 kV for 15 minutes at 100 °C by Corona poling, in order to test the orientation.

The spin-coating of thin polymer films onto substrates is usually followed by Al electrode deposition by thermal evaporation in vacuo 10^{-6} Torr (20 nm upper semi-transparent aluminium electrode). The resulting device consists of a polymer layer sandwiched between two electrodes (ITO as a bottom one). The active surface of the device was 28 mm^2. The structure of a typical cell fabricated by this procedure is shown in Fig. 3. In complete devices, the polar order is induced through applying the electric field directly to electrodes. Nevertheless, this requires a very precise control of the metal electrode deposition. In our studies, the Corona poling method was used, as it is much easier to realize than orientation through the electrodes of a cell and permits the procedure of orientation itself to be optimised, and to obtain the most stable polar order and largest internal electric field possible.

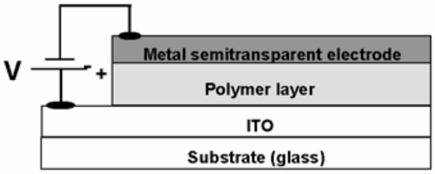

Fig. 3. Side-view of a Schottky type photovoltaic cell sandwich-type structure. The glass substrate is 10 mm thick, the ITO transparent electrode – 150 nm, the organic thin film – around 100 nm, and the semitransparent metal electrode (Al) – 20 nm

Experimentally, the molecular order was controlled using second harmonic generation, as the SH intensity is directly related to the induced dipolar molecules orientation [4]. The samples were always mounted in such a way that the ITO coated glass or glass surface faced directly toward the incident beam. The fundamental IR laser source at 1.064 μm was an actively Q–switched Nd:YAG laser with 25 ps pulses at a 10 Hz repetition rate. The fundamental p-polarized infrared light beam impinged upon the sample at a non-normal incidence angle, passing through the glass substrate and/or the ITO coating and then a polymer layer. The second harmonic signal generated by the sample was detected using a photomultiplier tube (PMT) and integrated by a boxcar. The whole experiment was computer controlled.

3. Results and discussion

The UV-Vis absorption spectra of the studied polymers were taken using a Lambda 19 Perkin-Elmer spectrometer. As can be noticed in Fig. 4 presenting

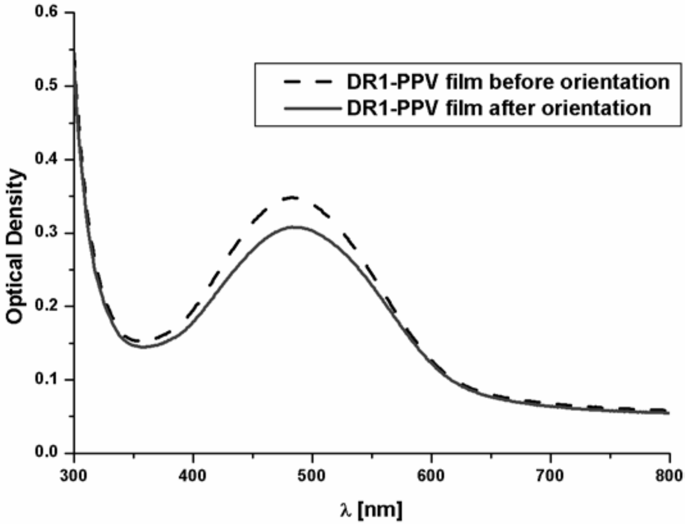

Fig. 4. UV-Vis absorption spectra of the DR1-PPV copolymer before (48 nm thick, dashed line, *OD* at 532 nm equal to 0.28) and after orientation by Corona poling (solid line, *OD* at 532 nm equal to 0.26). The absorption maximum is found at 483 nm (*OD* before and after orientation is 0.35 and 0.30, respectively)

the absorption spectra of DR1-PPV (before and after the polarization process), the optical density decreases after the orientation process. This means that, after the polarization process, a certain number of polar molecules are oriented perpendicular to the polymer surface, making the absorption lower. The maximal orientation degree obtained was 14% (±12%) (calculated as $\Delta OD_{\max}/OD_{\max}$, where $\Delta OD_{\max}$ is the change in optical density after the polarization process at the absorption maximum and $OD_{\max}$ is the optical density at the absorption maximum before orientation). The error of the optical density measurement is equal to 0.02, which is the value obtained from measuring the reference calibrated filters. The orientation degree obtained also seems to be rather low when compared to the value of 30% normally reached by grafted polymers. Due to a grafting ratio of 100%, however, there are problems of steric congestion and the movements of molecules may be hindered by the movements of others.

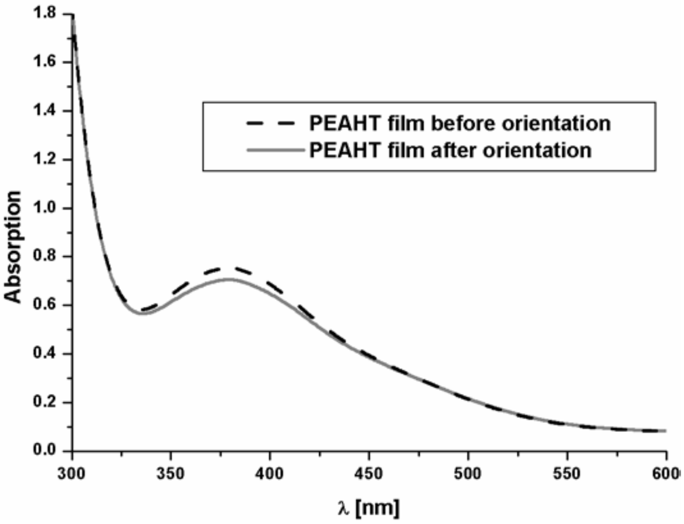

Fig. 5. UV-Vis absorption spectra of the PEAHT polymer film (130 nm thick) (dashed line, *OD* at absorption maximum at 380 nm equal to 0.75) and after orientation by Corona poling (solid line, *OD* at 380 nm equal to 0.70). The optical density at 532 nm almost does not change during the polarization process (*OD* before and after orientation is 0.138 and 0.135, respectively)

The absorption spectra of spin-coated thin films of PEAHT are given in Fig. 5 (before and after orientation, and on glass substrates). The degree of orientation obtained was 7% (±5%). The absorption maximum of the PEAHT polymer was found at 380 nm (*OD* was 0.92), which is typical of the π-π^* transition of the azobenzene moiety in the *trans* isomeric form; the broad band found around 450 nm corresponds to the overlapping of the π-π^* transition of the conjugated polythiophene backbone and the weaker n-π^* transition of the azobenzene group [8]. The error of the optical density measurement was 0.02.

Polythiophenes are very attractive materials in the class of intrinsically semiconducting polymers, because of their good thermal and chemical stability and ease of functionalisation with various chromophores, thus permitting their physical and electronic properties to be engineered [9]. The low ordering degree obtained for this polymer, however, may be attributed to a probable crosslinking of the polymer, which renders it more rigid with respect to non-crosslinked ones, and hence less prone to the poling process.

Second harmonic generation studies were performed for all oriented samples. These measurements are necessary as they permit the exact value of the SH generated signal to be calculated, which is in turn needed to determine the value of the internal field stored in an oriented structure. Moreover, this technique allows for the optimisation of the orientation process itself (the electric voltage applied, the temperature, the poling duration, the cooling conditions, etc.).

SHG in DR1-PPV on ITO and in PEAHT on glass substrates was measured in order to estimate their potential application in photovoltaic organic solar cells. The thermal and photostimulated relaxation of polar orientation was registered. By photostimulated relaxation we understand that an intense monochromatic light induces much faster relaxation than a moderate heating [10]. In both cases, the decay of the SH signal was tested until it disappeared completely due to continuous illumination with an infrared beam and thermal diffusion.

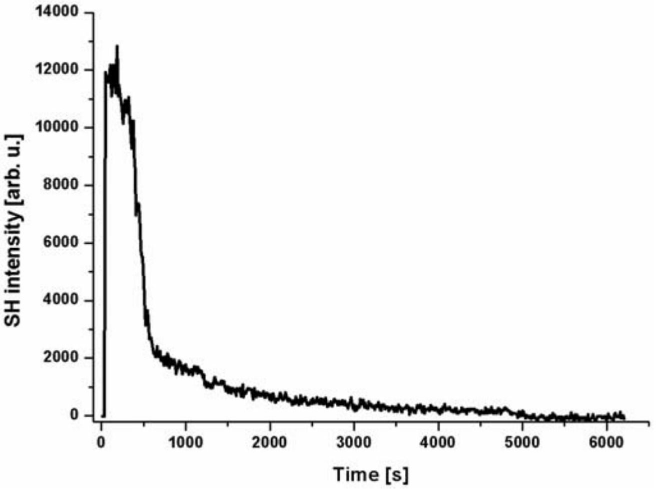

Fig. 6. A study of the temporal decrease of the SH signal generated by DR1-PPV on a glass substrate, oriented by Corona poling. The sample is heated up to 60 °C, starting at ambient temperature with a heating rate of 10 °C/minute. The SH signal decays as the molecular polar order disappears due to thermal diffusion. At the beginning of the measurement, a “zero” level signal is registered, for which there is no sample placed on the heating plate

In Figure 6, we present the decay of the SH signal generated by DR1-PPV. The sample, oriented by Corona poling (10 kV applied for 15 minutes at 60 °C), was cooled to room temperature and then heated up to 60 °C (a heating rate of 10 °C/min) and kept at this temperature. The decay of the SH signal with temperature indicates that the observed decrease in optical density in the absorption spectrum after orientation is due to the molecular ordering induced in the sample.

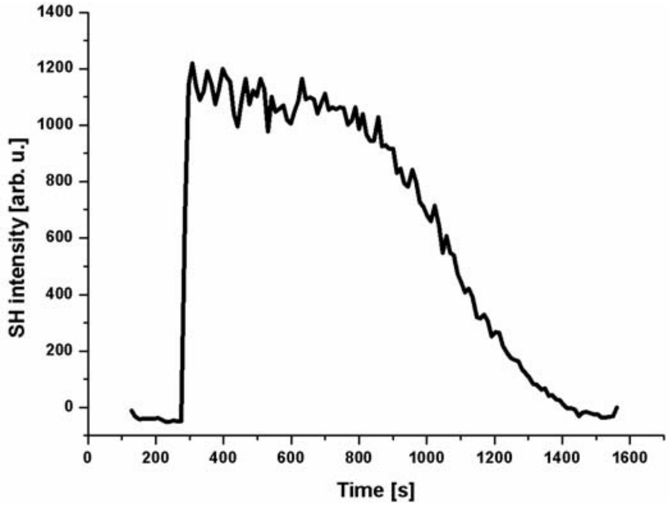

Fig. 7. The decay of the SH signal generated by PEAHT on a glass substrate, oriented by Corona poling. The sample is heated up to 100 °C, starting at ambient temperature with a heating rate of 2.6 °C/minute. The SH signal decreases as the molecular polar order disappears due to thermal diffusion. The "zero" level signal corresponds to no sample on the heating plate

In Figure 7, the decrease of the SH signal generated by PEAHT, heated up to T_g with a heating rate of 2.6 °C/minute and starting from ambient temperature, is shown, after Corona poling (a voltage of + 6 kV applied for 15 minutes at 100°C).

Thermally induced disorientation is at the origin of the decrease in the SH signal for both polymer systems, which permits the conclusion that both materials at least do not deteriorate chemically in a strong electric field. Although the errors of the calculated orientation degrees induced after Corona poling are quite high (several percent), the studies of the decay of the SH signal with temperature prove that the observed decrease in optical density after orientation is due to molecular ordering. Studies of this material are now under way in order to optimise the orientation parameters (the applied temperature and electric field, orientation duration, and cooling conditions), to optimise the internal field stored in the structure, and to realize organic photovoltaic devices.

4. Conclusions

In this paper, we have presented preliminary results of studies on the effects of Corona poling on dipolar dyes covalently attached as side chain substituents to two different conjugated polymers. An evidence for successful poling have been found for both considered polymers, although more work is required for a quantitative evaluation of the poling effectiveness.

Although preliminary, these results are very interesting in view of the potential applications of dye-substituted polymers in the realization of oriented single layer organic photovoltaic solar cells, since they indicate that it could be possible to realize devices that have a large electric field stored in the cell. This would in turn be an advantage in creating local strong electric fields, paving the way for fast exciton splitting on an intramolecular basis.

As an outlook, the main goal now is to optimise the polymeric material itself (i.e. the grafting ratio and glass transition temperature, solubility and processability, etc.) and the device construction conditions (poling conditions, photovoltaic cell structure, electrode choice and evaporation, etc).

Another optimisation process will concern the orientation method itself. Indeed, in semiconducting polymers, charge injection may occur during electric field poling, which reduces the efficiency of the whole process. Moreover, thin polymer films tend to degrade in strong electric fields. Different orientation techniques are therefore being optimised: optically assisted and all-optical polarization methods. The orientation degree attained by all-optical poling should be close to that obtained by Corona poling, since the efficiency of orientation by all-optical poling is the same as that of electric field poling [10].

We believe that the intrinsically semiconducting DR1-PPV and PEAHT polymer systems presented here are good candidates for potential photovoltaic applications.

References

[1] BURROUGHES J.H., BRADLEY D.D.C., BROWN A.R., MARKS R.N., MACKAY K., FRIEND R.H., BURN P.L., HOLMES A.B., Nature, 347 (1990), 539.

[2] GUSTAFSSON G., CAO Y., TREACY G.M., KLAVETTER F., COLANERI N., HEEGER A.J., Nature, 357 (1992), 477.

[3] BRABEC C.J., SARICIFTCI N.S., HUMMELEN J.C., Adv. Funct. Mater., 11 (2001), 1526; HOPPE H., SARICIFTCI N.S., J. Mater. Res., 19 (2004), 1924.

[4] SENTEIN C., FIORINI C., LORIN A., NUNZI J.-M., Adv. Mat., 9 (1997), 809.

[5] SENTEIN C., FIORINI C., LORIN A., NUNZI J.-M., RAIMOND P., SICOT L., Synth. Metals, 102 (1999), 989.

[6] SENTEIN C., FIORINI C., LORIN A., SICOT L., NUNZI J.-M., Optical Materials 9 (1998), 316.

[7] DELLA-CASA C., FRALEONI A., COSTA-BIZZARRI P., LANZI M., Synth. Metals, 124 (2001), 467.

[8] DELLA-CASA C., FRALEONI A., COSTA-BIZZARRI P., LANZI M., PAGANIN L., Macromol. Symp., 180 (2002), 217.

[9] PADINGER F., RITTBERGER R., SARICIFTCI N.S., Adv. Funct. Mat., 13 (2003), 1.

[10] FIORINI C., CHARRA F., NUNZI J.–M., RAIMOND P., J. Opt. Soc. Am. B, 14 (1997), 1984.

Received 20 October 2004
Revised 3 November 2004

Materials Science-Poland, Vol. 22, No. 4, 2004

Synthesis of gold nanoparticles in solid state by thermal decomposition of an organometallic precursor

DOROTA WOSTEK-WOJCIECHOWSKA[1], JEREMIASZ K. JESZKA[1*], PAWEL UZNANSKI[1],
CATHERINE AMIENS[2], BRUNO CHAUDRET[2], PIERRE LECANTE[3]

[1]Centre of Molecular and Macromolecular Studies, Polish Academy of Sciences, 90-364 Łódź, Poland.

[2]Laboratoire de Chimie de Coordination du CNRS 31077 Toulouse Cedex, France

[3]CEMES-CNRS, 29 rue Jeanne Marvig, BP 4347, 31055 Toulouse Cedex, France

Gold nanoparticles were obtained directly in solid polymer films by thermal decomposition of the $[O(Au(PPh_3))_3][BF_4]$ precursor molecularly dispersed in the polymer and by decomposition of microcrystals on different supports. The nanoparticles were characterized with transmission electron microscopy (TEM), scanning electron microscopy (SEM), UV-Vis spectroscopy, and wide-angle X-ray scattering (WAXS). In spite of high precursor concentration, the size of the obtained nanoparticles was similar to those prepared in diluted solutions.

Key words: *metal nanoparticles; polymer nanocomposites; organometallic precursor; TEM; WAXS*

1. Introduction

The synthesis as well as chemical and physical properties of metal and semiconductor nanoparticles (NPs) and nanocomposites are presently of considerable interest due to their potential application in materials science, including molecular electronics. Obtaining polymeric materials containing nanoparticles has been the subject of several studies (e.g. [1–4]). The nanoparticles are usually obtained in a separate process and dispersed in polymers using various methods. The surfaces of nanoparticles are covered by stabilizers screening interactions between the metal and polymer. It is also difficult to obtain a uniform dispersion of NPs in the matrix. The decomposition of organometallic precursors directly in the polymer film should lead to a “clean” metal surface (no strongly bound stabilizer layer between the metal and polymer) and good dispersion without using additional stabilizers.

---

[*] Corresponding author, e-mail: jkjeszka@cbmm.lodz.pl.

There are only a few reports on the preparation of metal particles *in situ* in solid polymer films. Tannenbaum et al. [1] obtained Fe particles by thermolysis and photolysis of carbonyl complexes. Polymer composites with several transition metal nanoclusters were also obtained by decomposing organometallic precursors in phase -separated block copolymers [2, 3].

We have found [5] that different organometallic precursors, e.g. Ru(COD)(COT) (COD – 1,5-cyclooctadiene, COT – 1,3,5-cyclooctatriene), $Co(\eta^3-C_8H_{13})(\eta^4-C_8H_{12})$, $Ni(COD)_2$, and $Rh(allyl)_3$ can be decomposed under dihydrogen yielding small metal nanoparticles also in the solid state. The nanoparticles obtained are only a few nanometers in size, not much more than when the decomposition is carried out in dilute solution.

In this paper, we report the preparation of gold nanoparticles by decomposition of an organometallic precursor dispersed in solid polymer films or as microcrystals. The organometallic complex, μ_3-oxo[tris(triphenylphosphine)gold](1+)tetrafluoroborate(1-) $[O-(Au(PPh_3))_3][BF_4]$, was chosen as the Au atom precursor, because it has been shown to be a good source of Au for NP synthesis in solution, well soluble in many organic solvents, and sufficiently stable to handle in an ambient atmosphere [6].

2. Experimental

$[O(Au(PPh_3))_3][BF_4]$, was synthesized according to [7]. The starting materials used to obtain nanocomposites with gold nanoparticles were polymer films with a dispersed organometallic complex. Poly(methyl methacrylate) (PMMA) (T_g = 115 °C) was used as the stabilizing matrix. The films were prepared by casting toluene (for PMMA) solutions and slowly evaporating the solvent. Initial solutions (4% of the polymer with respect to the solvent) contained the precursor (0.25–15 wt. % of the precursor with respect to the polymer). Two kinds of films were studied: standard free-standing films cast on glass plates (ca. 20 μm thick), which were used for UV-Vis and XRD measurements, and thin films (below 200 nm) prepared by placing a drop of the solution directly on a TEM copper support grid covered with a carbon layer. The decompositions of precursor crystals or thin layers obtained from solution, without the polymer, on TEM grids or on a solid support were also carried out. Samples for SEM were prepared by depositing a drop of the precursor solution or gold NPs in a suitable solvent on a freshly cleaved mica or Si support covered with a 100 nm SiO_2 layer.

Thermal decompositions of the gold precursor were performed in air at 130 °C (above T_g of the polymer). The initially transparent film turns red during the reaction due to absorption by surface plasmons. For comparison, the decomposition was also carried out in a mesitylene solution. The reaction was carried out in air (20 min. at 130 °C). Hexadecylamine was used as the stabilizing agent. Transmission electron microscopy (TEM) and scanning electron microscopy with a field emission gun (SEM-FEG) were used to determine the morphology, particle size, and size distribution. TEM measurements were performed on a JEOL 200 CX (200 kV), SEM measurements on a JEOL JSM 6700F – both at the TEMSCAN facility, Université Paul Sabatier, Toulouse. More than 200 particles were measured in order to draw a size histogram. UV-Vis transmission measurements of standard films with Au NPs were carried out using a Perkin-Elmer Lambda 35 spectrophotometer. Structural characterizations of NPs by wide angle X-ray scattering (WAXS) were performed in the solid state. The polymer film was rolled and measured in air. Measurements of the X-ray intensity scattered by the samples irradiated with graphite-monochromatised molybdenum K_α radiation (0.071069 nm) were performed using a dedicated two-axis diffractometer. Fluorescence of gold was removed in the measurement step by filtering. The data collection time was typically 30 hours for a set of 457 measurements collected at room temperature, in the range of $0° < \theta < 65°$ for equidistant s values [$s = 4\pi(\sin\theta/\lambda)$].

3. Results

Figure 1 shows TEM images of gold NPs obtained by the thermal decomposition of $[O(Au(PPh_3))_3][BF_4]$ in a thin PMMA film for various concentrations of the precursor. It can be seen that for precursor concentrations of 1–2 wt. %, the obtained NPs are small (ca. 5 nm) and uniformly distributed. For higher concentrations, the average size increases and the size distribution is much broader. This is probably caused by the coalescence of small NPs rather than by their continuous growth. At high concentrations, NPs have some tendency to agglomerate in the film and their distribution is not so uniform. The formation of gold nanoparticles gives rise to surface plasmon absorption in the visible range. In Figure 2, we show UV-Vis spectra of nanocomposites prepared by annealing PMMA standard films containing oxonium salt. Increasing the concentration above 2 wt. % of the precursor leads to a red shift of the surface plasmon resonance peak, caused by a change in the distances between NPs (agglomeration) and to some extent by an increase in their size.

Figure 3 shows the reduced radial distribution function (RDF) of Au NPs in a PMMA film (5 wt. % of the metal). The pattern observed is typical of Au NPs of fcc structure, and no distances above 4 nm are observed. The instrument used for WAXS measurements, however, introduces a significant peak broadening. Since the size observed by TEM (ca. 9 nm) is much larger than the related instrumental size limit (ca. 4.5 nm) and no evidence of polycrystallinity has been observed for the NPs, the former is retained as the actual size.

Figures 4 and 5 show SEM micrographs of Au NPs obtained by decomposition of precursor crystals and its layers deposited on a support. In spite of a very high, 100% concentration of the precursor, the size of the nanoparticles is only ca. 10 nm. The kind of support used (mica or Si) does not significantly influence the NP size. Non -uniform distribution of NPs seems to be caused by a inhomogeneous thickness of the initial precursor layer in some places.

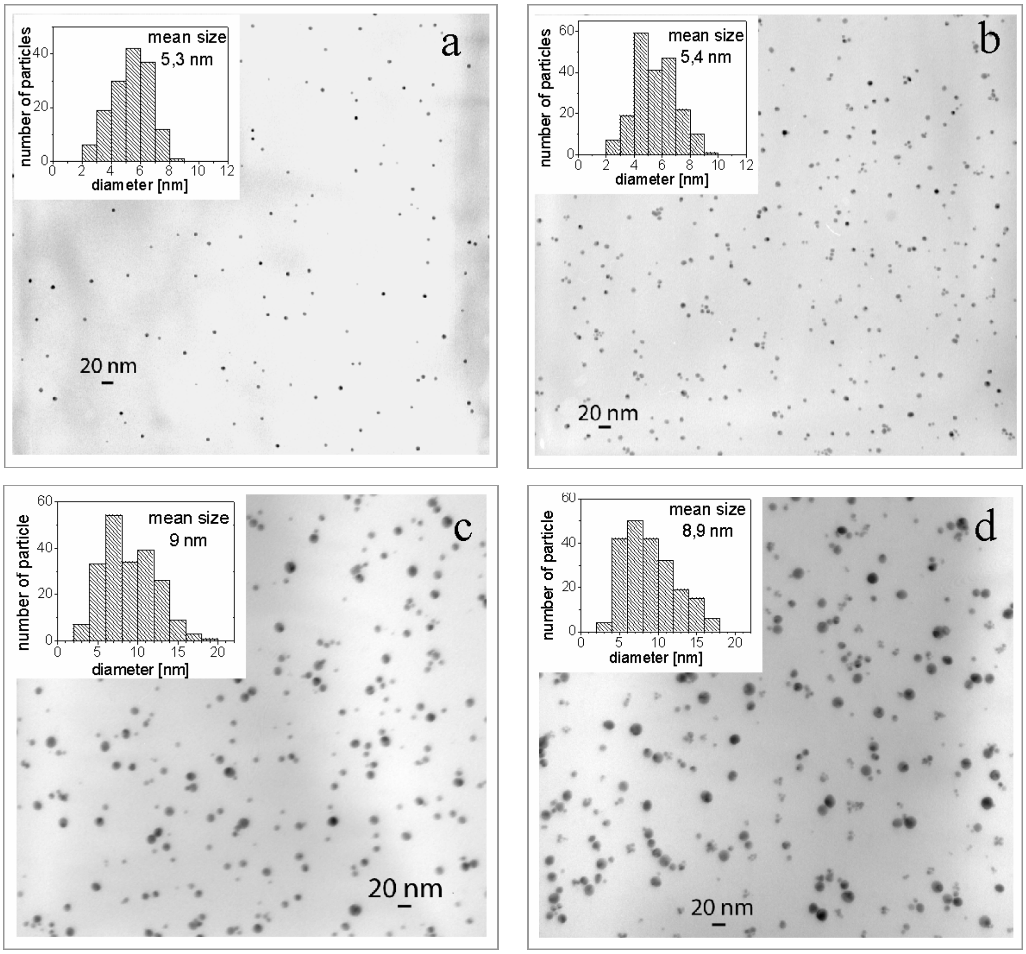

Fig. 1. TEM images of gold NPs obtained by the thermal decomposition of $[O(Au(PPh_3))_3][BF_4]$ dispersed in a thin PMMA film: a) 1%, b) 2%, c) 4%, d) 8wt. % of the precursor. The insets show size distributions

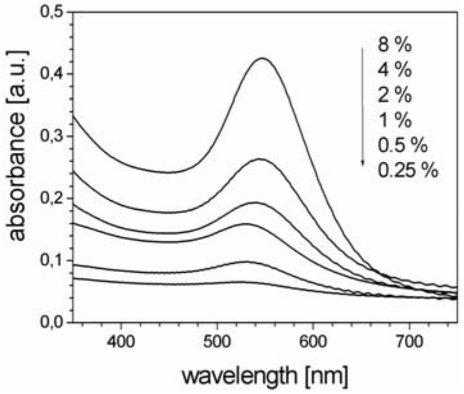

Fig. 2. UV-Vis spectra of gold nanoparticles prepared by annealing of $[O(Au(PPh_3))_3][BF_4]$ dispersed at different concentrations (from 0.25 to 8 wt. %) in PMMA standard films

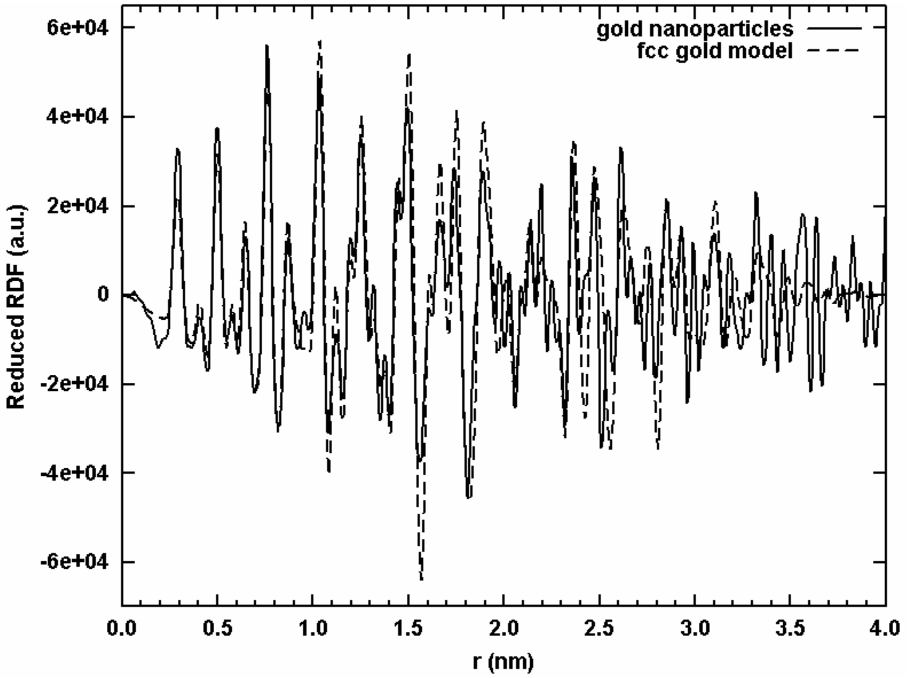

Fig. 3. RDF of Au NPs in PMMA films (5 wt. %),
compared to a computed RDF for a 4 nm fcc structure

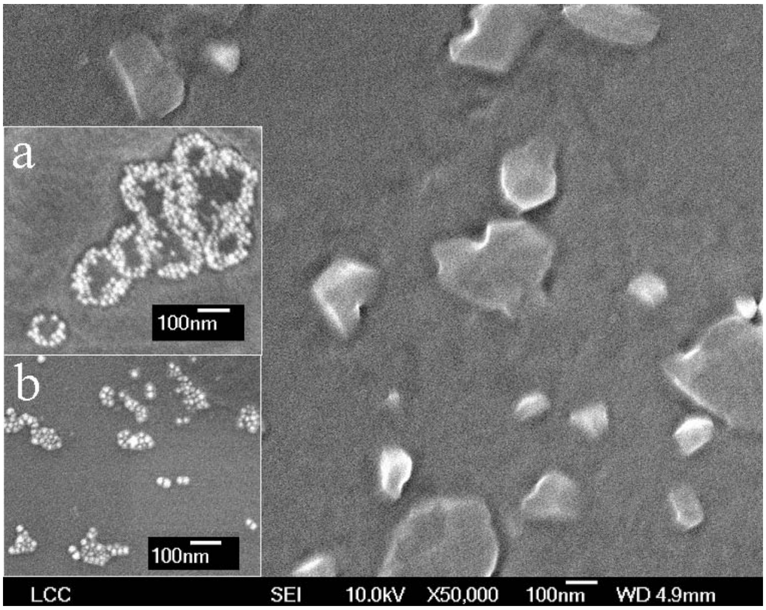

Fig. 4. SEM-FEG images of $[O(Au(PPh_3))_3][BF_4]$ microcrystals deposited on a Si support.
Insets show Au NPs obtained after the decomposition of the crystals (5 min. at 130 °C)

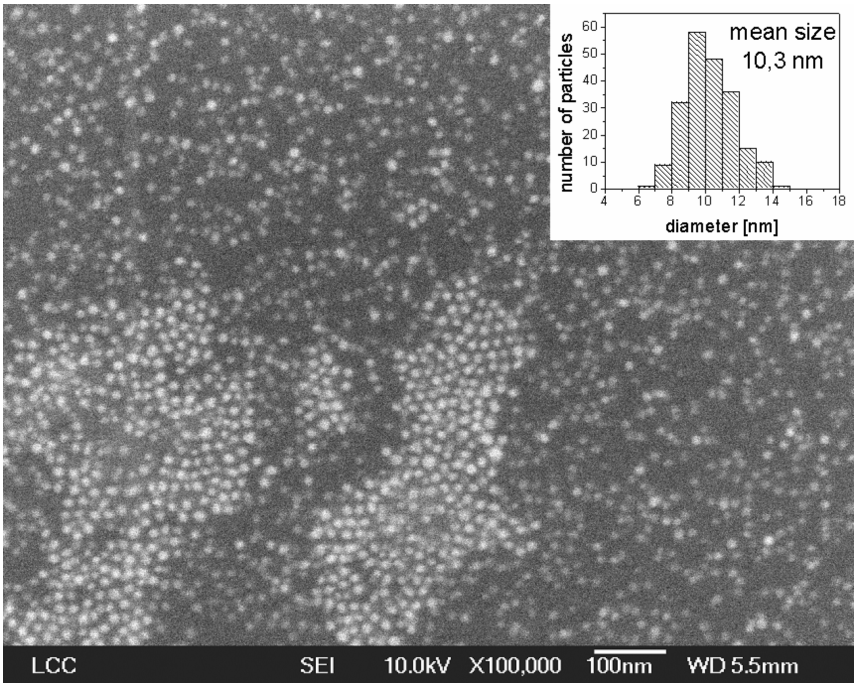

Fig. 5. SEM-FEG images of gold NPs obtained by decomposing (10 min. at 130 °C) a thin layer of $[O(Au(PPh_3))_3][BF_4]$ crystals deposited on a Si support

4. Discussion

Our results show that small metal nanoparticles can be obtained in the solid state not only by hydrogen reduction (described by us in detail elsewhere [5]), but also by thermal decomposition of the $[O(Au(PPh_3))_3][BF_4]$ precursor. The obtained Au NPs are much bigger than those of Ru, Co, and Rh obtained by us previously (ca. 2 nm, obtained, however, below T_g), but they are still only 5 nm in size, even when precursor concentration is very high, up to 100% in the case of precursor crystal or thin layer decomposition. This is interesting in view of the efforts of various groups that use diluted solutions, different stabilizing agents, or “nanoreactors”. It is not surprising that after the decomposition of the precursor in a polymer matrix, metal nanoparticles are formed (in agreement with results obtained by other groups [1–3]) but one could expect the formation of bigger particles by solid precursor decomposition. This result means that the products of precursor decomposition act as stabilizers, preventing the growth of NPs. These results also show that this effect is quite common, as we have observed it for several different precursors and for different metals.

From the point of view of polymer composite preparation, the relatively strong interaction of NPs with the products of precursor decomposition can be a disadvantage, since it means that the decomposition products are difficult to remove from the system and that the polymer may not be in direct contact with the metal. Comparing with the results for the carbonyl precursor decomposition presented in [1], our nanoparticles are several times smaller and more homogeneously dispersed. This can be related to a more homogeneous, probably molecular, distribution of the precursor in the matrix in our case.

5. Conclusions

We have shown that polymer nanocomposites with small metal nanoparticles can be prepared by the decomposition of organometallic precursors dispersed in solid polymer films and even precursor crystals or layers. The obtained NPs have fcc structure, that of bulk gold, with a coherence length of ca. 4 nm. Also, the decomposition of precursor microcrystals and thin layers yields small metal nanoparticles. The obtained nanoparticles were in all cases only a few nanometers big, not much larger than when the decomposition was carried out in dilute solution. The presented method can probably also be used to obtain semiconductor nanoparticles, and it offers new possibilities of preparing materials for molecular electronics.

Acknowledgement

This work was supported in part by EU project DESMOL (contract no. and Marie Curie Training Site fellowship for D.W-W. contract No. HPMT-CT-2001-00398).

References

[1] TANNENBAUM R., GOLDBERG E.P., FLENNIKEN C.L., *Decomposition of iron carbonyls in solid polymer matrices: preparation of novel metal-polymer composite*, [in:] J.E. Sheats, C.E. Carraher Jr, Ch.U. Pittman Jr (Eds.), *Metal-containing polymeric system*, Plenum Press, New York, 1985, p. 303.

[2] ABES J.I, COHEN R.E., ROSS C.A., Mat. Sci. Eng. C, 23 (2003), 641.

[3] CLAY R.T., COHEN R.E., Supramol. Sci., 2 (1995), 183.

[4] POMOGAILO A.D., Russ. Chem. Rev., 66 (1997), 679.

[5] WOSTEK-WOJCIECHOWSKA D., JESZKA J.K., AMIENS C., CHAUDRET B., LECANTE P., J. Coll. Interface Sci., accepted (2005).

[6] BARDAJI M., UZNANSKI P., AMIENS C., CHAUDRET B., LAGUNA A., Chem. Comm., (2002), 598.

[7] BRUCE M.I., NICHOLSON B.K., BIN SHAWKATALY O., Inorganic Synthesis, 26 (1989), 324.

Received 14 September 2004
Revised 13 October 2004

Materials Science-Poland, Vol. 22, No. 4, 2004

Zone casting – a universal method of preparing oriented anisotropic layers of organic materials

ADAM TRACZ[1*], TADEUSZ PAKULA[2], JEREMIASZ K. JESZKA[1]

[1]Centre of Molecular and Macromolecular Studies, Polish Academy of Sciences,
ul. Sienkiewicza 112, 90-364 Łódź, Poland

[2]Max-Planck-Institute for Polymer Research, Mainz, Germany

A method for the preparation of oriented, anisotropic layers of soluble molecular materials on substrates that were not pre-oriented (so-called zone casting) is presented. The method consists in casting a suitable solution, continuously supplied by a nozzle, onto a moving substrate. Solvent evaporation takes place from the surface of the meniscus formed between a special flat nozzle and the substrate. Due to a gradient of the solute concentration, its solidification proceeds in a narrow zone under highly anisotropic conditions. The conditions of stationary deposition and the influence of various parameters on the process, such as casting speed, the diffusion coefficient, evaporation rate, are discussed. It is shown that the zone casting can be used to obtain anisotropic layers of many different low-molecular-weight and macromolecular materials.

Key words: *zone casting; solution processing; orientation; anisotropy*

1. Introduction

Physical properties of organic molecules exhibiting interesting electrical and optical properties are usually highly anisotropic. Therefore, the preparation of materials in which molecules are appropriately arranged is of a great importance. Obtaining sufficiently large single crystals is usually very difficult or impossible. Anisotropic layers of organic materials of distinctive properties in the direction perpendicular to the substrate surface can be obtained by some methods, e.g. by the Langmuir–Blodgett technique or, to some extent, by vacuum deposition. It is more difficult to achieve good orientation in the direction parallel to the substrate, which can be obtained by mechanical deformation or by solution casting on pre-oriented substrates. In this communication, we present an alternative method of preparing oriented anisotropic layers

---

[*] Corresponding author, e-mail: atracz@cbmm.lodz.pl.

of molecular materials (which can be solution-processed) on substrates not having been pre-oriented. The conditions of stationary deposition in the zone casting method, developed in the Centre of Molecular and Macromolecular Studies of the Polish Academy of Sciences [1–4], are discussed and examples of applications for different classes of materials are presented.

2. Description of the technique

Zone casting consists in the deposition of a material from solution on a moving substrate. The casting process is schematically presented in Fig. 1.

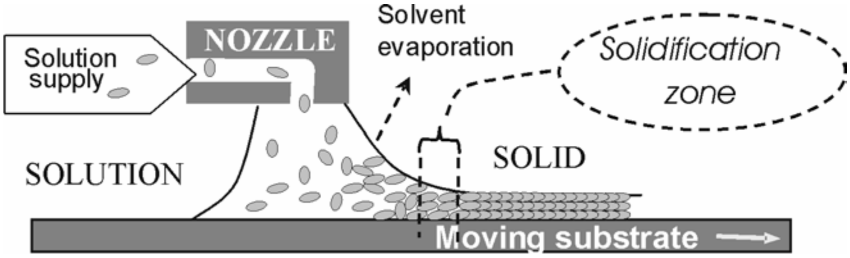

Fig. 1. Schematic presentation of the zone casting technique

The solution is continuously supplied to the evaporation zone by a flat nozzle. The solvent evaporates from the meniscus zone and the solute is deposited on the moving substrate. The solution supply rate, substrate velocity, initial solute concentration, solvent evaporation rate, and crystallisation rate must be chosen properly to obtain stationary conditions. The last two parameters can be controlled by a choice of the solvent and casting temperature.

3. Evaporation zone stability conditions

The profile of the evaporation zone is determined by the casting speed, evaporation rate, and the contact angle of the solution on the substrate (or on the deposited solid layer, especially for low molecular weight materials). The meniscus shape is stable if the volume of the solvent evaporated in a time dt equals the volume of the solution supplied to the nozzle. To a first approximation, assuming a triangular meniscus, we have

$$Sdx = \frac{V_e S}{\rho \sin\theta} dt \tag{1}$$

where V_e is the evaporation rate [kg/(m^2·sec)], ρ is the solvent density, θ is the contact angle which depends on surface tension, the kind of substrate, and the casting speed, and S is the nozzle cross-section; $S = hl$, where h denotes the nozzle height and l the width of the deposition zone.

The casting speed $v_s = dx/dt$ is thus related to the evaporation rate and contact angle:

$$v_s = \frac{V_e}{\rho \sin \Theta} \tag{2}$$

The contact angle cannot change too much (otherwise the solution/substrate contact is broken and the process is no longer stationary but step-wise). Therefore, the casting speed cannot be changed too much unless the evaporation rate is changed, for example by changing the casting temperature.

4. Phase separation conditions

The driving force of the orientation and anisotropy of the layer being formed is the solute concentration gradient in the region where the critical concentration is reached. The concentration profile depends on the relation between the solution supply rate, diffusion coefficient, and evaporation rate. Due to solvent evaporation, the solute concentration is not uniform in the evaporation zone. It increases from the initial concentration in the nozzle, in the casting direction, until the critical concentration for phase separation is reached.

The concentration profile depends on the relation between the evaporation rate and solute diffusion coefficient D. The critical concentration can be reached in different zones of the meniscus, and the direction of the concentration gradient can be different depending on the relationship between these parameters. Figure 2 presents the results of simulations of the solute concentration profile for two different ratios of the casting rate and diffusion coefficient, namely for $k = 10^4$ and 10^5. The simulation parameters were chosen arbitrarily, but were close to the range covered in the experiment (e.g., $D = 10^{-9}$ m^2/sec and a casting speed $v_s = 10^{-5}$ m/sec). The concentration dependence of D is neglected. The black region can be considered to be the region where the critical concentration is reached and phase separation takes place. One can see that for high k the concentration gradient is low and parallel to the casting direction. The critical concentration is reached close to the end of the evaporation zone. Orientation in the obtained layer is parallel to the casting direction. For larger k, the concentration gradient is high, but perpendicular to the solvent surface and not to the casting direction. The critical concentration is reached far from the end of the evaporation zone. Orientation in the layer obtained under such conditions (if the layer has any important anisotropy) is perpendicular to the surface.

A suitable choice of the parameters, in order to obtain a proper concentration gradient, is a necessary but not sufficient condition to obtain a continuous layer, since the casting speed must also match the crystallisation rate (or more generally, the phase separation rate).

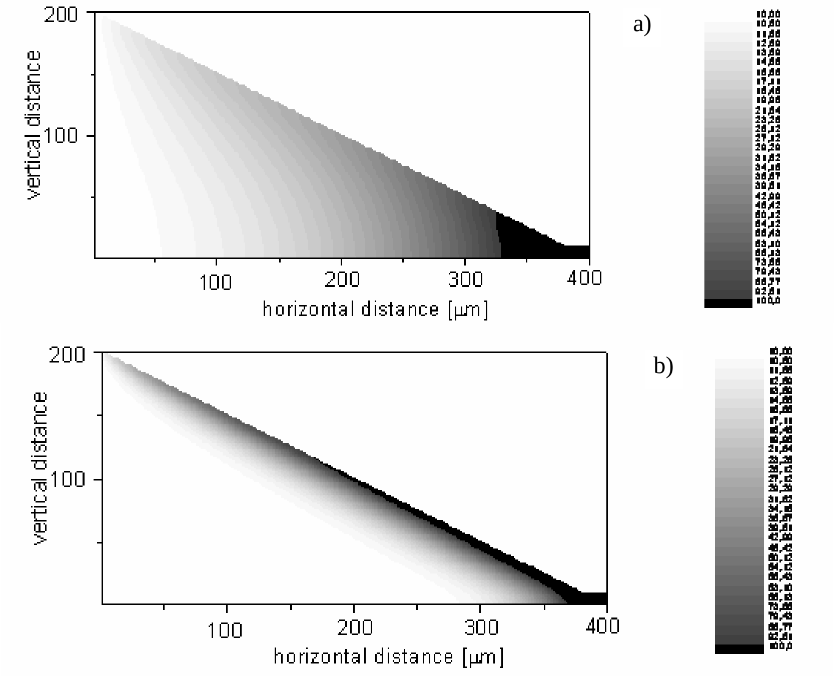

Fig. 2. Simulated solute concentration profile near the end of the evaporation zone for a slow and fast casting rate, relative to the diffusion coefficient $k = 10^4$ (a) and $k = 10^5$ (b)

5. Equipment

Figure 3 shows the zone casting equipment constructed at our laboratory. It consists of two heating blocks mounted on a metal substrate. The upper block houses a syringe used to continuously supply the solution to the nozzle. The substrate, on

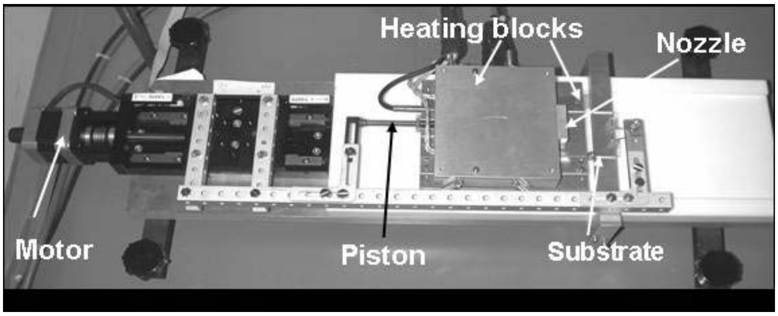

Fig. 3. Zone casting equipment

which the film is cast, is moved on the surface of the lower block. A step motor is used to move the piston in the syringe and the substrate. In other versions, a second motor drives the substrate independently. Temperatures and velocities are controlled electronically.

6. Selected applications

The first reported application of the zone casting technique was a successful preparation of anisotropic polymer/organic metal composites [1–5]. Highly oriented networks, micro- or nanowires of the molecular metal tetrathiotetracene-tetracyanoquinodimethane (TTT-TCNQ), embedded in a polymer matrix, were obtained (Fig. 4).

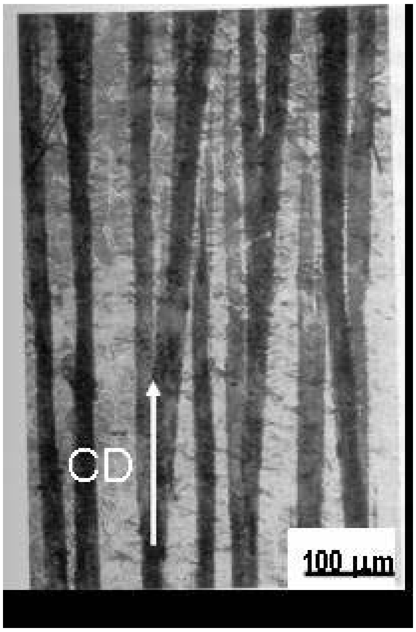

Fig. 4. Highly oriented network of TTT-TCNQ microcrystals in a polypropylene matrix. The arrow shows the casting direction (see [3] for details)

The systems exhibit a very high anisotropy of electrical conductivity (10^6) [1–4]. TTT-TCNQ networks in polypropylene (PP) also show a high anisotropy of optical properties, which allows the excitations that have transitions in the direction perpendicular and parallel to the long axis of the crystal to be identified [5]. Recently, oriented anisotropic thin layers of a discotic compound hexabenzocoronene derivative (HBC-C_{12}) of good quality have been obtained [6, 7]. They have good orientation on an area of square centimetres, with a highly ordered columnar structure and large coherence length, as evidenced by atomic force microscopy images (Fig. 5). Such layers have been shown to act as optical molecular switches [8] and active layers in organic field effect transistors [9, 10]. Other discotic compounds of perylene and HBC derivatives have also been used, and it has been shown that such layers have highly anisotropic optoelectric properties [7, 10]. Preliminary results have also been obtained for other low molecular-weight materials. Highly optically anisotropic thin layers of metallorganic dyes on glass have been obtained, in which the orientation in the obtained layer and the orientation of the optical axes is parallel to the casting direction (in cooperation with A. Pucci, F. Ciardelli, Universiti di Pisa, Dipartimentà di Chimica e Chimica Industriale, Italy).

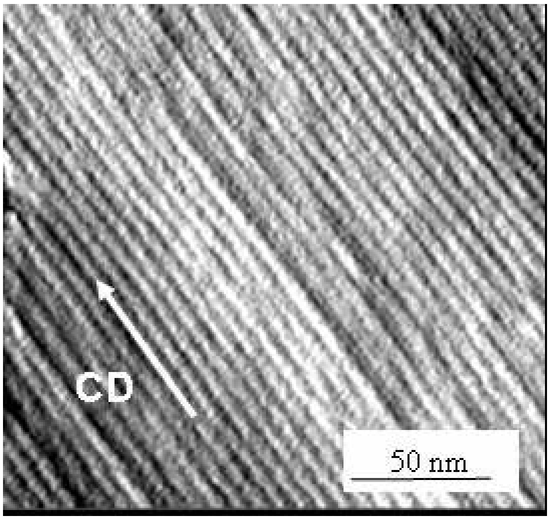

Fig. 5. AFM image of the columnar structure of a zone-cast film of HBC-C_{12}.
The arrow shows the casting direction (see [6] for details)

Very recently, we have found that the ZC technique can also be applied to obtain orientation in another class of materials – block copolymers. Phase separation in diblock copolymers leads to the formation of various morphological structures (cylinders, spheres, etc.), depending on block length and external conditions. We were able to obtain thin layers of highly oriented cylinders (in cooperation with T. Kowalewski and K. Matyjaszewski, Carnegie Mellon University, Pittsburgh PA, USA). An interesting feature of this system is that the long axis of the cylinders is oriented perpendicular to the casting direction (Fig. 6).

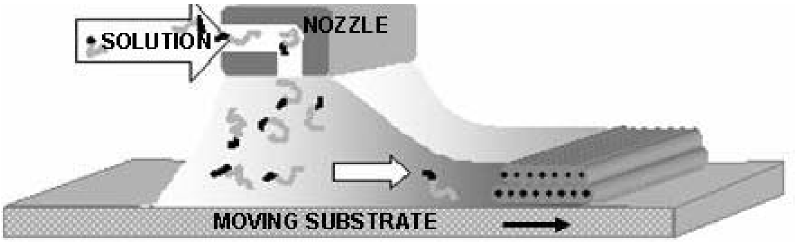

Fig. 6. The formation of the ordered cylinder morphology
of a diblock copolymer zone-cast film

7. Conclusions

Zone casting makes possible a continuous deposition of anisotropic layers of soluble materials. For each compound, stationary deposition conditions must be determined by choosing a proper solvent, initial concentration, and adjusting casting parameters such as temperature and casting speed. Under the appropriate conditions, the zone-cast films that are uniform in the centimetre scale and exhibit highly anisotropic macroscopic properties can be obtained for many compounds. The presented examples of different zone-cast materials (low molecular-weight conductors, discotic molecules, oligomers, and copolymers), which can be successfully processed using zone-casting, demonstrate the universality of this technique.

Acknowledgement

The work was supported in part by the State Committee for Scientific (KBN) project T08E 044 23 (2002–2005) and by the Fifth Framework Programme DESMOL (ICA1-CT-2000-70021).

References

[1] TRACZ A., ULAŃSKI J., PAKULA T., KRYSZEWSKI M., Polish Patent P-131986 (1986).

[2] BURDA L., TRACZ A., PAKULA T., ULANSKI J., KRYSZEWSKI M., J. Phys. D: Appl. Phys., 16 (1983), 1737.

[3] TRACZ A., EL SHAFEE E., ULANSKI J., JESZKA J.K., KRYSZEWSKI M., Mater. Sci., 14 (1988), 181.

[4] TRACZ A., EL SHAFEE E., ULANSKI J., JESZKA J.K., KRYSZEWSKI M., [in:] H. Kutzmany, M. Mehring, S. Roth (Eds.), *Electronic Properties of Conjugated Polymers*, Springer-Verlag, Berlin, 1989, p. 442–447.

[5] TRACZ A., EL SHAFEE E., ULANSKI J., JESZKA J.K., KRYSZEWSKI M., Synth. Met., 37 (1990), 175.

[6] TRACZ A., JESZKA J.K., WATSON M.D., PISULA W., MÜLLEN K., PAKULA T., J. Am. Chem. Soc., 125 (2003), 1682.

[7] MISKIEWICZ P., RYBAK A., JUNG J., GLOWACKI I., ULANSKI J., GEERTS Y., WATSON M., MÜLLEN K., Synth. Met., 137 (2003), 905.

[8] PIRIS J., PISULA W., TRACZ A., PAKULA T., MÜLLEN K., WARMAN J.M., Liq. Cryst., 31 (2004), 993.

[9] PISULA W., MENON A., STEPPUTAT M., LIEBERWIRTH I., KOLB U., TRACZ A., PAKULA T., MÜLLEN K., Adv. Mater., accepted)2005).

[10] MIŚKIEWICZ P., RYBAK A., JUNG J., GLOWACKI I., ULAŃSKI J., TRACZ A., PISULA W., PAKULA T., MÜLLEN K., PFLEGER J., Conference on New Concepts and Materials for Molecular Electronics and Nanotechnology, Poznań 2004, Conf. Abstracts, p. 20.

Received 20 October 2004
Revised 3 November 2004

Materials Science-Poland, Vol. 22, No. 4, 2004

Scaling organic transistors: materials and design

GERNOT PAASCH[1*], SUSANNE SCHEINERT[2]

[1]Leibniz Institute for Solid State and Materials Research IFW Dresden, D-01171 Dresden, Germany

[2]Ilmenau Technical University, D-98684 Ilmenau, Germany

Envisaged applications of organic thin-film transistors in future polymer electronics lead to requirements on the supply voltage, threshold voltage, subthreshold characteristics, on-off ratio, and cut-off frequency. We present an analysis of the corresponding requirements using both analytical estimates and numerical two-dimensional simulations. Of special importance are the connections between cut-off frequency, channel length and mobility, mobility and doping, thicknesses of the active layer and gate insulator, doping, interface charges and states, and threshold voltage, traps and subthreshold slope. They lead to demands on both material properties and transistor design. Considering a minimum application-relevant cut-off frequency and a limitation of the mobility for low-cost solution-based deposition, one is led inevitably to the need of a submicrometer channel length and rather thin organic gate insulator. Experimental realization is shown and an approach to submicrometer organic CMOS is discussed.

Key words: *polymer electronics; transistor; organics; scaling*

1. Introduction

Novel polymer (or "plastic") electronics is expected to present its first commercial products within the next few years. Possible applications, such as electronic watermarks, E-paper, replacements of the barcode, and smart cards, are generally characterized as low-performance and low-cost in a region where silicon technology will not be competitive. As an additional special feature, the new circuits should be flexible. One vision is a large scale printing of such circuits. It was only about twenty years ago that scaling down became a decisive issue in microelectronics, when the feature length, especially the channel length of MOS transistors, was reduced below one micrometer. That development was connected to Moore's law describing the transition to higher packaging and increased speed [1]. For the development of polymer electronics based on organic field-effect transistors (OFETs), in spite of encouraging demonstrations of different applica-

---

[*] Corresponding author, e-mail: g.paasch@ifw-dresden.de.

tions [2–4], there is actually a barrier for overcoming the minimum requirements for successful mass applications: scaling down of present OFETs is a *precondition*, even for the introduction of polymer electronics. In this article, the scaling of OFETs is outlined, based on analytical estimates and numerical simulations [5].

2. Analytical estimates

To begin with, some basic requirements should be mentioned. OFETs should operate at voltages less than 10 V. Correspondingly, a threshold voltage of only few volts and of the same polarity as the gate voltage (negative for a p-channel device) is needed (otherwise additional circuitry is required), connected with a subthreshold swing less than several hundred mV/dec. Thereby an on-off ratio of the current larger than 10^4 must be realized. The cut-off frequency (at which the voltage gain is reduced to unity) should be larger than 100 kHz.

The design and material parameters of OFETs are closely related. Most suitable polymers are thus unintentionally p-doped, source and drain are made from metals, and it is believed that inversion is hardly achievable. Therefore, thin-film transistors are used, which operate with an accumulation channel in the on-state. As a consequence, the off-state with depletion, and also clear saturation with depletion at drain, require a layer thickness d less than the depletion length l_{dep}, which in turn depends on the doping level ($l_{\mathrm{dep}} = [2\varepsilon\varepsilon_0|2\varphi_b|/eN_A]^{1/2}$, where $\varphi_b < 0$ is the bulk potential for the *p*-material, and N_A is the density of ionized acceptors). For poly(phenylene-vinylene) (PPV) and poly(3-alkyl thiophene) (P3AT), one has $l_{\mathrm{dep}} \approx 240$ nm up to 24 nm for doping levels from 10^{16} down to 10^{18} cm^{-3}. For high doping levels it becomes important to prepare layers in the 50 nm range and with small roughness compared to thickness.

The next important quantity is the threshold voltage, which is given for $d < l_{\mathrm{dep}}$ by

$$V_{\mathrm{th}} = V_{\mathrm{FB}} + \frac{eN_A d}{C''_{ox}} - 2\varphi_b \left(\frac{d}{l_{\mathrm{dep}}} \right)^2 \tag{1}$$

where V_{FB} is the flat band voltage and $C''_{ox} = \varepsilon_0 \varepsilon_{ox} / d_{ox}$ is the gate insulator capacitance per a unit area. Only the first term is negative when a low-work function gate is chosen. The second term, in particular, contributes high positive values in the unwanted direction for high doping. The main dependences are demonstrated in Fig. 1 (parameters: 2 eV gap of the active layer, $\varepsilon = 3.24$, affinity 3 eV, gate work function 5 eV, $\varepsilon_{ox} = 2.56$ for the organic insulator, $V_{\mathrm{FB}} = 1\ \mathrm{V} + \varphi_{\mathrm{b}}$). According to Fig. 1a, the threshold voltage is sufficiently low for the considered layer thicknesses only at low and moderate doping ($<10^{16}$–10^{17} cm^{-3}). For higher doping (Fig. 1b), a strong increase in the threshold voltage can be prevented only by choosing both a thin insulator and a thin active layer. Indeed, for all-polymer circuits the most stringent requirement concerns the rather thin organic gate insulator. In addition, a shift in threshold voltage can result from a flat band voltage shift caused by charges at the interface (areal charge Q''_{if}) between the active layer and gate insulator, according to

$$V_{FB} = \Delta\Phi_{MS} - \frac{Q''_{if}}{C''_{ox}} = \Delta\Phi_{MS} - \frac{eN''_{if}d_{ox}}{\varepsilon_0\varepsilon_{ox}} \tag{2}$$

where $\Delta\Phi_{MS}$ is the gate-semiconductor work function difference. Such interface charges can occur unintentionally. For $N''_{if} = 10^{12}\,\mathrm{cm}^{-2}$ and $\varepsilon_{ox} = 3$, the flat band voltage is shifted by 3 V (18 V) for a gate insulator thickness of 50 nm (300 nm), again showing the importance of a thin organic insulator. In principle, by introducing such a charged layer, one can shift the threshold voltage in the needed direction.

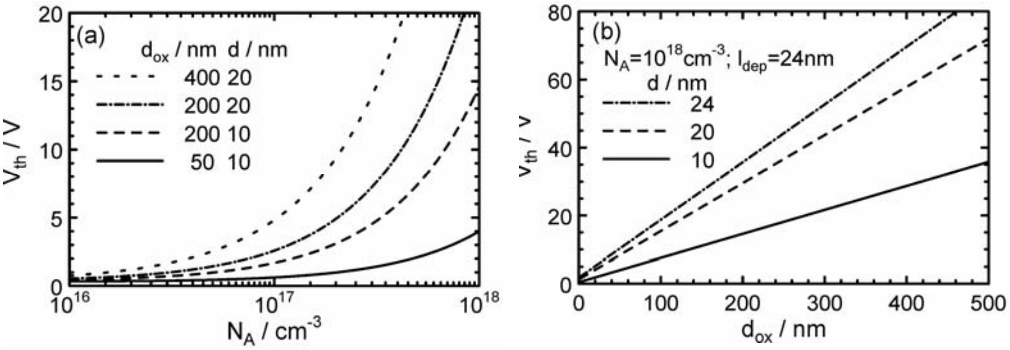

Fig. 1. Dependence of the threshold voltage in Eq. (1) on doping (a) and on gate insulator thickness (b) for the indicated parameters

For low-voltage transistor operation, the inverse subthreshold slope $S = \partial V_{GS}/\partial \lg(I_D)$, [A] must be as low as possible. At room temperature, its minimum value is 60 mV/dec, whereas experimental values for OFETs are often several V/dec, which is rather large. Actually, recharging the capacitances of the depletion layer and interface traps leads to higher values, according to

$$S = \frac{k_B T}{e}\ln 10\left(1 + \frac{C_{\mathrm{dep}} + C_{it}}{C_{ox}}\right) \tag{3}$$

Bulk traps contribute to the depletion capacitance. For the trap-free case in a thin layer, the layer is depleted and one would have the ideal minimum value. Bulk and interface traps in the thin layer thus cause a deviation from the ideal minimum value. Corresponding numerical simulations will be shown below.

Most important for scaling OFETs is the cut-off frequency $f_0 = g_m/(2\pi C_{GS})$, which is determined by the maximum transconductance g_m and the gate-source capacitance C_{GS}, which is larger than the gate insulator capacitance due to overlap capacitances.

An upper limit for the cut-off frequency is obtained from the simplest approximation for the drain current of a transistor with channel length L and width w

$$f_0 \leq \frac{1}{2\pi} \frac{g_m}{C''_{ox} wL} = \frac{\mu}{2\pi L^2} V_{GS,\mathrm{eff}} \tag{4}$$

where $V_{GS,\mathrm{eff}}$ is the gate voltage relative to threshold, for drain voltage $V_{DS} = V_{GS,\mathrm{eff}}$ pinch-off occurs and the transconductance has its maximum. The channel width cancels out in Eq. (4). For a given low operation voltage (e.g., $V_{GS,\mathrm{eff}} = 10$ V) and sufficiently large f_0 (100 kHz, 1MHz, 10MHz) one gets from Eq. (4) the required upper limit for the channel length as a function of the mobility of the active layer, as demonstrated in Fig. 2. Thus, for the mobility $\mu = 0.01$ cm^2·V^{-1}·s^{-1} (which seems to be achievable in low-cost solution deposition) and the lowest cut-off frequency, the upper limit for the channel length is already as small as 3 μm. Practically, one must expect that only submicrometer channel lengths will lead to the needed operation speed. Now another problem occurs: one must take care to avoid short-channel effects for such devices. These can be analyzed only by two-dimensional simulations.

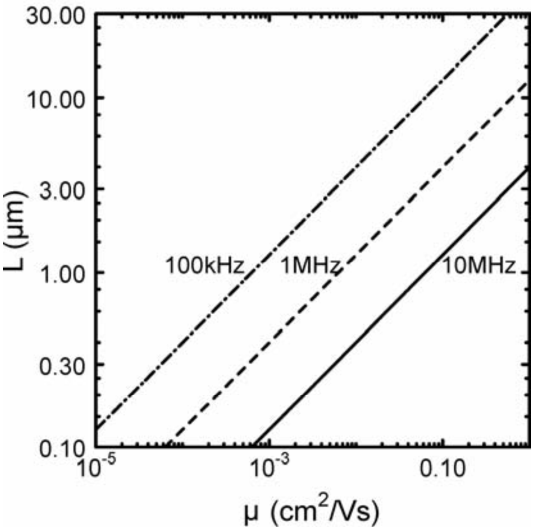

Fig. 2. Channel length as function of mobility, according to Eq. (4), which for a given effective voltage of 10 V leads to three different cut-off frequencies, namely 100 kHz, 1 MHz and 10 kMHz

3. Simulation of short-channel effects

As already discussed, down-scaling also concerns the gate insulator thickness, in order to enable operation at low voltage with an appropriate threshold voltage and reduced influence of possible interface charges. In addition, a thin gate insulator is needed to avoid short-channel effects. Since in a field-effect transistor the perpendicular field creating the accumulation channel must be much larger than the longitudinal field driving the current in the channel, the gate oxide thickness must be much smaller than the channel length. From experience in microelectronics, one expects roughly the condition $d_{ox} < L/10$. Detailed information, however, requires two-dimensional simulations. They have been carried out by us in advance, before preparing short channel transistors. The method and standard parameters are described in the appropriate references [6, 7]. In the simulations the prepared device is modelled (see the cross section in Fig. 5).

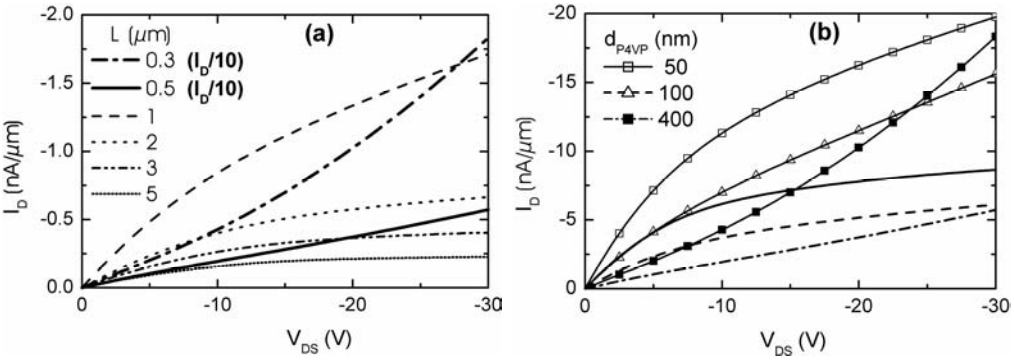

Fig. 3. Simulated output characteristics (current per unit channel width) for a 10 V gate-source voltage: a) for a 400 nm thick P4VP gate insulator the channel length is varied as indicated; b) for the two channel lengths 0,5 μm (lines) and 0,3 μm (with symbols), gate insulator thickness is varied. Other parameters: p-doping 10^{17} cm^{-3} of the 30 nm P3OT layer, mobility $\mu = 10^{-3}$ cm^2/(V·s)

In Figure 3a, the thickness of the organic insulator (poly-4-vinylphenol, P4VP) is 400 nm, as large as is practically realizable, in order to prevent leakage current. The output characteristics show saturation only for a channel length larger than 1 μm and a large supralinear current for shorter channels. Simulated field and concentration profiles prove that this is a short channel effect, due to drain-induced barrier lowering indeed caused by the decreasing ratio of transversal and longitudinal electric fields. A reduction of insulator thickness down to 50 nm for devices with 0.5 μm and 0.3 μm channel lengths reduces this effect, as shown in Fig. 3b. Such organic insulators are not yet available. Therefore, short-channel OFETs should be fabricated at present with a hybrid structure, in which the gate insulator is a thin (e.g. 30 nm) silicon dioxide layer on a n^+-silicon wafer that serves as the gate electrode. An example is given below.

4. Trap recharging and inverse subthreshold slope

In contrast to the ideal low value of the inverse subthreshold slope (Eq. (3)) and its need for the low voltage operation of organic transistors, one is usually confronted with rather large values [6, 8, 9]. An example is demonstrated in Fig. 4 [6] for a transistor with organics in the insulator and active layer. The source/drain contacts are deposited as finger structures on an organic substrate (poly(ethylenetherephthalate)), PET; channel length and width are $L = 2$ μm and $w = 10$ mm, respectively. Then the active layer, the organic insulator, and gate are deposited. The active layer (30 nm) is made from regioregular poly(3-dodecylthiophene) (P3DDT), and the gate insulator (500 nm) from poly(4-vinylphenol) (P4VP). For this device, the peculiarities in the subthreshold region have been described in detail in [6, 10], and a few main results will be summarized here. The transistor turns on (Fig. 4a) close to a threshold voltage of $V_{th} = 0$ V, indicating that the layer is fully depleted at positive gate voltages. Consequently, the maximum possible value of the doping concentration is $N_A \approx 6\times10^{17}$ cm^{-3}. The mobility estimated from the linear region of the transfer characteristics of Fig. 4a is $\mu_p = 5\times10^{-3}$ cm^2/(V·s) for drain voltages of –5 V and –10 V, and $\mu_p = 2\times10^{-3}$ cm^2/(V·s) for –1 V. The inverse subthreshold slope, estimated from the transfer curves in the logarithmic scale, is very large. For $V_{DS} = -1$ V one has $S = 7.7$ V/dec. Moreover, the subthreshold current depends on the drain voltage. This feature is usually considered to be a short channel effect, not expected for the investigated long channel device. To clarify the origin of such peculiarities, numerical two-dimensional simulations have been carried out. Thereby the mobilities, as determined from experimental data, have been used, along with the following parameters: static dielectric constants of both materials, $\varepsilon_{ox} = 2.56$ for P4VP and $\varepsilon = 3.24$ for P3DDT, a monomer density of 10^{21} cm^{-3}, and a work function of the gate, drain, and source electrodes (Au) of 5.0 eV.

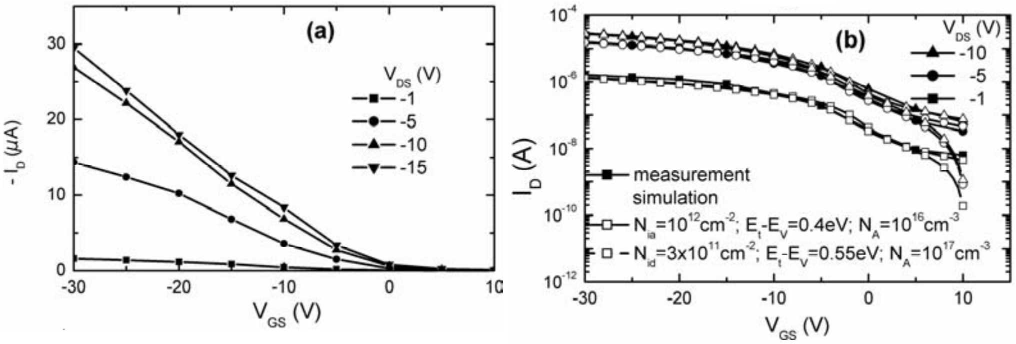

Fig. 4. Measured transfer characteristics of a thin film transistor with $w/L = 5000$, $L = 2$ μm (a); comparison of the measured and simulated transfer characteristics in a logarithmic scale for different drain voltages (b). Parameters for the acceptor-like or donor-like interface states are indicated in the figure

In the first step, the doping concentration was varied. According to Eqs. (1) and (2), the threshold voltage and hence all transfer characteristics are determined not only by doping, but also by fixed interface states. Above the threshold voltage the curves measured are well described by simulations with either $N_A = 10^{16}$ cm^{-3} without fixed interface states or with a higher doping concentration and positive interface charge. However, there is a large difference in the subthreshold region between the measured and simulated characteristics. Whereas the measured curve has the mentioned large inverse subthreshold slope, the simulation yields $S \approx 0.2$ V/dec. Furthermore, in contrast to the measurement, the simulated transfer characteristics approach a common subthreshold dependence. According to Eq. (3), the inverse subthreshold slope can be influenced either by interface or bulk traps. A systematic variation of acceptor concentration N_A, the concentration N_{ia} and energy of acceptor-like interface states (neutral if empty and negative if occupied by an electron), or the concentration N_{id} and energy of donor-like interface states, has shown that there is no influence of trapped interface charges on the drain current above the threshold voltage. In the off-state, however, the inverse subthreshold slope depends strongly on the occupancy of interface traps. Recharging with varying gate voltage then leads to the observed degradation of the inverse subthreshold slope and also to the drain voltage dependence of the subthreshold current. The experimental dependencies can actually be well described with either acceptor-like traps and lower acceptor doping (Fig. 4b) or with donor-like interface states and higher acceptor doping. The corresponding concentrations and positions of the trap energy level relative to the valence band are indicated in the Figure. In both cases, there is good agreement of the curves above the threshold voltage and in the subthreshold regime up to a gate voltage of 5 V. At higher voltages, the simulated curves with acceptor-like interface traps better describe the experimental data. The simulations thus reveal that anomalous subthreshold characteristics, with an extremely large inverse subthreshold slope and a drain voltage dependence of the subthreshold current, can arise from a recharging of interface states. Apart from interface traps, variations in bulk charges, caused for example by bulk traps, can also lead to such peculiarities [10]. To achieve the required low inverse subthreshold slope, materials and preparations are needed that avoid deep bulk and interface traps.

5. Submicron transistors by underetching

As described above, one must expect that only devices with submicrometer channel lengths lead to the needed OFET operation speed. Different patterning techniques, such as screen printing [11], soft lithographic stamping [12], and inkjet printing [13], have demonstrated neither the desired resolution nor alignment accuracy as yet. Photolithography [2] is expected to be too costly for the submicrometer regime. Recently, Stutzmann et al. [14] used embossing to fabricate vertical-channel field-effect transistors with submicrometer channel lengths, but could not observe saturation in the measured output characteristics.

We have developed [15, 5] high performace submicrometer channel length polymer field-effect transistors using only standard low-cost microelectronic techniques. In order to prevent short-channel effects, one needs also a rather thin gate insulator. Since until now no organics are available for this purpose, we used a hybrid technology – a 30 nm silicon dioxide layer on a highly doped silicon wafer serving as a gate. Source and drain, separated from each other by a short channel (1 μm or less in length), are fabricated by gold sputtering, low resolution photolithography, underetching, and the lift-off technique [15]. Finally, the active layer is spin coated. We used soluble poly(3-octylthiophene) (P3OT) and poly(3-hexylthiophene) (P3HT), which are unintentionally highly doped. To enable the off-state of the transistor, the layer thickness must be less than the depletion length. In our case, the thickness is as low as 30 nm, which is controlled by the spin coating process. Until now no scanning electron microscope (SEM) images of the cross sections of prepared OFETs have been published. Indeed, due to a low atomic weight of the polymer constituents, imaging requires special techniques. A perpendicular cut through a prepared OFET with 1 μm channel length was been prepared [16] using the focused ion beam (FIB) technique. Previous electrical measurements have proven a good performance of the device (see below). In order to visualize the surface of the top layer made of P3HT, an additional layer of gold was been evaporated (40 nm). The resulting SEM image[*] (5 kV, sample tilted by 45°) is shown in Fig. 5. As a guide for the eye, the structure is repeated schematically in the lower part. Notice the thin gate insulator, the short channel between source and drain, and the additional top gold layer to mark the P3HT surface.

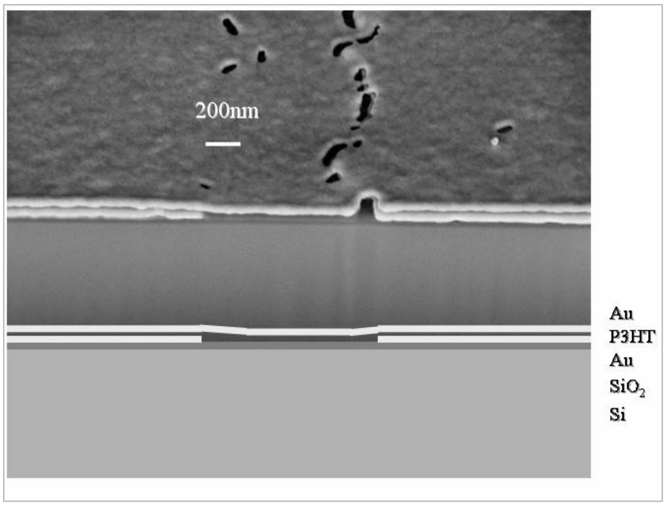

Fig. 5. SEM image of the cross section of an OFET with 1 μm channel length. The lower panel shows a schematic view

As an example of electrical properties, the output and transfer characteristics are depicted in Fig. 6. They demonstrate the following advantages: (i) operation at voltages lower than 5V, (ii) pronounced saturation of the output characteristics, (iii) only marginal short channel effects, (iv) a high on-off ratio (10^4), (v) a small inverse subthreshold slope (S = 0.5 V/dec), and (vi) negligible contact resistances. Hysteresis effects are still characteristic of OFETs [7, 17, 18]. In our case they are negligible for the drain voltage sweep at a given gate voltage (Fig. 6a), but different characteristics are obtained by decreasing or increasing the gate voltage. This is seen clearly in the

---

[*] The FIB–SEM image has been taken by Dr. S. Menzel [16].

transfer characteristics (Fig. 6b and c). The associated shift of the threshold voltage, however, is less than 1 V and thus small compared to literature values. Since the used P3AT were not specially treated, mobility is still low ($(2–3)\times10^{-5}$ $cm^2/(V\cdot s)$).

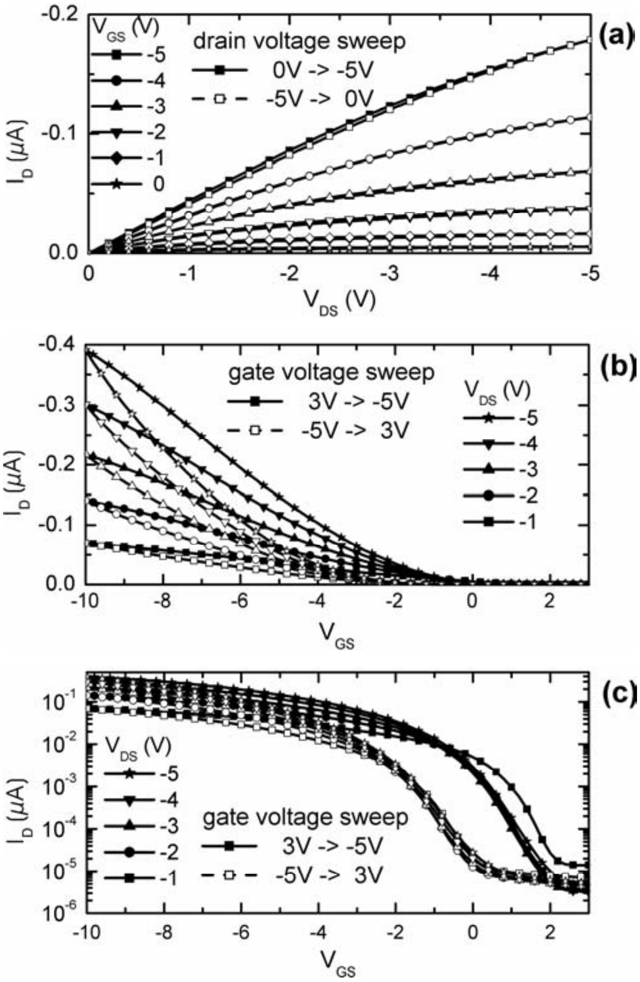

Fig. 6. Output characteristics of a P3HT transistor with a channel length of L = 740 nm and channel width of w = 1000 μm at different gate voltages and sweep directions (the hold and delay times are 180 s and 1 s, respectively) (a) ; transfer characteristics of the same transistor for different drain voltages and sweep directions: linear scale (b) and logarithmic scale (c); (the hold and delay times are 180 s and 10 s, respectively)

The success is that submicrometer OFETs with such a good performance can be fabricated without high-resolution lithography, and using only well established low-cost microelectronics processes. Before reaching the above mentioned goals, however, several problems remain unsolved. First, the mobility of the active layer must be enhanced by modifying the material and deposition process. Also, a thin organic gate insulator material is needed. Finally, circuits must be fabricated on plastic substrates, and in order to achieve high frequencies, parasitic capacitances must be reduced. The latter requires a self-aligned gate. Finally, for effective CMOS (complementary metal oxide semiconductor), circuits, n-channel devices are also needed.

6. Towards submicrometer organic CMOS

Until now, few n-channel OFETs have been described in literature [19, 20]. However, they are not likely for a common preparation with p-channel OFETs as submicron devices on the same substrate in a low-cost. In connection with recently prepared ambipolar OFETs, it has been suggested that they can serve as both p-channel and n-channel devices in CMOS circuits [21, 22]. In order to minimize power consumption in such circuits, one of the transistors (e.g. the n-channel OFET) should be in the off-state and the other in the on-state. Ambipolar OFETs, however, do not have an off-state with a sufficiently low current. Moreover, the current levels of both devices should be of the same order of magnitude.

Several rules can be formulated that lead to a proposal for n-channel OFETs for CMOS circuits. These rules are based on published results of single-layer (interpenetrating) networks of poly-[2-methoxy-5-(3′,7′-dimethyloctyloxy)]-p-phenylene vinylene (OC1C10-PPV) and [6,6]-phenyl C61-butyric acid methyl ester (PCBM), precursor-pentacene [21]) and hetero-layer ambipolar OFETs (pentacene as the hole transport layer and N,N′-ditridecylperylene-3,4,9,10-tetracarboxylic diimide (P13) as the electron transport layer [23]), on our simulations of a single-layer model ambipolar OFET [24], on simulations of top contact and bottom contact OFETs [25], especially with a Schottky-type material for source and drain, and on improved carrier injection by contact modification in organic light emitting diodes (OLEDs) [26]. The main problem with n-channel OFETs lies in the low affinity of the appropriate active layer organics, which is around 3 eV. This makes it hard to find a material for source/drain with a work function that is also comparably low. Even Mg (the work function from 3.6 eV to 3.7 eV) has an extremely large electron barrier, effectively a Schottky-type contact to the electron accumulation channel. According to our simulations [25], in this case the current for a top contact may be larger by orders of magnitude than that for a bottom contact. Nevertheless, the barrier is so large that one can hardly achieve balanced electron and hole currents, since good accumulation contacts are possible for the holes (e.g. with Au). The effect of this large barrier for electrons can be reduced in a way similar to OLED [26] (in this case, for the hole injecting anode) by an intermediate thin layer with somewhat larger affinity (between 3 eV and 3.6–3.7 eV) leading to a staggered barrier. Even then electron injection is still worse than hole injection at the Au accumulation contact. An active material is needed in which not only electron and hole mobilities are both large (c.a. $\mu = 0.01$ cm^2·V^{-1}·s^{-1}), but one in which electron mobility is the larger of the two. Results on a hetero-layer ambipolar OFET indicate that pentacene is a suitable candidate. Although the P13 layer was intended as an electron conducting layer, according to our simulations [24], both the p-channel and n-channel are formed in the pentacene layer and the P13 layer leads to a staggered barrier at the Mg top contact. For low-cost and solution-based preparation, the formation of pentacene from a soluble precursor [27] is preferred.

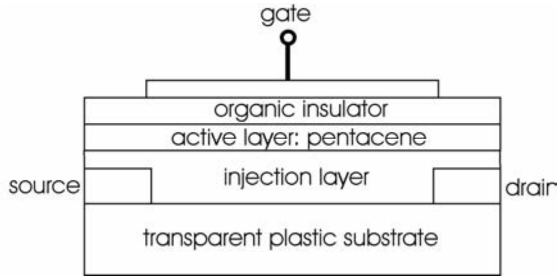

Fig. 7. Design of n-channel OFETs

A design for an n-channel OFET according to these considerations is shown in Fig. 7. The layer with an affinity larger than that of the active layer is denoted as the injection layer. Since the low-cost underetching technique for the preparation of submicron channel lengths [15] has already been realized with gold on a plastic substrate (Mylar), it should also work with Mg if an appropriate etching agent is used. For the design of the p-channel with Au as source and drain, no injection layer is needed. Problems to be solved include the need for a sufficiently thin and solution-processible organic gate insulator and the preparation of a self-aligned gate. For the latter, a recently published method [28] should be adapted. With an optically transparent substrate, source and drain can serve as an opaque optical mask for the gate definition.

7. Conclusions

A breakthrough in polymer electronics requires thin film-transistors that operate at voltages below 10 V. A threshold voltage of only a few volts and of the same polarity as the gate voltage is needed, connected with a subthreshold swing less than several 100 mV/dec. Thereby an on-off ratio of the current larger than 10^4 must be realized. The cut-off frequency should be larger than 100 kHz. Considering the connections between material properties and design, corresponding demands for the devices can be formulated. Since in low-cost solution-based fabrication the electron and hole mobilities can hardly exceed values of 10^{-2} cm^2/Vs, scaling down the channel length to the submicrometer region seems inevitable. For the definition of such short channels, an effective and cheap method based on underetching has been developed recently [15]. In addition, an (organic) gate insulator thickness less than 50–100 nm is required in order to avoid short channel effects. Analysis of transport and injection leads to a proposal for the design of n-channel OFETs suitable for CMOS circuits.

References

[1] *International Technology Roadmap for Semiconductors*, http://public.itrs.net/.
[2] DODABALAPUR A., BAO Z., MAKHIJA A., LAQUINDANUM J.G., RAJU V.R., FENG Y., KATZ H.E., ROGERS J., Appl. Phys. Lett., 73 (1998), 142.
[3] DRURY C.J., MUTSAERS C.M.J., HART C.M., MATTERS M., LEEUW D.M., Appl. Phys. Lett., 73 (1998), 108.
[4] SIRRINGHAUS H., TESSLER N., FRIEND R.H., Science, 280 (1998), 1741.
[5] SCHEINERT S., PAASCH G., phys. stat. sol. (a), 201 (2004), 1263.
[6] SCHEINERT S., PAASCH G., SCHRÖDNER M., ROTH H.-K., SENSFUß S., DOLL TH., J. Appl. Phys., 92 (2002), 330.
[7] SCHEINERT S., PAASCH G., POHLMANN S., HÖRHOLD H.-H., STOCKMANN R., Solid State Electronics, 44 (2000), 845.
[8] LIN Y.-Y., GUNDLACH D.J., NELSON S.F., JACKSON TH.N., IEEE Trans. Electron. Dev., 44 (1997), 1325.
[9] SIRRINGHAUS H., TESSLER N., THOMAS D.S., BROWN P.J., FRIEND R.H., Adv. Solid State Phys., 39 (1999), 101.
[10] SCHEINERT S., PAASCH G., DOLL T., Synth. Metals, 139 (2003), 233.
[11] BAO Z., FENG Y., DODABALAPUR A., RAJU V.R., LOVIGER A.J., Chem. Mat., 9 (1997), 1299.
[12] ROGERS J.A., BAO Z., MAKHIJA A., BRAUN P., Adv. Mater., 11 (1999), 741.
[13] SIRRINGHAUS H., KAWASE T., FRIEND R.H., SHIMODA T., INBASEKARAN M., WU W., WOO E.P., Science, 290 (2000), 2123.
[14] STUTZMANN N., FRIEND R.H., SIRRINGHAUS H., Science, 299 (2003), 1881.
[15] SCHEINERT S., DOLL T., SCHERER A., PAASCH G., HÖRSELMANN I., Appl. Phys. Lett., 84 (2004), 4427.
[16] PAASCH G., SCHEINERT S., SCHERER A., DOLL T., HÖRSELMANN I., MENZEL S., [in:] *Annual Report* 2003, Publisher Leibniz-Institut für Festkörper- und Werkstoffforschung IFW Dresden, (2003), p.23, http://www.ifw-dresden.de.
[17] HOROWITZ G., HAJLAOUI R., FICHOU D., KASSMI A.EL., J. Appl. Phys., 85 (1999), 3202.
[18] BROWN A.R., POMP A., DE LEEUW D.M., KLAASSEN D.B.M., HAVINGA E.E., HERWIG P., MÜLLEN K., J. Appl. Phys., 79 (1996), 2136.
[19] KATZ H.E., JOHNSON J., LOVINGER A.J., LI W., J. Am. Chem. Soc., 122 (2000), 7787.
[20] MALEFANT P.R.L., DIMITRAKOPOULOS C.D., GELORME J.D., KOSBAR L.L., GRAHAM T.O., Appl. Phys. Lett., 80 (2002), 2517.
[21] MEIJER E.J., DE LEEUW D.M., ESTALLES S., VAN VEENENDAAL E., HUISMAN B.-H., BLOM P.W.M., HUMMELEN J.C., SCHERF U., KLAPWIJK T.M., Nature Materials, 2 (2003), 678.
[22] SIRRINGHAUS H., Nature Materials, 2 (2003), 641.
[23] ROST C., GUNDLACH D.J., KARG S., RIEß W., J. Appl. Phys., 95 (2004), 5782.
[24] PAASCH G., LINDNER T., ROST C., RIEß W., KARG S., SCHEINERT S., in preparation.
[25] LINDNER T., PAASCH G., SCHEINERT S., J. Mater. Res., 19 (2004), 2014.
[26] NESTEROV A., PAASCH G., SCHEINERT S., LINDNER T., Synth. Metals, 130 (2002), 165.
[27] AFZALI A., DIMITAKOPOULOS C.D., BREEN T.L., J. Am. Chem. Soc., 124 (2002), 8812.
[28] BONFIGLIO A., MAMELLI F., SANNA O., Appl. Phys. Lett., 82 (2003), 3550.

Received 14 September 2004
Revised 29 September 2004

Materials Science-Poland, Vol. 22, No. 4, 2004

Spin-dependent transport and inter-wall coupling in carbon nanotubes

C. J. LAMBERT, S. ATHANASOPOULOS, I. M. GRACE[*], S. W. BAILEY

Department of Physics, Lancaster University, Lancaster LA1 4YW, United Kingdom

Theoretical results for electron transport through two structures involving carbon nanotubes are presented. The first structure was a nanotube inserted into another nanotube of a larger diameter. The electrical conductance of the resulting double-wall CNT is an oscillatory function of the length of the insertion. The frequency and amplitude of these oscillations reflect the position dependence of inter-tube interaction in multi-wall CNTs. The second structure was a single-wall carbon nanotube (CNT) in contact with ferromagnetic electrodes, exhibiting giant magnetoresistance (GMR). An intuitive picture of GMR in clean nanotubes with low-resistance contacts is presented and ab initio results are obtained for GMR in Nickel-contacted nanotubes.

Key words: carbon nanotubes; giant magnetoresistance; electron transport

1. Introduction

Multi-wall carbon nanotubes (MWNT) are coaxial cylinders with low translational and rotational energy barriers, which allow the inner tubes to easily slide with respect to the outer tubes [1]. This has been demonstrated by recent experiments, which have shown that it is possible to slide the inner-walls of a MWNT in a "telescope" motion [2, 3], and has led to the suggestion of low-friction, MWNT-based NEMS, such as oscillators with frequencies in excess of 1 GHz [4–6]. One aim of this paper is to demonstrate that the experiments of [2, 3] not only provide a new probe into mechanical inter-wall interactions in MWNTs, but that they also open up the possibility of probing the effect of inter-wall interactions on electronic properties. For single wall nanotubes (SWNTs), electronic properties are primarily determined by chirality [7], whereas in MWNTs the inter-wall interaction can cause the formation of pseudogaps [8] and in the case of telescoping nanotubes, resonances in the differential conductance of ballistic structures [9–11].

---

[*] Corresponding author, e-mail: i.grace@lancaster.ac.uk.

Another aim of this paper is to examine spin-polarized transport in CNTs connected to ferromagnetic contacts. Experiments suggesting that CNT-spintronic devices could soon become a reality, including early observations [12] of hysteretic magnetoresistance in Co-contacted nanotubes showed a maximum resistance change of 9%. More recently, Jensen et al. [13] have measured a magnetoresistance ratio of almost 100% in single wall carbon nanotubes contacted with Fe electrodes. In this paper, we investigate Giant Magnetoresistance (GMR) in clean CNTs connected to (n,n) CNT leads coated with Nickel. We compute the change in electrical conductance when the orientation of the magnetization is switched from parallel to antiparallel. The conductance is given by the Landauer formula $G = G_0 Trtt^\dagger$, where $G_0 = 2e^2/h$ and t is the transmission matrix.

2. Transport in telescopes and shuttles

We begin with an analysis of the electron transport properties of the telescoping MWNT shown in Fig. 1a, as a function of the displacement δx of the inner tube relative to the outer tube. Using a first principles approach, we predict that transport properties are strongly modified by displacements δx of the order of the interatomic spacing. We also analyse the shuttle structure shown in Fig. 1b, whose electronic properties are closely related to those of the corresponding telescope. Although the mechanical properties of telescoping nanotubes have been investigated experimentally as a function of the length of the telescoping region, no electrical measurements are currently available and the predictions are intended to stimulate such experiments.

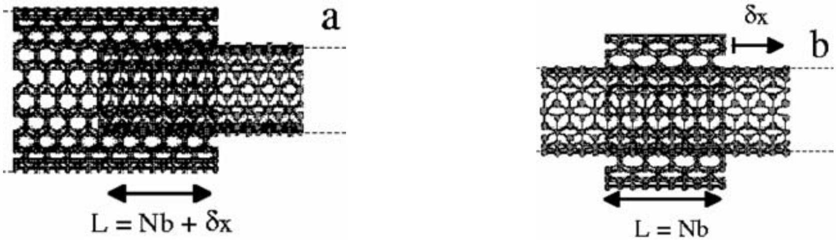

Fig. 1. Telescoping MWNT, in which a small-diameter NT is inserted a distance *L* into a larger diameter NT (a). The NTs are each connected to reservoirs on the left and right of the structures. In both cases, electrons are scattered at the points, separated by the distance *L*, where the NTs terminate. A "shuttle" system, in which a large-diameter SWNT (the shuttle) of the length *L* is placed outside a small-diameter inner wall NT, which in turn is connected to external reservoirs (b)

The problem of computing the δx-dependence of conductance is quite different from the problem considered in [10], where the energy dependence of the electron transmission coefficient is computed for $\delta x = 0$ only. To illustrate this, we note that since a NT is formed by repeatedly joining together identical slices of carbon atoms (which form the unit cells of the NT), the length L of the overlap region in a telescope can be written as $L = Nb + \delta x$, where b is the length of a slice of the inner or outer NT and δx is a displacement lying between $\pm b/2$ (i.e., $\delta x = L$ modulo b). For an infinite MWNT, the ab initio, mean-field Hamiltonian H is a periodic function of δx, with a period of b, and therefore H must be recomputed self-consistently for each value of δx in order to compute transport properties as a function of displacement.

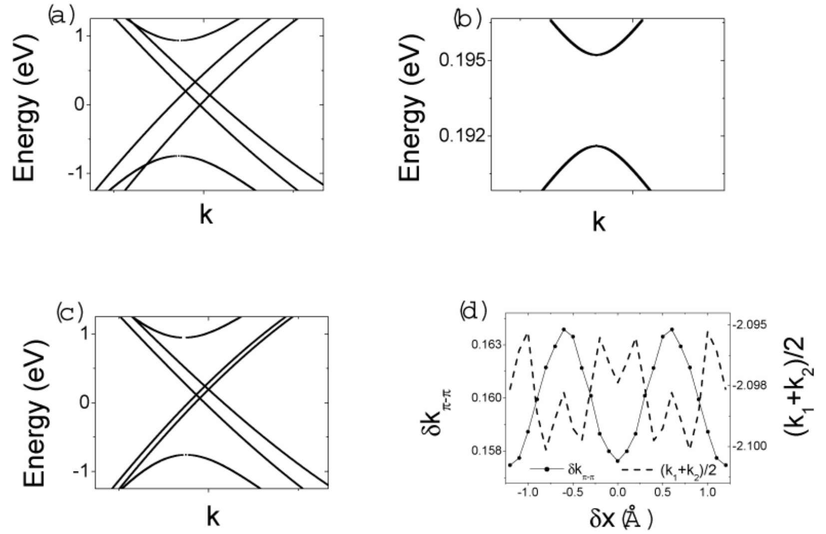

Fig. 2. Ab initio (6,6)@(11,11) band structure close to the Fermi Energy (0 eV) (a). Gap opening due to interwall interaction (b). Band structure with no interwall interaction (c). The difference, $\delta k_{\pi-\pi} = k_2 - k_1$, and average of the π band Fermi wave vectors k_1 and k_2 as a function of δx (d)

The telescope shown in Fig. 1a comprises two coaxial SWNTS, with the inner NT connected to a SWNT extending to $+\infty$ and the outer NT connected to a SWNT with a larger diameter extending to $-\infty$. As a definite example, we focus on the armchair (6,6)@(11,11) MWNT, which has an inter-wall separation of 3.4 Å. This system is typical of most armchair MWNTs, as it does not possess axial symmetry.

In what follows, transport properties are computed using the recursive Greens function scattering technique developed in ref. [14], combined with a Hamiltonian generated using the first principles density functional theory code SIESTA [15]. We use the local density approximation as parameterised by Perdew and Zunger [16] and nonlocal norm-conserving pseudopotentials [18]. The valence electrons are described by a single-ζ basis set. The cut-off radius for the s and p orbitals is chosen to be 4.1 a.u. Before computing transport properties, it is useful to examine the band structure of an infinite (6,6)@(11,11) MWNT. Since the Hamiltonian and overlap matrix elements depend on the positions of the carbon atoms of the inner NT relative to those on the outer NT, this band structure depends on the displacement δx of the inner NT relative to the outer NT. Figures 2a and b show the calculated band structure of an infinite, non-displaced (6,6)@(11,11) MWNT, corresponding to $\delta x = 0$.

Figure 2a shows that for positive k, in the vicinity of the Fermi energy, the band structure of an infinite MWNT possesses two π bands with positive slope and two π^* bands with negative slope. Several features of this band structure are relevant to understanding transport in telescopes and shuttles. First, as shown in Fig. 2b, in the vicinity of the Fermi energy, small energy gaps of the order of 2meV open at the band crossings. In what follows, we demonstrate that oscillations in transport properties arise over a wide energy range and therefore these gaps are unimportant at most energies. Secondly, the π^* bands of the inner NT are shifted relative to those of the outer NT, mainly due to charge transfer between the NTs. This feature is demonstrated in Fig. 2c, which shows the band structure when all matrix elements between orbitals on the outer and inner NT are artificially set to zero. In this case, the π bands are almost coincident, whereas the π^* bands on the different tubes remain shifted relative to each other. Finally, the π band of the inner NT is shifted relative to that of the outer NT, mainly due to the inter-wall interaction. This is demonstrated by the fact that the main effect of switching on the inter-wall matrix elements (i.e., in going from Fig. 2c to Fig. 2a) is a shift in the π bands, whilst leaving the others almost unaffected. The latter feature is crucial, since it produces large π-π scattering in telescopes and shuttles, while scattering involving other channels remains negligible. In view of the linearity of the bands near E_F, the wave vector difference $\delta k_{\pi\text{-}\pi} = k_2 - k_1$ between the two π

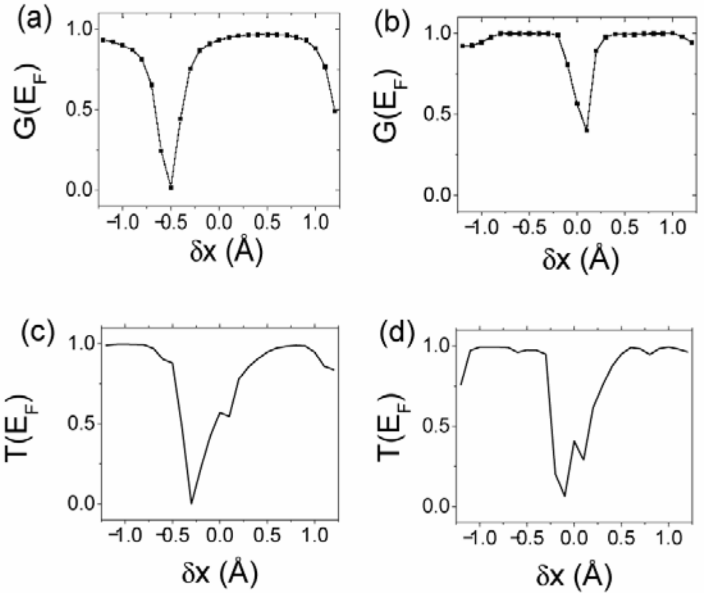

Fig. 3. Ab initio conductance $G(E_F)$ as a function of δx in a (6,6)@(11,11) telescope, for scattering regions of the length: a) $N = 10$, b) $N = 250$. Analytic description of $T(E)$ for the telescope model, for the lengths: c) $N = 10$ and d) $N = 250$

bands is almost independent of energy. The Fermi wave vectors k_1 and k_2 of the π bands, however, are extremely sensitive to the displacement δx of the inner tube relative to the outer tube. This is illustrated in Fig. 2d, which shows the dependence of $\delta k_{\pi\text{-}\pi}$ and $(k_1 + k_2)/2$ on δx. For an infinite MWNT, these quantities are periodic functions of δx, with a period equal to the repeat distance $b = 2.45$Å of the MWNT.

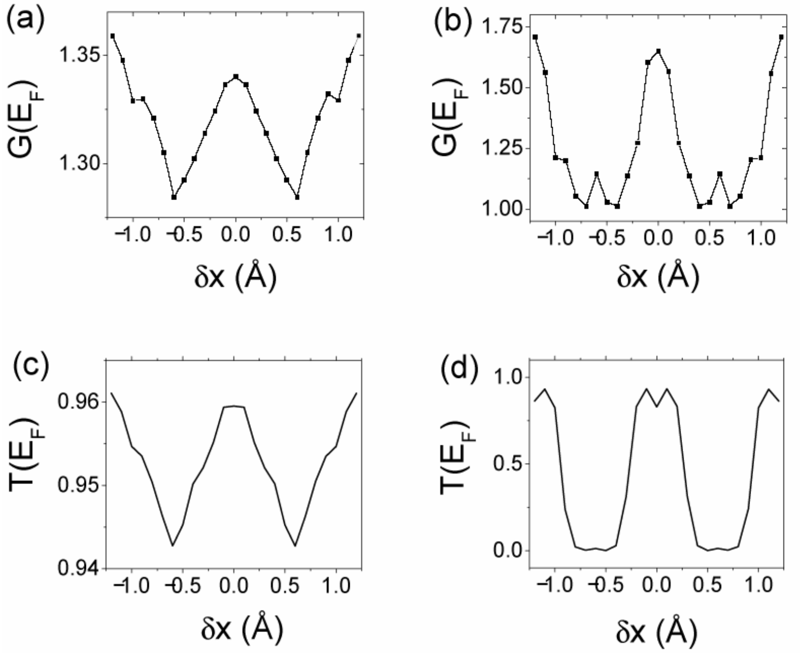

Fig. 4. Ab initio conductance of the shuttle (6,6)@(11,11) nanotube as a function of δx, for scattering lengths: a) $N = 10$, b) $N = 250$. Analytic description of transmission for the shuttle model, for the lengths: c) $N = 10$ and d) $N = 250$

Having examined the band structure as a function of displacement δx, we now turn to the transport properties of the telescoping (6,6)@(11,11) double wall nanotube and demonstrate that the above δx-dependence of the π wave vectors is accessible via conductance measurements on telescopes and shuttles. For scattering regions of the length $L = Nb + \delta x$, Figs. 3a and b (4a and b) show ab initio results for the electrical conductance $G(E_F) = T(E_F)$ in units of $2e^2/h$ as a function of δx, for a telescope (shuttle) with two values of the number of overlapping slices N. Perhaps the most striking feature of these results is the presence of large oscillations for $\delta x < b$. To demonstrate that these unexpected oscillations are a direct consequence of the δx-dependence of the Hamiltonian, we have developed [19] an analytical description of these oscillations based on retaining only the π-π inter-wall coupling. This approximation is partly justified by comparing Figs. 2a and 2c, which shows that switching on the inter-wall coupling yields a large shift in the π bands, while leaving the other bands almost unchanged.

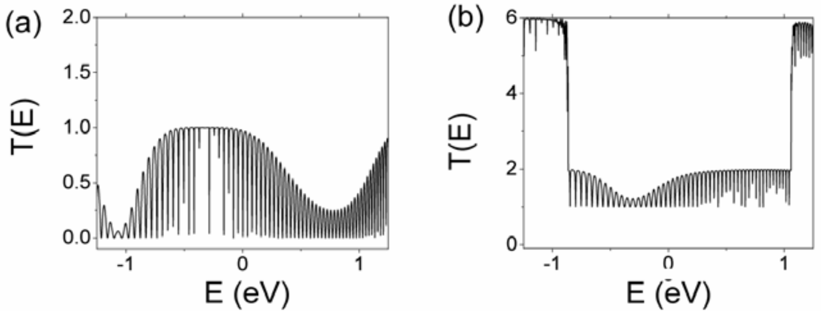

Fig. 5. Transmission coefficient versus energy for a telescope (a) and shuttle (b)

A restriction to π-π coupling is further suggested by comparing the energy dependence of the transmission coefficient for shuttles and telescopes. For $\delta x = 0$, Fig. 5 shows the electron transmission coefficient $T(E)$ versus energy for fixed values of N. For energies in the approximate range ±1 eV, where only the π and π^* scattering channels are open, the transmission coefficient of the telescope (shuttle) oscillates between 0 and 1 (1 and 2). For higher energies, where four additional scattering channels are open, both exhibit remarkably different behaviours. Namely, $T(E)$ for the telescope continues to oscillate between 0 and 1, whereas $T(E)$ for the shuttle increases by 4 and oscillates between 5 and 6. This difference reflects the fact that for the telescope only the π band of the outer tube scatters into the π band of the inner tube and no other channels are transmitted, whereas for the shuttle only the π band of the inner tube is scattered by the presence of the shuttle, while all other channels are transmitted with a probability of almost one. For comparison, Figs. 3c, d, 4c, and 4d show results for this π-π analytical description, the details of which are given in [19].

3. Giant magnetoresistance (GMR) in single-wall CNTs

Using the above first principles approach, we now examine spin-polarised transport in single-wall NTs contacted to ferromagnetic electrodes. Before presenting the exact results, it is useful to have a simple picture of the origin of GMR. Consider the case of armchair (n,n) CNTs, which are metallic with a finite conductance $2G_0$ at the Fermi energy. For an infinitely long CNT with uniform magnetization, the differential conductance of the up-spin carriers, $G_{++}^{\uparrow}$, is shifted by the exchange energy h, and for the down-spin carriers, $G_{++}^{\downarrow}$, by $-h$. The total conductance of the system is $G_{++} = G_{++}^{\uparrow} + G_{++}^{\downarrow}$. In the case of two semi-infinite leads with antiparallel alignment of magnetization, a crude approximation for the conductance G_{+-} is $G_{+-} = \min 2\left\{G^{\uparrow}_{++}, G^{\downarrow}_{++}\right\}$. As shown in Fig. 6, this simple picture predicts that the difference $G_{++} - G_{+-}$ is non zero only near step edges, where the change in conductance is $\Delta G = (G_{++} - G_{+-})/G_0 = 2$. A similar argument can be applied to zig-zag CNTs.

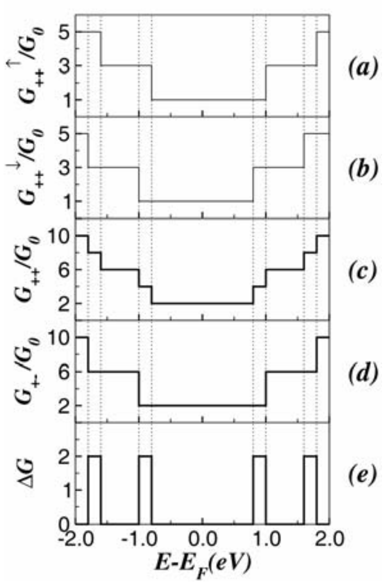

Fig. 6. Differential conductance for the: a) up and b) down spin carriers, total conductance for: c) ferromagnetic and d) antiferromagnetic alignment, and e) relevant change in conductance for metallic armchair CNTs

As a first material-specific calculation of GMR in CNTs, we consider the simplest possible case of a single wall CNT in contact with CNT leads. To induce a magnetic moment in the leads, magnetic Ni impurities are placed along the axis of the leads. For a Ni electrode in contact with a CNT, this situation may occur if Ni atoms migrate along the axis of the CNT. To perform ab initio self-consistent transport calculations, we work within the generalized gradient approximation (GGA) of Perdew–Burke–Ernzerhof [17]. Core electrons are replaced by nonlocal, norm-conserving pseudopotentials (Troulier–Martins) [18], while the valence electrons are described by a linear combination of numerical orbitals. We use a single-zeta basis set for Carbon and a double-zeta singly polarized basis set for Nickel. Real space integrations are performed on a regular grid with an equivalent plane wave mesh cut-off of 150 *Ry*. The atomic positions are relaxed until all force components are smaller than 0.02 eV/Å. After relaxation, the tight binding Hamiltonian for the system can be extracted. Using the recursive Green's function technique [14] we calculate the transmission for a hybrid system consisting of two semi-infinite nanotube leads with Ni atoms located on the CNT axis, in contact with a finite length clean CNT (Fig. 7).

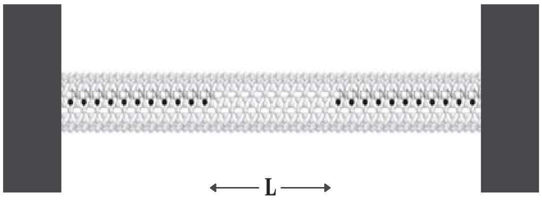

Fig. 7. Armchair carbon nanotube in contact with ferromagnetic electrodes. Ni atoms encapsulated along the axis of a (5,5) CNT

Consider the case of an armchair CNT with Ni atoms located on the axis of the tube, as shown in Fig. 7. Results will be presented for a (5,5) CNT, using a unit cell (i.e., a supercell with a lattice constant $a = 2.46$ Å) of 20 C atoms and one Ni atom. In the relaxed structure, the Ni atoms remain near their initial positions on the axis of the tube. The total magnetization of the unit cell is $M = 1.71\mu_B$.

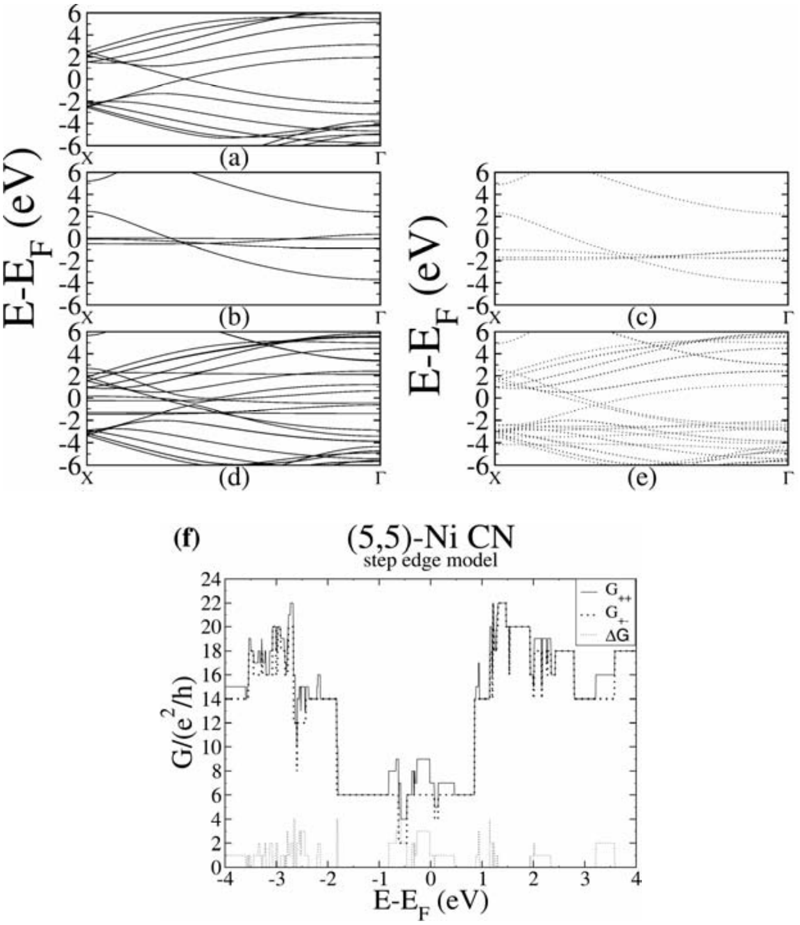

Fig. 8. Band structure for a clean (5,5) CNT (a), the (b) majority and (c) minority spin carriers of a 1-D Ni chain, the (d) majority and (e) minority spin carriers of a (5,5) CNT with coaxial Ni atoms. Step edge model of GMR for a (5,5)-Ni CNT (f)

Figures 8d and e show the band structures for majority and minority spin carriers, respectively. For comparison, Fig. 8a shows the band structure of a clean (5,5) CNT, and Figs. 8b and c the band structures of a 1-D Ni chain for majority and minority spin carriers, respectively. We use a single-zeta basis set for Carbon in the clean (5,5) CNT and a double-zeta singly polarized basis set for Ni in the 1-D chain calculation. The lattice constant for the Ni chain was $a = 2.46$ Å in order to keep the same interatomic distance between the Ni atoms as in the CNT calculation.

As a prelude to a full transport calculation, we first examine this structure using the above step-edge model of GMR by counting the number of open channels at a specific energy. The resulting step-edge approximation is presented in Fig. 8f, which shows the dimensionless conductances $G_{++}/(e^2/h)$ and $G_{+-}/(e^2/h)$ and the change in conductance $\Delta G = (G_{++} - G_{+-})/(e^2/h)$. To obtain the corresponding ab initio result, we consider two semi-infinite (5,5)-Ni CNT leads, in contact with a clean tube L cells long. For $L = 20$, the corresponding G_{++} and G_{+-} are shown in Fig. 9a, while the magnetoconductance ΔG is plotted in Fig. 9b. At zero temperature, the GMR ratio $\delta G = \Delta G/G_{++}$ vanishes at the Fermi energy, whereas for nearby energies it takes positive values ≈34%. Fig. 9b also shows that small negative values of GMR occur as well. These are due to multiple scattering from the ends of the CNT and are sensitive to the length L of the scattering region, as discussed in [20].

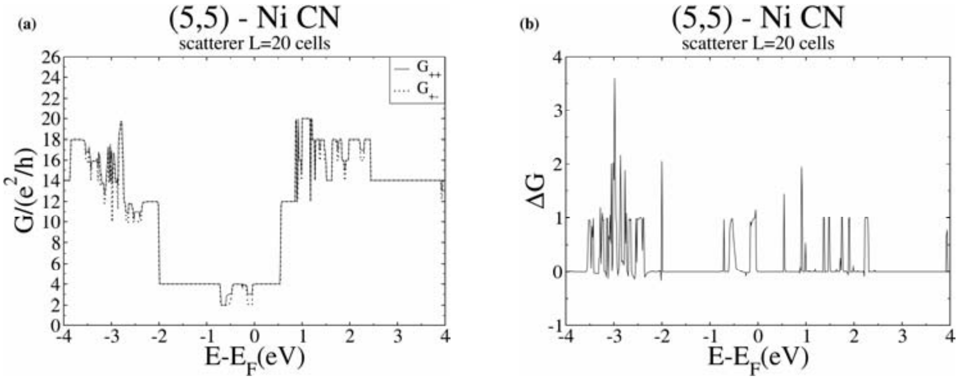

Fig. 9. Differential conductance for ferromagnetic and antiferromagnetic alignment (a) and the relevant change in conductance for a (5,5)-Ni CNT in contact with a clean CNT of the length $L = 20$ cells

Compared with the step edge model, we find that high values of ΔG are indeed associated with conductance steps in the spin conductances. The ab initio conductances, however, are suppressed compared to the step-edge picture, because the absence of Ni in the scattering region removes a significant number of conducting channels.

4. Conclusions

We have calculated conductance oscillation as a function of the displacement in CNT telescopes and shuttles and argued that these oscillations arise from the dependence on displacement of the coupling between inner and outer tube π channels. The non-monotonic behaviour in the conductance as a function of displacement δx can therefore be used to probe the electronic inter-wall coupling. We have also calculated the magnetoconductance of Ni-contacted CNTs and compared this with a simple step-edge model of GMR. We find that GMR ratios of the order of 34% can be expected in (5,5) armchair CNTs when Ni atoms migrate along the axis of the CNT leads.

Acknowledgements

We are pleased to acknowledge helpful discussions with S. Sanvito and J. Ferrer and support from the EU MCRTN-CT-2003-504574, EPSRC, MoD and the Royal Society.

References

[1] BOURLON B., GLATTLI D.C., BACHTOLD A., FORRO L., http://arxiv.org/abs/cond-mat/0309465 (2003).
[2] CUMMINGS J., ZETTL A., Science 289 (2000), 602.
[3] MIN-FENG YU, YAKOBSON B.I., RUOFF R.S., J. Phys. Chem B, 104 (2000), 8764.
[4] ZHENG Q., JIANG Q., Phys. Rev. Lett., 88 (2003), 45503.
[5] LEGOAS S.B., COLUCI V.R., BRAGA S.F., COURA P.Z., DANTAS S.O., GALVAÕ D.S., Phys. Rev. Lett., 90 (2003), 55504.
[6] RIVERA J.L, MCCABE C.AND CUMMINGS P.T., Nano. Lett., 3 (2003), 1001.
[7] MINTMIRE J.W., DUNLAP B.I., WHITE C.T., Phys. Rev. Lett., 68 (1992), 631.
[8] KWON Y.K., TOMANEK D., Phys. Rev B, 58, R16001 (1998).
[9] SANVITO S., KWON Y.K., TOMANEK D., LAMBERT C.J., Phys.Rev. Lett., 84 (2000), 1974.
[10] KIM D.-H., CHANG K.J., Phys. Rev. B, 66 (2002), 155402.
[11] KIM D.-H., SIM H.-S., CHANG K.J., Phys. Rev. B, 64 (2001), 115409.
[12] TSUKAGOSHI K., ALPHENAAR B.W., AGO H., Nature, 401 (1999), 572.
[13] JENSEN A., NYGARD J., BORGGREEN J., [in:] H. Takayanagi and J. Nitta (Eds.), *Toward the Controllable Quantum States*, Proc. MSS 2002, World Scientific, 2003 , p. 33–37.
[14] SANVITO S., LAMBERT C.J., JEFFERSON J.H., BRATKOVSKY A., Phys. Rev. B, 59 (1999), 11936.
[15] SOLER J.M., ARTACHO E., GALE J.D., GARCÍA A., JUNQUERA J., ORDEJÓN P., SÁNCHEZ-PORTAL D., J. Phys. Condens. Matter., 14 (2002), 2745.
[16] PERDEW J.P., ZUNGER A., Phys. Rev. B (1981), 23, 5048.
[17] PERDEW J.P., BURKE K., ERNZERHOF M., Phys. Rev. Lett., 77 (1996), 3865.
[18] TROULLIER N., MARTINS J.L., Phys. Rev. B, 43 (1991), 1993.
[19] GRACE I.M., BAILEY S.W., LAMBERT C.J., submitted to Phys. Rev. B., 2004.
[20] BABIACZYK W.I., BULKA B.R., http://arxiv.org/abs/cond-mat/0207672 (2002).

Received 15 September 2004
Revised 3 November 2004

Materials Science-Poland, Vol. 22, No. 4, 2004

Spin transport through nanostructures

B. KRAMER[1*], K. DITTMER[1], S. DEBALD[1], J. OHE[1],
F. CAVALIERE[1, 2], M. SASSETTI[2]

[1]Institut für Theoretische Physik, Universität Hamburg, Jungiusstraße 9, 20355 Hamburg, Germany

[2] INFM-Lamia, Dipartimento di Fisica, Università di Genova, Via Dodecaneso 33, 16146 Genova, Italy

The influences of non-Fermi liquid correlations and spin-orbit scattering on the transport properties of quantum nanostructures connected to interacting leads are studied. Signatures of the spin are investigated in the transport. One-dimensional quantum dot is studied in the sequential tunnelling regime using the master equation approach. Quantum coherent conductance is calculated using the transfer matrix method for a quasi-one dimensional system with the Rashba coupling Hamiltonian, and for a two -dimensional quantum dot in a multi-terminal geometry modelled by the Ando Hamiltonian. In the sequential tunnelling regime, states with a higher total spin can be stabilized by suitably adjusting bias and gate voltages. Spin polarized current can be achieved by locally applying a magnetic field. For coherent linear transport through a multi-terminal device at zero magnetic field, we find a spin polarized current at certain energies, induced by spin-orbit scattering.

Key words: *spin transport; nanostructures; quantum dot; Rashba coupling*

1. Introduction

Transport properties of nanostructures related to the charge of the electron have been extensively studied during the past two decades, since the discovery of the conductance quantisation of quantum point contacts and two-dimensional electron systems in a quantising magnetic field, and of the Coulomb blockade in quantum dots connected to conducting leads by high tunnel barriers[**]. The latter can be used to construct a single electron transistor (SET), in which switching between non-conducting and conducting states is done essentially with a single charge.

Transport phenomena in nanostructures related to the spin of the electron have attracted considerable interest only during the past few years[***], after the theoretical

---

[*]Corresponding author, e-mail: kramer@physnet.uni-hamburg.de.

[**]Overviews of the field can be found in Ref. [1].

[***]Some recent overviews can be found in Ref. [2].

proposal of a “spin transistor” [3]. Central issue of such a device is the possibility of producing a spin-polarized current that can be controlled by external means. In analogy to the SET device, the ultimate spin device could be imagined as a “single spin transistor” (SST), which would be switched between an “on-state” and “off-state” with a single electron spin. The discoveries of the spin blockade in sequential transport through quantum dots due to spin selection rules [4] and spin charge separation [5, 6] were important steps for achieving such a goal.

The standard way to generate a spin-polarized current is to inject electrons into a semiconductor from a ferromagnet [7], where it can be subsequently influenced by gate voltages. This is not very efficient due to scattering at the interface. The spin polarization is very small and there is also an accompanying charge current. Theoretically, several means of obtaining spin-polarized currents in nanostructures based on spin-orbit coupling have been discussed [8–13]. They are based on the fact that spin-orbit interaction has a polarizing effect on the quantum mechanical scattering of particles [14].

In the present paper, we address two issues. First, we investigate the control of spin in sequential transport through quantum dots in the presence of electron correlations. We show that by suitably adjusting source-drain voltage and the heights of tunnelling barriers one can stabilize states with higher total spin in a quantum dot. These states can lead to a negative differential conductance. By Zeeman splitting, one can achieve a spin polarization of the current, enhanced by electron correlation [15]. Differential spin conductance is strongly enhanced in the region of a higher spin state. Secondly, we study possibilities of achieving spin-polarization without using an external magnetic field. We find that in the presence of spin-orbit scattering, individual scattering states in low dimensional quantum nanostructures, such as quantum wires and quantum dots, can have spatially modulated spin polarizations. In non-equilibrium, such as is realized by linear dc current flow, the spatial modulation of the spin polarization of the states can lead to a polarization of the current. This happens when the Fermi energy is adjusted near the energy of a scattering state with a specific spatial polarization pattern and current and voltage probes are suitably attached to the nanostructure.

2. Spin blockade in sequential tunnelling

In this section, we summarize the theory of sequential transport through quantum dots in the presence of correlations, taking electron spin into account.

2.1. The Hamiltonian of a quantum dot with correlated electrons

For studying the interplay between spin polarized sequential tunnelling and correlations, we consider a one-dimensional quantum dot of length a, described as a Luttinger liquid, connected to non-interacting leads [15]. The Hamiltonian is (adopted units are such that $\hbar = 1$)

$$H_0 = \sum_{\nu=\rho,\sigma} \sum_q \omega_\nu(q) b_\nu^+(q) b_\nu(q) + \frac{E_\rho}{2}\left(n - n_g\right)^2 + \frac{E_\sigma}{2}\left(s - s_B\right)^2, \qquad \nu = \rho, \sigma \tag{1}$$

The first two terms take the collective charge ($\nu = \rho$) and spin ($\nu = \sigma$) density waves into account with the creation and annihilation operators b_ν^+ and b_ν, respectively. Here, n and s represent the total number of charges and the z-component of the total spin (units $\hbar/2$) of the electrons in the quantum dot, respectively. The total charge and spin are defined with respect to the average background values $\langle n \rangle = N_0$ and $\langle s \rangle = 0$, and are constrained by even $n + s$. The third term represents the energy necessary in order to change the charge n in the dot. An external gate voltage V_g has been incorporated into the Hamiltonian via the charge induced by the gate voltage $n_g e = C_g V_g$, with C_g being the gate capacitance and $-e$ the electron charge. The fourth term is analogous to the third one, and describes the energy needed to change the total spin s. An external magnetic field B induces a Zeeman splitting of $-g_B \mu_B B$, where g_B is the Landé factor and μ_B is the Bohr magneton. This in turn induces an effective average "spin number"

$$s_B = \frac{g \mu_B B}{E_\sigma} \tag{2}$$

which is the ratio between the Zeeman splitting and the spin addition energy E_σ. Note that the roles of n_g and s_B are very similar, as the last two terms in Eq. (1) describe the energy contributions due to charge and spin addition. Their physical origins, however, are very different. The charge addition energy is due to classical Coulomb repulsion, whereas the spin addition energy is a consequence of the Pauli principle [16] and is present in a system of finite size even without interaction.

2.2. Energy scales

An eigenstate of the Hamiltonian (1) can be represented by a state vector

$$|j\rangle = \left| n, s, \left\{ l_q^\rho \right\}, \left\{ l_q^\sigma \right\} \right\rangle \tag{3}$$

with $\left\{ l_q^{\rho,\sigma} \right\}$ being the integer occupation numbers for a charge and spin collective mode. The energy of such a state can be written in terms of addition and excitation energies [15, 6]

$$U = \sum_q \left[l_q^\rho \omega_\rho(q) + l_q^\sigma \omega_\sigma(q) \right] + \frac{E_\rho}{2}\left(n - n_g\right)^2 + \frac{E_\sigma}{2}\left(s - s_B\right)^2 \tag{4}$$

The dispersion relation of the collective modes is linear due to the liberalization of the free spectrum around the Fermi level and to the assumption of short-range interactions

$$\omega_\nu(q) = \frac{v_F}{g_\nu} q \tag{5}$$

where v_F is the Fermi velocity. The parameters g_ν parameterise the electronic interactions, g_ρ^{-2} being essentially the spatial average of the interaction potential. Here we neglect the exchange interaction, assuming a SU(2) spin invariance, such that $g_\sigma = 1$. For a noninteracting system $g_\sigma = 1$, while for repulsive interactions $g_\rho < 1$. A linear spectrum of the collective modes gives rise to a constant level spacing of charge and spin density waves

$$\varepsilon_\rho = \frac{\pi v_F}{a g_\rho}, \qquad \varepsilon_\sigma = \frac{\pi v_F}{a} \tag{6}$$

The two remaining energy scales are the charge and spin addition energies E_ρ and E_σ, respectively. The charge addition energy

$$E_\rho = \frac{\pi v_F}{2 a g_\rho^2} \tag{7}$$

is strongly renormalized by the repulsive interactions between the electrons. On the other hand, spin addition is given by the noninteracting level spacing

$$E_\sigma = \frac{\pi v_F}{2a} \tag{8}$$

As mentioned above, this energy scale is basically a result of the Pauli principle. In the model presented above, many physical effects affecting E_ρ have been disregarded, such as coupling with the external gates or a nearby 2D electronic gas. Such effects can lead to significant deviations from (7). Therefore, we will treat E_ρ as a free parameter in what follows.

2.3. Sequential transport

We assume that the quantum dot is connected via tunnelling barriers (H_t) to noninteracting left (L) and right (R) leads ($H_{L,R}$), which are kept at the chemical potentials μ_L and μ_R, respectively. The bias voltage applied to the quantum dot is $eV = \mu_L - \mu_R$. The total Hamiltonian is

$$H = H_0 + H_t + H_L + H_R \tag{9}$$

We assume very large left and right tunnelling resistances, $R_{L,R} >> R_K = h/e^2$. We also assume that the excited *collective* states in the quantum dot relax instantaneously to the ground state. With this assumption, it is still possible to tunnel into an excited state. Since the relaxation time of the collective excitations is assumed to be much faster than any other time scale of the system, however, it is not possible to tunnel out of the quantum dot via such a state. In contrast, states with additional charge and/or spin are assumed to be stable. Therefore, the states of the dot that are relevant for transport can be labelled by the number of charges n and spin s alone, by the vector $\left|n,s\right\rangle$. We study transport in the sequential tunnelling regime, with tunnelling through left and right barriers being independent. The time-dependent occupation probabilities of the states in the quantum dot, $P_{\left|n,s\right\rangle}(t)$, satisfy the master equation

$$\partial_t P_{\left|n,s\right\rangle}(t) = \sum_{\lambda=L,R}\sum_{n'=n\pm1}\sum_{s'=s\pm1}\left[P_{\left|n',s'\right\rangle}\Gamma^{(\lambda)}_{\left|n',s'\right\rangle\to\left|n,s\right\rangle} - P_{\left|n,s\right\rangle}\Gamma^{(\lambda)}_{\left|n,s\right\rangle\to\left|n',s'\right\rangle}\right] \tag{10}$$

with the tunnelling rates Γ determined in the lowest order of perturbation theory for H_t [6]. For low temperatures, $k_B T << E_\sigma$, they have the form

$$\Gamma^{(\lambda)}(\Delta E) = \Gamma_0^{(\lambda)} \sum_{l_\rho=-\infty}^{\infty}\sum_{l_\sigma=-\infty}^{\infty} a^\rho_{l_\rho} a^\sigma_{l_\sigma} \gamma\left(\Delta E + l_\rho\varepsilon_\rho + l_\sigma\varepsilon_\sigma\right) \tag{11}$$

where

$$\Gamma_0^{(\lambda)} = \frac{2\omega_C}{e^2 R_\lambda}\left(\frac{\varepsilon_\sigma}{\omega_C}\right)^{1/2}\left(\frac{\varepsilon_\rho}{\omega_C}\right)^{1/2g_\rho} \tag{12}$$

Here, ω_C is a cut-off frequency and $\Delta E \equiv E_f - E_i$ is the energy associated with a particular transition between an initial and a final state. We have defined the Fermi function for the leads as

$$\gamma(x) = \frac{1}{1+e^{\beta x}} \tag{13}$$

with $\beta = 1/k_B T$. The weights $a^\rho_{l_\rho}$, $a^\sigma_{l_\sigma}$ arise from the density of states in the quantum dot. In the low temperature regime considered here, they are

$$a^\rho_{l_\rho} = \frac{\Gamma\left(1/2g_\rho + l_\rho\right)}{\Gamma\left(1/2g_\rho\right) l_\rho!}, \qquad a^\sigma_{l_\sigma} = \frac{(2l_\sigma - 1)!!}{2^{l_\sigma}\, l_\sigma!} \tag{14}$$

where $\Gamma(x)$ represents the Euler gamma function. In the stationary limit, the left hand side of Eq. (10) is zero. The normalized probability distribution $P_{\left|n,s\right\rangle}$ is given by the solution of a linear system of equations, with $\sum_{n,s} P_{|n,s\rangle} = 1$. We define the current for spin-up (+) and spin-down (–) electrons as

$$I_{\pm}(V) = e\sum_{n,s}\sum_{\Delta s=\pm 1} P_{|n,s\rangle}\left[\varphi_{\pm}\Gamma^{(R)}_{|n,s\rangle\to|n+1,s+\Delta s\rangle} - \varphi_{\mp}\Gamma^{(R)}_{|n,s\rangle\to|n-1,s+\Delta s\rangle}\right] \tag{15}$$

where $\varphi_{\pm} = (1 \pm \Delta s)/2$. The charge conductance is given by the derivative of the total current $I_{\rho} \equiv I_{+} + I_{-}$ with respect to the bias voltage

$$G_{\rho}(V, n_g, s_B) = \frac{\partial I_{\rho}}{\partial V} \tag{16}$$

The transport of spin is described by the spin-polarized current, $I_{\sigma} = I_{+} - I_{-}$, with a corresponding differential spin conductance

$$G_{\sigma}(V, n_g, s_B) = \frac{\partial I_{\sigma}}{\partial V} \tag{17}$$

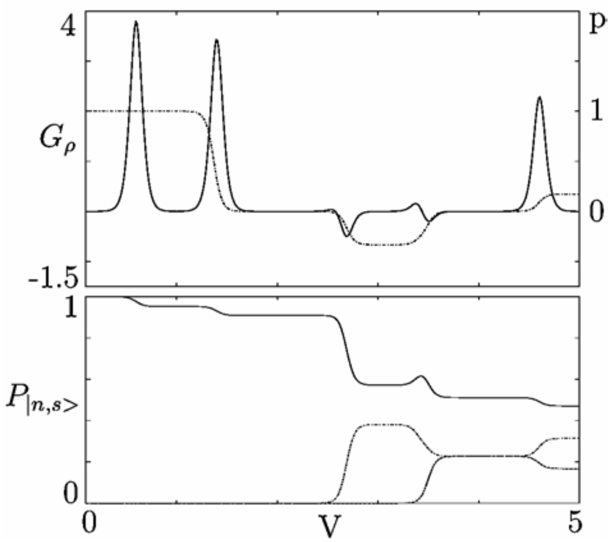

Fig. 1. Top: Differential conductance G_{ρ} (solid line, units $e^2\Gamma_0^{(R)}$) and spin polarization p (dash-dot line) as a function of V (units E_{σ}/e) along the dotted horizontal line in Fig. 3 (top), with $n_g = 0.5$. Bottom: the corresponding stationary occupation probabilities $P_{|n,s\rangle}$ for $|n,0\rangle$ (solid line), $|n,2\rangle$ (dash-dot line), and $|n,-2\rangle$ (dashed line). The small probabilities $P_{|n+1,\pm 1\rangle}$ are not displayed in this plot. Note, however, that the population of the states $|n+1,\pm 1\rangle$ gives rise to positive conductance peaks (top panel) near $V \approx 0.6$ and $V \approx 1.4$. The parameters are $g_{\sigma} = 1$, $g_{\rho} = 0.4$, $E_{\rho} = 25E_{\sigma}$, $s_B = 0.2$, $k_BT = 0.02E_{\sigma}$, and $R_R/R_L = 20$

Figure 1 shows the voltage dependences of $P_{|n,0\rangle}$, $P_{|n,2\rangle}$, and $P_{|n,-2\rangle}$ near a Coulomb blockade peak for a transition from even n to $n + 1$, the corresponding differential conductance, and the spin polarization $p \equiv I_\sigma / I_\rho$. Negative differential conductances occur when states with $s = \pm 2$ become occupied (Fig. 3).

Let us discuss the behaviour of the transport in more detail. Charge and spin density waves represent collective excitations of the system. These modes, however, are not the only excited states of the system. For instance, $|n = 2q, s = 2p, 0, 0\rangle$ (p and q are integers with $|p| \geq 1$) are excited states with $2p$ partially aligned spins, without collective excitations. At zero magnetic field, the total-spin up and total-spin down components are energetically degenerate, and separated from the ground state $|n = 2q, s = 0, 0, 0\rangle$ by $\delta E_p = 2p^2 E\sigma$. States with an odd number of electrons, $n = 2q + 1$, can be considered similarly. Here, the excited states with partially aligned spins have spin $|s| = 2p + 1$, $(p \geq 1)$.

States with higher spins can be accessed in the non-linear transport regime. In order to relax to the ground state, the total spin has to be changed. This is not possible without spin-flip scattering processes, apart via a tunnelling event. Even in the presence of spin-flip processes it remains difficult to relax to an energetically lower state and simultaneously change the total spin [17]. It is thus reasonable to assume that, in contrast to internal collective excitations, excited states with higher spins do not intrinsically relax. Dynamical states are characterized by their total number of charges n and the total spin s.

Such high-spin states play an important role in the transport, particularly in systems with asymmetric barriers, as discussed below. At finite, non-zero magnetic fields, such states can become ground states of the system due to Zeeman splitting of the total-spin up and total-spin down components.

2.4. Results

In this section, we summarize some of the results obtained for sequential tunnelling, including the identification of parameter regions for which high-spin states yield the dominant contributions to transport [6]. We also summarize some recent results on spin polarized differential conductivity in the presence of a magnetic field localized at the quantum dot. It appears that the contributions of higher-spin states can not only lead to negative differential conductances but also increase the differential spin conductance.

In the following, we concentrate on the region close to a resonance in the linear conductance. This is given by the condition that the chemical potentials in the left and right leads are the same as the chemical potential of the quantum dot, defined as the difference in the ground states of n and $n + 1$ electrons

$$\mu_d = E_\rho\left(n+\frac{1}{2}-n_g\right)+E_\sigma\left(\bar{s}_{n+1}-\bar{s}_n\right)\left[\frac{\bar{s}_n+\bar{s}_{n+1}}{2}-s_B\right] \qquad (18)$$

with $\bar{s}_n$, $\bar{s}_{n+1}$ being the spin of the ground state for n, $n+1$ electrons, respectively. For a fixed n_g, the ground state of the dot can be found by minimizing the total energy (4) with respect to $n, s \in z$, with $l_q^\rho = l_q^\sigma \equiv 0$.

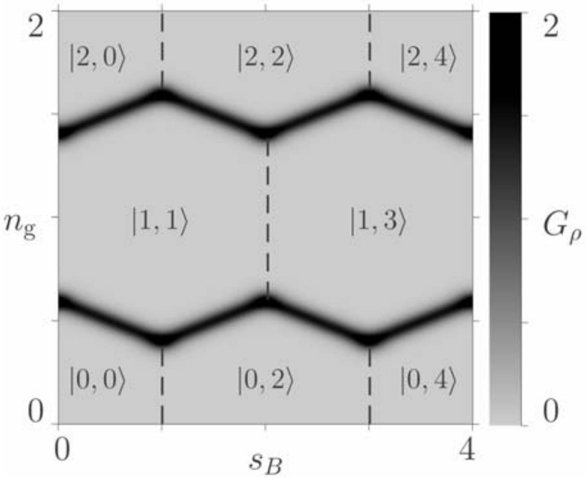

Fig. 2. Greyscale plot of the differential conductance G_ρ (units $e^2\Gamma_0^{(R)}$) as a function of s_B and n_g for $V \rightarrow 0$. $E_\rho = 5E_\sigma$, $k_BT = 0.1E_\sigma$, and other parameters as in Fig. 1. In each region, the corresponding ground state $|n, \bar{s}_n\rangle$ of the dot is shown. Starting with small values of n_g, peaks for the transitions $n = 0 \leftrightarrow n = 1$ and $n = 1 \leftrightarrow n = 2$ appear. With increasing B, the states $|n+1,1\rangle, |n,2\rangle, |n+1,3\rangle\ldots$ successively become ground states of the quantum dot. This is indicated by the zigzag behaviour of the conductance peak positions as a function of s_B

Figure 2 shows the linear conductance ($V \rightarrow 0$) in the plane of n_g and s_B. The zigzag behaviour of the peaks with increasing B is due to the fact that states with successively higher spins become ground states of the quantum dot.

With increasing voltage V, higher spin states can contribute to the transport. A scheme of the spin transitions near $|n,s\rangle \rightarrow |n+1, s\pm 1\rangle$, with n even and $0 < s_B < 1$, is shown in Fig. 3 together with numerical results for asymmetric barriers. When transitions to the state with $s = 2$ become possible, the latter accumulates transition probability at the expense of the states with $s = 1$ and $s = 0$ (Fig. 1). This leads to a negative differential conductance, indicated in the lower panel of the figure.

Figure 4 shows greyscale plots of the differential conductance G_ρ and spin conductance G_σ for asymmetric barriers ($R_R/R_L = 20$) in the plane of bias voltage V and magnetic field s_B, for a value of n_g in the Coulomb blocked region and n even, such that states with successively higher spins become ground states (cf. Fig. 2). For $V = 0$

(Fig. 4, top), we clearly observe the above-mentioned analogy between s_B and n_g. This is indicated by the equidistant conductance peaks at $s_B = 1/2, 3/2, 5/2, 7/2, \ldots$ and the constant current regions between them. In these regions, spin states with higher spins $s_B = 1, 2, 3, 4, \ldots$ become stabilized, in close analogy to the Coulomb blocked charge states along n_g at $V = 0$ for $s_B = 0$. As soon as higher spin states become occupied in the non-linear regime, the conductance becomes negative as mentioned earlier [5, 6].

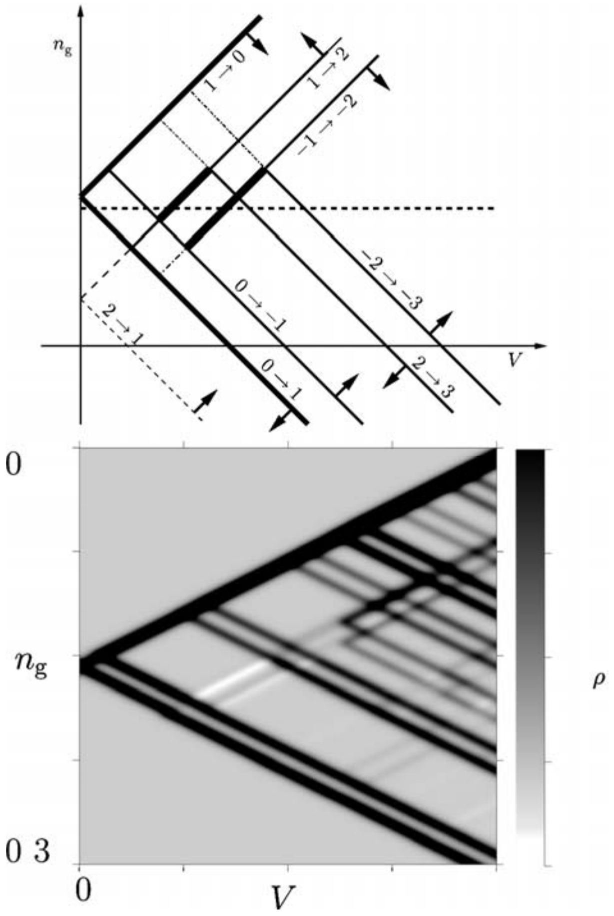

Fig. 3. Top: scheme of the possible transitions for sequential transport through a quantum dot, with $0 < s_B < 1$ in the plane of V (units E_σ/e) and n_g, around the resonance between the states $|n,0\rangle$ and $|n+1,1\rangle$, for even n and low spin values. Each transition line is labelled by the spin involved. Dashed transition lines do not contribute to the differential conductance. Dash-dotted lines: transitions involving a spin density wave. Arrows: movement of the transition lines with increasing B. Horizontal dotted line: cut along which the conductance, current polarization and occupation probabilities are shown in Fig. 1. Bold lines: regions of negative differential conductance. Bottom: greyscale plot of the differential conductance (arbitrary units) for $k_BT = 0.1E_\sigma$, and other parameters as in Fig. 1; black/white lines: positive/negative differential conductance

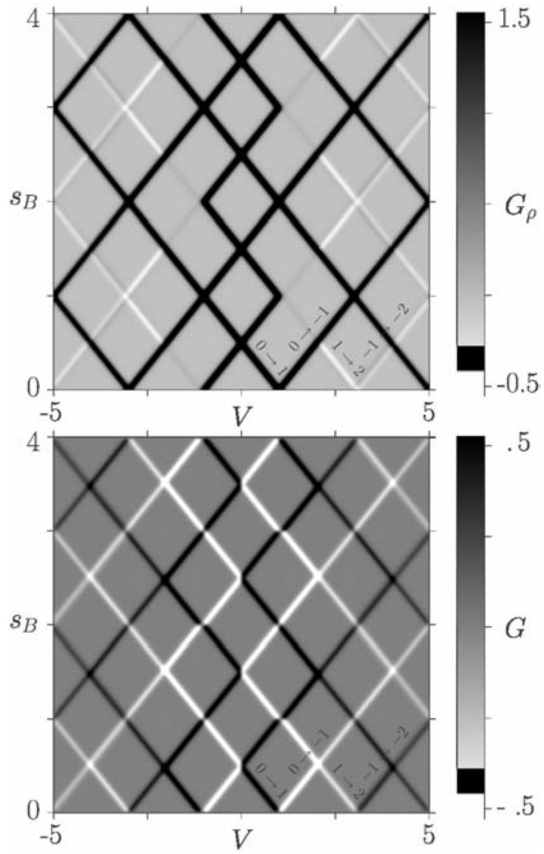

Fig. 4. Greyscale plots of differential conductances (units $e^2\Gamma_0^{(R)}/E_\sigma$) as a function of s_B and V (units E_σ/e), for $n_g = 0.5$ and even n, such that successively higher-spin states become ground states with increasing B; parameters: $g_\sigma = 1$, $g_\rho = 0.4$, $E_\rho = 25E_\sigma$, $k_BT = 0.02E_\sigma$ and $R_R/R_L = 20$. Top: total conductance G_ρ; starting with small values of s_B, for $V = 0$ equidistant conductance peaks occur at $s_B = 1/2, 3/2, 5/2, 7/2$ ... for the ground-state-to-ground-state transitions $|n,0\rangle >\leftrightarrow |n+1,1\rangle$, $|n+1,1\rangle >\leftrightarrow |n,2\rangle$, etc. Bottom: spin conductance G_σ; exactly at $V = 0$, the spin conductance vanishes, since temperature is finite; spin conductance becomes large when the transition lines involved with higher spin states intersect

The behaviour of the spin conductance (Fig. 4, bottom) is the most interesting. The spin conductance vanishes for non-zero temperature exactly at zero bias voltage, since positive and negative spin conductances cancel around $V = 0$ in the temperature window given by k_BT. At the points where transition lines involving higher spins intersect, however, the spin conductance is enhanced. This is related to the fact that the spin polarization p changes from positive to negative at these points.

3. Spin polarization via spin-orbit interaction

In this section, we investigate the influence of spin-orbit scattering on transport through quantum wires and dots in the metallic regime, i.e. where resistance is of the order of resistance quantum, $R \approx h/e^2$. We will show that even without a magnetic field the current can become spin polarized, given the quantum structure is suitably contacted.

3.1. Spin-orbit Hamiltonian

In the inversion layer of heterostructures, spin-orbit interaction can be described in the effective mass approximation by the Rashba Hamiltonian [18]

$$H_R = \frac{1}{2m}\left(\vec{p}+e\vec{A}\right)^2 + V\left(x,y\right) + \frac{1}{2}g\mu_B B\sigma_z - \frac{\alpha}{\hbar}\left[\left(\vec{p}+e\vec{A}\right)\times\vec{\sigma}\right] \tag{19}$$

Here, $\vec{p} = \left(p_x, p_y\right)$ is the momentum operator in the plane of the inversion layer, $\vec{A}$ is the vector potential of the magnetic field $\vec{B} = \left(0,0,B\right)$ perpendicular to the inversion layer, m is the effective mass, g is the Landé factor of the electron and $V(x,y)$ is an additional confining potential. The Rashba parameter α describes the average strength of the electric field, due to the asymmetric potential well confining electrons in the inversion layer at $z = 0$. In general, in addition to the Rashba term, there is also a band structure contribution [19], due to the absence of inversion symmetry. It can be neglected in InAs, in which Rashba spin-orbit interaction is strong.

For a zero magnetic field and no additional confinement, the Rashba Hamiltonian can be diagonalised. The energy eigenvalues are

$$E_\pm = \frac{\hbar^2}{2m}k^2 \pm \alpha k \tag{20}$$

and the corresponding eigenspinors

$$\psi_{1,2} = \begin{pmatrix} 1 \\ \pm e^{-i\varphi} \end{pmatrix} e^{i\vec{k}\cdot\vec{r}} \tag{21}$$

with $\vec{k} = \left(k_x, k_y\right)$, $\vec{r} = \left(x, y\right)$, $k_y = k\cos\varphi$, and $k_x = k\sin\varphi$. For a given energy, there are two wave numbers contributing to the propagation of the particle. This has two important consequences. First, the spin rotates upon propagation in a given direction. A spin-up state at $x = 0$ will be converted into a spin-down state at $x\ \pi/\Delta k \equiv \pi\hbar/2m\alpha$. This may be easily seen by considering one-dimensional propagation in the x-direction. Second, when a plane wave with a given wave vector and energy is reflected from a hard wall, say along the x-direction, the reflected wave consists of partial waves with different x-components of the wave vector. This implies that there is a spatial modulation of the spin polarization, which depends on the incidence angle of the plane wave. This is a special case of a general result in quantum mechanical scattering theory, namely that the spin polarization of the scattering wave function of a strong spin-orbit scatterer is spatially modulated [14]. Generally, this is simply a consequence of the spin *not* being a good quantum number due to the spin-orbit scattering term in the Hamiltonian. It should be emphasized that in equilibrium, without a magnetic field, this does not yield any spin polarization. Since the Hamiltonian is time reversal invariant, such that Kramers degeneracy remains intact, each energy corresponds to two degenerate states, which have exactly opposite spin polarizations. In the above example of Rashba states, these degenerate are the states with opposite wave vectors.

3.2. Spin polarization in a quantum wire

As a more detailed illustration, we consider the states in a quasi-one dimensional system described by Eq. (19), along the y-direction with a symmetric confinement $V(x) = V(-x)$ and $B = 0$. In this case, the Hamiltonian commutes with p_y and the unitary operator

$$U_x = P_x \sigma_x \tag{22}$$

where P_x is the inversion operator for the x-coordinate. Without spin-orbit interaction, P_x and σ_x are conserved separately. The operator U_x is called spin parity. This symmetry is broken for $B \neq 0$.

Spin parity symmetry at $B = 0$ has two consequences. First, there is a degeneracy of the energy spectrum at $k = 0$, even without Zeeman splitting. This degeneracy disappears for $B \neq 0$, which yields a quantisation of the dc conductance, in units of e^2/h instead of $2e^2/h$, as a function of the Fermi energy. The latter is significantly different from that due to simple Zeeman splitting of the subbands (Fig. 5). For large B, the splitting of energy bands converges towards spin split Landau levels.

Second, at $B = 0$, spin-parity invariance $[H,U_x] = 0$ implies, for the components of an eigenspinor of the Hamiltonian

$$\psi(x,y) = e^{ik_y y} \begin{pmatrix} \psi^{\uparrow}(x) \\ \psi^{\downarrow}(x) \end{pmatrix} \tag{23}$$

the symmetry property

$$\psi^{\uparrow}(x) = \pm \psi^{\downarrow}(-x) \tag{24}$$

This, for the *local* spin density in a given eigenstate, in general yields

$$\sigma_z(x) = \left|\psi^{\uparrow}(x)\right|^2 - \left|\psi^{\downarrow}(x)\right|^2 = \left|\psi^{\uparrow}(x)\right|^2 - \left|\psi^{\uparrow}(-x)\right|^2 \neq 0 \tag{25}$$

since P_x alone is not a symmetry operation. The average spin density vanishes for $B = 0$, but $\langle \sigma_z \rangle \neq 0$ for $B \neq 0$. Also, due to Kramers degeneracy, the local spin density at a given energy vanishes for $B = 0$, since there is a second, time-reversed state, corresponding to the wave vector $-k_y$ if the former had k_y, with exactly the opposite polarization.

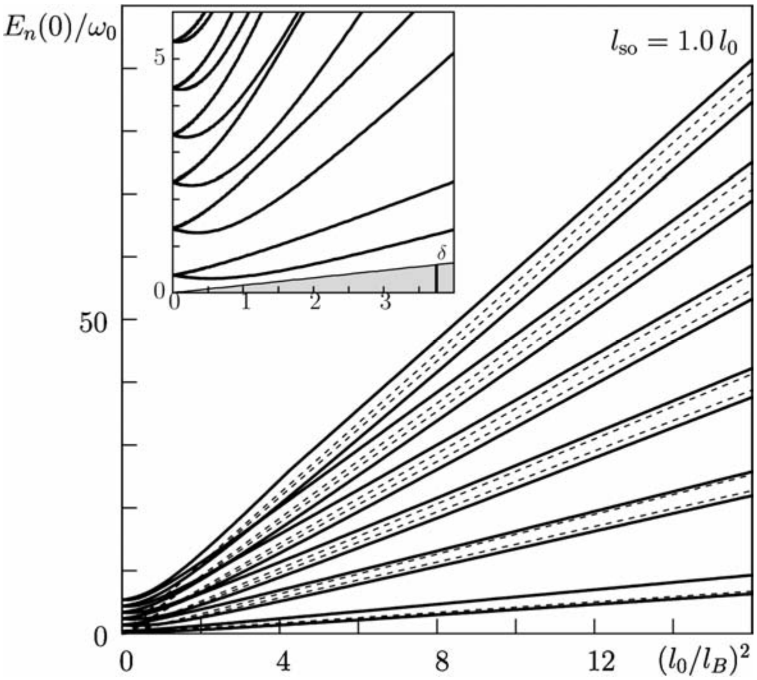

Fig. 5. The lowest twelve eigenenergies of a quantum wire at $k = 0$ as a function of the magnetic field, for $l_{SO} = l_0$ and typical InAs parameters: $\alpha = 1.0\times10^{-11}$ eVm, $g = -8$, and $m = 0.04m_0$. Dashed lines: a fan of Landau levels $\hbar\omega_C(n + 1)/(n + 1/2) \pm \delta/2$; inset: results for low fields; shaded region: bulk Zeeman splitting δ

In order to obtain a non-zero polarization at a given energy, time reversal symmetry has to be broken. This can normally be achieved by applying a magnetic field or by magnetic scattering.

3.3. The conductance of a spin-orbit scatterer

Even without a magnetic field, however, the time reversal symmetry can be broken, namely by injecting a current into the system and thus generating a stationary non-equilibrium state. This can be done in a transport experiment. Quantum mechanically, this corresponds to a scattering experiment in which an incoming wave with wave number $\vec{k}$ is scattered. The stationary scattering wave function, corresponding to a *given* wave vector, will thus exhibit a spatial modulation of the spin polarization for a spin-orbit scatterer. If such a wave function is then locally probed, it should be possible to detect local spin polarization.

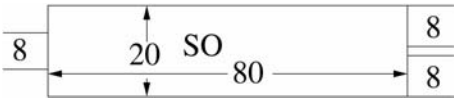

Fig. 6. The fork-shaped three-terminal device used for calculating the quantum conductance shown in Fig. 7. The conductance is measured between the left and uppermost right contacts

In nanostructured quantum systems, such local probing can be achieved by contacting the system and performing a dc-transport experiment. Theoretically, this can be done by calculating the conductance via the Landauer formula

$$G = \frac{e^2}{h} \mathrm{Tr} t^{+} t \tag{26}$$

with t being the transmission matrix of the scatterer.

For numerical purposes, it is convenient to use the corresponding tight binding Hamiltonian [20] instead of Eq. (19). On a two dimensional lattice with ($l.m$) points and a lattice constant a

$$H = V \sum_{lm} \begin{pmatrix} \cos\theta & i\sin\theta \\ i\sin\theta & \cos\theta \end{pmatrix} |lm-1\rangle\langle lm| + \begin{pmatrix} \cos\theta & -\sin\theta \\ \sin\theta & \cos\theta \end{pmatrix} |l-1m\rangle\langle lm| + h.c \tag{27}$$

where $V(\cos\theta(= \hbar^2/2ma^2)$ is the energy unit, and the angle θ describes the spin-orbit scattering. This angle can be related, via the discretisation of Eq. (19), to the parameter α according to

$$\tan\theta = \frac{ma\alpha}{\hbar^2} \tag{28}$$

Numerical results for the spin-resolved conductance of a rectangular quantum dot attached to three quantum wires (Fig. 6) are shown in Fig. 7. Current flows from the contact on the left hand side to the contact on the upper right. The predicted strong spin polarization due to spin-orbit scattering of the conductance is clearly observed at certain Fermi energies.

4. Conclusion

In this contribution, we have discussed several features of the transport properties of quantum dots related to electron spin. Two transport regions have been considered. In sequential transport, we have described features related to the occupation of correlated many-electron states with higher total spins, namely the spin blockade phenomena that lead to negative differential conductance in the non-linear transport regime. We have seen that these higher spin states also give rise to strong differential spin conductances in the presence of a magnetic field in the quantum dot.

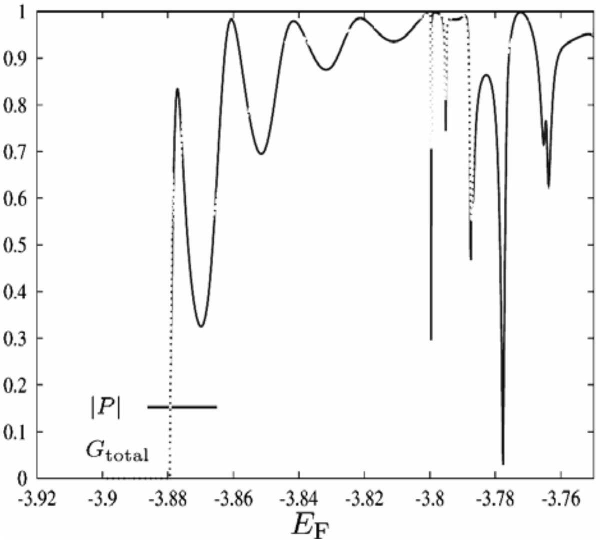

Fig. 7. The linear total conductance (dashed, units e^2/h) and the spin polarization $\vec{P} = \mathrm{Tr}\left(t^{+}\vec{\sigma}t\right)/G_{\text{total}}$ (full line) as functions of the Fermi energy of a rectangular quantum dot connected to three leads in the geometry of a fork

Furthermore, we have considered a spin-orbit scatterer in the quantum coherent metallic regime. We have argued that scattering states exhibit a spatial modulation of spin polarization. When time reversal invariance is broken, this can be used to generate a spin-polarized current, even when no magnetic field is applied and no magnetization is present. It has been argued that such a situation can be achieved in stationary non-equilibriums such as a dc-transport experiment.

The effects discussed here might be of importance for designing a pure-semiconductor based spin transistor.

Acknowledgments

This work was supported by the EU via contracts FMRX-CT98-0180 and HPRN-CT2000-00144, and by the Deutsche Forschungsgemeinschaft via SFB 508 of the Universität Hamburg and the

Graduiertenkolleg *Nanostrukturierte Festkörper*. Useful discussions with Stefan Kettemann, Tobias Brandes, and Tomi Ohtsuki are gratefully acknowledged.

References

[1] *Quantum transport in semiconductor submicron structures*, B. Kramer (Ed.), NATO ASI Ser. E 326, Kluwer Acad. Publ., Dordrecht, 1996; *Semiconductor quantum structures*, B. Kramer (Ed.), Landolt-Börnstein, New Series, Group III, Vol. 34, Subvol. B, Part 1, *Quantum point contacts and quantum wires*, Springer Verlag, Berlin 2001; *Mesoscopic Electron Transport*, L.L. Sohn, L.P. Kouwenhoven, and G. Schön (Eds.), Kluwer Acad. Publ., Dordrecht, 1997.

[2] *Semiconductor spintronics and quantum computation,* D.D. Awshalom, D. Loss, N. Samarth (Eds.), Springer Verlag, Berlin, 2002; WOLF S.A., AVSCHALON D.D., BUHRMAN R.A., DAUGHTON J.M., VON MOLNÁR S., ROUKES M.L., CHTCHELKANOVA A.Y., TREGER D.M., Science, 294 (2001), 1488.

[3] DATTA S., DAS B., Appl. Phys. Lett., 56 (1990), 665.

[4] WEINMANN D., HÄUSLER W., KRAMER B., Phys. Rev. Lett., 74 (1995), 984.

[5] CAVALIERE F., BRAGGIO A., STOCKBURGER J.T., SASSETTI M., KRAMER B., Phys. Rev. Lett., 93 (2004), 036803.

[6] CAVALIERE F., BRAGGIO A., SASSETTI M., KRAMER B., Phys. Rev. B, 70 (2004), 125323.

[7] BRATAAS A., NAZAROV YU.V., BAUER G.E.W., Phys. Rev. Lett., 84 (2000), 2481.

[8] BRUNO P., Phys. Rev. Lett., 79 (1997), 4593.

[9] PAREEK T.P., BRUNO P., Phys. Rev. B, 63 (2001), 165424.

[10] KISELEV A.A., KIM K.W., Appl. Phys. Lett., 78 (2001), 775.

[11] DITTMER K., Diplomarbeit, Universität Hamburg, 2004.

[12] PAREEK T.P., Phys. Rev. Lett., 92 (2004), 076601.

[13] KHODAS M., SHEKHTER A., FINKELSTEIN A.M., Phys. Rev. Lett., 92 (2004), 086602.

[14] LANDAU L.D., LIFSHITZ E.M., *Theoretical Physics*, Vol. 3, *Quantum Mechanics*, Pergamon Press, Oxford, 1980.

[15] BRAGGIO A., SASSETTI M., KRAMER B., Phys. Rev. Lett., 87 (2001), 146802.

[16] KLEIMANN T., SASSETTI M., KRAMER B., YACOBY A., Phys. Rev. B, 62 (2000), 8144; KLEIMANN T., CAVALIERE F., SASSETTI M., KRAMER B., Phys. Rev. B, 66 (2002), 165311.

[17] KHAETSKII A.V., NAZAROV YU.V., Phys. Rev. B, 61 (2000), 12639.

[18] RASHBA E.I., Fiz. Tverd. Tela, 2 (1960), 1224 (Sov. Phys. Sol. State, 2 (1969), 1109); BYCHKOV YU.A., RASHBA E.I., Pis'ma Zh. Eksp. Teor. Fiz., 39 (1984), 66 (Sov. Phys. JETP Lett., 39 (1984), 78).

[19] DRESSELHAUS G.F., Phys. Rev., 100 (1955), 580.

[20] ANDO T., Phys. Rev. B, 40 (1989), 5325.

Received 5 November 2004
Revised 10 November 2004

Materials Science-Poland, Vol. 22, No. 4, 2004

Spin-dependent transport in ferromagnetic single-electron transistors with non-collinear magnetizations

JUSTYNA WIŚNIEWSKA[1*], IRENEUSZ WEYMANN[1], JÓZEF BARNAŚ[1,2]

[1]Department of Physics, Adam Mickiewicz University, Umultowska 85, 61-614 Poznań, Poland

[2]Institute of Molecular Physics, Polish Academy of Sciences,
Smoluchowskiego 17, 60-179 Poznań, Poland

Electronic transport in a ferromagnetic single-electron transistor is analysed theoretically in the sequential tunnelling regime. One of the external electrodes and the central part (island) of the device are assumed to be ferromagnetic, with the corresponding magnetizations being non-collinear. The analysis is based on the master equation method, and the respective transition rates are determined from the Fermi golden rule. It is shown that the electric current and corresponding tunnel magnetoresistance (TMR) strongly depend on the angle between the magnetizations. For an arbitrary magnetic configuration, TMR is modulated by charging effects, which give rise to characteristic dips (cusps) at the bias voltages corresponding to the Coulomb steps in the current–voltage characteristics.

Key words: *single electron transistor; spin-polarized transport; tunnel magnetoresistance*

1. Introduction

Electronic transport in single electron transistors (SETs) with nonmagnetic islands has already been the subject of extensive experimental and theoretical studies [1–3]. The problem of spin-polarized transport in SETs based on quantum dots or metallic particles, however, has been addressed only recently [4–6]. The transport properties of such devices have mainly been investigated in situations where magnetic moments are aligned either in parallel or antiparallel. Nevertheless, in real systems the magnetic moments of the leads can form an arbitrary angle and such a non-collinear configuration may strongly affect transport characteristics.

---

[*] Corresponding author, e-mail: justynka@spin.amu.edu.pl.

In this paper, we present the results of our theoretical analysis of spin-polarized electronic transport in a ferromagnetic single-electron transistor (FM SET), whose one external electrode and the central part (referred to as the island) are ferromagnetic, while the second external electrode is nonmagnetic. The angle β between the spin polarizations of the ferromagnetic lead and the island is arbitrary. Our main objective is to analyse the dependence of electric current and tunnel magnetoresistance (TMR) on the angle β. It is shown that the transport characteristics of an FM SET strongly depend on its magnetic configuration. Such a dependence stems from the spin asymmetry of tunnelling rates for spin-majority and spin-minority electrons.

In order to analyse transport in FM SETs, we have employed the lowest-order perturbation theory. The corresponding transition rates are then given by the Fermi golden rule, whereas the relevant probabilities that the island is in respective charge states are determined from the appropriate master equation. We have analysed numerically the electric current flowing through the system and the corresponding TMR in various magnetic configurations. It is shown that both current and TMR exhibit a nontrivial dependence on the angle between magnetic moments of the ferromagnetic lead and island. In addition, discrete charging has been shown to modulate TMR, with characteristic dips (or cusps) at the bias voltages corresponding to the Coulomb steps.

The consecutive sections of this paper deal with the following. In Section 2 we present the model and theoretical description, numerical results are shown and discussed in Section 3, and conclusions are given in Section 4.

2. Model and theoretical description

A scheme of the single-electron transistor under consideration is shown in Fig. 1. The first lead as well as the island is made of a ferromagnetic material, whereas the second lead is nonmagnetic. There is a nonzero angle β between the spin moments of the left electrode and island. Further, a gate voltage is attached capacitively to the island, enabling a tuning of system operation.

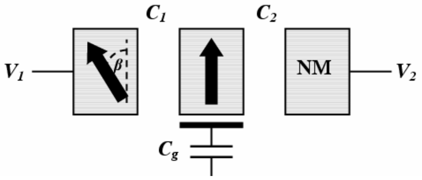

Fig. 1. Schematic diagram of the ferromagnetic single-electron transistor. The arrows indicate the net spin moments of the island and left electrode, forming an angle β. The electrode on the right is nonmagnetic

If thermal energy is smaller than the charging energy, then the energy needed to transfer an extra electron onto the island becomes dominant and establishes a new relevant energy scale. Discrete charging effects then become observable and the current flowing through the system displays current–voltage characteristics with typical Coulomb steps. Apart from this, Coulomb oscillations of electric current occur with increasing gate voltage. We show that these effects lead to characteristic dips (cusps) in TMR with increasing bias voltage.

When the applied voltage does not exceed a certain threshold voltage, sequential tunnelling is exponentially suppressed and the system is in the Coulomb blockade regime. Although first-order tunnelling is then prohibited by the energy conservation rule in the Coulomb blockade, the current can still be mediated by higher-order tunnelling processes (like co-tunnelling) which take place through the virtual states of the island.

In our considerations, however, we take into account only sequential tunnelling processes and assume that the contribution coming from higher-order processes is small compared to the first-order. This is justifiable when the barrier resistances significantly exceed the quantum resistance, $R_j >> R_q = h/e^2$ (j = 1, 2), which implies that the island is in a well defined charge state and the orthodox tunnelling theory is applicable. Electrical resistance of the first (left) tunnel barrier depends on the tunnelling matrix elements between the corresponding states in the left lead and the island, which in turn depend on the relative angle between their magnetizations. The resistance of the second barrier is independent of the magnetic configuration. We further take into account only spin-conserving tunnelling processes and assume that spin relaxation time on the island is shorter than the time between two successive tunnelling events, which means that there is no spin accumulation. Moreover, the island is assumed to be relatively large, so that the quantization of the corresponding energy levels can be neglected.

Electric current flows through the system due to successive tunnelling events. The tunnelling rate of a spin-majority (+) electron from the first lead to the spin-minority (–) electron band in the island can be expressed in terms of the Fermi golden rule as:

$$\Gamma_{1\to i}^{+-} = \frac{2\pi}{\hbar} \left| \langle \Psi_{1+} | H_T | \Psi_{i-} \rangle \right|^2 \delta(\varepsilon_f - \varepsilon_i) \tag{1}$$

where $|\Psi_{1+}\rangle$ and $|\Psi_{i-}\rangle$ are the wave functions for majority electrons in the first electrode and minority electrons in the island, respectively, ε_i (ε_f) is the energy of the initial (final) state of the system, whereas H_T is the tunnelling Hamiltonian. The wave functions are written in local reference systems (with local quantization axes determined by the local spin moments). As the global reference system, we assume the local one in the island. When a bias voltage V is applied to the system, the tunnelling rates from the first (ferromagnetic) lead to the island, which is already occupied by N excess electrons, can be written in the form:

$$\Gamma_{1\to i}^{++}(N,V) = \cos^2\frac{\beta}{2}\,\Gamma_{1\to i}^{p+}(N,V) \tag{2a}$$

$$\Gamma_{1\to i}^{--}(N,V) = \cos^2\frac{\beta}{2}\,\Gamma_{1\to i}^{p-}(N,V) \tag{2b}$$

$$\Gamma_{1\to i}^{+-}\left(N,V\right)=\sin^2\frac{\beta}{2}\Gamma_{1\to i}^{ap}\left(N,V\right) \tag{2c}$$

$$\Gamma_{1\to i}^{-+}\left(N,V\right)=\sin^2\frac{\beta}{2}\Gamma_{1\to i}^{ap}\left(N,V\right) \tag{2d}$$

with $\Gamma_{1\to i}^{p+(-)}\left(N,V\right)$ denoting the tunnelling rate of spin majority (+) and spin minority (–) electrons in the parallel configuration, whereas $\Gamma_{1\to i}^{ap}\left(N,V\right)$ is the tunnelling rate for both spin orientations in the antiparallel configuration. The tunnelling rates $\Gamma_{1\to i}^{p+(-)}\left(N,V\right)$ are defined as:

$$\Gamma_{1\to i}^{p+(-)}\left(N,V\right)=\frac{1}{e^2R_1^{p+(-)}}\frac{\Delta E_1\left(N,V\right)}{\exp[\Delta E_1\left(N,V\right)/k_BT]-1} \tag{3}$$

where $-e$ is the electron charge ($e > 0$), $R_1^{p+(-)}$ denotes the spin-dependent resistance of the left junction in the parallel configuration, k_B is the Boltzmann constant, and T stands for temperature. Here, $\Delta E_1(N,V)$ describes a change in the electrostatic energy of the system caused by the respective tunnelling event. A similar expression also holds for $\Gamma_{1\to i}^{ap}\left(N,V\right)$, but with $R_1^{p+(-)}$ replaced by R_1^{ap}. Since both ferromagnetic electrodes are assumed to be made of the same material, R_1^{ap} is independent of the electron spin. In a similar way one can derive the tunnelling rates from the island back to the first electrode.

The rates for tunnelling through the second junction are also spin-dependent, but they are independent of the angle β. For any magnetic configuration, they are given by formula (3) with $R_1^{p+(-)}$ replaced by $R_2^{+(-)}$ and $\Delta E_1(N,V)$ replaced by $\Delta E_2(N,V)$.

The electrostatic energy of the system is given by:

$$E\left(N,Q\right)=\frac{\left(Ne-Q\right)^2}{2C} \tag{4}$$

where $C = C_1 + C_2 + C_g$ is the total capacitance of the island, C_1 and C_2 are the capacitances of the first and second junctions, C_g is the gate capacitance, whereas $Q = C_1V_1 + C_2V_2 + C_gV_g$ represents the charge on the island induced by the applied voltages.

In order to calculate the electric current flowing through the system in a stationary state, we take into account the fact that the net transition rate between charge states with N and $N + 1$ excess electrons on the island is equal to zero in a steady state [7]. The corresponding master equation then determines the probability $P(N,V)$ of finding the island in a state with N excess electrons when a bias voltage V is applied to the system. The steady-state master equation reads:

$$
\begin{aligned}
&- \sum_{\sigma,\sigma'=+,-} \left[\Gamma^{\sigma\sigma'}_{1\to i}(N,V) + \Gamma^{\sigma\sigma'}_{i\to 1}(N,V) + \Gamma^{\sigma}_{2\to i}(N,V) + \Gamma^{\sigma}_{i\to 2}(N,V)\right] P(N,V) \\
&+ \left[\sum_{\sigma,\sigma'=+,-} \Gamma^{\sigma\sigma'}_{1\to i}(N-1,V) + \sum_{\sigma=\uparrow,\downarrow} \Gamma^{\sigma}_{2\to i}(N-1,V)\right] P(N-1,V) \\
&+ \left[\sum_{\sigma,\sigma'=+,-} \Gamma^{\sigma\sigma'}_{i\to 1}(N+1,V) + \sum_{\sigma=\uparrow,\downarrow} \Gamma^{\sigma}_{i\to 2}(N+1,V)\right] P(N+1,V) = 0
\end{aligned}
\tag{5}
$$

Finally, the electric current flowing through the system can be calculated from the formula:

$$
I(V) = -e \sum_{\sigma,\sigma'=+,-} \sum_{N=-\infty}^{\infty} \left[\Gamma^{\sigma,\sigma'}_{1\to i}(N,V) - \Gamma^{\sigma,\sigma'}_{i\to 1}(N,V)\right] P(N,V) \tag{6}
$$

Equation (6) corresponds to the current flowing through the first junction, which in the stationary limit is equal to the current flowing through the second junction.

3. Numerical results and discussion

Equation (6) can be used to calculate the tunnelling current for any magnetic configuration. For a given bias voltage V, the tunnel magnetoresistance is quantitatively described by the ratio

$$
TMR = \frac{I(\beta = 0) - I(\beta)}{I(\beta)} \tag{7}
$$

where $I(\beta)$ is the current flowing when the angle between spin moments of the lead and island is equal to β ($\beta = 0$ corresponds to the parallel configuration). Below we present the results of our numerical calculations of electric current flowing through the system and the corresponding *TMR* as a function of the bias voltage (Fig. 2) and the angle β (Fig. 3).

For all magnetic configurations, the dependence of electric current on the bias voltage is non-linear and exhibits characteristic Coulomb steps, as shown explicitly in Fig. 2a for a few values of the angle β. The electric current decreases with increasing angle over the whole bias range. This dependence of electric current on magnetic configuration leads to a non-zero TMR effect, as shown in Fig. 2b. Two local minima (dips) in TMR, visible in Fig. 2b, occur at bias voltages corresponding to the positions of Coulomb steps in the current–voltage characteristics of Fig. 2a. It is worth noting that this is not a general behaviour and that for some other parameters one finds maxima (cusps) instead of minima in TMR at the current steps [5]. It also follows from Fig. 2b that the magnitude of TMR increases monotonously with an increasing angle between magnetizations.

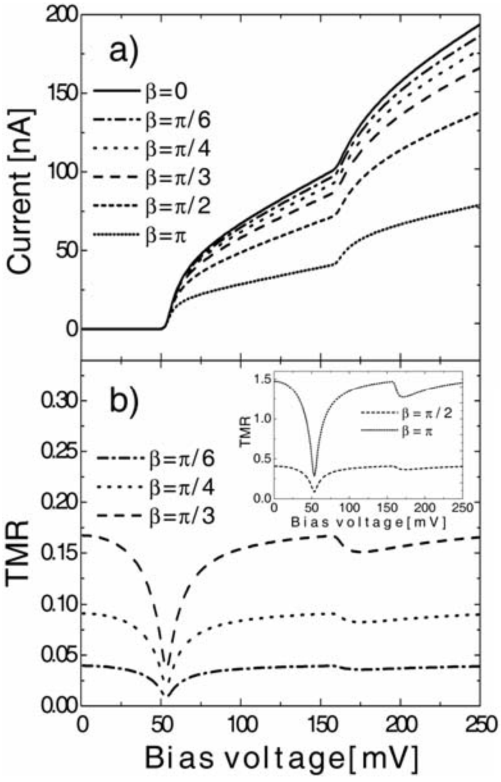

Fig. 2. The bias dependence of electric current (a) and TMR (b) in a symmetrically biased ($V_1 = V/2$, $V_2 = -V/2$) FM SET with non-collinear magnetizations for several values of the angle between magnetic moments. The parameters used in the numerical calculations are: $C_1 = C_2 = C_g$ 1 aF, V_g 0, $R_1^{p+} = 25$ MΩ, $R_1^{p-} = 1$ MΩ, $R_2^{+} = 0.5$ MΩ, $R_2^{-} = 0.1$ MΩ, and $R_1^{ap+} = R_1^{ap-} = \sqrt{R_1^{p+} R_1^{p-}}$

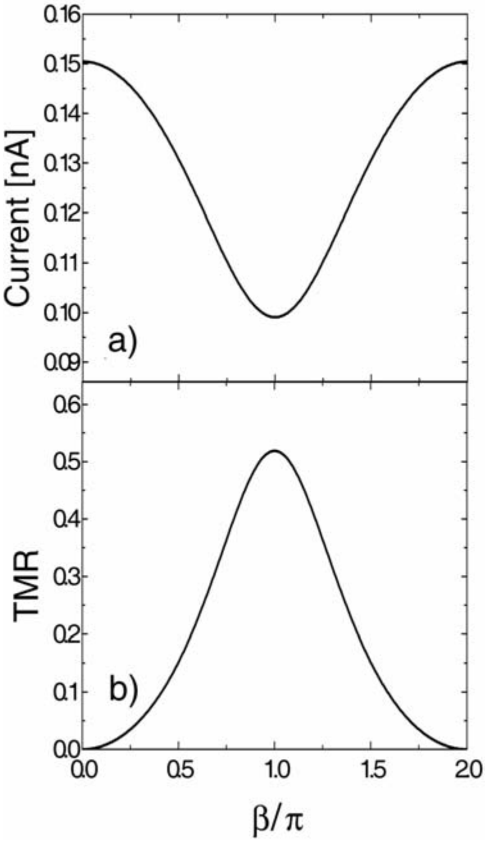

Fig. 3. Electric current (a) and the corresponding tunnel magnetoresistance (b) as a function of the angle between spin moments of the left lead and island. The bias voltage is $V = 50$ mV ($V_1 = 25$ mV, $V_2 = -25$ mV), while the other parameters are the same as in Fig. 2

The dependence of electric current flowing through the system on the angle β, and the corresponding TMR, are shown explicitly in Fig. 3a and b, respectively, for a particular bias voltage. The minimum in electric current occurs in the antiparallel magnetic configuration, which corresponds to a maximum in TMR. This behaviour is qualitatively similar to the normal spin valve effect observed in magnetic layered structures.

4. Conclusions

In this paper, we have calculated and analysed in detail the current flowing through a ferromagnetic single-electron transistor with non-collinear magnetizations and the corresponding tunnel magnetoresistance. The FM SET device consists of a ferromagnetic island and one ferromagnetic electrode, whereas the second external electrode is nonmagnetic. The bias dependence of electric current reveals a characteristic Coulomb staircase. Furthermore, the current flowing through the system, as well as the tunnel magnetoresistance, strongly depend on the angle between magnetizations.

References

[1] GRABERT H., DEVORET M.H., *Single Charge Tunnelling*, NATO ASI Series, Vol. 294, Plenum Press, New York, 1992.
[2] AVERIN D.V., KOROTKOV A.N., LIKHAREV K.K., Phys. Rev. B, 44 (1991), 6199.
[3] SCHOELLER H., SCHÖN G., Phys. Rev. B, 50 (1994), 18436.
[4] BARNAŚ J., FERT A., Phys. Rev. Lett., 80 (1998), 1058.
[5] TAKAHASHI S., MAEKAWA S., Phys. Rev. Lett., 80 (1998), 1758.
[6] WEYMANN I., BARNAŚ J., Phys. Status Solidi, 236 (2003), 651.
[7] AMMAN M., WILKINS R., BEN-JACOB E., MAKER P.D., JAKLEVIC R.C., Phys. Rev. B, 43 (1991), 1146.

Received 14 September 2004
Revised 28 October 2004

Materials Science-Poland, Vol. 22, No. 4, 2004

Weak antilocalization and spin relaxation in integrable quantum dots

OLEG ZAITSEV[*], KLAUS RICHTER

Institut für Theoretische Physik, Universität Regensburg, D-93040 Regensburg, Germany

We study spin relaxation and weak (anti)localization arising from Rashba spin-orbit interaction in ballistic quantum dots with integrable orbital dynamics. We employ a recently developed semiclassical theory for spin-dependent quantum magneto-transport to reveal the dependence of spin dephasing on different types of regular, spatially confined motion. In particular, we analytically derive spin relaxation in circular cavities and compare it with corresponding numerical results. Moreover, we show that different integrable confinement geometries show remarkable differences in their spin evolution.

Key words: *spin relaxation; antilocalization; spin dephasing; circular cavity*

1. Introduction

During the last years research on the effects of spin-orbit (SO) interactions on transport has again received increasing attention. The reason for the revival of such studies, both experimentally and theoretically, lies in an important role SO interactions play in spin electronics and spin-based quantum information processing: in spintronics research, spin interference devices have been suggested, such as spin transistors [1], spin rotators [2], and spin pumps [3], based on SO interactions; in proposals for spin-based quantum computing using quantum dots, SO effects can influence the time scales T_1 for coherent spin relaxation (dephasing) and T_2 for decoherence processes [4].

A useful experimental probe for SO-effects in quantum transport is, on one hand, the beating pattern of Shubnikov-de Haas oscillations in the magneto-conductivity of high-mobility bulk semiconductors [5, 6], which, however, require additional moderate magnetic fields. On the other hand, weak localization (WL) and antilocalization (AL) are prominent examples for SO-interaction-induced quantum interference effects on the conductance in low-dimensional electronic systems [7, 8]. While WL arises

---

[*] Corresponding author, e-mail: oleg.zaitsev@physik.uni-regensburg.de.

from the constructive interference of backscattered waves, reducing the conductance for systems with time-reversal symmetry, SO coupling turns constructive interference into destructive interference and hence causes an enhanced conductance, i.e. AL. Recently, weak AL has been reconsidered in a number of corresponding experiments, both for GaAs- [9] and InAs-based [6, 10, 11] two-dimensional (2d) electron gases, as well as for ballistic quantum dots [12, 13]. While SO scattering in (disordered) bulk systems is reasonably well understood [8], the new experiments pose the question of how spatial confinement affects spin relaxation, which is also theoretically of interest and pertinent for the proposals on quantum dot-based quantum computing.

Hence, recently a number of theoretical papers appeared that treat spin relaxation and the interplay between SO and Zeeman coupling in quantum dots [14–17]. Most of these approaches, however, rely on random-matrix assumptions [15, 16, 18, 19], thereby assuming disordered or completely chaotic cavities. In this contribution, we will focus on the opposite case, on integrable confinement geometries giving rise to regular orbital dynamics, where random matrix theory (RMT) is not applicable. To this end, we will employ a recently developed semiclassical approximation to the Landauer formula for spin-dependent quantum transport [17, 20]. This approach constitutes a link between classical orbital dynamics and quantal spin evolution, and it is rather generally applicable to quantum dots with different types of classical dynamics. In a first application of this tool, spin relaxation in extended disordered and confined ballistic systems with Rashba SO interaction has been compared [17]. As a result, spin relaxation is much slower in confined chaotic cavities than for diffusive motion, in accordance with experiments [12] and related theoretical work [14, 18]. Moreover, this preliminary analysis reveals that certain integrable confinement potentials give rise to a saturation of spin relaxation, i.e. an initial spin polarization is preserved to a certain degree even for long times.

Here we will address this interesting finding in detail and present a case study for two representative examples of integrable quantum dots that give rise to rather distinct spin evolution behaviours: a circular billiard with conserved angular momentum and its desymmetrised version, a quarter circle in which angular momentum is no longer a constant of motion. Spin relaxation in the circular geometry has also been recently numerically studied in a closely related semiclassical approach [21]. Here, besides presenting numerical results, we derive an analytical formula for the spin relaxation exhibiting characteristic oscillations. Furthermore, we include the effect of an additional magnetic flux and give predictions for weak (anti)localization for the two geometries.

2. Semiclassical Landauer formula for spin-dependent transport

We consider a Hamiltonian linear in the spin operator $\hat{\mathbf{s}}$

$$\hat{H} = \hat{H}_0(\hat{\mathbf{q}},\hat{\mathbf{p}}) + \hbar\hat{\mathbf{s}}\cdot\hat{\mathbf{C}}(\hat{\mathbf{q}},\hat{\mathbf{p}}) \qquad (1)$$

where $\hat{H}_0$ represents the spatial part, including the confinement potential, and $\hat{\mathbf{C}}(\hat{\mathbf{q}},\hat{\mathbf{p}})$ is a rather general vector function of the position and momentum operators $\hat{\mathbf{q}},\hat{\mathbf{p}}$. The term $\hat{\mathbf{C}}(\hat{\mathbf{q}},\hat{\mathbf{p}})$ can include SO coupling, as well as an external (inhomogeneous) magnetic field. For a large number of systems of interest, and usually in experiments, as in those mentioned above

$$\hbar s|\mathbf{C}(\mathbf{q},\mathbf{p})| \ll H_0 \tag{2}$$

even if the spin-precession length, i.e. the distance a particle travels in space during one period of precession of its spin vector, is of the order of the system size. In Eq. (2), s is the particle spin, and the phase-space functions without the hat denote the classical counterparts (Wigner–Weyl symbols) of the respective operators. As a consequence of inequality (2), the back action of the spin dynamics on orbital motion can be neglected. This regime, which we study in this paper, is formally realized by taking $\hbar \to 0$, while keeping all other quantities finite. This corresponds to the orbital subsystem H_0 being in the semiclassical regime, i.e. the typical classical actions $\mathcal{S} \gg \hbar$. In other words, the Fermi wavelength λ_F must be much smaller than the system, which is well fulfilled if the quantum dots are of μm size, as e.g. in Ref. [12].

Hence, only H_0 governs the classical trajectories $\gamma = (\mathbf{q}(t),\mathbf{p}(t))$, along which an effective time-dependent magnetic field $\mathbf{C}_\gamma(t) = \mathbf{C}(\mathbf{q}(t),\mathbf{p}(t))$ acts on spin via the Hamiltonian $\hat{H}_\gamma(t) = \hbar\hat{\mathbf{s}}\cdot\mathbf{C}_\gamma(t)$. We thus employ a *semiquantal* approach, in which the spin dynamics is treated *quantum-mechanically* in terms of a (time-ordered) propagator

$$\hat{K}_\gamma(t) = T\exp\left[-i\int_0^t dt'\,\hat{\mathbf{s}}\cdot\mathbf{C}_\gamma(t')\right] \tag{3}$$

In this way, a weak SO coupling was incorporated into the Gutzwiller trace formula [22] for the semiclassical density of states of s = 1/2-particles [23]. This approach was generalized to arbitrary spin using path integrals in orbital and spin variables [24, 25]; a general semiclassical approach to SO interaction, without relying on inequality (2) and including the back action of the spin onto the orbital degrees of freedom can be found in [24, 26].

Our approach to spin-dependent coherent quantum transport through quantum dots is based on a semiclassical Landauer formula [27, 28] that we generalize to systems with SO and Zeeman interaction. To this end, we start from the Landauer formula in 2d relating the two-terminal conductance $G = (e^2/h)\mathcal{T}$ to the transmission coefficient [29]

$$\mathcal{T} = \sum_{n=1}^{N'}\sum_{m=1}^{N}\sum_{\sigma,\sigma'=-s}^{s}\left|t_{n\sigma',m\sigma}\right|^2 \tag{4}$$

The leads support N and N' open orbital channels m and n, respectively. We distinguish $2s + 1$ spin polarizations in the leads, labelled by $\sigma = -s, ..., s$, and assume that there is no spin-orbit interaction or external magnetic field in the leads. In Eq. (4), $t_{n\sigma',m\sigma}$ is the transition amplitude between the incoming channel $|m,\sigma\rangle$ and outgoing channel $|n,\sigma'\rangle$; a corresponding equation holds for the reflection coefficient $\mathcal{R}$, satisfying the normalization condition $\mathcal{T} + \mathcal{R} = (2s+1)N$, which follows from the unitarity of the scattering matrix.

The transmission and reflection amplitudes can be represented with Green functions. Starting from a path-integral representation of the Green functions, and following the lines of [27] for the spinless case, our semiclassical evaluation yields the spin-dependent transmission amplitudes [20]

$$t_{n\sigma',m\sigma} = \sum_{\gamma(\bar{n},\bar{m})} (\hat{K}_{\gamma})_{\sigma'\sigma} \mathcal{A}_{\gamma} \exp\left(\frac{i}{\hbar}\mathcal{S}_{\gamma}\right) \tag{5}$$

The transmission amplitudes (and, again, correspondingly the reflection amplitudes) are semiclassically approximated as a coherent sum over classical transmitted (back-reflected) paths at fixed energy. A similar Ansatz has been used in Ref. [30]. The sum runs over classical trajectories $\gamma(\bar{n} = \pm n, \bar{m} = \pm m)$ that enter (exit) the cavity at "quantised" angles Θ_m ($\Theta_{\bar{n}}$), measured from the normal at the lead cross section. For hard-wall boundary conditions in the leads, $\sin\Theta_{\bar{m}} = \bar{m}\pi / kw$ and $\sin\Theta_{\bar{n}} = \bar{n}\pi / kw'$, where k is the wave number, and w, w' are the lead widths. In (5), $\mathcal{A}_{\gamma}$ is the classical stability amplitude [27], and $\mathcal{S}_{\gamma} = \int \mathbf{p} \cdot d\mathbf{q}$ is the action along a path γ. For the case of billiards considered below, $\mathcal{S}_{\gamma} = \hbar k L_{\gamma}$, where $L_{\gamma} = vT_{\gamma}$ is the orbit length, v is the magnitude of the (Fermi) velocity, and T_{γ} is the time. The entire spin effect is contained in the matrix elements $(\hat{K}_{\gamma})_{\sigma'\sigma}$ of the spin propagator $\hat{K}_{\gamma} \equiv \hat{K}_{\gamma}(T_{\gamma})$ (Eq. (3)) between the initial and final spin states.

Inserting Eq. (5) into (4), we find the transmission $\mathcal{T}$ and reflection $\mathcal{R}$ for spin-dependent magneto-transport in a semiclassical approximation [17]

$$(\mathcal{T}(E,\mathbf{B}),\mathcal{R}(E,\mathbf{B})) = \sum_{nm} \sum_{\gamma(\bar{n},\bar{m})} \sum_{\gamma'(\bar{n},\bar{m})} \mathcal{M}_{\gamma,\gamma'} \mathcal{A}_{\gamma} \mathcal{A}_{\gamma'}^{*} e^{(i/\hbar)(\mathcal{S}_{\gamma}-\mathcal{S}_{\gamma'})} \tag{6}$$

In the case of transmission (reflection), the paths γ, γ' connect different leads (return to the same lead). Equation (6) is still rather general and contains SO and Zeeman interactions. The orbital contribution of each trajectory pair is weighted by the spin *modulation factor*

$$\mathcal{M}_{\gamma,\gamma'} = \mathrm{Tr}(\hat{K}_{\gamma} \hat{K}_{\gamma'}^{\dagger}) \tag{7}$$

where the trace is taken in spin space.

3. General discussion

In many physical situations one is interested in the *energy average* of the reflection $\mathcal{R}(E,\mathbf{B})$ (Eq. (6)), subject to an external arbitrarily directed magnetic field **B**. The actions $\mathcal{S}_\gamma(E,\mathbf{B})/\hbar$ are rapidly changing functions of E in the semiclassical limit. Therefore, only the orbit pairs γ,γ' with (nearly) equal actions yield non-vanishing contributions to the energy average.

The *classical* reflection is obtained after summing up the terms $\gamma' = \gamma$ [27], for which the phase in the exponent of Eq. (6) disappears. The modulation factor is then $\mathcal{M}_{\gamma,\gamma} = \mathrm{Tr}(\hat{K}_\gamma \hat{K}_\gamma^\dagger) = 2s+1$, independent of SO interaction, and is reduced to trivial spin degeneracy.

In a system with time-reversal symmetry, i.e. **B** = 0, each trajectory has a time-reversed partner with identical action. Such pairs contribute to terms with $n = m$ of the semiclassical sum (6) for reflection $\mathcal{R}$ (but not $\mathcal{T}$). The corresponding modulation factor is $\mathcal{M}_{\gamma,\gamma^{-1}}=\mathrm{Tr}(\hat{K}_\gamma^2)$, where γ^{-1} is the time reversal of γ. Upon energy average, the pairs γ,γ^{-1} form a *diagonal* quantum correction $\delta\mathcal{R}_{\mathrm{diag}}$ [27].

The diagonal contribution alone would violate the conservation of current, making it necessary to account for other types of orbit pairs with close actions [27, 28]. No effective way of adding up these terms in a cavity with regular or mixed classical dynamics is known, however. Therefore, we will stay within the diagonal approximation when considering the following examples (see [27] for a similar treatment of the spinless case), and direct the reader to Refs. [17, 28] for a study of chaotic cavities.

In the presence of a constant and uniform magnetic field **B**, the diagonal terms in the sum (6) will be modified. First, due to Zeeman interaction, the modulation factor $\mathcal{M}_{\gamma,\gamma^{-1}}$ is no longer $\mathrm{Tr}(\hat{K}_\gamma^2)$ and should be calculated directly from Eq. (7). Second, the field component B_z perpendicular to the cavity generates an additional Aharonov–Bohm (AB) phase factor $\varphi = \exp\left[(i/\hbar)(\mathcal{S}_\gamma - \mathcal{S}_{\gamma^{-1}})\right] = \exp\left(i4\pi \mathsf{A}_\gamma B_z/\Phi_0\right)$ (the field is assumed to be weak enough to neglect the bending of trajectories by the Lorentz force). Here, $\mathsf{A}_\gamma \equiv \int \mathbf{A}\cdot d\mathbf{l}/B_z$ is the effective enclosed area accumulated along the orbits γ, and $\Phi_0 = hc/e$ is the flux quantum. For a uniform treatment of the SO interaction and magnetic field effects, we thus introduce a generalized modulation factor, $\mathcal{M}_\varphi \equiv \mathcal{M}_{\gamma,\gamma^{-1}}\varphi$. Its average $\overline{\mathcal{M}_\varphi}(L;\mathbf{B})$ over an ensemble of trajectories with fixed length L characterizes the effective evolution of the spinor (both direction and phase) of a particle transported along classical trajectories in a given cavity. The **B**-dependence includes both the AB phase and Zeeman interaction. We estimate the relative quantum correction to reflection as the average $\left\langle \overline{\mathcal{M}_\varphi} \right\rangle_L$ over L

$$\delta\mathcal{R}_{\mathrm{diag}}/\delta\mathcal{R}^{(0)}_{\mathrm{diag}} = \left\langle \overline{\mathcal{M}_\varphi}(\mathbf{B}) \right\rangle_L \equiv \int_0^\infty dL\, P(L)\, \overline{\mathcal{M}_\varphi}(L;\mathbf{B}) \tag{8}$$

where $P(L)$ is the distribution of orbit lengths before they escape from the cavity, and the superscript (0) refers to zero spin and zero magnetic field. Strictly speaking, an expression similar to Eq. (8) has been derived in [27] for a chaotic cavity and used for integrable systems with an appropriate $P(L)$. On an equal footing, we may treat the r.h.s. of (8) as an estimate for the *full* relative quantum corrections to transmission and reflection, $\delta\mathcal{T}/\delta\mathcal{T}^{(0)}$ and $\delta\mathcal{R}/\delta\mathcal{R}^{(0)}$, since the relative diagonal and off-diagonal contributions are the same in the chaotic case [20, 28].

4. Application to integrable billiards

For the remainder of the paper we will focus on the case of spin $s = 1/2$ and Rashba SO interaction [31], which is often present in 2d semiconductor heterostructures. It is described by an effective magnetic field

$$\mathbf{C} = (2\alpha_R\, m_e/\hbar^2)\,\mathbf{v}\times\hat{\mathbf{z}}, \tag{9}$$

where α_R is the Rashba constant, m_e is the effective mass, $\mathbf{v}$ the (Fermi) velocity, and $\hat{\mathbf{z}}$ is the unit vector perpendicular to the cavity[*]. In a billiard with fixed kinetic energy, $\mathbf{C}$ is constant by magnitude and its direction changes only at the boundary. We will characterize the SO coupling strength by the mean spin-precession angle per bounce, $\theta_R = 2\pi L_b/L_R$, where L_b is the average distance between two consecutive bounces and $L_R = 2\pi v/C$ is the Rashba length.

Of the two systems chosen for our numerical study, the quarter-circle billiard can be thought of as a „typical“ representative of integrable billiards, while the circular billiard is rather exceptional. In the latter case, owing to angular-momentum conservation, *all* trajectories efficiently accumulate area. Hence, the AB phase grows linearly in time and the spin modulation factor is also affected in a similar fashion (see below).

The dependence of the average modulation factor $\overline{\mathcal{M}}(L) \equiv \overline{\mathcal{M}_\varphi}(L;\mathbf{B}=0)$ on the orbit length for two SO coupling strengths is shown in Figs. 1 and 2. The average was performed over $50,000$ trajectories (in the closed system, i.e. disregarding the leads), with random initial velocity directions and positions at the boundary. Note that as the trace of a unitary matrix, the modulation factor (7) is defined in the interval $[-2,2]$ (for spin 1/2). All curves in Figs. 1, 2 begin at $\overline{\mathcal{M}}(0) = 2$ due to the initial condition of $K_\gamma(0)$ being a unit matrix. The value $\overline{\mathcal{M}}(L_b) \approx 2 - \theta_R^2$ is also predetermined: before

---

[*] $\alpha_R/\hbar^2$ is kept fixed in the formal semiclassical limit $\hbar \to 0$.

its first encounter with the boundary, a particle moves along a straight line, irrespective of the geometry of the cavity.

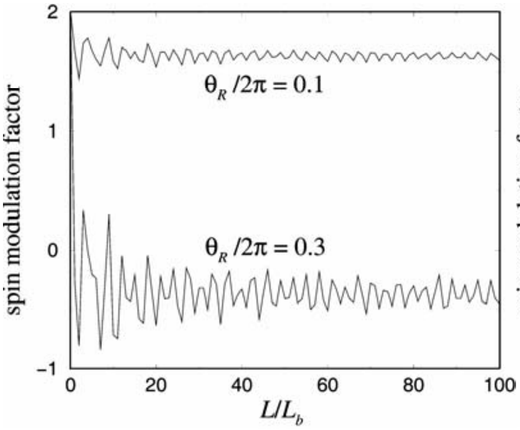

Fig. 1. Average spin modulation factor $\overline{\mathcal{M}}(L)$ for the quarter-circle billiard at two values of spin-orbit coupling strength, $\theta_R/2\pi = 0.1, 0.3$. The orbit length is measured in units of the average distance between two consecutive bounces L_b

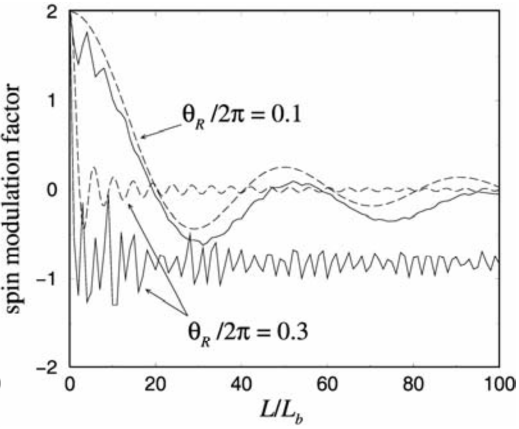

Fig. 2. Solid curves: same as in Fig. 1 for the circular billiard. Dashed curves: analytical prediction by Eq. (10) of the respective values of θ_R

The shape of the billiard becomes important on scales $L >> L_b$. We find that for the quarter-circle billiard (Fig. 1), $\overline{\mathcal{M}}(L)$ oscillates around a constant saturation value. With increasing θ_R, this value decreases down to –1, the level corresponding to a fully randomised spin state [20]. The oscillation frequency is independent of θ_R. The observed behaviour of $\overline{\mathcal{M}}(L)$ can be explained by nearly periodic changes in the spin direction and phase during orbital motion in an integrable billiard. The average over many trajectories results in the saturation value (the remaining oscillations cannot be removed by averaging).

For the circular billiard (Fig. 2), we see a completely different situation. Here, for a weak SO coupling the modulation factor can be estimated as

$$\overline{\mathcal{M}}(L) \simeq 2\frac{\sin x}{x}, \qquad x = \theta_R^2 \frac{Lr}{2L_b^2}, \qquad \theta_R \ll 1 \tag{10}$$

where r is the radius (see Appendix A). The analytical curve (2) (dashed curve in Fig. 2) shows a reasonable agreement with the corresponding numerical results for $\theta_R/2\pi = 0.1$. As θ_R increases, the oscillations of $\overline{\mathcal{M}}(L)$ become irregular and the saturation value falls to approximately –1.

Figure 3 presents the relative quantum correction (8) as a function of θ_R. It is well known that $\delta\mathcal{R}^{(0)} > 0$ [27, 28], which is a consequence of a *weak localization*. The enhancement of reflection due to the quantum interference between different paths in Eq. (6) is responsible for this effect. SO interaction reverses the sign of the quantum correction. This phenomenon is called *weak antilocalization*. According to Eq. (8), AL occurs if the average modulation factor $\overline{\mathcal{M}}(L)$ becomes negative. Contrary to the situation in chaotic quantum dots [17], the shape of the length distribution $P(L)$ is of lesser importance here, since $\overline{\mathcal{M}}(L)$ quickly saturates in most integrable cavities. In our examples, AL occurs in the circular billiard at weaker SO-coupling strengths than in the quarter-circle billiard.

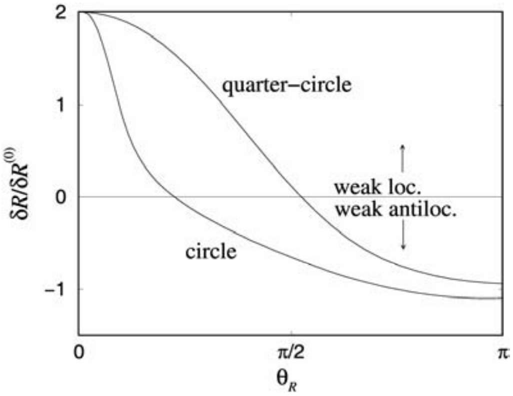

Fig. 3. Relative quantum correction to the reflection $\delta\mathcal{R}_{\rm diag}/\delta\mathcal{R}^{(0)}_{\rm diag}$ (Eq. (8)) vs. spin-orbit coupling strength θ_R for the quarter-circle and circular billiards. Positive (negative) values indicate weak localization (antilocalization). The length distributions $P(L)$ were evaluated at perimeter/lead width equal to 60

A magnetic field AB flux destroys the time-reversal symmetry, thus suppressing the WL and AL. We have also found numerically that Zeeman interaction destroys the AL.

5. Conclusions

We have applied a general semiclassical theory of spin-dependent transport in ballistic quantum dots [17] to 2d cavities with integrable classical dynamics. We compared the properties of two billiards with rather distinct dynamics – the quarter-circle billiard, as a typical integrable example, and the circular billiard, where trajectories accumulate area linearly with time. The two systems have qualitatively different average spin evolutions, which is reflected in the dependences of their average modulation factors on the orbit length. For the circular billiard, we have derived the analytical form of this function for weak spin-orbit coupling. As a consequence of the spin dynamics generated by the orbital motion, AL is predicted to appear in the circular billiard at weaker spin-orbit interactions than in the quarter-circle billiard.

Acknowledgements

We thank M. Brack for useful discussions and continuous support. This work has been supported by the Deutsche Forschungsgemeinschaft.

Appendix A: Average modulation factor in the circular billiard for weak SO coupling

We derive a generalization of Eq. (10) in the presence of an AB flux (neglecting Zeeman interaction). To this end, we apply a unitary transformation [18] $\hat{H} \to \hat{U}^\dagger \hat{H} \hat{U}$ to the Hamiltonian (1) with the Rashba interaction, where

$$\hat{U} = \exp\left[i \frac{2\pi}{L_R} \left(q_x \hat{s}_y - q_y \hat{s}_x \right) \right]. \tag{11}$$

Here, q_i are the 2d Cartesian coordinates in the billiard plane, and $\hat{s}_i$ are the respective spin operators ($i = x, y$). Carrying out this transformation to the order θ_R^2, we obtain the new Hamiltonian with a rescaled SO coupling. Its effective magnetic field is

$$\widetilde{C}_z = -\frac{1}{2} \left(\frac{2\pi}{L_R} \right)^2 \mathbf{v} \cdot \left(\hat{\mathbf{z}} \times \mathbf{q} \right), \qquad \widetilde{C}_x = \widetilde{C}_y = 0 \tag{12}$$

With this field, the spin propagator along a trajectory γ becomes

$$\hat{K}_\gamma(t) = \exp\left[i \left(\frac{2\pi}{L_R} \right)^2 \mathsf{A}_\gamma(t)\, \hat{s}_z \right] \tag{13}$$

where $\mathsf{A}_\gamma(t)$ is the area enclosed by the orbit. Clearly, the SO contribution to the semiclassical sum (6) is similar to the AB contribution with the magnetic field $\widetilde{B}_z = \pm \pi \Phi_0 / L_R^2$, the sign being dependent on spin polarization [18].

By including the additional external field B_z, we find the generalized modulation factor for a pair of mutually time-reversed orbits of length L to be

$$\mathcal{M}_\varphi(L) = \sum_\pm \exp\left[i \frac{4\pi}{\Phi_0} \left(B_z \pm | \widetilde{B}_z | \right) \mathsf{A}_\gamma(L) \right] \tag{14}$$

The enclosed area can be estimated as $\mathsf{A}_\gamma(L) \simeq (M / 2 m_e v) L$ for an orbit in the circular billiard with angular momentum M. The average of $\mathcal{M}_\varphi(L)$ (Eq. (14)) over M yields the required expression

$$\overline{\mathcal{M}_\varphi}(L; B_z) = \sum_\pm \frac{\sin x_\pm}{x_\pm}, \qquad x_\pm = \frac{2\pi}{\Phi_0} (B_z \pm | \widetilde{B}_z |) r L, \tag{15}$$

where r is the billiard radius. Note the partial compensation of the external and SO magnetic fields when one of the $x_\pm$ is zero (cf. [19]).

Here, a final remark is in order. A careful transformation [20] of the modulation factor corresponding to the unitary transformation (11) of the Hamiltonian brings about an additional contribution that is not included in (14). Approximately, it equals $\delta\mathcal{M}_\varphi \simeq -(2\pi/L_R)^2\,|\Delta\mathbf{q}_\gamma|^2$, where $|\Delta\mathbf{q}_\gamma|$ is the distance between the initial and final points of the orbit γ. Neglecting this term is justified, since the relevant orbits start and end within the lead width. In all our numerical calculations of Sec. 4, however, we started and ended the orbits at random points on the boundary. In this case, the correction $\delta\mathcal{M}_\varphi \sim -\theta_R^2$ corresponds to the spin relaxation before the first encounter with the boundary (see above). This contribution is not important for long orbits when $\theta_R << 1$. It would be desirable to refine our calculations by checking if θ_R^2-relaxation is present when $\theta_R \backsim 1$ even for closed orbits (as we currently assume).

References

[1] Datta S., Das B., Appl. Phys. Lett., 56 (1990), 665.
[2] Frustaglia D., Richter K., Phys. Rev. B, 69 (2004), 235310.
[3] Watson S.K., Potok R.M., Marcus C.M., Umansky V., Phys. Rev. Lett., 91 (2003), 258301.
[4] Golovach V.N., Khaetskii A., Loss D., Phys. Rev. Lett., 93 (2004), 016601.
[5] Nitta J., Akazaki T., Takayanagi H., Enoki T., Phys. Rev. Lett., 78 (1997), 1335.
[6] Schierholz Ch., Kürsten R., Meier G., Matsuyama T., Merkt U., phys. stat. sol. (b), 233 (2002), 436.
[7] Bergmann G., Phys. Rep., 107 (1984), 1.
[8] Chakravarty S., Schmid A., Phys. Rep., 140 (1986), 193.
[9] Miller J.B., Zumbühl D.M., Marcus C.M., Lyanda-Geller Y.B., Goldhaber-Gordon D., Campman K., Gossard A.C., Phys. Rev. Lett., 90 (2003), 076807.
[10] Minkov G.M., Germanenko A.V., Rut O.E., Sherstobitov A.A., Golub L.E., Zvonkov B.N., Willander M., http://arxiv.org/abs/cond-mat/0312074 (2003).
[11] Meijer F.E., Morpurgo A.F., Klapwijk T.M., Koga T., Nitta J., http://arxiv.org/abs/cond-mat/0406106 (2004).
[12] Zumbühl D.M., Miller J.B., Marcus C.M., Campman K, Gossard A.C., Phys. Rev. Lett., 89 (2002), 276803.
[13] Hackens B., Minet J.P., Faniel S., Farhi G., Gustin C., Issi J.P., Heremans J.P., Bayot V., Phys. Rev. B, 67 (2003), 121403(R).
[14] Khaetskii A.V., Nazarov Y.V., Phys. Rev. B, 61 (2000), 12639.
[15] Brouwer P.W., Cremers J.N.H.J., Halperin B.I., Phys. Rev. B, 65 (2002), 081302.
[16] Falko V.I., Jungwirth T., Phys. Rev. B, 65 (2002), 081306.
[17] Zaitsev O., Frustaglia D., Richter K., http://arxiv.org/abs/cond-mat/0405266 (2004).
[18] Aleiner I.L., Falko V.I., Phys. Rev. Lett., 87 (2001), 256801.
[19] Cremers J.-H., Brouwer P.W., Falko V.I., Phys. Rev. B, 68 (2003), 125329.
[20] Zaitsev O., Frustaglia D., Richter K., unpublished results.
[21] Chang C.-H., Malshukov A.G., Chao K.A., http://arxiv.org/abs/cond-mat/0405212 (2004); Phys. Rev. Lett. (in print).
[22] Gutzwiller M.C., J. Math. Phys. 12, 343 (1971) and references therein.
[23] Bolte J., Keppeler S., Phys. Rev. Lett., 81 (1998), 1987; Ann. Phys. (N.Y.) 274 (1999), 125.
[24] Pletyukhov M., Zaitsev O., J. Phys. A: Math. Gen., 36 (2003), 5181.
[25] Zaitsev O., J. Phys. A: Math. Gen., 35 (2002), L721.
[26] Pletyukhov M., Amann Ch., Mehta M., Brack M., Phys. Rev. Lett., 89 (2002), 116601.

[27] Baranger H.U., Jalabert R.A., Stone A.D. , Phys. Rev. Lett., 70 (1993), 3876; Chaos 3 (1993), 665.
[28] Richter K., Sieber M., Phys. Rev. Lett., 89 (2002), 206801.
[29] Fisher D.S., Lee P.A., Phys. Rev. B, 23 (1981), 6851.
[30] Chang C.-H., Mal'shukov A.G., Chao K.-A., Phys. Lett. A, 326 (2004), 436.
[31] Bychkov Y., Rashba E., J. Phys. C, 17 (1984), 6039 and refs. therein.

Received 14 September 2004
Revised 28 October 2004

Materials Science-Poland, Vol. 22, No. 4, 2004

Manipulation of electron spin in a quantum dot using a magnetic field and voltage gates

D. GIULIANO[1, 2], P. LUCIGNANO[1, 3], A. TAGLIACOZZO[1, 3*]

[1]Coherentia – INFM (Istituto Nazionale di Fisica della Materia), Unità di Napoli

[2]INFN and Dipartimento di Fisica Università di Calabria, Arcavacata di Rende, Italy

[3]Dipartimento di Scienze Fisiche Università di Napoli "Federico II", Napoli, Italy

In this paper, we show that it is possible to manipulate the many-body wave function of an isolated dot with a few electrons by locally applying magnetic and electric fields. We polarize the dot at a level crossing, where the sensitivity is at its maximum. Time-dependent fields produce a superposition of the states involved in the avoided crossing. In the case of $N = 2$ and $N = 3$ electrons, the results of exact diagonalisation give information about the nature of these states and allow us to construct an effective Hamiltonian describing the coupling. The formalism for evaluating the Berry phase arises naturally. We argue that a quantum dot, capacitively coupled to a quantum point contact, can influence its conductance. The quantum superposition of the states produced by cycling the fields on the dot can be measured this way.

Key words: *quantum transport device; quantum dot; Berry phase; qubits*

1. Introduction

Manipulating the phase of a quantum electronic system in a controlled fashion is presently one of the challenges of nanophysics, especially in view of its possible applications in quantum computing [1]. The most promising route to achieve such a task is probably provided by coherent solid-state devices. For instance, a superconducting Josephson qubit has already been realized as the Cooper pair box, namely a small superconducting island weakly coupled to a charge reservoir via the Josephson junction [2]. The quantum state of the box can be tuned to a coherent superposition of the charge-zero and charge-one states. The possibility of realizing superpositions of flux states has been considered as well [3]. Entanglement in semiconducting devices made of two quantum dots (QD), one on top of each other ("quantum dot molecule") has recently been optically measured, and double dots have been inserted into a transport device [4]. Double QD have been proposed as possible qubits [5]. The state of a QD

---

[*] Corresponding author, e-mail: Arturo.Tagliacozzo@na.infn.it.

can be finely tuned by means of external magnetic and electric fields or by changing the coupling between the dot and the contacts [6].

Quantum algorithms usually assume that either the system dynamically evolves through a sequence of unitary transformations or that a set $\vec{\lambda}$ of external control parameters of the Hamiltonian *H* smoothly changes in time (“adiabatic evolution”) [7]. Accidental level degeneracies are quite common in QD’s, which is seen both theoretically and experimentally [8]. In this work, we show that they can be used to add a Berry phase to the dot and to manipulate it. In fact, if adiabatic evolution is realized across a closed path γ in parameter space close enough to an accidental level degeneracy, the nontrivial topology of the Hilbert space makes the state of the system take up a “geometrical” phase Γ, referred to as the “Berry phase” [9]. The value of Γ may be controlled by properly choosing γ.

Here we discuss the case of a vertical dot with a few electrons in a rather strong orthogonal magnetic field *B*. By increasing *B*, the energy levels undergo crossings to higher angular momenta states and spin states. We will show that the Rashba spin -orbit perturbing term, implemented by polarizing a voltage gate on top of an isolated dot, can turn one of these crossings into an anticrossing by mixing states of different quantum numbers and opening a gap. Cycling the voltage in an appropriate way allows an *SU*(2) Berry phase to be added to the many body wave function of the electrons in the dot. This phase could be monitored by means of transport measurement.

In Chapter 2 we set up a model for a vertical QD with a few interacting electrons based on exact diagonalisation results and describe the crossover to the state with maximum spin and maximum angular momentum. The effect of the Rashba spin-orbit (SO) term on the ground state of the system is discussed. In Chapter 3 we concentrate on the case where *N* = 2. There is an avoided crossing at the singlet–triplet transition [10] which can be described by an equivalent Hamiltonian $\tilde{H}$ involving just one effective spin $\tilde{S} = 1/2$. We shall make the state of the system evolve in time by means of a time-dependent SO coupling, which could be implemented by a microwave driven gate voltage. The spin state is shown to acquire the usual SU(2) Berry phase. In Chapter 4 we argue that a dot with *N* = 3 electrons gives the chance of producing an SU(3) Berry phase. In order o perform a nontrivial γ circuit, however, there are too many parameters to control. This makes the realization of a full SU(3) Berry phase unrealistic at the present time. Nevertheless, we show that a simpler setup can be imagined based on a three-level avoided crossing and that this setup allows further phase manipulation. The final chapter collects comments on possible methods for reading out the added phase.

2. Vertical quantum dot with azimuthal symmetry

We consider an isolated, vertical QD, disk-shaped in the (*x*,*y*)-plane (θ and ρ are the polar coordinates in the plane). An external static magnetic field *B* and electric field *E* are applied along the *z*-axis. The dot’s Hamiltonian H_D adiabatically depends on these external parameters, generically referred to as $\vec{\lambda}$ in the following. The dot’s Hamiltonian is

$$H_D = H_{0D} + \mu \sum_i l_i^z B + \frac{1}{2}\hbar\omega_c(B) \sum_i \sigma_i^z + \frac{\alpha}{\hbar} \sum_i \left(\vec{E} \times \vec{\pi}_i\right) \cdot \vec{\sigma}_i \tag{1}$$

where H_{0D} includes the confining parabolic potential of frequency ω_d and the Coulomb interaction $U(B,\omega_d)$. $\omega_c(B) = eB/m^*_c$ is the cyclotron frequency. The second and third terms at the r.h.s. of Eq. (1) are the orbital and spin Zeeman terms, respectively. The $\vec{l}_i$ are the components of the electron angular momentum orthogonal to the dot disk, and μ is the electronic magnetic moment $\mu = e\hbar/(2m^*c)$. The last term is the spin-orbit (Rashba) term with a coupling constant $\alpha \propto \vec{E}$, which has the dimension eV·Å. The generalized momentum is $\vec{\pi}_i = \vec{p}_i + (e/c)\vec{A}(r_i)$, where $\vec{p}_i$ is the linear momentum of particle i and $\vec{A}$ is the vector potential due to the magnetic field B. In a symmetric gauge it takes the form $\vec{A} = B/2\,(-y, x, 0)$. From now on we neglect the Zeeman spin splitting, since it only lifts the spin degeneracy. The orbital wave function for an electron in a two-dimensional harmonic confining potential and an external B field along $\hat{z}$ is

$$\Psi_{n,m}(\rho,\theta) = \frac{e^{im\theta}}{l\sqrt{\pi}} R_{n|m|}(t), \tag{2}$$

where n, m are the orbital quantum numbers, $t = \rho^2/l^2$, and $l = \sqrt{\hbar/m^*\omega_0}$ ($\omega_0 = \sqrt{\omega_d^2 + \omega_c^2(B)/4}$). The radial wave function in Eq. (2) is expressed in terms of the Laguerre polynomials L_ν^μ as

$$R_{n|m|}(t) = C_{n|m|}\, e^{-1/2}\, t^{|m|/2}\, L^{|m|}_{(n-|m|)/2}(t); \qquad C_{n|m|} = \left[\frac{\left(\frac{n-|m|}{2}\right)!}{\left(\frac{n+|m|}{2}\right)!}\right]^{\frac{1}{2}} \tag{3}$$

We label the single electron states in the dot by $|n, m, s = 1/2, s^z>$ (s, s^z are the electron spin and z-component).

In the absence of both interaction and magnetic field, the lowest lying single particle states are occupied with minimum spin. The GS Slater determinant for $N = 5$ is sketched pictorially in Fig. 1a, where energy is plotted on the vertical axis. Each box represents a single particle state labelled by n,m, and each arrow represents the spin projection along the quantisation axis of the electron occupying the corresponding box.

In Figure 2 (left panels) we show the lowest lying total energy levels at a fixed angular momentum M versus M for $U = 13$ meV and three values of B. These are $B = 5$ meV (top), $B = B^* = 7$ meV (middle), and $B = 11.5$ meV (bottom).

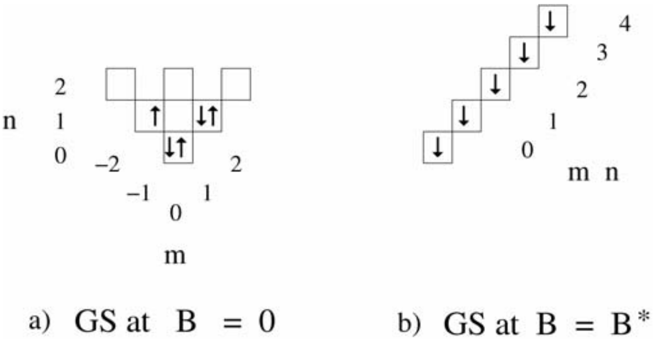

Fig. 1. The Slater determinants quoted in the text. Quantum numbers are $N = 5$, $S = 1/2$ for the state at $B = 0$ (a) and $S = 5/2$ for the state at $B = B^*$, which is the magnetic field at which the maximum absolute value of S is achieved (b)

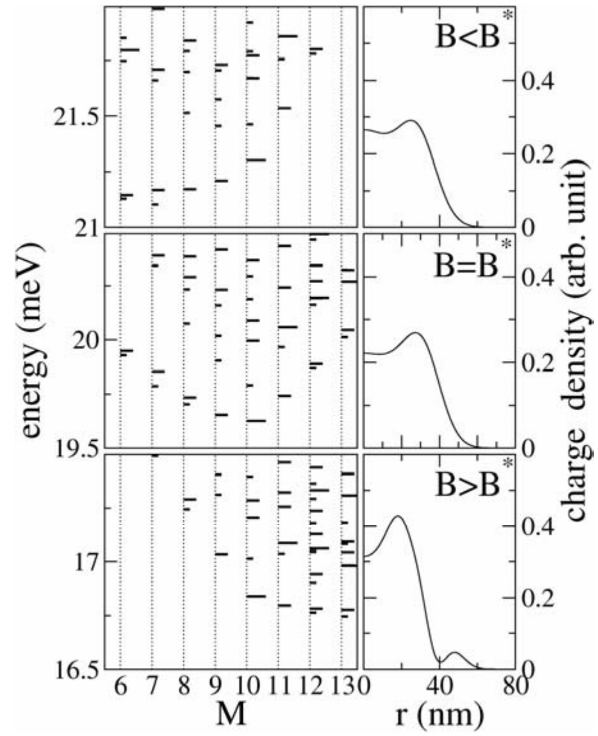

Fig. 2. Energy levels without SO coupling for a dot with $N = 5$ electrons at $U = 13$ meV and $\omega_d = 5$ meV. Magnetic field values are (in units of $\hbar\omega_c$): $B = 5$ meV (top), $B = B^* = 7$ meV (middle), $B = 11.5$ meV (bottom). Total M is on the x axis. Levels are drawn with short, medium, or long dashes, corresponding to the total spin: $S = 1/2, 3/2, 5/2$

This level structure, as well as the radial charge and spin densities, are calculated by exact diagonalisation using a basis of 28 single particle orbitals. Slater determinants are constructed and span the Hilbert space up to matrices ($10^5 \times 10^5$), depending on the number of electrons. Unscreened Coulomb electron-electron interaction matrix elements are calculated analytically basing on the states given by Eq. (2).

At each *M*, the spin degeneracy is marked by dashes of different length: short dashes for $S = 1/2$ (doubly degenerate level), medium dashes for $S = 3/2$ (fourfold degeneracy), and long dashes for $S = 5/2$ (sixfold degeneracy). On the r.h.s. of the picture, the radial charge density of the corresponding GS is plotted vs. the distance *r* from the dot centre. Figure 2 (left panels) shows that the levels cross with increasing *B* when *M* or *S* increase. Electron-electron correlations imply that when *M* increases *S* also increases.

At $B = B^* = 7$ meV, the spin *S* reaches its maximum value of $S = N/2$. The largest contribution to the GS wave function is given by the Slater determinant depicted in Fig. 1b (for $N = 5$), corresponding to $M = \sum_0^{N-1} m = 10$. We concentrate on the state at $B = B^*$, namely the Fully Spin Polarized (FSP) GS. This corresponds to the "maximum density droplet" state discussed in literature [11]. Qualitatively we can say that at $B = B^*$ the dot has the smallest radius. As can be seen from the GS charge density, a further increase in *B* leads to the so-called reconstruction of the charge density of the dot. For $B > B^*$, the value of *M* for the GS increases, but *S* is no longer at its maximum. In the bottom panel of Fig. 2 it is shown that at $B = 11.5$ meV the GS energy is achieved for $M = 13$ with a doublet ($S = 1/2$) state. The corresponding charge density of the dot, depicted on the r.h.s., is strongly modified close to the edge [12]: it displays a node, followed by an extra non-zero annulus at a larger distance. In view of the fact that our expansion of the wave function includes only rotationally invariant components, the breaking of azimuthal symmetry is impossible. By contrast, this is found to occur in density functional calculations, and the corresponding GS is referred to as the de Chamon-Wen phase [13]. The GS at $B = B^*$ can be compared with a FSP quantum Hall state of an extended disk in the absence of lateral confinement (Quantum Hall Ferromagnet (QHF) at a filling of one). Indeed, Fig. 1b resembles the occupancy of the lowest Landau level (LLL) up to a maximum $m = N - 1$, except that in our case the single particle levels corresponding to the LLL are not all degenerate in energy. In the language of the quantum Hall effect, the unperturbed levels are:

$$\varepsilon_{\nu,m} = (2\nu + |m| + 1)\hbar\omega_o - \frac{m}{2}\hbar\omega_c \tag{4}$$

where $\nu = (n - |m|)/2$ and $\omega_o = \sqrt{\omega_d^2 + \omega_c^2/4}$. The LLL is for $\nu = 0$ and $m \geq 0$. The Slater determinant for the LLL has a charge density that is flat as a function of r up to the disk edge, at which it rapidly falls to zero. In our case, this feature is lost due to *U* and the fact that the number of electrons is small.

We now add spin-orbit interaction to the dot. This can be tuned by applying an electric field *E* in the $\hat{z}$ direction, which couples the spin of the electrons in the dot.

At $E \neq 0$, the spin-orbit term couples states with opposite spin components: $s^z = \pm(1/2)$. The matrix elements can be easily calculated

$$H_{so}=\frac{\alpha}{l}\sum_{nn'}\sum_{m}\left\{B_{n'm+1,nm}\left(1-\frac{\omega_c}{\omega_0}\right)c^{\dagger}_{n'm+1\downarrow}c_{nm\uparrow}+A_{n'm-1,nm}\left(1-\frac{\omega_c}{\omega_0}\right)c^{\dagger}_{n'm-1\uparrow}c_{nm\downarrow}\right\}$$

with

$$A_{n',m',nm}=\delta_{m'+1,m}\int_0^{\infty}dtR_{n'|m'|}(t)\left(2\sqrt{t}\frac{\partial}{\partial t}+\frac{m}{\sqrt{t}}\right)R_{n|m|}(t)$$

and

$$B_{n',m',nm}=\delta_{m'-1,m}\int_0^{\infty}dtR_{n'|m'|}(t)\left(2\frac{\partial^{\dagger}}{\partial t}\sqrt{t}+\frac{m'}{\sqrt{t}}\right)R_{n|m|}(t) \tag{5}$$

Here $B_{nm,n'm-1}=A^{*}_{n'm-1,nm}$, which implies that the Hamiltonian is hermitian. A pictorial sketch can help to understand what happens in the presence of both the orthogonal magnetic field and SO Rashba coupling. SO coupling tends to shift the $\downarrow$ spin density radially w.r.to the $\uparrow$ spin density. This is confirmed by plotting the occupation numbers $n_{nm\sigma}=<GS\,|\,c^{\dagger}_{nm\sigma}c_{nm\sigma}\,|\,GS>$ with $n = m$ (see Fig. 3 and [14]).

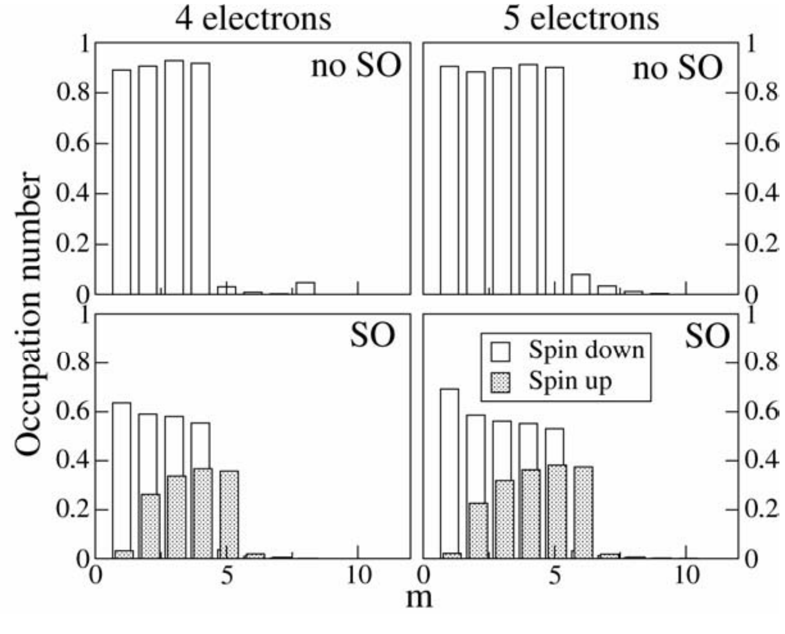

Fig. 3. Occupation numbers $n_{n=m,m,\sigma}$ in the *GS* with *N* 4 (5) electrons (left(right)), without SO (top) and with SO (α = 100 meVÅ) (bottom). Other parameters are: *B* = 7 meV, *U* = 13 meV, and ω_d = 5 meV. White bars refers to spin down, grey bars refer to spin up. The *FSP* GS of the dot with *N* = (4) 5 electrons has a total spin *S* = 2 (5/2) and a *z*-component of the total angular momentum J_z = 15/2

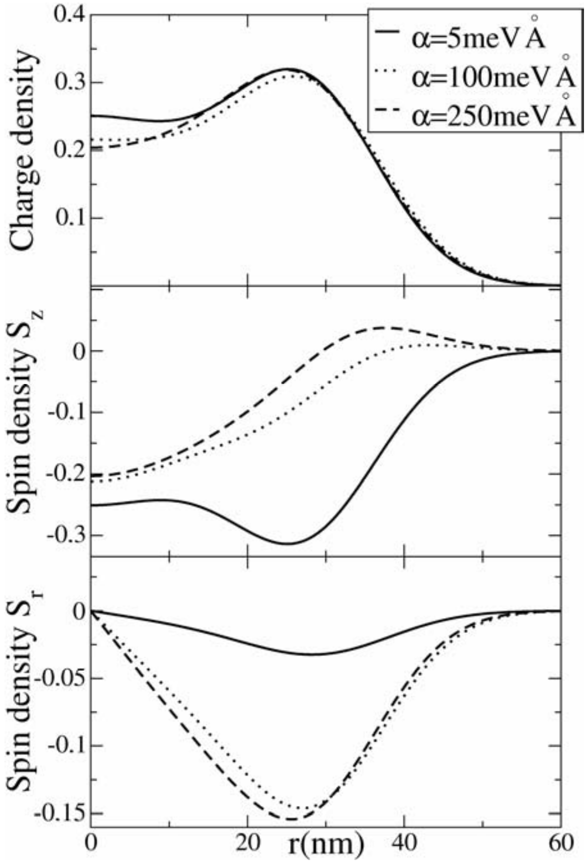

Fig. 4. Charge density, azimuthal spin density S_z, and radial in plane spin density S_r in the GS ($N = 5$, $J = 15/2$) at SO couplings $\alpha = 5, 100, 250$ meV·Å. Here, $B = 7$ meV, $U = 13$ meV, and $\omega_d = 5$ meV

The spin density is quite sensitive to the addition of SO up to the saturation. Now the z-component of the total spin is no longer a good quantum number and some mixing with down spin electrons appears. While s_z and m are no longer separately conserved, their sum $j_z = s_z + m$ (with j_z being a half integer) is still conserved. In result, the Rashba coupling acts as an effective in plane magnetic field that forces the precession of electron spins in the dot plane. The out of plane component of B tends to tilt spin out of the plane, acting oppositely to the Rashba coupling. Our calculation confirms the intuitive idea that SO coupling is weakened by an orthogonal magnetic field. Indeed, by increasing ω_c in Eq. (2), the strength of the SO interaction decreases. The z-component of spin density and its radial component for the GS with $N = 5$ and $J_z = 15/2$ for $U = 13$ meV are plotted vs. the distance from the dot centre in Fig. 4, for three different values of SO coupling. They are also compared to the charge density distribution. As it appears from Fig. 4 (top panel), the charge density of the GS is only mildly changed when we increase the SO coupling.

The SO interaction lifts the degeneracy of J_z. The multiplet with $N = 5$, $S = 5/2$, and $M = 10$ at $B = B^* = 7$ meV and $U = 13$ meV splits when the strength of SO coupling α is increased. The strength of U is responsible not only for the fact that the GS belongs to this multiplet, but also for the order in the sequence of energies: $J_z = 15/2$, 17/2, 19/2, 21/2, 23/2, 25/2 (from bottom to top). At small values of U, this sequence has the order $J_z = 25/2$, 23/2, 21/2, 19/2, 15/2, 17/2, as shown in Fig. 5. With increasing U, some level crossings occur. This crossing defines B^*, which is rather insensitive to SO coupling.

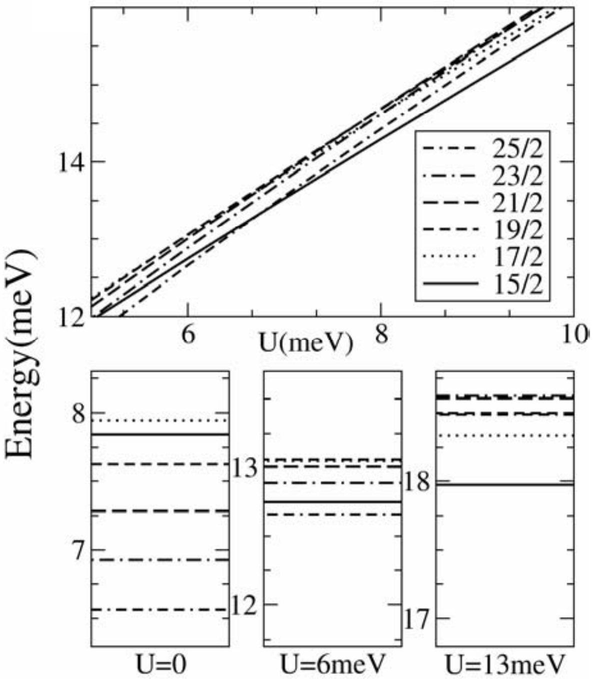

Fig. 5. Energy levels for $N = 5$, $B = 7$ meV, $\omega_d = 5$ meV, and $\alpha = 100$ meVÅ, for different values of U. In the upper panel the crossings that allow the *FSP* polarized state to be the ground state when U is large are shown. The order of the levels is magnified in the bottom panels for three different values of U

The order at three different values of U is magnified in the bottom panels of Fig. 5. The case for $U = 13$ meV is shown in the bottom right panel of Fig. 5 – the lowest state in energy is for $J_z = 15/2$, followed by $J_z = 17/2$, 19/2 (almost degenerate with 25/2), and 25/2, 21/2, 23/2. At $U = 13$ meV a sizeable gap is formed between the $J_z = 15/2$ GS and the first excited state $J_z = 17/2$. The other states of the multiplet are bunched together at higher energies.

We discuss the peculiarity of the first excited state elsewhere [15], which displays a spin texture with some analogies to the Skyrmion state of the QHF.

3. The N = 2 singlet–triplet avoided crossing

In this chapter, we consider two electrons ($N = 2$) only. In particular, B is tuned close to the singlet–triplet transition that occurs at $B = B^*$. In the absence of SO coupling, the states of a vertical dot are usually denoted as $|M, S, S^z>$, where M is the orbital angular momentum, S is the total spin, and S^z is its z-component [8]. The low-lying energy levels are reported vs. B and in the absence of SO in Fig. 1, to be compared with the ones when SO has been added.

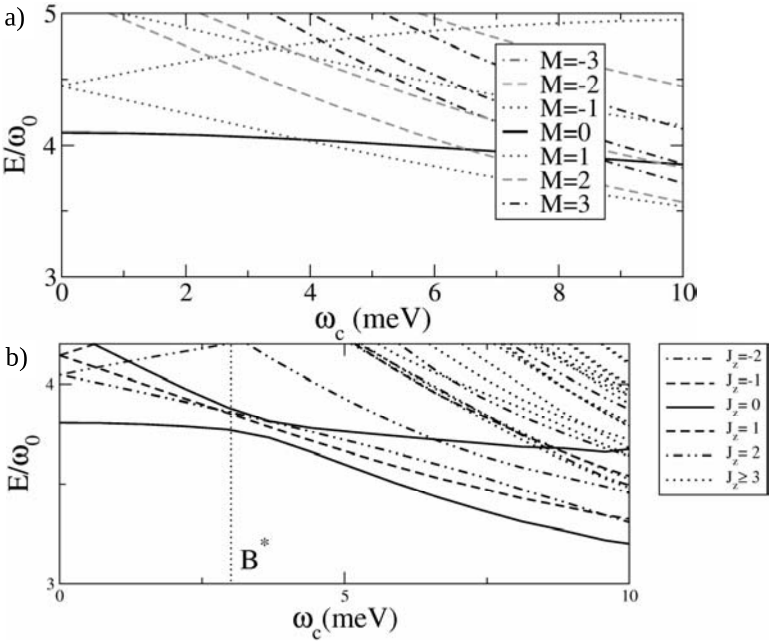

Fig. 6. A dot with $N = 2$ particles: energy spectrum vs. magnetic field ω_c in the absence of SO for $\omega_d = 5$ meV, and $U = 13$ meV (left box); energy spectrum vs. magnetic field ω_c in the presence of SO for the same parameters and $\alpha = 250$ meV·Å (right box)

The lowest lying singlet–triplet crossing is converted into an anticrossing. The Slater determinants that are involved the most corresponding to the states

$$|M = 0, S = 0, S_z = 0 >= d^\dagger_{-\downarrow} d^\dagger_{-\uparrow} |0>$$

$$|M = 1, S = 1, S_z = -1 >= d^\dagger_{+\downarrow} d^\dagger_{-\downarrow} |0>$$

$$|M = 1, S = 1, S_z = 0 >= \frac{1}{\sqrt{2}}\left(d^\dagger_{+\uparrow} d^\dagger_{-\downarrow} + d^\dagger_{+\downarrow} d^\dagger_{-\uparrow}\right)|0>$$

$$|M = 1, S = 1, S_z = 1 >= d^\dagger_{+\uparrow} d^\dagger_{-\uparrow} |0> \tag{6}$$

Here, $d^{\dagger}$ are creation operators for dot electrons and the label $-$ refers to the single particle orbital n = 0, m = 0, while the label $+$ represents n = 1, m = 1. As seen in Fig. 6, SO couples the first and second of these states, both of which belong to the total angular momentum $J = M + S_z = 0$ (the other two belong to J_z =1 and j_z = 2, respectively).

We want to show that under some special circumstances the Hamiltonian close to B^* can be reduced to the one of Eq. (11). The Hilbert space spanned by the four states in Eq. (6) can be mapped onto a pseudospin representation in terms of two spins, 1/2: $\vec{S}_1$ and $\vec{S}_2$ and with the corresponding basis $|S_+, S_+^z>$, with $\vec{S}_{\pm} = \vec{S}_1 \pm \vec{S}_2$ [16]. A comparison of the matrix elements onto the basis space show that the following correspondence holds

$$P\sum_{s} d_{ns}^{\dagger} d_{n's} P \;\Rightarrow\; n\delta_{n,n'}\left[\vec{S}_1\cdot\vec{S}_2 - \frac{1}{4} + n\right]$$

$$P\sum_{ss'} d_{ns}^{\dagger}\frac{1}{2}\vec{\sigma}_{ss'} d_{n's'} P \;\Rightarrow\; \frac{1}{2}\delta_{n,n'}\vec{S}_+ + \delta_{n,-n'}\frac{1}{2\sqrt{2}}\left[\vec{S}_- + 2in\vec{T}\right] \qquad (7)$$

where $\vec{T} = \vec{S}_1 \times \vec{S}_2$. P projects onto the Hilbert space of the four states. States $|S_+, S_+^z>$ are eigenstates of $\vec{S}_+$ and $\vec{S}_1\cdot\vec{S}_2$, while $\vec{S}_+$ and $\vec{T}$ produce transitions from the singlet state to triplets.

In this representation, the Hamiltonian close to $B = B^*$ takes the form:

$$H_{S_1,S_2} = K\vec{S}_1\cdot\vec{S}_2 - \mu B S_+^z + \frac{1}{2\sqrt{2}}\left[b_+\left(\vec{S}_-^- + 2in\vec{T}^-\right) + h.c.\right] \qquad (8)$$

where $b_+ = \alpha/l$. The second term is the Zeeman splitting in the triplet and the first two terms account for crossing at B^*. SO, by coupling the singlet and triplet with $S_+^z = -1$, opens up a gap and produces the anticrossing observed in Fig. 1. It can be shown that while $\vec{S}_1\cdot\vec{S}_2$ and $\vec{S}_+$ commute, they do not commute with $\vec{S}_-$ and $\vec{T}$, nor do $\vec{S}_-$ and $\vec{T}$ commute with each other. This proves that SO couples the centre of mass coordinates with the relative ones. Hence, the Kohn's theorem does not apply and microwave radiation shed onto the dot probes interactions as well.

As seen in Fig. 6, SO does not couple the states $|1,1>$, $|1,0>$, $|0,0>$, and $|1,-1>$. As far as SO is concerned, they are frozen. If we retain only the two states involved in anticrossing, we can further simplify the problem to a single spin 1/2: $\tilde{S}$. The correspondence between states is $|0,0>\to|\uparrow>$ and $|1,-1>\to|\downarrow>$. Defining P' as the projector on the two state basis, we have

$$P'S_{+}^{z}P' \;\Rightarrow \tilde{S}^{z}-\frac{1}{2}; \qquad P'\vec{S}_{1}\cdot\vec{S}_{2}P' \;\Rightarrow -\tilde{S}^{z}-\frac{1}{4}$$

$$P'S_{-}^{\pm}P' \;\Rightarrow -\sqrt{2}\,\tilde{S}^{\pm}, \qquad P'T^{\pm}P' \;\Rightarrow \mp\frac{i}{\sqrt{2}}\tilde{S}^{\pm} \tag{9}$$

It follows that the effective Hamiltonian of Eq. (8), rewritten in the new representation, reads

$$H_{\tilde{S}} = -\frac{1}{2}\left(\frac{K}{2}-\mu B\right)-\vec{\tilde{b}}\cdot\vec{\tilde{S}} \tag{10}$$

where $\tilde{b}^{z} = K+\mu B$ and $\tilde{b}^{\pm} = 2b^{\pm}$. This maps the two-electron Hamiltonian of Eq. (1), close to the anticrossing point, onto the Hamiltonian

$$\hat{H}_{\tilde{S}} = -\vec{b}\cdot\vec{\tilde{S}} \equiv -\begin{bmatrix} b\cos\vartheta & b\sin\vartheta e^{i\omega t} \\ b\sin\vartheta e^{-i\omega t} & -b\cos\vartheta \end{bmatrix} \tag{11}$$

where

$$b=\sqrt{\omega_o^2+\alpha^2/l^2}\,, \quad \tan\vartheta = \frac{\alpha}{\omega_o l} \quad (\text{or } b_z = b\cos\vartheta = \omega_o, \;\; b_{\pm} = b\sin\vartheta e^{\pm i\omega t} = \frac{\alpha\, e^{\pm i\omega t}}{l})$$

and we have assumed an oscillating time dependence for the electric field

$$E \rightarrow E\, e^{\pm i\omega t}$$

The dot state may be controlled by properly tuning the external control parameters *B* and *E*. An adiabatic cycle is realized by keeping *B* fixed, and by slowly and periodically varying *E* with a time period *T*.

As the first step, we find the instantaneous eigenstates of $\hat{H}_{\tilde{S}}(t)$ in Eq. (11), corresponding to the eigenvalues $\varepsilon = \pm b$

$$\left|+,t\right\rangle = \begin{pmatrix} \cos\frac{\vartheta}{2} \\ \sin\frac{\vartheta}{2}e^{i\omega t} \end{pmatrix}, \qquad \left|-,t\right\rangle = \begin{pmatrix} -\sin\frac{\vartheta}{2}e^{-i\omega t} \\ \cos\frac{\vartheta}{2} \end{pmatrix} \tag{12}$$

The Berry phase accumulated by the states $|\pm>$, by adiabatically operating along a period *T*, is

$$\Gamma_{\pm}(T) = i\oint_{\gamma} d\vec{\lambda}\cdot\left\langle \pm,\vec{\lambda}\right|\vec{\nabla}_{\vec{\lambda}}\left|\pm,\vec{\lambda}\right\rangle \tag{13}$$

Here, $\vec{\lambda} \equiv \vec{b}$ is the set of parameters describing the system.

$$\frac{d\Gamma_\pm}{dt} = \mp\frac{\omega}{2}\left(1-\cos\left(\vartheta\right)\right) \Rightarrow \Gamma_\pm\left(t\right) = \mp\frac{\pi t}{T}\left(1-\cos\left(\vartheta\right)\right) \tag{14}$$

It is useful to fix the phases of the adiabatic basis $|\pm,t>$ in such a way that they satisfy the parallel transport condition between successive times, namely

$$<\pm,t|\frac{d}{dt}|\pm,t>=0 \tag{15}$$

This choice implies that non-adiabatic terms (i.e., terms of $O(1/T)$ are always off -diagonal. Let us choose such an initial condition that the spin $\tilde{S}$ is in the state $|+>$ with an energy of $-b$. In the basis of states $e^{-i\Gamma_\pm(t)}\,|\pm(t)>$, at later times the spin wave function takes the form:

$$|u(t)>=e^{-i\omega t/2}\begin{pmatrix}\cos bt - i\cos\vartheta\sin bt + i\dfrac{\omega}{2b}\sin bt \\ -i\sin\vartheta\sin bt\end{pmatrix} \tag{16}$$

This state is a superposition of the two states that correspond to the anticrossing levels. In Chapter 5 we briefly discuss how to read out this mixture.

4. Three electrons: a very special Berry phase

In Figure 7 we show the avoided crossing that appears in the spectrum of $N = 3$, involving states with total angular momentum $J = M + S_z i = 3/2$. They are:

$$|S=3/2, M=3\,S_z=-3/2>,|S=1/2, M=2\,S_z=-1/2>,|S=1/2, M=1\,S_z=1/2>$$

The SU(3) Berry phase requires eight parameters to be available for the 3×3 hermitian Hamiltonian matrix. This is far too much for present fabrication possibilities. We have considered the possibility of controlling a smaller amount of degrees of freedom, which produces an accidental crossing of a third level in an otherwise SU(2) parameter manifold. The states given above are coupled by spin-orbit when the electric field is of the kind

$$E_z(t) = e + g_1(t)\cos\theta + g_2(t)\sin\theta \tag{17}$$

with $g_1 + ig_2 = |g|\,e^{i\omega t}$. In fact, they contain Slater determinants whose single particle states have non zero matrix elements of the spin orbit interaction between some constituents of single particle states.

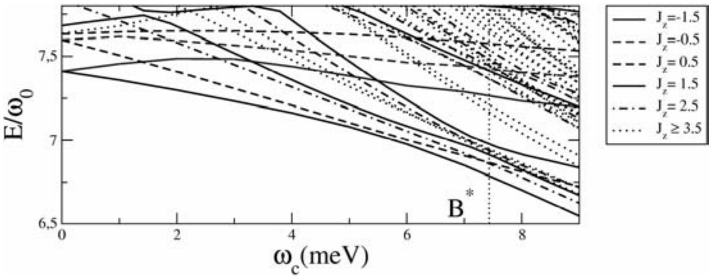

Fig. 7. A dot with $N = 3$ particles: energy spectrum vs. magnetic field ω_c in the presence of SO for $\omega_d = 7$ meV, $U = 13$ meV, and $\alpha = 250$ meV·Å. The GS is $J_z = 3/2$, the FES is $J_z = 5/2$

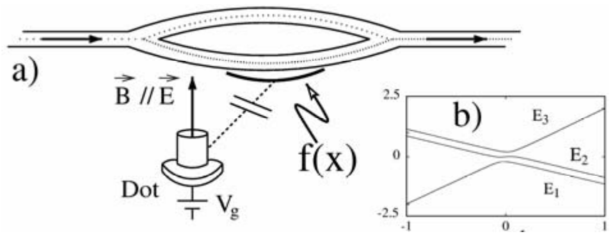

Fig. 8. A sketch of a possible experimental setup for detecting the Berry phase (a); $f(x)$ accounts for the spatial modulation of the coupling between the dot and interferometer (see text); energy levels of the dot, E_ℓ, vs. $b = (3/2)(B - B^*)$ (b)

Let us denote the relevant single particle states by the sequence of quantum numbers $(n, m, s = 1/2, s^z)$. The states $(1, \vec{\lambda}) \equiv (11, 1/2, -1/2, \vec{\lambda})$, $(3, \vec{\lambda}) \equiv (22,\ 1/2, -1/2, \vec{\lambda})$, and $(2, \vec{\lambda}) \equiv (11, 1/2, 1/2, \vec{\lambda})$ are present in some of the Slater determinants that form the many-body states given above and have non vanishing matrix elements of the spin orbit interaction of Eq. (17), according to the Hamiltonian:

$$\hat{h}[b, g_1, g_2, e] = \begin{bmatrix} -b & 0 & g^* \\ 0 & 2b & e \\ g & e & -b \end{bmatrix} \tag{18}$$

If $b = 3(B - B^*)/2$, the three eigenvalues become degenerate at $B = B^*$ and $E = 0$. $\hat{h}[b, g_1, g_2, e]$ is a traceless 3×3 Hermitian matrix, belonging to the SU(2)-algebra. Its eigenvalues take a simple form in terms of the “polar” coordinates R, Ψ

$$R = \sqrt{b^2 + \frac{e^2 + |g|^2}{3}}, \qquad \sin(3\Psi) = -\frac{b(b^2 + \frac{e^2}{2} - |g|^2)}{R^3} \tag{19}$$

In decreasing order, the energies are given by [17]:

$$E_\ell = 2R\sin\left[\Psi + \frac{2}{3}(\ell - 1)\pi\right], \quad \ell = 1, 2, 3 \tag{20}$$

In Figure 8b, we plot E_1, E_2 and E_3 versus b for small but nonzero e and g. The corresponding eigenvectors will be denoted further by $|e_\ell, \vec{\lambda}>$, $\ell = 1, 2, 3$. Figure 8b shows the avoided crossing vs. b. In particular, if $b < 0$, then the level E_1 is almost degenerate with E_2, and the degeneracy at $e = g = 0$ takes place at $\Psi = \pi/6$. On the other hand, if $b > 0$, then it is E_3 that is almost degenerate with E_2, and the degeneracy takes place at $\Psi = \pi/2$. At $b = 0$ an "exceptional" three-level degeneracy arises, when $e = g = 0$ ($R = 0$), which is not, however, an accidental three-level degeneracy.

The explicit calculation of the Berry phase for a closed path γ at fixed b, lying in the subspace of the coordinates (g_1, g_2, e), can be found in [17].

For $b < 0$, there is an energy gap of order b between E_3 and the next available energy level (E_2), so that we do not expect any Berry phase to arise within such a region. On the other hand, we do expect a Berry phase to appear for $b > 0$ when E_3 is almost degenerate with E_2. Therefore, whether the Berry phase arises or not is just a matter of whether $b > 0$ or $b < 0$. Clearly, no fine tuning of the external field is required, provided it is possible to move B across B^*.

Our realization of the Berry phase in a quantum dot is the simplest setup that can be theoretically studied retaining the required features. Actually, its experimental realization is quite demanding, at least as long as one is concerned with a single dot. For instance, one can imagine a setup where the maximum of E could be off-centre in the dot area and rotating in time. Alternatively, asymmetries in the shape of the dot that slowly depend on time might produce a Berry phase.

5. Comments on detecting the superposition of dot states

In conclusion, by applying a rather strong orthogonal magnetic field $B \perp z$, a disk shaped Quantum Dot (QD) with a few electrons becomes a droplet of maximum electron density (MDD), maximum total angular momentum M, and maximum spin S. An increase of S and M occurs via crossings between levels. A prototype of this occurrence is the singlet–triplet transition in a two-electron dot. A gate voltage induces the Rashba (spin-orbit) term, which couples S to the electric field orthogonal to the QD disk. M and S_z are no longer good quantum numbers, but $J_z = M + S_z$ is. This changes the crossing into an avoided crossing, because of the level repulsion between levels with equal J_z. We monitor these crossings for a dot with a few electrons by means of exact diagonalisation (up to $N = 5$ electrons). By operating the electric field, one can construct a superposition of the states involved in the anticrossing. Their phase is controlled by changing the applied electric field in time.

The level structure of the dot close to the anticrossing can be modelled by an effective spin Hamiltonian. We have studied an isolated QD at fixed N elsewhere [17], with a weak capacitive contact to one arm of a two path interferometer. By operating with a gate voltage on the dot cyclically in time, we have proposed to modulate the transmission across the interferometer (see Fig. 8). Electrons travelling in the edge states of the interferometer's arm that are coupled to the dot may feel the charge-

charge correlations at different times and be reflected by what looks like a change in the effective dielectric constant in time.

Here, we have discussed only the cases of $N = 2$ and $N = 3$, which show marked avoided crossings in the level structure versus B. At larger N, these features are smeared out substantially and a different physics takes over. A closer look at the QD energy spectrum shows that e-e correlations and spin-orbit produce a spin texture in the first excited state beyond B^*, with a reversed spin density concentrated at the origin [14]. The situation resembles a quantum Hall ferromagnet (QHF) with filling close to one. In the QHF, symmetry breaking due to full spin polarization sustains a gapless collective spin excitation, named the “skyrmion”. In the QD, the gap is finite and it is tuned by the Rashba coupling. This opens up many unexpected possibilities of controlling electron spin density at the dot and the possibly underlying nuclear spins coupled via hyperfine interaction.

References

[1] DiVincenzo D.P., Science, 270 (1995), 255.

[2] Nakamura Y., Pashkin Y.A., Tsai J.S., Nature, 398 (1999), 768.

[3] Mooij J.E. Orlando T.P., Levitov L., Tian L., van der Wal C.H., Lloyd S., Science, 285 (1999), 1036.

[4] Bayer M., Hawrylak P., Hinzer K., Fafard S., Korkusinski M., Wasilewski Z.R., Stern O., Forchel A., Science, 291 (2001), 451; Petta J.R., Johnson A.C., Marcus C.M., Hanson M.P., Gossard A.C., Phys. Rev. Lett., 93 (2004), 186802.

[5] Schliemann J., Loss D., MacDonald A.H., Phys. Rev. B, 63 (2001), 085311.

[6] Kastner M.A., Ann. Phys., 9 (2000), 885; Sasaki S., de Franceschi S., Elzerman J.M., van der Wiel W.G., Eto M., Tarucha S., Kouwenhoven L.P., Nature, 405 (2000), 764.

[7] Farhi E., Goldstone J., Guthann S., Lapan J., Lundgren A., Preda D., Science, 292 (2001), 472; Pachos J., Zanardi P., Rasetti M., Phys. Rev. A, 61 (2000), 010305(R).

[8] Jouault B., Santoro G., Tagliacozzo A., Phys. Rev. B, 61 (2000), 10242; Kouwenhoven L.P., Oosterkamp T.H., Danoesastro M.W., Eto M., Austing D.G., Honda T., Tarucha S., Science, 278 (1997), 1788.

[9] Berry M.V., Proc. R. Soc. London, Ser. A, 392 (1984), 45.

[10] Merkt U., Huser J., Wagner M., Phys. Rev. B, 43 (1991), 7320; Tarucha S., Austing D.G., Honda T., van der Hage R.J., Kouwenhoven L.P., Phys. Rev. Lett., 77 (1996), 3613.

[11] Oosterkamp T.H., Janssen J.W., Kouwenhoven L.P., Austing D.G., Honda T., Tarucha S., Phys. Rev. Lett., 82 (1999), 2931.

[12] Rokhinson L.P., Guo L.J., Chou S.Y., Tsui D.C., Phys. Rev. Lett., 87 (2001), 166802.

[13] Chamon C. de C., Wen X.G., Phys. Rev. B, 49 (1994), 8227; Reimann S.M., Koskinen M., Manninen M., Mottelson B.R., Phys. Rev. Lett., 83 (1999), 3270.

[14] Lucignano P., Jouault B., Tagliacozzo A., Phys. Rev. B, 69 (2004), 045314.

[15] Lucignano P., Jouault B., Tagliacozzo A., Altshuler B., to be published.

[16] Pustilnik M., Glazman L.I., Phys. Rev. Lett., 85 (2000), 2993; Eto M., Nazarov Y., Phys. Rev. Lett., 85 (2000), 1306; Pustilnik M., Avishai Y., Kikoin K., Phys. Rev. Lett., 84 (2000), 1756.

[17] Giuliano D., Sodano P., Tagliacozzo A., Phys. Rev. B, 67 (2003), 155317.

Received 20 September 2004
Revised 9 November 2004

Materials Science-Poland, Vol. 22, No. 4, 2004

Effects of Coulomb interactions in electron transport through short molecular chains

TOMASZ KOSTYRKO[1*], BOGDAN R. BUŁKA[2]

[1]Institute of Physics, A. Mickiewicz University, Umultowska 85, 61-614 Poznań, Poland

[2]Institute of Molecular Physics, Polish Academy of Sciences, Smoluchowskiego 17, Poznań, Poland

Charge transport properties of short molecular chains connected to electrodes are studied using the non-equilibrium Green function method. The chains are described using a single-orbital Hubbard model. In the weak interaction range and low-temperature limit, the current flowing through the system was analysed within the Hartree–Fock approximation (HFA). It was found that for a weak coupling between the molecule and the leads *I–V* characteristics can be represented as a sequence of plateaus, alternating with regions of a finite slope. This finite slope in the *I–V* characteristics is related to the self-consistent molecular level being pinned down to the Fermi levels of the electrodes over a finite voltage regions. It is also related to a continuous change in the charge state of the molecule. In the strong repulsion limit, the HFA method is no longer credible and we resort to decoupling the equations of motion (EOM) for the Green functions of the chains, in order to treat all intrachain correlations and hopping exactly but to neglect some correlations between the molecule and the leads. A comparison of the results obtained with these two approaches for the same parameters allows us to make general observations concerning the role of correlations in transport through molecular junctions.

Key words: *charge transport through molecule; electron–electron interactions*

1. Introduction

Fast development of nanotechnology has led to manufacturing molecular junctions which are expected to replace silicon-based devices in electronic applications in a near future [1]. Several experimental methods are currently being used to obtain junctions with nanometer-sized molecules trapped between their macroscopic metallic leads. Despite technical differences between various experimental methods, the accumulated data show some general features of molecular junctions that involve short atomic and molecular wires.

---

[*] Corresponding author, e-mail: Akos@hts1.physd.amu.edu.pl.

Monatomic chains, for instance gold atoms pulled out from gold leads by a STM tip [2–4] or an H_2 molecule trapped between platinum electrodes [5], behave like perfect ballistic conductors at small voltages, with the conductance hardly depending on chain length. All the damping and Joule heating takes place in the electrodes up to the voltage threshold (of the order of several dozens of millivolts), when the onset of inelastic scattering due to electron coupling with intrachain vibrations starts to reduce the current in a step-wise fashion by several percent. For atoms with partially filled s-levels, the zero-voltage conductance is close to the quantum unit, $G_0 = 2e^2/h$, and the current can be as large as 80 μA (for a voltage of about 1 V). This indicates that a strong coupling exists between the electrodes and atomic chains, as well as that there is a single channel for transmission.

Junctions involving short organic wires, like benzene dithiolate, [6], bithiol-terthiophene [7], alkane dithiolates [8], or 4,4-bipyridinium [8] usually support relatively low currents, rarely exceeding 1 μA. The resistance of polymeric wires usually grows exponentially with their length [8]. A much smaller conductance of junctions with organic wires as compared to ones with s-orbital atomic wires is due to, first of all, a rather small overlap of the s-orbital of the metallic leads and p-orbitals of the HOMO-LUMO subsystem of the molecules. Also, a Schottky-like barrier created at the bonding atom of the molecule (often sulphur, nitrogen, or carbon) can be responsible for this weak coupling. Despite weak coupling to the leads, this coupling significantly perturbs the molecular levels and the differential conductance exhibits relatively wide peaks with halfwidths of the order of 1 V, even at temperatures much smaller than estimated for the coupling and separations of the levels.

Theoretical works aiming to describe transport characteristics in molecular junctions range from simple parametric models using tight binding models, [9–11] through extended Hückel calculations [7, 12–15], to *ab initio* methods [16–21] using density functional theory (DFT). While these methods differ in the number of atomic orbitals of the molecules included in computations and the way of treating the electron –electron interactions, they all belong to the class of single-particle approaches and neglect the effects of electron correlation. On the quantitative level, first principles computations often overestimate the current transmitted through junctions with organic molecules by more than an order of magnitude [18, 21], even if the shape of the I–V curves is fairly well reproduced. Parametric (semiempirical) calculations can be used to fit experimental values of current for a given voltage by a proper choice of the coupling parameter (or a function) Γ but in this case the overall shape of the current –voltage (I–V) curve is not described well [13, 7]. The value of Γ, taken in order to reproduce the values of the current, usually gives too narrow peaks in the corresponding differential conductance curves or too sharp steps in the I–V curve.

In the face of a quantitative disagreement between results for single particle computations and experimental findings, it is natural to ask about the role of the hitherto neglected effects of electron correlation in a more complete understanding of the transport properties of molecular junctions including organic molecules. As we know from work performed on systems of lithographically defined artificial atoms, i.e. quantum dots (QD), the effects of electron correlation can be very important, and manifest themselves in the Coulomb blockade [22] or Kondo effect [23]. Although correlation driven phenomena in QDs are observed at very low temperatures (1 K or less), the corresponding effects in molecular junctions could play a role in a higher temperature range as a result of much higher (by a factor of 10^3) energy parameters, i.e. intradot Coulomb repulsion, coupling to the leads, coupling between neighbouring QDs, etc.

The purpose of the present work is to provide some examples of computations, supported by parametric models, for a very simple system (2-atom molecule), using both a quasiparticle approach and a method that treats electron correlations within the molecule in an exact manner. A comparison of the two approaches, within the same parameter range, may elucidate the role of electron correlation in transport through molecular junctions. Although such a comparison is possible only for systems with a very small number of electron degrees of freedom (atomic orbitals), an extension of the present work to larger systems could reveal some generalizations of the observed tendencies.

2. Quasiparticle description of electron transport

We describe the system of a molecule connected to macroscopic leads by the following Hamiltonian

$$H = \sum_{\alpha=L,R} H_\alpha + H_T + H_M \tag{1}$$

where H_α is the one-particle Hamiltonian of the left (for $\alpha = L$) or right (for $\alpha = R$) lead, H_T describes one-particle tunneling between the leads and the molecule (for simplicity, we assume that the molecule is attached to the leads by means of a single atom), and H_M is the Hamiltonian of the molecule.

The molecular part of the system is described by a single-orbital Hubbard Hamiltonian:

$$H_M = \sum_{jm\sigma} t_{jm} d^+_{j\sigma} d_{m\sigma} + \sum_{j\sigma} E_j n_{j\sigma} + U \sum_j n_{j\sigma} n_{j-\sigma} \tag{2}$$

where t_{jm} is the intramolecular hopping parameter, U is the on-site electron repulsion, and the site energy E_j includes a contribution from the bare external potential generated by a voltage applied to the leads (the potential ramp [15]).

In order to analyse the transport characteristics of such a molecular junction, we use the non-equilibrium Green function method*. The current is computed using a general formula obtained by Meir and Wingreen [25]

---

*For the technique of the non-equilibrium Green functions and its applications in electronic transport, see Ref. [24].

$$J=\frac{ie}{h}\int d\omega \Gamma_L\left[f_L(G^r_{LL\sigma}-G^a_{LL\sigma})+G^<_{LL\sigma}\right] \tag{3}$$

where $G^{r,a,<}_{jm\sigma}=\left\langle d_{j\sigma}\,|\,d^+_{m\sigma}\right\rangle^{r,a<}$ denotes the retarded, advanced, and the lesser Green functions, respectively, f_α is the Fermi function, and the function Γ_α describes the coupling between the lead α and the molecule. Γ_α is proportional to the local surface density of states in the leads and the squared parameter for hopping between the molecule and leads ($v_{k\alpha}$). In what follows, Γ_α is considered to be a phenomenological constant.

Because of the presence of the Hubbard interaction in the molecular Hamiltonian H_M, it is necessary to resort to an approximative method for computing the Green functions in Eq. (3). Applying the quasiparticle approach, which is common to all first-principle calculations, we replace the molecular Hamiltonian by a single-particle form using the mean-field approximation (MFA) [26]

$$H_M\to H^{MFA}_M=\sum_{jm\sigma}t_{jm}d^+_{j\sigma}d_{m\sigma}+\sum_{j\sigma}E^{eff}_j n_{j\sigma},\qquad E^{eff}_j=E_j+\frac{U}{2}\sum_{\sigma}\left\langle n_{j\sigma}\right\rangle \tag{4}$$

The non-equilibrium values of electron occupation $\left\langle n_{j\sigma}\right\rangle$ are then computed self -consistently using the lesser Green functions, $G^{r<}_{jj\sigma}$. Within the MFA, the interacting region was replaced by some effective non-interacting region with a voltage-dependent electronic structure of the Hamiltonian (4).

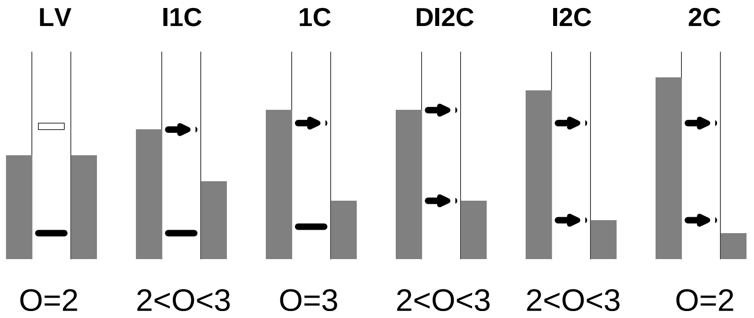

Fig. 1. Voltage ranges in the transport of a molecular junction including a 2-atom molecule. Shaded areas: occupied electron levels in the electrodes. Thick solid black lines: molecular SCE levels, fully occupied in the weak coupling limit non-contributing to the total current. Grey lines: empty and non-conducting levels in the weak coupling limit. Lines with arrows: partially occupied levels participatinge in transport. The total electron charge of the molecule in the zero coupling limit (Q) does not include an extra contribution from the voltage ramp

The main features of the voltage dependence of current in an arbitrary junction can be qualitatively understood by using a simple example of the two-atom system. The electronic structure of such a system includes just two self-consistent energy

(SCE) levels: the bonding level (E_B) and the antibonding one (E_A). In Figure 1, the subsequent voltage ranges in the transport through the 2-atom chain are indicated.

Let us discuss a typical situation for low-conducting molecular systems with weak molecule–lead coupling ($\Gamma << E_A - E_B = \Delta$) in the low temperature region ($k_BT << \Delta$). In the low-voltage (LV) range, the electrochemical potentials of the leads are usually positioned somewhere inside the HOMO-LUMO gap. In this region, and in the weak -coupling limit, the antibonding level is nearly completely empty and the bonding one is nearly completely filled and as a result the molecule is approximately neutral. The current is exponentially small in the LV region, as it requires an electron (or a hole) excitation through the gaps, $|\mu_{L,R} - E_{A,B}|$. On increasing the voltage, one of the electrochemical potentials reaches one of the SCE levels, say E_A. In the absence of electron interaction in the molecular Hamiltonian, this level would be immediately loaded by about one electron charge (in the case of symmetric coupling to both leads) and the current would exhibit a step-wise increase. The system would be in a one-channel (1C) transport range, where charge transfer between the leads does not require electron excitation.

In the presence of an electron repulsion U, the positions of the SCE levels depend on charge. When the electrochemical potential of the source lead hits the SCE antibonding level (see the second diagram in Figure 1), the process of its filling is counteracted by a corresponding rise of the level in the energy scale. In result, for finite U, the SCE antibonding level follows the position of the electrochemical potential of the source lead for some finite voltage range, and the width of this range increases with the repulsion. In this incomplete one-channel (I1C) transport range, the current grows gradually with the voltage, along with a smooth increase of the electron charge on the molecule. With a further increase in the voltage, the interacting system goes through a 1C transport range sequence and enters the I2C (incomplete 2-channel) transport range, where the electrochemical potential of the drain lead reaches the other SCE level (i.e. the bonding level in the present case). The molecule is gradually discharged and the current undergoes a second stage of rapid, but continuous increase with the voltage. This evolution ends with the 2-channel (2C) transport range, where both SCE levels are found inside the source-drain voltage window, become half -occupied (i.e. the molecule is neutral again), and the current does not increase with the voltage anymore.

The above analysis can easily be generalized to a system with an arbitrary amount of levels. The evolution of the current with changing voltage can be described as a sequence of ranges: LV...(n – 1)C–InC–nC... etc., where nC denotes the n-channel transport range. Each range with incomplete n-channel (InC) transport is characterized by a continuous increase of the current with the voltage and by an accompanying gradual charging (for odd n) or discharging (for even n) of the molecule with rising voltage. The transport ranges of fast current increase alternate with the nC ranges, where both the current and molecule charge depend on the voltage only weakly (for the weak coupling limit).

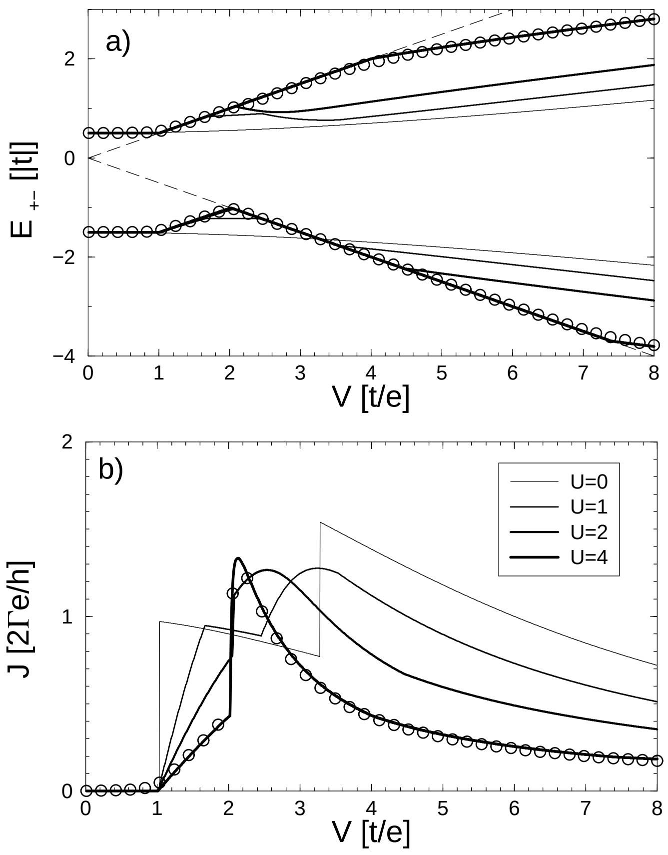

Fig. 2. Molecular junction with a 2-atom molecule: a) voltage dependence of SCE levels, as obtained from HFA for several values of Coulomb repulsion; solid lines: $\Gamma \to 0$ limit, circles: $\Gamma = 0.01$ for $U = 4.0$; all data are obtained for constant $E + U/2 = -0.5$. Broken lines denote the positions of the electrochemical potential in the leads, b) voltage dependence of the current, as obtained from HFA for several values of Coulomb repulsion; lines: $\Gamma \to 0$ limit, circles: $\Gamma = 0.01$ for $U = 4.0$; all data were obtained for constant $E + U/2 = -0.5$

In Figure 2a, we present voltage dependences of the SCE levels for the 2-atom molecule in the weak coupling limit for $E + U/2 = -0.5|t|$, whereas in Fig. 2b we show the corresponding I–V characteristics. One can see that SCE level pinning (Fig. 2a) is accompanied by a linear rise of the current (Fig. 2b) and that the slope of this rise generally decreases with increasing U for weak-to-moderate repulsion. For U strong enough ($U > 2|t|$ for $E + U/2 = -0.5|t|$), for which both SCE levels are simultaneously pinned (see the fourth diagram in Fig. 1), the current jumps rapidly and then decreases with increasing voltage; we call this range the double-incomplete 2-channel (DI2C) range. In the high voltage regime, i.e. for the 2C range, the current decreases with the voltage, which is due to the strong distortion of the SCE levels by the steep potential ramp.

3. Strongly correlated molecular junctions

The above discussion of the effects of electron interactions on transport is limited to the range of weak-to-intermediate interactions and to low temperatures. In the limit of strong on-site repulsion, the electron structure of the molecule (or a collection of coupled artificial atoms, like quantum dots) is significantly modified by such interactions [27]. In particular, the repulsion leads to an extra splitting of the one-particle peaks in the conductance spectrum, as is well known from the Coulomb blockade phenomena [22, 28].

Previous studies on transport through atomic or molecular junctions in the strongly correlated regime have usually been restricted to the weak coupling (i.e. Coulomb blockade) regime [28–30], where $\Gamma << |t|, U$. Other studies have used approximations in the sequence of the equations of motion for the Green functions, which are difficult to control [31–34]. Here, we outline a general approach that allows us to accurately reproduce the well-known limiting cases of the non-interacting model (for arbitrary values of coupling and temperature) and the strongly correlated limit of the Coulomb blockade [28, 29] (for weak coupling and not too low temperature).

We start from rewriting the molecular Hamiltonian using Hubbard operators [35]

$$H_M = \sum_{\lambda} E_{\lambda} X_{\lambda\lambda} \tag{5}$$

E_{λ} denotes the exact eigenvalue of the molecular Hamiltonian (in the presence of an external potential generated by the leads). The Hubbard operators are constructed using the exact eigenstates of H_M, $X_{\mu\nu} = |\mu><\nu|$. The one-particle Green functions from Eq. (3) can be written in terms of linear combinations of "mixed" Green functions, redefined in terms of Hubbard operators and single particle operators

$$G_{jm\sigma} = \sum_{\lambda\lambda'} \langle \lambda | d_{j\sigma} | \lambda' \rangle G_{\lambda\lambda',m\sigma}, \qquad G_{\lambda\lambda',m\sigma} = \left\langle X_{\lambda\lambda'} \middle| d^{+}_{m\sigma} \right\rangle \tag{6}$$

The equations of motion for the Green functions defined in Eq. (6) generate a chain of higher-order Green functions, e.g.:

$$\frac{d}{dt} \left\langle X^{F}_{\lambda\lambda'} \middle| d^{+}_{m\sigma} \right\rangle \to v_{k\alpha} \left\langle X^{B0(B2)}_{\mu\mu'} c^{(+)}_{k\alpha\sigma'} \middle| d^{+}_{m\sigma} \right\rangle \tag{7}$$

$$\frac{d}{dt} \left\langle X^{B0} c_{k\alpha\sigma'} \middle| d^{+}_{m\sigma} \right\rangle \to v_{k'\alpha'} \left\langle X^{F}_{\varsigma\varsigma'} c^{+}_{k'\alpha'\sigma''} c_{k\alpha\sigma'} \middle| d^{+}_{m\sigma} \right\rangle \tag{8}$$

where B_n indicates a boson-like Hubbard operator [36] which reduces the number of electrons in a state by n, F denotes a fermion-like Hubbard operator, which removes a single electron from a state, and $c_{k\alpha\sigma}$ is the fermion operator for the state k_{σ} in the lead α. In order to close the set of equations, we neglect electron correlations between the molecule and the leads and decouple the higher order Green function from Eq. (8) in the following way

$$\left\langle X^{F}_{\varsigma\varsigma'} c^{+}_{k'\alpha'\sigma''} c_{k\alpha\sigma'} \middle| d^{+}_{m\sigma} \right\rangle \to \delta_{k'\alpha'\sigma'',k\alpha\sigma'} f_{k\alpha} \left\langle X^{F}_{\varsigma\varsigma'} \middle| d^{+}_{m\sigma} \right\rangle \tag{9}$$

where $f_{k\alpha}$ is the Fermi factor. In the case of a one-atom molecule, this approximation reduces to the results of Meir et al [37] and correctly describes the limit of the Coulomb blockade. In the non-interacting limit of the Hubbard model, it reproduces the exact results. For finite repulsions *U*, neglecting lead–molecule correlations is credible for temperatures higher than the Kondo temperature. In our numerical computation, we evaluated the poles of the Green functions in the high-temperature approximation (setting $f_{k\alpha} = 1/2$), neglecting the Kondo divergences. The residues of the Green functions can be expressed by the averages of boson-like Hubbard operators which were computed here in a self-consistent manner using appropriate lesser Green functions.

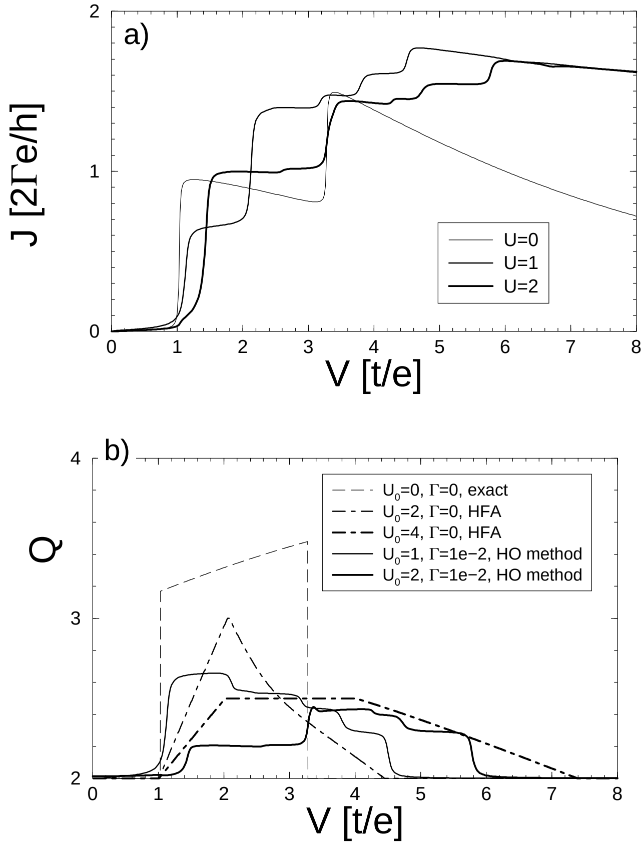

Fig. 3. Molecular junction with a 2-atom molecule: a) voltage dependence of the current, as obtained from the equation of motion method using the Hubbard operators, for several values of Coulomb repulsion for $\Gamma = 0.01$; all data were obtained for constant $E + U/2 = -0.5$; b) total electron charge as a function of the voltage, as obtained from HFA and the equation of motion method with second order decoupling

In Figure 3a, we present *I–V* characteristics for a junction with a 2-atom molecule, as obtained from the equation of motion approach, for several values of repulsion. One can see that the current rises in a step-wise manner with increasing voltage, unlike in the HFA computation. The electronic structure of the 2-atom molecule, with all intramolecular electron correlations taken exactly into account, is much more complex [27] than the one obtained in the quasiparticle approach. The current steps in Fig. 3a reflect electron transitions including all excited states of the 2-atom Hubbard molecule.

In Figure 3b, we show the total electronic charge in the molecule as a function of the voltage, as obtained from both the HFA method and the equation of motion. Quantitatively, the results of both methods are similar, except for the fact that HFA tends to overestimate the value of the charge as compared to the equation of motion approach. Again, the HFA method gives a quasilinear change of the charge with voltage, which is consistent with SCE level pinning, whereas in the equation of motion method changes of the charge are step-wise.

4. Final remarks

We have analysed transport characteristics of a molecular junction including a 2-atom molecule, described by the Hubbard model. We compared the results obtained with the self-consistent quasiparticle approach (HFA) and equation of motion method, where all the intramolecular electron correlations were treated exactly and some lead–molecule correlations were neglected. While the HFA method showed SCE level pinning, accompanied by a continuous quasi-linear rise of the current for some U-dependent voltage ranges, the calculation including electron correlations does not show this effect. Concerning the charge–voltage characteristics, both methods show a suppression of the excess transferred charge Q with increasing repulsion. The observed differences are strongest for weak values of Γ, whereas for strong coupling the results of the two approaches are quantitatively and qualitatively more similar.

More theoretical work is needed to understand the role of the neglected lead –molecule correlations. One can expect that the Kondo correlations are important at least in the low temperature region and for finite charge transfer from the lead to the molecule ($Q > 2$ for $E + U/2 < 0$). Since these correlations promote the formation of resonance states at the Fermi levels of the leads, a screening of the unpaired spin of the molecule may lead to a tendency for correlated level pinning as well. In such a case, one might expect the I–V characteristics to be somewhat smoother and a region of quasi-linear increase to appear in the current–voltage dependences.

Acknowledgments

This work is supported by the State Committee for Scientific Research (Poland), project PBZ KBN 044 P03 2001 and in part (B.R.B) by the Centre of Excellence for Magnetic and Molecular Materials for Future Electronics within the European Commission Contract No. G5MA-CT-2002-04049.

References

[1] TOUR J.M., *Molecular Electronics: Commercial Insights, Chemistry, Devices, Architecture and Programming*, World Scientific, Singapore, 2003.

[2] Ohnishi H., Kondo Y., Takayanagi K., Nature, 395 (1998), 780.

[3] Yanson A.I., Rubio-Bollinger G., van den Brom H.E., Agrait N., van Ruitenbeek J.M., Nature, 395 (1998), 780.

[4] Agrait N., Untiedt C., Rubio-Bollinger G., Vieira S., Phys. Rev. Lett., 88, 216803 (2002).

[5] Smit R.H.M., Noat Y., Untiedt C., Lang N.D., van Hemert M.C., van Ruitenbeek J.M., Nature, 419 (2002), 906.

[6] Reed M.A., Zhou C., Muller C.J., Burgin T.P., Tour J.M., Science, 278 (1997), 252.

[7] Kergueris C., Bourgoin J.-P., Palacin S., Esteve D., Urbina C., Magoga M., Joachim C., Phys. Rev. B, 59 (1999), 12 505.

[8] Xu B., Tao N.J., Science, 301 (2003), 1221.

[9] Mujica V., Kemp M., Roitberg A., Ratner M., J. Chem. Phys., 104 (1996), 7296.

[10] Magoga M., Joachim C., Phys. Rev. B, 57 (1998), 1820.

[11] Emberly E.G., Kirczenow G., Phys. Rev. B, 61 (2000), 5740; Phys. Rev. B, 62 (2000), 10451.

[12] Samanta M.P., Tian W., Datta S., Henderson J.I., Kubiak C.P., Phys. Rev. B, 53 (1996), R7626.

[13] Datta S., Tian W., Hong S., Reifenberger R., Henderson J.I., Kubiak C.P., Phys. Rev. Lett., 79 (1997), 2530.

[14] Emberly E.G., Kirczenow G., Phys. Rev. B, 58 (1998), 10911.

[15] Tian W., Datta S., Hong S., Reifenberger R., Henderson J.I., Kubiak C.P., J. Chem. Phys., 109 (1998), 2874 .

[16] Lang N.D., Phys. Rev. B, 52 (1995), 5335.

[17] Lang N.D., Avouris Ph., Phys. Rev. Lett., 84 (2000), 358.

[18] Di Ventra M., Pantelides S.T., Lang N.D., Phys. Rev. Lett., 84 (2000), 979.

[19] Damle P., Ghosh A.W., Datta S., Chem. Phys., 281 (2002), 171.

[20] Brandbyge M., Mozos J.-L., Ordejon P., Taylor J., Stokbro K., Phys. Rev. B, 65 (2002), 165401.

[21] Xue Y., Ratner M.A., Phys. Rev. B, 68 (2003), 115406.

[22] Kastner M.A., Rev. Mod. Phys., 64 (1992), 849.

[23] Goldhaber-Gordon D., Shtrikman H., Mahalu D., Abusch-Magder D., Meirav U., Kastner M.A., Nature, 391 (1998), 156.

[24] Haug H., Jauho A.-P., *Quantum Kinetics in Transport and Optics of Semiconductors*, Springer -Verlag, Berlin, 1998, Ferry D.K., *Transport in nanostructures*, Cambridge University Press, Cambridge, 1997, Datta S., *Electronic Transport in Mesoscopic Systems*, Cambridge University Press, Cambridge, 1995.

[25] Meir Y., Wingreen N.S., Phys. Rev. Lett., 68 (1992), 2512.

[26] Kostyrko T., Bułka B.R., Phys. Rev. B, 67 (2003), 205331.

[27] Harris A.B., Lange R.V., Phys. Rev., 157 (1967), 295.

[28] Klimeck G., Chen G., Datta S., Phys. Rev. B, 50 (1994), 2316.

[29] Chen G., Klimeck G., Datta S., Chen G., Goddard III W.A., Phys. Rev. B, 50 (1994), 8035.

[30] Stafford C.A., Phys. Rev. Lett., 77 (1996), 2770.

[31] Niu C., Liu L., Lin T., Phys. Rev., 51 (1995), 5130.

[32] Pals P., MacKinnon A., J. Phys. Condens. Matter, 8 (1996), 5401.

[33] You J.Q., Zheng H.Z., Phys. Rev. B, 60 (1999), 13314.

[34] Lamba S., Joshi S.K., Phys. Rev. B, 62 (2000), 1580.

[35] Hubbard J., Proc. Roy. Soc., A 277 (1964), 237.

[36] Haley S.B., Erdos P., Phys. Rev., 5 (1972), 1106.

[37] Meir Y., Wingreen N.S., Lee P.A., Phys. Rev. Lett., 66 (1991), 3048.

Received 20 September 2004
Revised 9 November 2004

Materials Science-Poland, Vol. 22, No. 4, 2004

Electron transport through single molecular wires

I.M. GRACE[1*], S.W. BAILEY[1], J. JEFFERSON[2], C.J. LAMBERT[1]

[1]Department of Physics, Lancaster University, Lancaster LA1 4YW, UK

[2]Qinetiq, Sensors and Electronic Division, Great Malvern, Worcestershire, UK

Using a scattering technique combined with density-functional theory, a computational study of electron transport through two recently synthesized molecules is presented. The effect of connecting the molecules to gold electrodes is studied by iteratively increasing the number of gold layers, treated self-consistently as part of the molecule.

Key words: *molecular wires; single molecule; transport*

1. Introduction

Molecular electronics, in the sense of electronic devices whose active region consist of a few molecules or even a single molecule, has been proposed at the conceptual level for many years [1]. A typical molecular device consists of a metal–molecule–metal junction, formed between macroscopic electrodes and a single organic molecule or a monolayer of molecules. To form a reliable molecular junction, a gap of the length of the active molecule has to be formed between the electrodes.

At the moment, various techniques are used to probe the properties of single molecule junctions. These are scanning probe [2], break junctions [3, 4], and electro migration [5] methods. While these techniques provide convenient laboratory tools for probing single molecular junctions, it is unlikely that they will be employed for the large-scale production of devices. One possible way forward is to employ longer molecules than benzene dithiol or nitroamine, which were measured by Reed et al. [3, 4], since longer molecules would impose less stringent requirements on the contact lithography. In this paper, we theoretically investigate the equilibrium transport properties of two such recently synthesized molecules [6] (Fig. 1), which are approximately 4 nm and 7 nm in length. These structures are soluble fluorenone-based

---

[*] Corresponding author, e-mail: i.grace@lancaster.ac.uk.

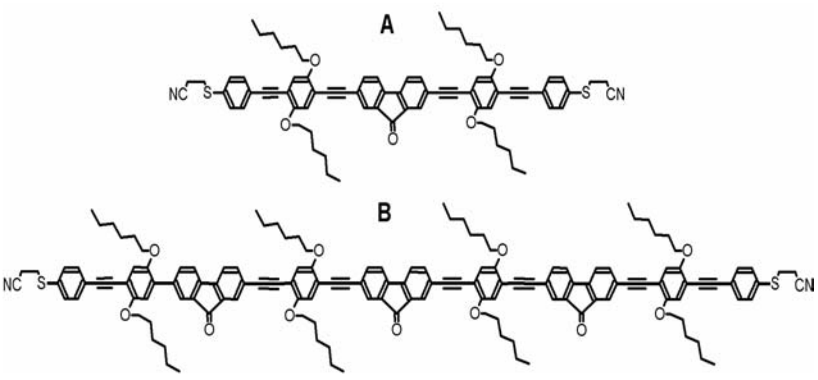

Fig. 1. Two rigid-rod conjugated molecules (A and B) approximately 4 and 7 nm in length, which have protected terminal thiol groups

molecular wires, which are suitable for single molecule device fabrication and could serve as building blocks in the construction of other molecular wires with precise conjugation lengths.

2. Theoretical method

One of the most important features in modelling a molecular device is the interface between the molecule and electrode surface. A systematic approach, therefore, has to be developed to ensure that the effects of the interface are included as part of the calculation.

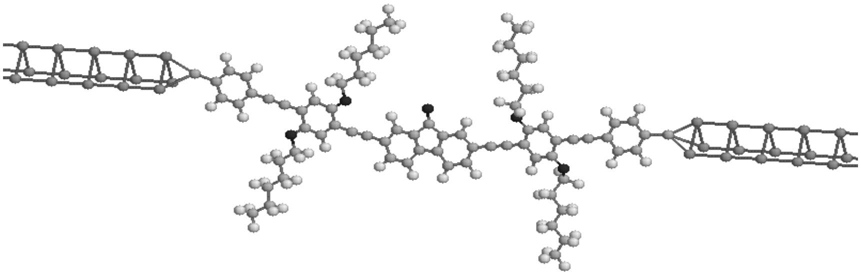

Fig. 2. Molecule A extended to include the surface of the gold lead

The structure of a molecule transport calculation can be broken down into three parts. The first is the structure of the lead, the second is the molecule, and the third is the interface between the surface of the leads and the end of the molecule. A hierarchical theoretical consisting of three stages approach is used here to calculate transport through a molecule contacted between two semi-infinite leads. The first stage is calculating the relaxed geometry of the molecule. This, in principle, could be achieved using any first principles quantum chemistry code. Here we use the density functional theory code SIESTA [7], combined with a super cell approach. We use the local density approximation as parameterised by Perdue and Zinger [8], non-local norm-conserving pseudopotentials [9], and valence electrons described by a single -zeta basis set. This stage of the calculation also gives useful information about the energetics of the isolated molecule.

One of the main problems in such calculations is correctly modelling the contact region between the molecule and the two leads. Both of the molecules studied here have terminal protected thiol groups, which are known to bond well with gold electrodes. In these calculations, the contact region consists of three gold atoms arranged in an equilateral triangle, to which the sulphur atom covalently bonds. To accurately determine the bonding between the surface of the gold lead and the end of the molecule self consistently, the molecule is extended to include several layers of the gold leads at each of its ends (Fig. 2). One unknown with these new molecules is the optimal distance between the sulphur atom and the surface of the lead. It is found by minimization with respect to the total energy. This parameter is varied for one of these molecules, so as to investigate the effect of changing the coupling strength.

Once the relaxed structure has been calculated, the tight binding Hamiltonian for this extended molecule and contacts can be extracted using the SIESTA code. The final stage in the approach is to utilize this material-specific Hamiltonian in a transport calculation, using single electron, scattering codes [10] developed at Lancaster. This technique determines the quantum-mechanical scattering matrix of a phase coherent region connected to ideal external reservoirs. At zero temperature, the zero-bias conductance is given by the Landauer–Büttiker [11] formula

$$G(E)=\frac{2e^2}{h}T(E_F)$$

where $T(E_F)$ is the total transmission coefficient evaluated at an energy of $E = E_F$.

In what follows, the contact region of the extended molecule consists of triangular layers of three gold atoms, with triangular leads whose cross-section also contains a triangle of three gold atoms (Fig. 2). This allows for a simple continuation between the semi-infinite leads and the ends of the molecule. Our results clearly demonstrate that a non self-consistent treatment of the contacts can yield erroneous results for $T(E)$. By increasing the number of gold atoms that are self-consistently included as a part of the molecule contacts, however, the conductance across the molecule is found to converge, due to the fact that charge transfer effects at the gold-molecule interface decay over a small number of slices into the bulk gold lead.

3. Results

The first molecule, A, that we investigate is shown in Fig. 1. After computing the optimal geometry of its structure, its length was found to be approximately 36.93 Å. This is in good agreement with a S–S length of 37.4 Å determined by X-ray diffraction [6]. The iterative process of increasing the number of gold atoms in the contact region, until transmission through the molecule converges, can be seen in Figs. 3a and b. In Figure 3a, transmission through molecules containing 2, 3, and 4 layers in the contact region is shown, and while there are small differences in most of the transmission peaks, there is a large difference in the magnitude of the HOMO peak. Figure 3b shows that transmission through 5 layers is identical to transmission through 6 layers. Therefore, transmission through the molecule in this case has converged after including 5 layers of gold.

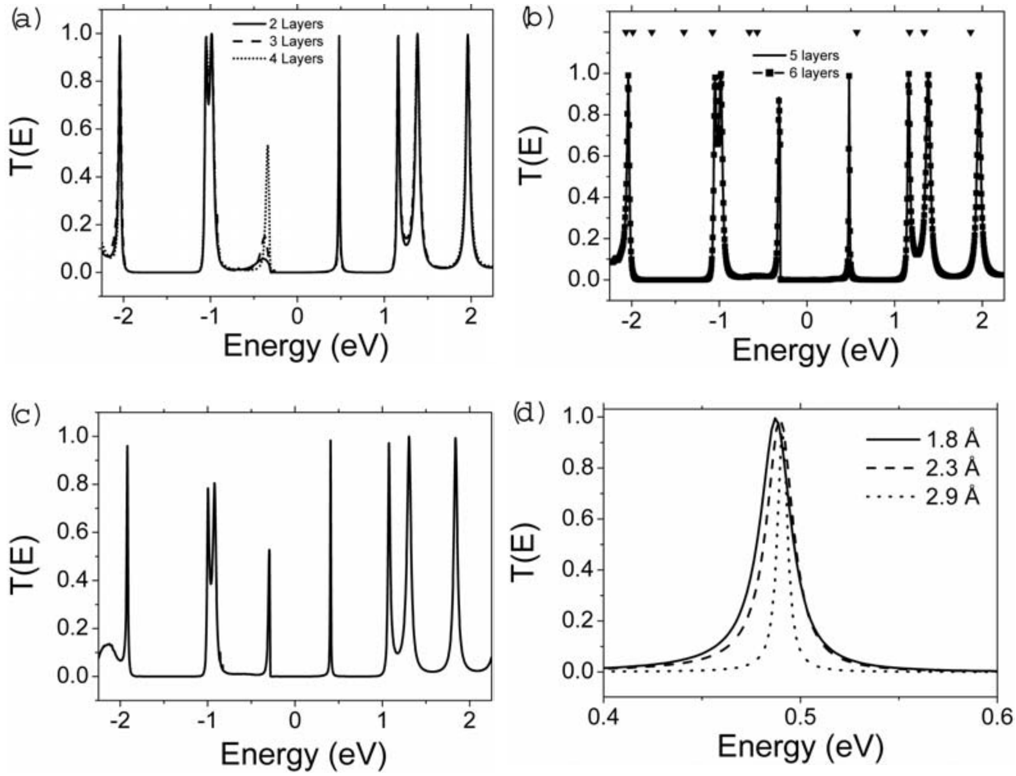

Fig. 3. Transport through molecule A for a contact region of: 2, 3, and 4 slices (a), and 5 and 6 slices (b). Transmission through molecule A with methyl replacing side groups and 6 slices of self-consistently treated gold (c). Variation in the Au–S contact distance (d)

A closer inspection of the zero bias conductance computed for molecule A (Fig. 3b) shows that it has resonant peaks on each side of the Fermi energy (0 eV) and shows a conducting gap of approximately 0.8 eV. This behaviour is typical of transport through a system with discrete energy levels and weakly connected to external reservoirs. To show this more clearly, the energy levels of the isolated molecule, predicted using SIESTA, are represented by the small triangles in Fig. 3b. Conductance shows a resonance peak for the HOMO (Highest Occupied Molecular Orbital) level at approximately 0.32 eV below the Fermi energy, and the LUMO (Lowest Unoccupied

Molecular Orbital) peak is 0.48 eV above the Fermi energy. Therefore, this predicts a conducting gap of approximately 0.8 eV, which is smaller than the predicted gap of the isolated molecule (SIESTA energy levels show a gap of 1.1 eV). One of the reasons for this is the interaction between the molecule and gold leads, which causes the molecular levels to broaden and shift.

Both of the molecules studied here contain complex side groups (Fig. 1), mainly to aid the solubility of these long structures. These groups, however, greatly increase the number of atoms in the molecule. In the case of longer molecules such as B, this will cause the computation time to increase significantly. These side groups can be replaced by methyl without altering the electronic properties of the molecule, simplifying the structure of a long molecular wire. The transmission plot for molecule A with methyl replacing the original side groups is shown in Fig. 3c, showing identical positions for the resonant peaks and only a slight change in the magnitude of the HOMO peak. Therefore, in dealing with the second molecule B, we further consider only the structure with the original side groups replaced by methyl. For this structure, such a substitution reduces the number of atoms in the molecule by 120.

As mentioned previously, the sulphur-gold distance at the lead surface is an unknown parameter, found by minimising the total energy with respect to this distance. In the case of molecule A, this was found to be 2.1Å. Figure 3d shows the effect that altering this distance has on the LUMO resonance in the transmission. Due to symmetry, a weakening of the coupling strength causes the width of the transmission resonances to decrease, and causes no change in the magnitude of the transmission peak.

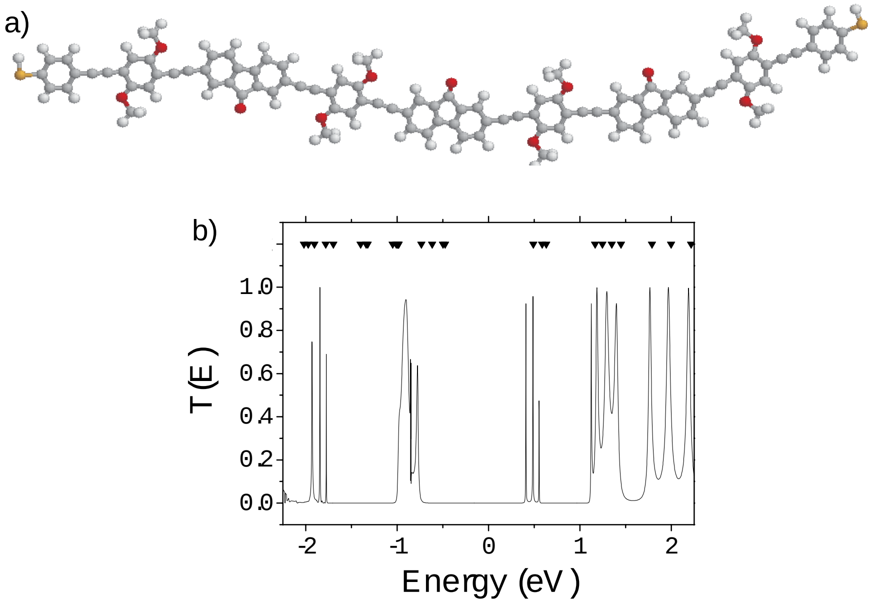

Fig. 4 Optimised geometry for molecule B (a) and zero bias transmission through molecule B with 6 slices of gold (b)

The second molecule, B (Fig. 1), is much longer than molecule A and is partly formed by doubling molecule A. An interesting feature of this molecule is that it has various metastable configurations and, depending on the initial orientation of various parts of the molecule, its length can vary between approximately 68 Å and 74 Å. Using the configuration predicted to be the most stable (i.e., minimises the energy), SIESTA predicts a S–S length of 72.3 Å. The geometry of this structure can be seen in Fig. 4a. Therefore, this molecule would allow the electrode gap to be increased to approximately 7.5 nm.

The computed transmission through this structure can be seen in Fig. 4b, along with the energy levels predicted by SIESTA for the isolated molecule. In this case, the HOMO peak is positioned at approximately –0.7 eV, and there are three peaks close together at the LUMO level, at approximately 0.4 eV. Therefore, for this much longer molecule, formed by effectively doubling the size of molecule A, the conducting gap has increased to approximately 1.1 eV. This is comparable to the gap of the molecule, which SIESTA predicts to be 1 eV.

4. Conclusions

A hierarchical, theoretical approach has been employed to calculate the transport properties of recently synthesized molecular wires, whose relatively long lengths offer the technical advantage of increasing the electrode gap. A method has been described and implemented to accurately include the effect of the molecule-lead interface in the calculations. In the present paper, we have confined our calculations to the transmission coefficient $T(E)$ and stable molecular geometries. In order to build a single molecule device that could perform some basic electronic function, an understanding of finite bias effects is also required. The calculations presented here provide a starting point to understanding such effects, which may take the form of charge or conformation changes in the molecule.

References

[1] AVIRAM A., RATNER M.A., Chem. Phys. Lett., 29 (1974), 277.
[2] GITTENS D., BETHELL D., SCHIFFRIN D., NICHOLS R., Nature, 408 (2000), 67.
[3] REED M., ZHOU C., MULLER C., BURGIN P., TOUR J., Science, 278 (1997), 252.
[4] CHEN J., REED M.A., RAWLETT A.M., TOUR J.M., Science, 286 (1999), 1550.
[5] PARK H., LIM A., ALIVISATOS A., PARK J., MCEUEN P., Appl, Phys, Lett., 75 (1999), 301.
[6] WANG C., BATSANOV A., BRYCE M., SAGE I., Org. Lett., 6 (2004), 2181.
[7] SOLER J.M., ARTACHO E., GALE J.D., GARCÍA A., JUNQUERA J., ORDEJÓN P., SÁNCHEZ-PORTAL D., J. Phys.: Condens. Matter, 14 (2002), 2745.
[8] PERDEW J.P., ZUNGER A., Phys. Rev. B, 23 (1981), 5048.
[9] TROULLIER N., MARTIN J.L., Phys. Rev. B, 43 (1991), 1993.
[10] SANVITO S., LAMBERT C.J., JEFFERSON J., BRATKOVSKY A., Phys. Rev. B, 59 (1999), 11936.
[11] BUTTIKER M., IMRY Y., LANDAUER R., PINHAS S., Phys. Rev. B, 31 (1985), 6207.

Received 14 September 2004
Revised 3 October 2004

Materials Science-Poland, Vol. 22, No. 4, 2004

Spin-dependent transport through a double dot system

S. LIPIŃSKI[*], B.R. BUŁKA, D. KRYCHOWSKI

Institute of Molecular Physics, Polish Academy of Sciences,
ul. M. Smoluchowskiego17, 60-179 Poznań, Poland

The coherent transport through a set of two capacitively coupled quantum dots placed in a magnetic field and coupled to ferromagnetic electrodes is considered in the limit of infinite intra- and interdot interactions. The densities of states are calculated in an approximation that favours separate fluctuations of spin, orbital isospin, and simultaneous fluctuations of both of them. Apart from the Kondo peak, satellite many-body peaks are also found in the densities of states. Their positions and weights depend on the magnetic field and polarization of electrodes. This is reflected in the spin dependence of conductance remarkably varying for the voltage bias corresponding to the peak positions.

Key words: *electronic transport; nanoscopic systems; Kondo effect*

1. Introduction

There is currently much interest in understanding spin-dependent electron transport in nanostructures. Spin-based devices hold promises for future applications in conventional [1] as well as quantum computer hardware [2]. Recent interest in manipulating spins in nanostructures is based on the ability to control and maintain spin coherence over practical length and time scales. In nanoscopic dots, the charging energy plays a dominant role and correlation effects are of importance. At low temperatures and strong coupling Γ between the dot and the leads ($k_B T << \Gamma$), quantum fluctuations in the charge and spin degrees of freedom strongly affect transport through the dot. Spin fluctuations lead to the Kondo effect, which has been verified by many experiments on single dots [3]. Recently, the Kondo effect has also been observed in double dot structures [4]. The Kondo effect has two possible sources in coupled quantum dots (DQD): spin and “orbital” degeneracies. The large number of tunable parameters in DQD systems allows delicate manipulation of the Kondo physics. An

---

[*] Corresponding author, e-mail: lipinski@ifmpan.poznan.pl.

interesting issue is how the Kondo physics is affected by the polarization of electrodes. The attachment of ferromagnetic leads to carbon nanotubes has been reported [5], and carbon–nanotube QDs have been shown to display the Kondo physics below an unusually high temperature [6]. Other possible realizations of magnetic nanostructures are spin-polarized STMs and magnetic tunnel junctions with magnetic impurities in the barrier [7, 8].

Motivated by these experiments, we discuss in the present paper a spin-dependent transport within a simple model of a double dot system (DQD). It is assumed that the dots are capacitively coupled and that magnetic electrodes are attached to them. The aim of our work is to discuss the influence of the magnetic field and polarization of the leads on the many-body structure of the density of states and on the spin dependence of conductance.

2. Model

We discuss a system of two capacitively coupled quantum dots placed in a magnetic field. Each dot is connected to separate pairs of ferromagnetic electrodes. The system is modelled by the two-dot Anderson Hamiltonian with a single level at each dot and an additional term for interdot interaction

$$H = \sum_{kri\sigma} \varepsilon_{kri\sigma} c^{+}_{kri\sigma} c_{kri\sigma} + \sum_{i\sigma} \varepsilon_{i\sigma} c^{+}_{i\sigma} c_{i\sigma} + \sum_{i} U_i n_{i+} n_{i-} + U \sum_{\sigma\sigma'} n_{1\sigma} n_{2\sigma'} + \sum_{kri\sigma} t_{ri} (c^{+}_{kri\sigma} c_{i\sigma} + h.c) \quad (1)$$

where i numbers the dots ($i = 1, 2$), and leads being labelled (i, r) ($r = L, R$). $\varepsilon_{i\sigma} = \varepsilon_i + \sigma h$, $\sigma = \pm 1$ (we set $|e| = g = \mu_B = k_B = 1$). The first term describes electrons in the electrodes, the second represents the field-dependent site energies, the third and fourth account for intra and intercoulomb interactions, and the last one describes the tunnelling.

The ferromagnetism of the leads is accounted for by different densities of states for up and down-spin electrons. The wide-band limit is used, with the densities of states of the electrons in the leads assumed constant, $\rho_{i\sigma} = 1/2D_{i\sigma}$, where $|\varepsilon| < D_{i\sigma}$, and $D_{i\sigma}$ is half of the bandwidth.

For simplicity, we restrict ourselves to the case of identical dots ($\varepsilon_i \equiv \varepsilon_0$), identical electrodes, and equal couplings to the dots, i.e. $t_{ri} \equiv t$. The bare Green's functions of the electrodes

$$g_{r\sigma} = \sum_{k} g_{kr\sigma} = \sum_{k} \frac{1}{\omega - \varepsilon_{kr\sigma}} \equiv g$$

are taken in the form $g = -i\pi\rho_0$. Consequently, the elastic couplings to the electrodes are independent of energy: $\Gamma_{ir\sigma}(\omega) = 2\pi t^2 \rho_0 \equiv \Gamma_\sigma$. One can define the spin polarization of the electrodes as $p = (\Gamma_\uparrow - \Gamma_\downarrow)/(\Gamma_\uparrow + \Gamma_\downarrow)$.

Within the Keldysh formalism, the current in the DQD, $I = \sum_{i\sigma} I_{i\sigma}$ [9], has the form

$$I_{i\sigma}=\frac{e}{\hbar}\int d\omega\frac{\Gamma_{iL\sigma}(\omega)\Gamma_{iR\sigma}(\omega)}{\Gamma_{iL\sigma}(\omega)+\Gamma_{iR\sigma}(\omega)}[f_{iL}(\omega)-f_{iR}(\omega)]\rho_{i\sigma}(\omega) \tag{2}$$

where $\rho_{i\sigma}(\omega)=(-1/\pi)\mathrm{Im}\,G^r_{i\sigma}(\omega)$, and f_{ir} are the Fermi distribution functions of the electrodes. The current, the distribution functions, and Green's functions are also functions of temperature, field, polarization, and voltage bias. Spin-resolved, non -linear conductance can be calculated from Eq. (2) by a numerical derivative $\breve{G}_\sigma(V)\equiv\frac{\partial I_\sigma}{\partial V}$, $I_\sigma=I_{1\sigma}+I_{2\sigma}$.

For strong interactions, $(U_1, U_2, U)\to\infty$, and a deep dot level $(-\varepsilon_{i\sigma}>>\Gamma)$, retarded Green's function can be approximated by the following multipole expression

$$G^r_{i\sigma}(\omega)=\frac{1-n_\Omega}{3}\sum_{l\in\Omega}\frac{1}{\omega-\varepsilon_{i\sigma}-\Sigma_0-\Sigma^1_{i\sigma,l}(\omega)} \tag{3}$$

where $\Sigma_0=-i\Gamma$ is the self-energy for the noninteracting QD due to tunnelling of the $i\sigma$ electron, Ω is a set of quantum numbers labelling the virtual intermediate states in the tunnelling, and n_Ω denotes the average total occupation of these states. $\Omega=\{(\bar{i}\,\sigma),(i,-\sigma),(\bar{i},-\sigma)\}$, $n_\Omega=\sum_{l\in\Omega}\langle n_l\rangle$, and $\{\sum^1_{i\sigma,l}\}$ denotes the correlation parts of the self-energy ($\bar{1}=2$, $\bar{2}=1$). Expression (3) is a simple generalization of the single dot formula of Meier et al. [9] to the DQD system case, derived by the equation of motion (EOM) technique with the decoupling procedure for higher order Green's functions, which neglect correlations in the leads. Formulae (3) and (4) correspond to the approximation that separately takes into account isospin fluctuations, spin fluctuations, and fluctuations in strongly coupled spin and isospin

$$\sum\nolimits^1_{i\sigma,i'\sigma'}=t^2\sum_{k\in L,R}\frac{f_{L,R}(\varepsilon_{ki'\sigma'})}{\omega-\varepsilon_{i\sigma}+\varepsilon_{i'\sigma'}-\varepsilon_{ki'\sigma'}+i\delta_{i\sigma'}} \tag{4}$$

$\delta_{i\sigma}$ describes decoherence due to a finite voltage bias or field-induced level splitting. An estimate of the lifetime can be obtained from perturbation theory [9].

The first sequence of correlated tunnelling, represented by $\sum^1_{i\sigma,\bar{i}\sigma}$, ccurs through the intermediate virtual states of the same spin but from a different dot. They induce fluctuations in single dot occupations (the orbital isospin flips). As a result, the orbital Kondo resonances are built up for each spin channel. The second type of tunnelling process, $\sum^1_{i\sigma,i\text{-}\sigma}=\sum^1_{i\sigma,\bar{i}\text{-}\sigma}$, links the non-degenerate states and causes the singularity of self-energy in regions separated from the Fermi level by Zeeman splitting. In the limit of vanishing magnetic field, they correspond to the spin Kondo effect and to simultaneous fluctuations in spin and isospin. The neglected processes which mix the above-mentioned three types of fluctuations are of special importance for systems close to full fourfold spin-orbital degeneracy. Their role is under investigation by a more careful treatment of EOM equations, and the results will be published elsewhere.

3. Numerical results

We present numerical results for the deep Kondo limit $\varepsilon_0 = -4\Gamma$. $\Gamma = \Gamma_\uparrow$ is taken as the energy unit. The bandwidth of the leads is taken as $D_\uparrow = 50\Gamma$. We do not discuss any decoherence effects, and the calculations were performed with $\delta = \delta_{i\sigma} = 10^{-4}$.

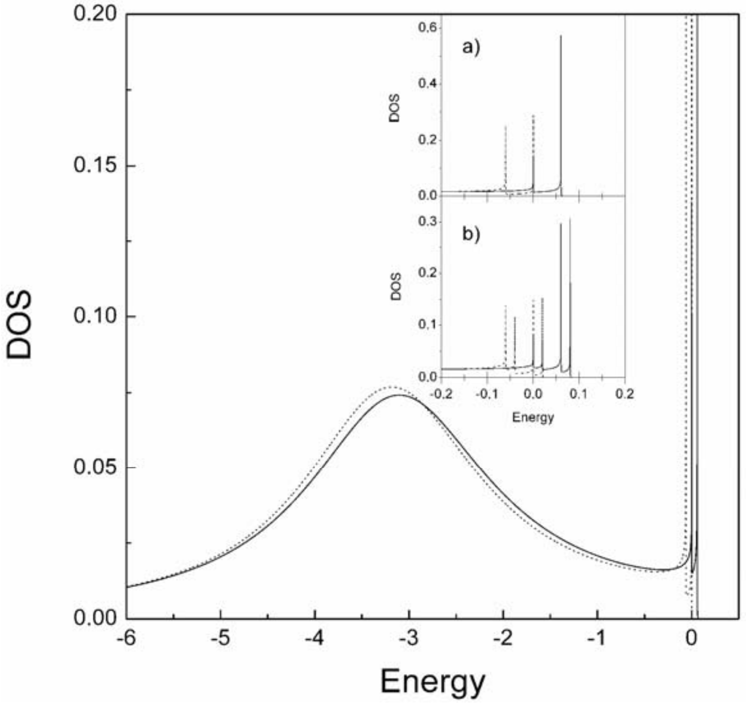

Fig. 1. Total density of states of a capacitively coupled double quantum dot in a magnetic field $h = 0.03$ and for a polarization of the leads $p = 0.05$, calculated for the bare dot energy $\varepsilon_0 = -4$. Spin up is represented by the solid line and spin down by the dotted line. Inset (a) shows the many-body structure for zero bias voltage, $V = 0$, and inset (b) for $V = 0.02$

In Figure 1, we plot the spin-dependent DOS of DQD for a finite magnetic field, a small polarization of the leads, and vanishing voltage bias. The broad charge fluctuation peak is split by the field. The widths of the spin-dependent peaks are slightly different, which is a consequence of the polarization-introduced difference in the tunnelling rates Γ_σ. Also, a shift of the centre of mass of the charge fluctuation peak is observed reflecting the renormalization of the dot levels by spin and orbital isospin fluctuations. The triple-peak many-body structure is seen close to the Fermi level. A similar result was reported earlier by Pohjola et al., who performed the calculations within the resonant-tunnelling approximation [10].

For clarity, we also show the curves of DOS in a narrower energy region in the inset. Both spins contribute to the central peak (orbital isospin fluctuations). The satellite peaks, located roughly in the positions $\pm 2h$, are characterized by different spin polarizations. This property should manifest itself in the spin dependence of boson -assisted tunnelling but the possible experimental observation can be masked by decoherence. Inset b) shows the many-body structure of DOS for finite V. The source -drain voltage causes the peaks to split.

For $V \approx \pm 2h$, the satellite peaks of opposite spin polarization enter the energy region between the Fermi levels of the leads from opposite sides, and consequently peaks in the differential conductance build up. This is illustrated in Fig. 2. The fact that the positions of the non-linear conductance peaks are determined by the strength of the field can be used for measuring the field.

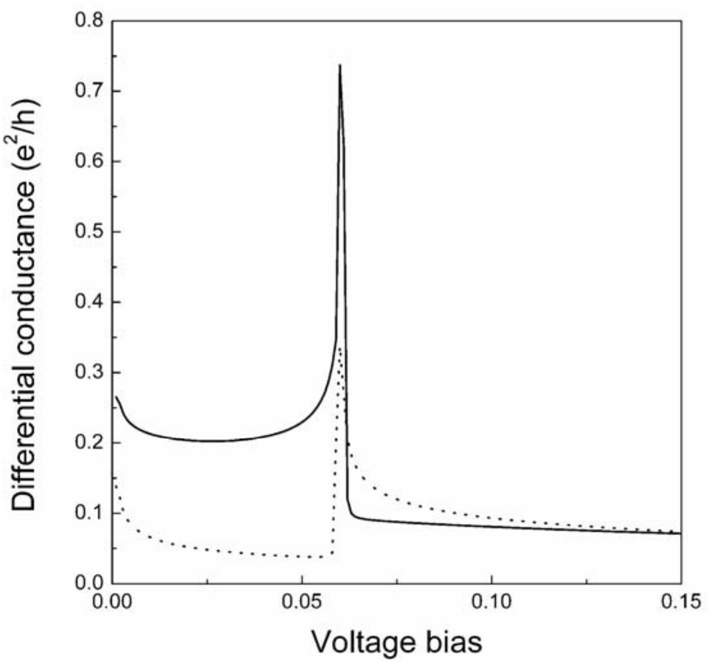

Fig. 2. Differential conductance vs. applied bias for spin up (solid line) and spin down (dotted line). A magnetic field $h = 0.03$ and an electrode polarization $p = 0.05$ were chosen

In the following pictures, we discuss the spin dependence of conductance by presenting its polarization, defined as $P_{\text{con}} \equiv (\breve{G}_{\uparrow} - \breve{G}_{\downarrow})/(\breve{G}_{\uparrow} + \breve{G}_{\downarrow})$. Figure 3a presents the polarization of conductance for a fixed magnetic field and three different polarizations of the leads. Similar dependencies but for a fixed polarization of the electrodes and different fields are shown in Fig. 3b.

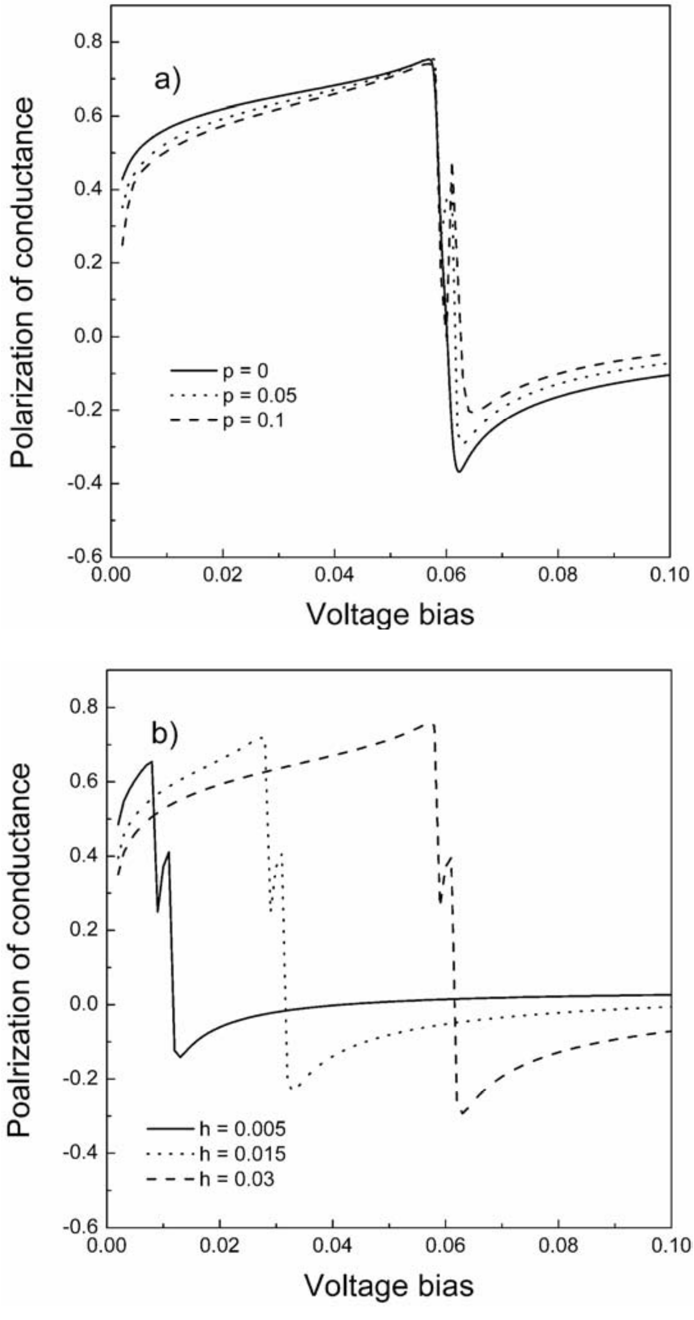

Fig. 3. The polarization of differential conductance vs. applied bias for: a) a magnetic field $h = 0.03$ and three different electrode polarizations, b) $p = 0.05$ and three different values of the magnetic field

Remarkable changes in the spin polarization of conductance are observed for voltages determined by the peak positions ($eV \approx 0$ and $eV \approx \pm 2h$). They reflect the spin asymmetry of the density of states, which increases with increasing field or polarization. Apart from the intensity differences (see, e.g., inset b) of Fig. 1), the positions of

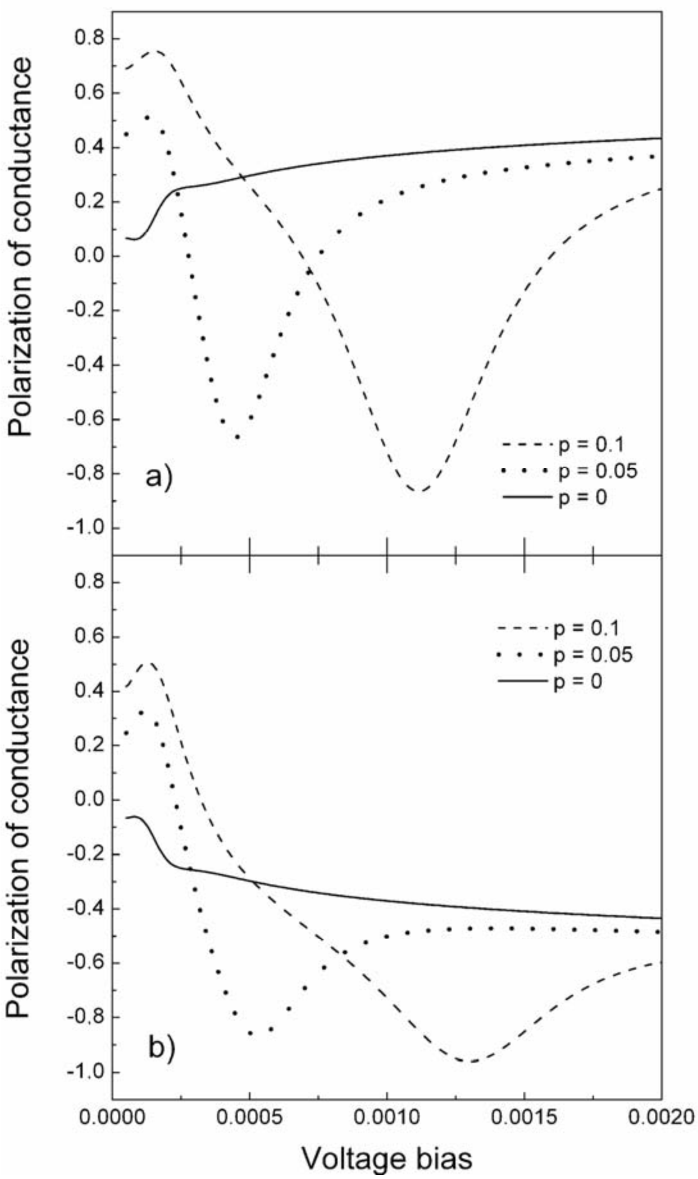

Fig. 4. Polarization of conductance for a magnetic field $h = 0.03$ and three different electrode polarizations for small bias

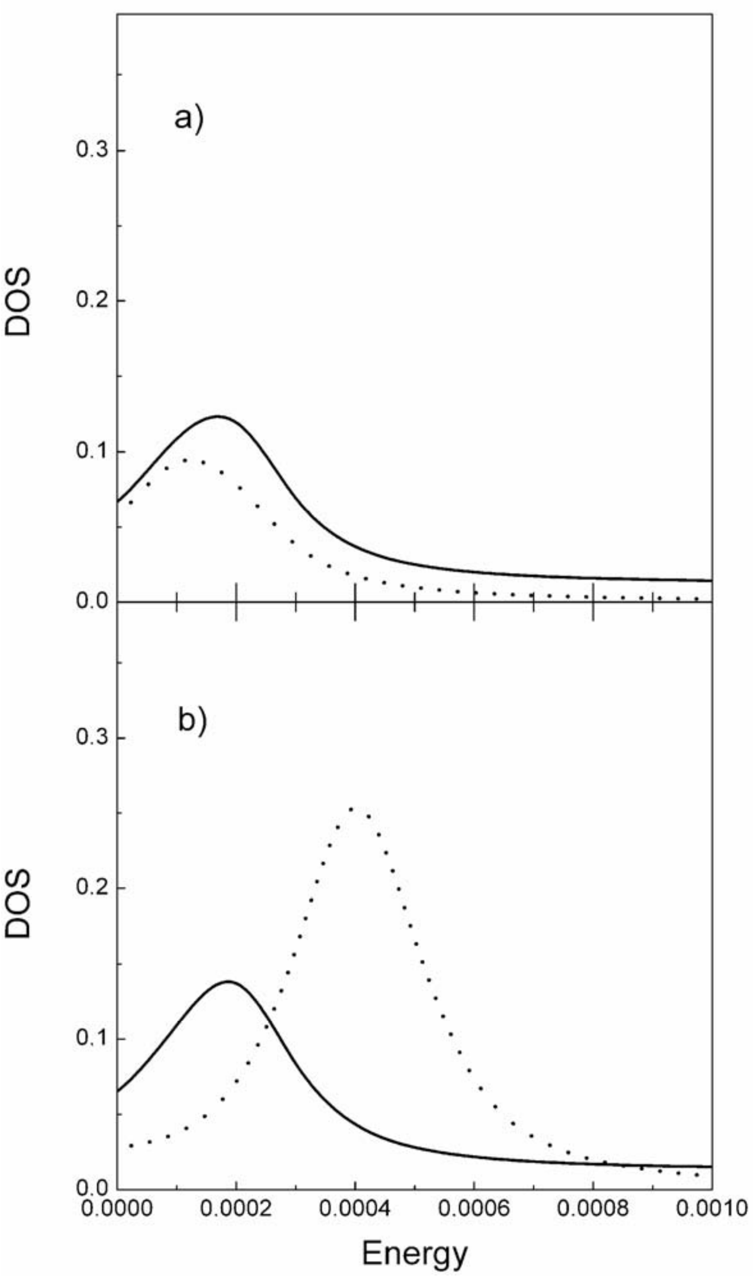

Fig. 5. Densities of states for spin up (solid line) and spin down (dotted line) for: a) $p = 0$, b) $p = 0.05$ in the narrow energy region close to the Fermi level

the corresponding peaks with opposite spin orientations also differ slightly. The latter effect is only weakly reflected in Fig. 3; its traces are seen in the narrow oscillations of some curves near the satellite peaks. The many-body peaks are very narrow and the mentioned shift of the peaks is small. The results in Fig. 3 are presented for a voltage step of $\Delta V = 10^{-3}$. To get a more detailed insight into the mentioned subtle effect, we focus in the following exclusively on the narrow voltage region $V < 2\cdot10^{-4}$, presenting these curves with the voltage steps of $\Delta V = 10^{-5}$. Figure 4a shows polarization of conductance for $h = 0.03$ for unpolarised leads ($p = 0$) and for two small values of polarizations. Figure 4b presents analogous curves but for a reversed field at the dot. For $p = 0$, the curve is a mirror reflection of the corresponding curve from Fig. 4a. For a finite polarization of the leads, the consequence of changing the relative orientation of the field and polarization in the leads from antiparallel (Fig. 4a) to parallel (Fig. 4b) is visible. To understand the presented spin dependencies, in Fig. 5 we show the evolution of the DOS with the lead polarization for the relevant energy region. The oscillations in the polarization of conductance observed for voltages close to $V = 0$ reflect the polarization-induced separation of opposite spin peaks located in the vicinity of the Fermi level. The approach adopted in this paper is rather crude, hence the results obtained, describing subtle effects, should be taken with some caution. Only a qualitative agreement can be expected, moreover, the effects mentioned can be easily masked by temperature.

4. Conclusions

We have studied spin-dependent electronic transport through a capacitively coupled double quantum dot placed in a magnetic field and attached to a ferromagnetic lead. The influence of the field and polarization of electrodes was examined. Apart from the central Kondo peak, two satellite peaks below and above the Fermi level are observed in the many-body structure of DOSs. The satellite peaks are characterized by different spin polarizations. The field and polarization of electrodes introduce weak asymmetry in the weights and positions of the peaks, which rises when the field or polarization is increased or when moving towards the mixed valence range. This reflects strong variation of the polarization of conductance in the vicinity of many body resonances, where even a change in the sign of polarization is observed. The purpose of this paper was to obtain only a preliminary, very crude picture of possible influence of external magnetic field on the polarization of conductance in DQDs. More advanced considerations of this problem are under way.

Acknowledgements

This work was supported by the State Committee for Scientific Research (Poland), within project no. PBZ KBN 044 P03 2001 and by the Centre of Excellence for Magnetic and Molecular Materials for Future Electronics within the EC Contract. No. G5MA-CT-2002-04049.

References

[1] PRINZ G., Phys. Today, 48 (1995), 58.
[2] LOSS D., Di VINCENZO D. P., Phys. Rev., A57 (1998), 120.

[3] GOLDHABER-GORDON D. SHTRIKMAN H., MAHALU D., ABUSH-MAGDER D., MEIRAV U., KASTNER M.A., Nature, 391 (1998), 156; CRONENWETT S.M., OOSTERKAMP T.H., KOUWENHOVEN L., Science, 281 (1998), 540.
[4] JEONG H., CHANG A.M., MELLOCH M.R., Science, 293 (2001), 2221.
[5] TSUKAGOSHI K., ALPEHENAAR B.W., AGO H., Nature, 401 (1999), 572.
[6] BUITELAAR M.R. BACHTOLD A., NUSSBAUMER T., IQBAL M., SCHÖNENBERGER C., Phys. Rev. Lett., 88 (2002), 156801.
[7] RALPH D.C., BUHRMAN R.A., Phys. Rev. Lett., 72 (1994), 3401.
[8] KUBETZKA A, BODE M., PIETZSCH O., WIESENDANGER R., Phys. Rev. Lett., 88 (2002), 057201.
[9] MEIER Y., WINGREEN N.S, LEE P.A., Phys. Rev. Lett., 70 (1993), 2601.
[10] POHJOLA T., SCHOELLER H., SCHÖN G., Europhys. Lett., 54 (2001), 241.

Received 20 October 2004
Revised 3 November 2004

Materials Science-Poland, Vol. 22, No. 4, 2004

Effective exchange interaction in tunnelling junctions based on a quantum dot with non-collinear magnetic moments of the leads

W. RUDZIŃSKI[*]

Department of Physics, Mesoscopic Physics Division, Adam Mickiewicz University,
Umultowska 85, 61-614 Poznań, Poland

Electron tunnelling through a spin-split discrete level of an interacting quantum dot coupled to two ferromagnetic electrodes (leads) is investigated theoretically in the sequential-tunnelling regime. Spin-splitting of the dot level is induced by an effective exchange interaction between the spin on the dot and spins in the leads. The calculations apply to arbitrary angles enclosed between the magnetizations of the external electrodes. It is shown that the interplay between effective exchange field and Coulomb correlations on the dot may enhance the tunnel magnetoresistance at certain bias voltages. It is also found that a large spin splitting appearing for strong Coulomb correlations gives rise to an enhanced diode-like effect. Finally, it is shown that by rotating the magnetization of one of the electrodes, one can modulate the amplitude of the spin-polarized current, from a blockade in the parallel or antiparallel configuration to its maximum value in the non-collinear case.

Key words: *quantum dot; tunnelling; spin-valve effect; spin-polarized transport*

1. Introduction

Extensive studies on spin-polarized transport phenomena in microelectronic devices have contributed recently to progress in fabricating extremely small transistors, consisting of metallic grains or semiconductor quantum dots (QD) coupled through tunnel barriers to external electrodes [1, 2]. In this paper, we consider sequential electron tunnelling through an atomic spacer coupled to two ferromagnetic leads with magnetic moments polarized at an arbitrary angle Θ with respect to each other. The atomic spacer is assumed to be an interacting QD with a single discrete level, which is spin-split due to effective exchange interaction between the spin on the dot and spins

---

[*] E-mail: wojrudz@amu.edu.pl.

in the electrodes. It is shown that the interplay of Coulomb correlations on the dot and the effective molecular field can significantly enhance tunnel magnetoresistance (TMR) in systems with non-collinearly polarized external source and drain ferromagnetic electrodes. Moreover, a previous analysis [3, 4] of the diode effect, predicted for collinear magnetic configurations in a device with one electrode being half metallic, is extended by taking into account modifications due to non-collinear magnetic states as well as due to the effective field. Therefore, an enhancement of the diode-like behaviour in a junction with collinearly aligned lead magnetizations is found. In turn, by presenting the angular dependencies of the transport characteristics, we show that a suppression of the diode effect occurs in non-collinear configurations.

2. Model

In the model Hamiltonian of the system, the left and right ferromagnetic electrodes are taken in the non-interacting quasi-particle limit. The term corresponding to the dot includes a single-particle energy level ε_d and the Coulomb correlation described by the parameter U. The spin eigenstates of the dot are denoted by $\sigma = \uparrow$ for spin-up electrons and $\sigma = \downarrow$ for spin-down electrons. In turn, the tunnelling part describes spin-dependent tunnelling processes through the left and right barrier. Since the magnetic moments of the external electrodes form an arbitrary angle Θ, the tunnelling terms of the model Hamiltonian are written in the corresponding local reference frames, where the tunnelling matrices are diagonal in the spin space. The spin asymmetry of the tunnelling rates across the left (l) and right (r) barriers, $\Gamma_l^{\pm} = \Gamma_0(1 \pm p_l)$ and $\Gamma_r^{\pm} = \alpha\Gamma_0(1 \pm p_r)$ (+ and – denote majority and minority electrons, respectively), is described by the parameters p_l and p_r. We also introduce a parameter Γ_0, which is the value of the tunnelling rate $\Gamma_{l,r}^{\pm}$ at $p_{l,r} = 0$, and α, which determines the ratio of the tunnelling matrix elements through the right and left barriers. Finally, the electrostatic potential of the dot is assumed to be an average value of the electrostatic potentials of the electrodes.

The transport properties of the system will be described in the sequential tunnelling regime. In order to calculate the current–voltage characteristics in a stationary state, we have generalized the master equation method [5]. The master equation allows the occupation numbers for the dot to be obtained, which in turn can be used to calculate the tunnelling current $J(\Theta)$ for arbitrary magnetic configurations Θ. The corresponding TMR has been defined qualitatively as TMR = $[J_P - J(\Theta)]/J(\Theta)$, with J_P denoting the electric current for the parallel ($\Theta = 0$) configuration. The bias variations of transport characteristics in the non-equilibrium situation are governed by the bias voltage (V_t) dependencies of the effective exchange interaction between the dot spin and spin of electrons in the external magnetic leads. To determine the exchange interaction energy, E_{eff}, we adopted the second-order perturbation theory, developed for the Anderson Hamiltonian [6]. The explicit formula for E_{eff} is given by

$$E_{\text{eff}} = \sqrt{\Delta E_l^2 + \Delta E_r^2 + 2\Delta E_l \, \Delta E_r \cos\Theta} \tag{1}$$

$$\Delta E_{l,r} = (\Gamma_{l,r}^{-} - \Gamma_{l,r}^{+})\left[\operatorname{Re}\Psi\left(\frac{1}{2} + \frac{\varepsilon_d + U - \mu_{l,r}}{2\pi K_B T} i\right) - \operatorname{Re}\Psi\left(\frac{1}{2} + \frac{\varepsilon_d - \mu_{l,r}}{2\pi K_B T} i\right)\right] \tag{2}$$

where the symbol $\Psi(z)$ is the digamma function, and $\mu_{l,r}$ denotes the chemical potential of the left or right electrode. Using Eqs. (1) and (2), one finally obtains the energies of the spin-split discrete level, $\varepsilon_{d\downarrow(\uparrow)} = \varepsilon_d \pm E_{\text{eff}}/2$. The external magnetic leads are thus considered as the source of mean fields which influence the tunnelling processes through the QD spin channels $\varepsilon_{d\sigma}$ and $\varepsilon_{d\sigma} + U$.

3. Numerical results

Consider first non-linear transport through a symmetrical junction, assuming an empty level at equilibrium, $\varepsilon_d > 0$. In Figure 1a we show the bias dependence of the difference between the energies of the dot spin channels $\varepsilon_{d\downarrow}$ and $\varepsilon_{d\uparrow}$, plotted for selected Θ angles. A maximum of spin-splitting appears at a threshold voltage, for which either the level ε_d or $\varepsilon_d + U$ crosses the Fermi level of the source electrode. For voltages below the first peak in Fig. 1a, the discrete level of the dot lies above the Fermi level of the source electrode and the sequential tunnelling processes are exponentially suppressed. For voltages between the maxima, QD may be singly occupied. Finally, above the second threshold voltage two electrons may reside on the dot. A minimum in Fig. 1a is observed at the bias voltage for which a reorientation of the effective field occurs, relative to the spin quantization axes of the magnetic electrodes. The latter feature originates from bias-dependent dot–lead exchange interactions. In non-collinear cases, the interplay between these interactions and Coulomb correlations on the dot may lead to a negative differential conductance in the bias range between the threshold voltages, as is clearly seen in Fig. 1b (the curve for $\Theta = \pi/2$).

Since in this voltage range the dot is singly occupied, then in a non-collinear configuration one may observe an increased accumulation of the average spin component $\langle S_z \rangle$ on the dot. This is due to the fact that the mean field tends to align parallel relative to the magnetization of the source lead with increasing bias, and thus the number of spin states available for an electron residing on the dot in the local reference system of the drain electrode effectively diminishes. Consequently, as displayed in Fig. 1c, a significant enhancement of the corresponding TMR may be observed between the two threshold voltages. This is the case until the probability of occupying the level $\varepsilon_d + U$ starts to increase at a certain bias voltage. When $\varepsilon_d + U$ crosses the Fermi level of the source lead, both tunnelling channels become active, the spin-polarized current increases relatively quickly and finally saturates at a certain level.

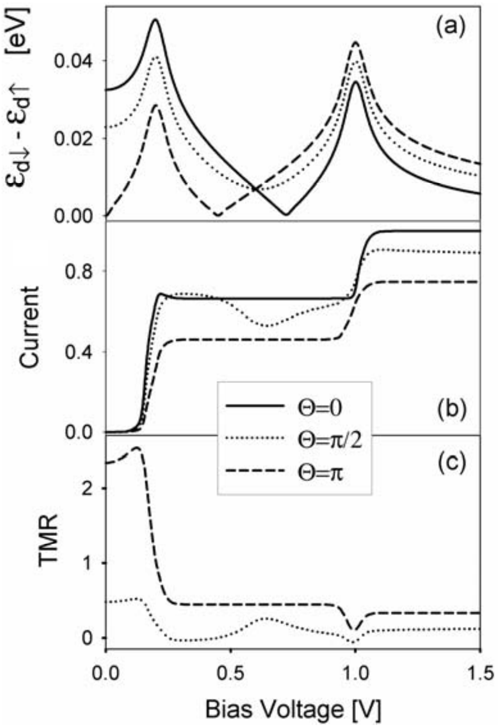

Fig. 1. Bias dependence of the difference between the energies $\varepsilon_{d\downarrow}$ and $\varepsilon_{d\uparrow}$ (a), tunnelling current (b), and the corresponding TMR (c) for the indicated angles Θ. The parameters are: $\varepsilon_d = 0.1$ eV, $p_l = p_r = 0.5$, $U = 0.4$ eV, $\alpha = 1$, and $T = 100$ K

Now consider the situation when the drain electrode (the right one) is half metallic, whereas the source electrode is an ordinary 3D ferromagnet, like Co or Fe. Moreover, assume again that at $V_t = 0$ one has $\varepsilon_d > 0$, whereas $\varepsilon_d + U >> 0$, which implies that the dot may only be empty or singly occupied. From [3, 4] it is known that in collinear configurations such a junction can work as a mesoscopic diode, i.e. the electric current can flow for one bias polarization, whereas it is suppressed or even blocked for the opposite bias polarization. The results for the electric current in the considered device with the mean field switched on, and for different angles Θ, are shown in Fig. 2. As discussed above, the effective field yields a maximum of discrete level spin-splitting at the threshold voltage. The spin-up electrons of energy $\varepsilon_{d\uparrow}$, which enter the electron window first, may hence tunnel through the QD, giving rise to a significant enhancement of the resonant bump that occurs at a positive bias ($V_t > 0$) in the parallel configuration ($\Theta = 0$). This is true until the spin channel $\varepsilon_{d\downarrow}$ crosses the Fermi level of the source electrode. After that, at voltages above the bump, a blockade of the electric current appears, due to the spin-down electron that tunnelled to the dot from the source (left) lead. When the magnetic configuration of the junction becomes non-collinear, then in general an electron that has tunnelled to the QD has spin with both spinor components in the local reference. If only the spin channel $\varepsilon_{d\uparrow}$ is active in tunnelling, then effectively both leads contain less available spin states for these electrons, and a suppression of the resonant bump occurs.

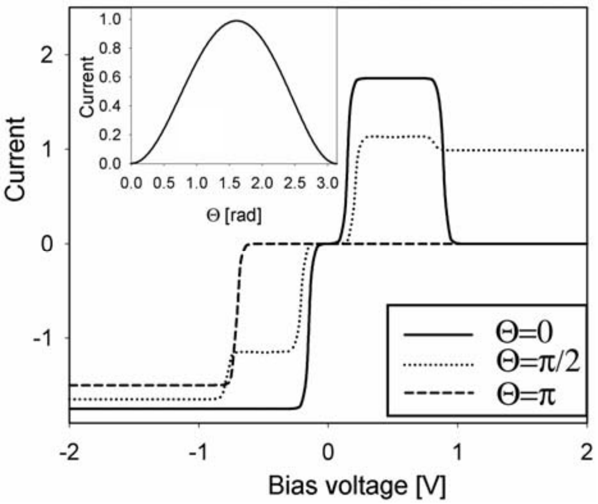

Fig. 2. Bias dependence of the electric current, calculated for the large *U* limit, with the empty state in equilibrium and for the indicated angles Θ. The inset shows the angular dependence of the electric current, calculated for a bias voltage of $V_t = 1$ V. The other parameters are: $\varepsilon_d = 0.25$ eV, $p_l = 0.4$, $p_r = 1$, $\alpha = 0.1$, and T = 100 K

The same mechanism is also responsible for current suppression in the vicinity of the threshold voltage at negative bias ($V_t < 0$). On the other hand, when both spin channels are in the tunnelling window, then for positive voltages above the bump the current blockade is lifted. Finally, in the antiparallel case the current is blocked in the entire range of positive bias voltages and also in a certain range of negative bias. The diode effect presented here for $\Theta = \pi$ is thus more pronounced as compared to the previous predictions, evaluated for a system with spin-degenerate discrete levels [3, 4]. The inset in Fig. 2 shows in detail how the current varies with the angle Θ at selected bias voltages above the resonant bump. From this it evidently follows that collinear configurations are important for diode behaviour. Furthermore, the amplitude of the current can be modulated with Θ, from a blockade in collinear configurations to a maximum intensity in the non-collinear case.

To summarize, we have investigated sequential tunnelling through a spin-split discrete level of an interacting quantum dot coupled to non-collinearly polarized external ferromagnetic electrodes. In particular, we have shown that in non-collinear configurations the interplay of the effective exchange field, originating from the external electrodes, and Coulomb correlations on the dot may lead to a negative differential conductance between the threshold voltages, at which a new transport channel becomes open for tunnelling. Moreover, we have found that in systems with a half-metallic electrode the diode effect is suppressed when the magnetic moments of the leads are non-collinear. On the other hand, an interesting enhancement of diode-like behaviour is found in the antiparallel configuration. We predict that the latter feature is most significant in junctions with strong Coulomb repulsion between electrons on the dot.

References

[1] PRINZ G.A., J. Magn. Magn. Materials, 200 (1999), 57.
[2] DYAKONOV M.I., LANL http://arxiv.org/labs cond-mat/0401369 (2004).
[3] BUŁKA B.R., Phys. Rev. B 62 (2000), 3186.
[4] RUDZIŃSKI W., BARNAŚ J., Phys. Rev., B 69 (2001), 085318.
[5] GLAZMAN L.I., MATVEEV K.A., JETP Lett., 48 (1988), 445.
[6] YOSIDA K., *Theory of Magnetism*, Springer-Verlag, Berlin, 1998.

Received 14 September 2004
Revised 28 October 2004

Materials Science-Poland, Vol. 22, No. 4, 2004

Formation of the Kondo resonance in two-atom molecular systems for various interaction limits

W. I. BABIACZYK[*], B. R. BUŁKA

Institute of Molecular Physics, Polish Academy of Sciences,
ul. Smoluchowskiego 17/19, 60-179 Poznań, Poland

We consider a two-atom molecule connected to ferromagnetic leads, in the Kondo transport regime. To investigate the Kondo effect in the system, we use the slave–boson mean field approximation (SBMFA) techniques. Results are obtained for both the strong interaction limit, in which an infinite Coulomb repulsion U_{1-2} between atoms is assumed, and a finite U_{1-2} case. The transport is considered in the $T = 0$ and $V = 0$ equilibrium limit.

Key words: *Kondo resonance; interaction; two-atom molecule*

1. Introduction

In the last decade, the Kondo resonance has been observed in semiconductor nanodevices (quantum dots) [1, 2], and recently also in the molecular nanodevices [3]. Due to the different geometry of nanodevices, the Kondo effect observed varies from that for doped metals. The minimum at low temperatures is achieved not by the resistivity, but by conductance. The mechanism of forming of the resonance is, however, similar. Namely, second order processes like co-tunnelling enhance transmission through the system when an unpaired spin occurs on the quantum dot or a single molecule. These processes add coherently, which results in a correlated many-electron state coupling of the electrons from the electrodes and allows current to flow even in the Coulomb blockade regime.

2. The model and slave–boson techniques

We focus on non-equilibrium spin-dependent transport phenomena in devices based on two-atom molecules attached to para- and ferromagnetic leads. Such a model can be a useful tool helping us to understand transport through real systems with bi-partite

---

[*] Corresponding author, e-mail: iwo@ifmpan.poznan.pl.

molecules, like biphenyl, other similar aromatic-type molecules, or the divanadium molecule [3].

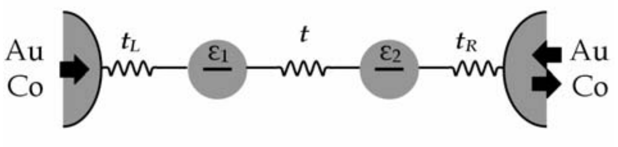

Fig. 1. Schematic view of a two-atom molecule connected to metallic leads. In the ferromagnetic case, it is possible to change the orientation of spin polarization in one of them

Figure 1 schematically shows a two-atom molecule connected to para- and ferromagnetic leads – Au and Co, respectively. The leads in the ferromagnetic system are spin-polarized, and one can change the polarization alignment in the system by changing the polarization orientation in one of the leads. For simplicity, each atom is represented by a single level. Such a system can be described with the double impurity Anderson Hamiltonian:

$$\begin{aligned} H = \sum_{i,j,\sigma}\left(t+\varepsilon_i\delta_{i,j}\right)c^{+}_{i\sigma}c_{j\sigma} + U_{1-2}\sum_{i,j} n_i n_j + \\ \sum_{k,\sigma}\left(t_{L1}c^{+}_{kL\sigma}c_{1\sigma} + t_{R2}c^{+}_{kR\sigma}c_{2\sigma} + h.c.\right) + \sum_{k,\sigma,\alpha\in L,R}\varepsilon_{k\alpha}c^{+}_{k\alpha,\sigma}c_{k\alpha,\sigma} \end{aligned} \tag{1}$$

The first two terms correspond to the two-atom molecule, the first describing the hopping of electrons between atoms and the potential energy ε_i of electrons on the site i, the second one includes the Coulomb interactions of two electrons on different sites, U_{1-2} being the Coulomb integral treated as an adjustable parameter. The on-site Coulomb repulsion is assumed to be infinite, and thus a double occupancy of the atom is forbidden.

We use the slave–boson mean field approximation (SBMFA) techniques in our calculations to include partially electronic correlations. The Coleman–Barnes representation of the auxiliary operators was chosen, as it gives reliable results for the paramagnetic case and describes the evolution of the physical quantities properly when magnetization appears in the leads. In the SBMFA Coleman–Barnes [4] representation, the electron creation operator reads $c^{+}_{i\sigma} = f^{+}_{i\sigma}e_i$, where $f_{i\sigma}{}^{+}$ is the pseudofermion operator creating an electron at site i with spin σ, and e_i is the mean value of the boson operator creating an empty state at a site i. The condition $Q_i = e_i^2 + f^{+}_{i\sigma}f_{i\sigma} = 1$ limits the action of the auxiliary operators to physical space. This constraint enforces an additional term in the Hamiltonian: $H \to H + \sum_i \lambda_i\left(Q_i - 1\right)$, where λ_i is a Lagrange multiplier. The mean field approximation reduces the problem to the free electron Anderson model with shifted energies $\tilde{\varepsilon}_{i\sigma} = \varepsilon_{i\sigma} + \lambda_i$, and renormalized hopping parameters $\tilde{t}_\alpha = e_i t_\alpha$ and $\tilde{t} = e_i e_j t$:

$$\begin{aligned} H = {} & \sum_{i,j,\sigma}\left(\tilde{t} + \tilde{\varepsilon}_i\delta_{i,j}\right) f^{+}_{i\sigma} f_{j\sigma} + U_{1-2}\sum_{i,j}\left(1-e_i^2\right)\left(1-e_j^2\right) \\ & + \sum_{k,\sigma}\left(\tilde{t}_{L1} c^{+}_{kL\sigma} f_{1\sigma} + \tilde{t}_{R2} c^{+}_{kR\sigma} f_{2\sigma} + h.c.\right) + \sum_{k,\sigma,\alpha\in L,R} \varepsilon_{k\alpha} c^{+}_{k\alpha,\sigma} c_{k\alpha,\sigma} + \sum_i \lambda_i\left(e_i^2 - 1\right) \end{aligned} \tag{2}$$

To obtain stable solutions for the considered system, one has to find the minima of the free energy *F* by solving a set of self-consistent equations:

$$\begin{cases} \dfrac{\partial F}{\partial \lambda_i} = 0, \qquad \dfrac{\partial F}{\partial e_i} = 0 \end{cases} \tag{3}$$

with respect to the parameters e_i and λ_i. The boson part of the free energy reads $F_b = \sum_i \lambda_i\left(e^2 - 1\right)$. The fermion part of the free energy can be determined within the Green functions techniques: $F_f = \frac{2}{\pi}\int_{-\infty}^{+\infty} d\omega f_\alpha(\omega)\,\mathrm{Im}\left[\ln G^r_{1\sigma,2\sigma}(\omega)\right]$, where $f_\alpha(\omega)$ is the Fermi function for the left (α = L) and right (α = R) lead, and the retarded Green function reads $G^r_{1\sigma,2\sigma}(\omega) = \int d\omega \frac{\tilde{t}\,\tilde{\Gamma}_{L\sigma}\tilde{\Gamma}_{R\sigma}}{(\omega - \tilde{\varepsilon}_{+\sigma})(\omega - \tilde{\varepsilon}_{-\sigma})}$. The coefficients $\tilde{\Gamma}_{\alpha\sigma}$ denote renormalized molecule-lead tunnelling rates, and

$$\tilde{\varepsilon}_{\pm\sigma} = \frac{1}{2}\left(\tilde{\varepsilon}_{1\sigma} + \tilde{\varepsilon}_{2\sigma} \pm \sqrt{\left(\tilde{\varepsilon}_{1\sigma} - \tilde{\varepsilon}_{2\sigma}\right)^2 + 4\tilde{t}^{\,2}}\right)$$

are the effective energies of the bonding (–) and antibonding (+) levels of the molecule, which are formed in the diagonalisation of the Hamiltonian (2).

3. Transport in the limit of $U_{1-2} \to \infty$

In the strong interactions limit of $U_{1-2} \to \infty$, where only a single occupancy of the whole molecule is allowed, it is sufficient to use only one slave–boson *e* and one Lagrange multiplier λ to describe the system. The completeness relation and renormalization then reads: $Q = e^2 + \sum_i f^{+}_{i\sigma} f_{i\sigma} = 1$. Two self-consistent equations (3) can be solved using the Green functions techniques:

$$\begin{aligned} 1 - e^2 &= \frac{2}{\pi}\sum_{\alpha,\sigma}\frac{\Gamma_{\alpha\sigma}}{\Gamma_\sigma}\int d\omega f_\alpha(\omega)\,\mathrm{Im}\left[G^r_{1\sigma,2\sigma}(\omega)\right] \\ \lambda &= \frac{4}{\pi}\sum_{\alpha,\sigma}\Gamma_{\alpha\sigma}\int d\omega f_\alpha(\omega)\,\mathrm{Re}\left[G^r_{1\sigma,2\sigma}(\omega)\right] \end{aligned} \tag{4}$$

where $\Gamma_\sigma = \Gamma_{L\sigma} + \Gamma_{R\sigma}$. The conductance *G* is determined from:

$$G = \frac{e^2}{h}\sum_\sigma \frac{4\Gamma_{L\sigma}\Gamma_{R\sigma}}{\Gamma^2_\sigma}\left|G^r_{1\sigma,2\sigma}\right|^2 \tag{5}$$

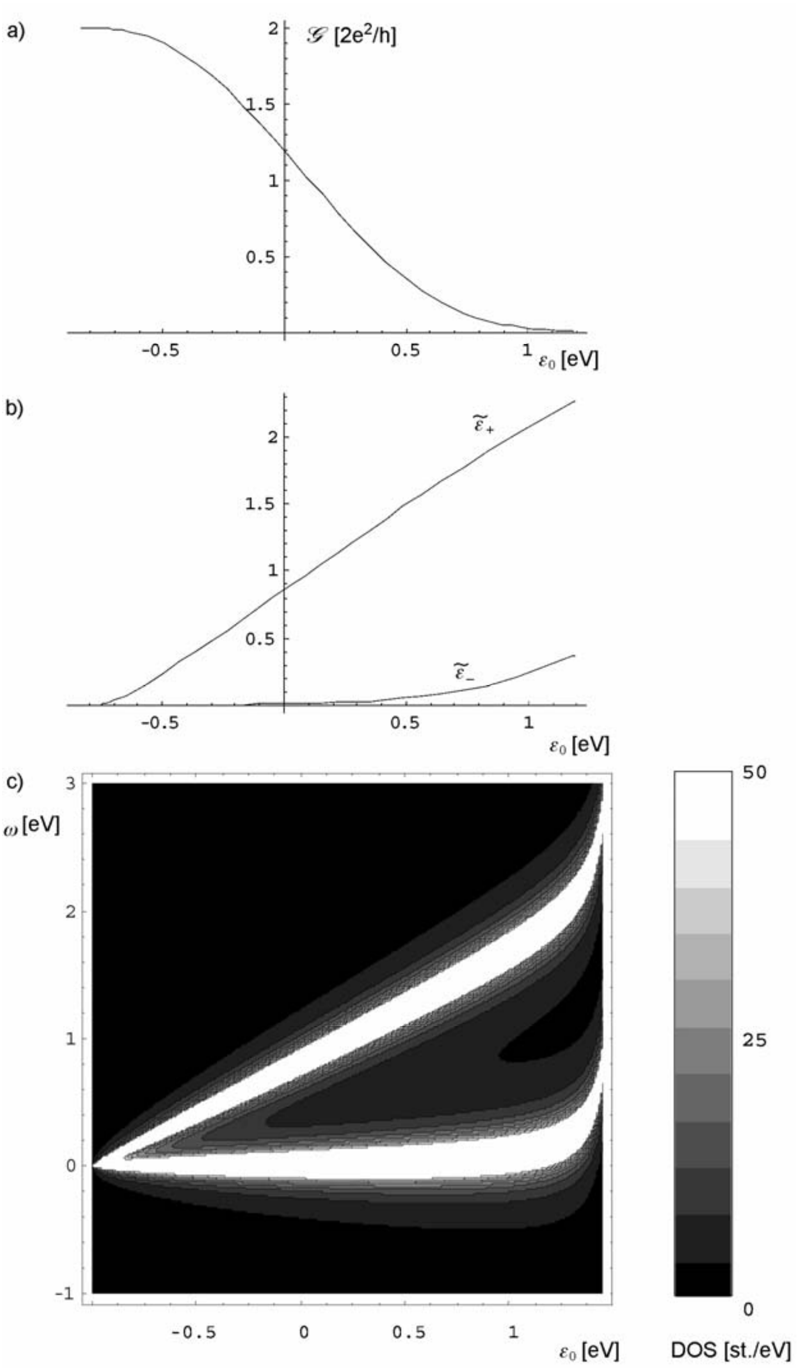

Fig. 2. Conductance in a symmetrical junction (a), effective positions of the molecular levels (b), and the grey-level plot of the densities of states in the leads. Densities of states in the leads are assumed $\rho_\alpha = 0.294$ states/eV, $t_L = t_R = 0.2$ eV

In Figure 2a, the conductance of the symmetrical junction ($t_L = t_R$, $\varepsilon_1 = \varepsilon_2 \equiv \varepsilon_0$) is shown. In the empty state regime, for large positive ε_0, G tends to zero. With decreasing ε_0, G increases and reaches its maximal theoretical value, $2e^2/h$, in the Kondo regime. The conductance behaviour reflects changes in the positions of the effective molecular levels, which are presented in Fig. 2b. In the empty state regime, the levels are not renormalized due to a lack of electronic correlations in the system. The energy gap is constant in this regime. With decreasing ε_0, $\tilde{\varepsilon}_\pm$ approaches the Fermi level ($E_F = 0$). Due to renormalization, $\tilde{\varepsilon}_-$ is strongly occupied and stays near E_F. The higher, antibonding level $\tilde{\varepsilon}_+$ is still weakly renormalized. In the Kondo regime, for ε_0 deeply below E_F, both levels are strongly renormalized and stay near E_F. In Figure 2c, a grey-level plot of the densities of states (DOS) of the effective molecular levels is presented. In the empty state regime, DOS peaks are separate and broad. The energy gap between them is constant. When approaching the Kondo resonance regime, the energy gap narrows, and eventually the DOS peaks merge and become extremely narrow and high.

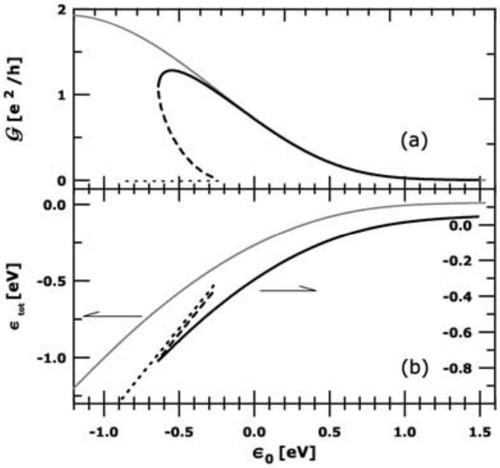

Fig. 3. Comparison of the conductance (a) in the symmetrical junction $t_L = t_R = 0.2$ eV, for the cases $\varepsilon_1 = \varepsilon_2$ and $\varepsilon_1 \neq \varepsilon_2$. A free energy plot (b) for the considered cases. The grey line denotes plots for the case $\varepsilon_1 = \varepsilon_2$, and the black for $\varepsilon_1 \neq \varepsilon_2$. Dotted and dashed lines correspond to unstable solutions

A comparison of the conductance in the asymmetrical and symmetrical junction is presented in Fig. 3a. For a non-zero gap between the local sites energies, the loop of G can be formed, because an unstable solutions appears. The system chooses a solution corresponding to the lowest energy. To decide which solution is stable, the total energy plot is shown in Fig 3b. The energy decreases monotonically with decreasing ε_0 till the unstable regime, where three solutions appear. For very low ε_0, the levels are no longer renormalized, and the energy is equal to the occupied level energy. In the resonance regime, G exhibits a sudden drop to zero. The reason for such behaviour is the transport blockade in the system, when ε_1 and ε_2 are deeply below E_F. In such a case, the symmetry of the molecule is broken, and the lower level is occupied with the whole electron (as the double occupancy is forbidden). In a symmetric case, the electron is distributed equally to the both levels; in the asymmetric case, it prefers the lower level. The result is a consequence of the approximation adopted.

In the ferromagnetic system, DOS in the leads are approximated with constant values on the Fermi level: $\rho_\uparrow = 0.174$ and $\rho_\downarrow = 1.735$ st./eV [5]. The magnetizations of the leads can be aligned parallel (P configuration) or antiparallel (AP configuration). The conductance in the symmetrical and asymmetrical junctions is shown in Fig. 4a. Unlike in the P configuration, G does not reach a value of $2e^2/h$ in the AP configuration due to lower contact efficiencies. For the asymmetric case, loops of G can be observed in the unstable solution regime; in the empty state regime, G tends to zero in all cases. G_{AP} can be larger than G_{P} when differences in t_α and ε_i are opposite in sign and minority spin transfer is preferred. Magnetoresistance, shown in Fig. 4b, is defined as the relative difference in conductance between the P and AP configurations, $MR = (G_{\mathrm{P}}-G_{\mathrm{AP}})/G_{\mathrm{P}}$. In the resonance regime, MR can be positive or negative due to the asymmetry of the junction; in the empty state regime, MR tends to the value determined by the Julliere formula for the given DOS values, $MR_{\mathrm{Julliere}} = 2p^2/(1+p^2) \approx 0.55$ for all considered cases, where $p = (\rho_\downarrow - \rho_\uparrow)/(\rho_\downarrow + \rho_\uparrow)$ is the magnetic polarization of the leads.

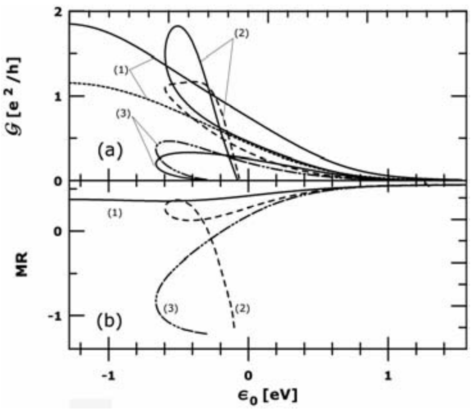

Fig. 4. Conductance (a) and magnetoresistance (b) for the system with ferromagnetic leads. Curves (1) denote the symmetric junction $\varepsilon_1 = \varepsilon_2$, $t_L = t_R = 0.2$ eV; (2) – asymmetric junction with $\varepsilon_1-\varepsilon_2 = 0.1$ eV and $t_L- t_R = -0.13$ eV; (3) – asymmetric junction with $\varepsilon_1-\varepsilon_2 = 0.1$ eV and and $t_L-t_R = +0.13$ eV. The solid lines in (a) denote a parallel (P) alignment of magnetization in the leads, and dashed lines an antiparallel alignment (AP)

4. Transport in the finite U_{1-2} limit

In the finite U_{1-2} limit, double occupancy of the molecule is allowed. In such a case, we apply two slave–bosons and two Lagrange multipliers to describe the system. The completeness and renormalization relations then read: $Q_i = e_i^2 + f_{i\sigma}^+ f_{i\sigma} = 1$ and $\tilde{t} = e_1 e_2 t$, $\tilde{t}_L = e_1 t_L$, $\tilde{t}_R = e_2 t_R$, $\tilde{\varepsilon}_{i\sigma} = \varepsilon_{i\sigma} + \lambda_i$, $i = 1, 2$. In this case, the four self-consistent equations (3) can only be solved numerically. Conductance G is again determined from (5). We consider only the symmetric paramagnetic junction, as the calculations for the asymmetrical junction and ferromagnetic cases are still in progress. The conductance for $U_{1-2} \approx 0$ is presented in Fig. 5a. In the empty state regime, the conductance is close to zero. With decreasing ε_0, G increases. Unlike the strong interaction limit, G drops to zero for very low ε_0 after attaining the value of $2e^2/h$ near the Fermi level $E_F = 0$. Conductance for higher values of U_{1-2} shows the behaviour similar to that of $U_{1-2} \approx 0$; the G peak, however, is broadened and shifted toward lower ε_0. The positions of the effective molecular levels are shown in Fig. 5b. In the empty state regime, the levels behave like in the strong interaction cases. In both cases, when the resonance regime is approached, $\tilde{\varepsilon}_-$ (which is closer to the Fermi level) is fully occupied and pushed down below E_F due to renormalization between the effective levels. Now, the transport takes place only through $\tilde{\varepsilon}_+$ now. A further filling of $\tilde{\varepsilon}_+$ renormalizes hopping to the leads, and transport gradually drops to zero. In Figure 6, the conductance and number of electrons are shown, proving that the resonance and therefore G have maxima of $2e^2/h$ exactly for $n = 1$.

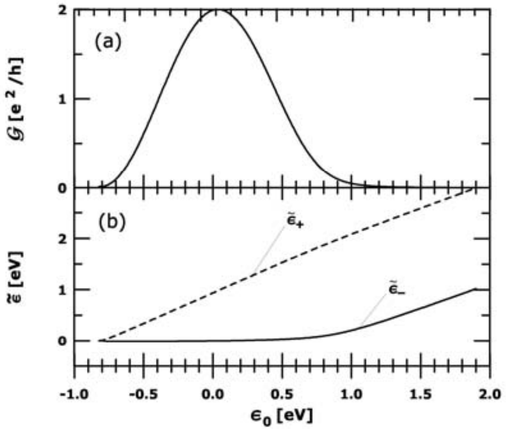

Fig. 5. Conductance (a) and positions of the effective molecular levels (b) for the symmetric paramagnetic junction in the limit of $U_{1-2} \to 0$. All parameters are the same as in Fig. 2

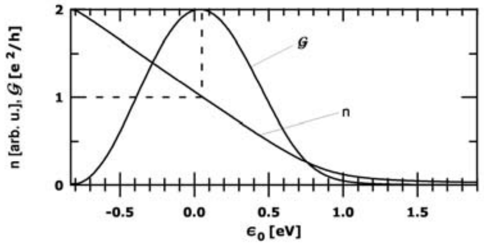

Fig. 6. Conductance and total number of electrons for the symmetric junction in the case of $U_{1-2} = 0$. The dotted line is just a guide for the eye

5. Conclusions

We have analysed the electronic transport in systems of two-atom molecules connected to para- and ferromagnetic leads, including electronic correlations for the molecule by applying the SBMFA techniques. The Kondo resonance and finite Coulomb repulsion between sites were observed in systems with a strong interaction limit of $U_{1-2} \to \infty$. We have shown that the resonance is formed when the local atomic levels are deeply below the Fermi level. The conductance can form loops when a difference in the atomic energy levels appears due to energetically unstable solutions. In the magnetic system, conductance for a parallel alignment of the magnetization of the leads is larger than for the antiparallel case, due to larger contact efficiencies in the symmetric junction. The situation, however, can be reversed in the asymmetric system. In the case of a non-zero energy levels gap, unstable solutions appear similarly to the paramagnetic case. Depending on the asymmetry of the system, its magnetoresistance positive or negative values in the Kondo regime.

In the empty state regime, it tends to the Julliere value for all considered cases. For finite values of U_{1-2}, the Kondo resonance arises for levels positions corresponding to an occupancy of the molecule of $n = 1$, which can also be observed as a maximum in conductance. When the system is occupied by two electrons ($n = 2$), electronic correlations are irrelevant due to electron–hole symmetry, and the conductance behaviour is the same as for the empty state limit ($n = 0$).

Acknowledgements

The work was partially supported by the Committee for Scientific Research under the Grant No. 2 P03B 118 25 (W. I. B.) and PBZ KBN 044 P03 2001 (B. R. B.)

References

[1] GOLDHABER-GORDON D., SHTRIKMAN H., MAHALU D., ABUSCH-MAGDER D., MEIRAV U., KASTNER M.A., Nature, 391 (1998), 156.
[2] CRONENWETT S. M., OOSTEKAMP T. H., KOUWENHOVEN L. P., Science, 281 (1998), 540.
[3] LIANG W., SHORES M.P., BOCKRATH M., LONG J.R., PARK H., Nature, 417 (2002), 725.
[4] BARNES S.E., J. Phys. F: Met. Phys., 6 (1976), 1375; COLEMAN P., Phys. Rev. B, 29 (1984), 3035.
[5] SZAJEK A., unpublished results.
[6] JULLIERE M., Phys. Lett., 54A (1975), 225.

Received 20 October 2004
Revised 9 November 2004

Materials Science-Poland, Vol. 22, No. 4, 2004

Influence of interface spin-flip processes on spin accumulation and spin currents in magnetic multilayers

M. WAWRZYNIAK[1*], J. BARNAŚ[1, 2]

[1]Department of Physics, Adam Mickiewicz University, ul. Umultowska 85, 61-614 Poznań, Poland

[2]Institute of Molecular Physics, Polish Academy of Sciences,
ul. M. Smoluchowskiego 17, 60-179 Poznań, Poland

Macroscopic description of electronic transport in magnetic layered structures has been extended by including effects due to spin-flip scattering at interfaces. Such processes lead to spin-memory losses at the interfaces and therefore play a significant role in giant magnetoresistance and spin switching phenomena. They also modify distribution of spin currents, electric fields and spin accumulation in the vicinity of interfaces. A system consisting of two oppositely magnetized semi-infinite ferromagnets, and the case of magnetic/nonmagnetic superlattices in parallel and anti-parallel magnetic configurations are analysed in detail.

Key words: *magnetic multilayers; spin accumulation; spin-flip scattering*

1. Introduction

Since the discovery of the giant magnetoresistance (GMR) effect in magnetic multilayers, electronic transport in artificially layered structures has been extensively studied, both experimentally and theoretically. The GMR effect was first observed in the current-in-plane (CIP) geometry [1, 2], but later it was also found for electric currents flowing perpendicularly to the layers (current-perpendicular-to-plane (CPP) geometry) [3]. In the latter case, the effect was even larger. The electronic transport along the axis normal to the layers leads to some non-equilibrium phenomena, for instance spin-splitting of the chemical potential (spin accumulation) at interfaces.

One of the theoretical descriptions commonly used to interpret such experimental data is the macroscopic description proposed by Valet and Fert [4]. Owing to its simplicity, this description allows basic parameters (for instance spin diffusion lengths)

---

[*]Corresponding author, e-mail: wawrzyniak@spin.amu.edu.pl.

to be easily extracted from the experimental data on CPP GMR [5, 6]. The macroscopic description takes into account spin accumulation at the interfaces and its relaxation in the bulk due to spin-flip scattering. However, the description ignores spin-flip scattering at the very contact between different layers. Some experimental data cannot be described properly by this simplified description and one should take into account the fact that electrons can partially lose their spin memory when crossing the interface between magnetic and nonmagnetic films [7, 8]. This problem is addressed in the present paper, where we extend the Valet–Fert model by including the influence of spin-flip scattering processes at the interfaces. These processes are effectively included into the boundary conditions via the corresponding spin-mixing interfacial resistance.

We consider a layered structure and assume that electric current flows along the axis z normal to the interfaces. At the beginning we consider a simplified situation, where two semi-infinite ferromagnetic systems are in direct contact at the plane $z = 0$. Then, we analyse a magnetic superlattice, in which magnetic layers are separated by nonmagnetic metallic films. In both cases, we neglect interfacial spin-conserving scattering and take into account only spin-flip processes.

2. Macroscopic description of Fert and Valet

Starting from the kinetic Boltzmann equation, Valet and Fert [4] showed that when the spin diffusion length l_s (for both spin orientations) is much longer than the corresponding mean free path, electronic transport is well described by the macroscopic equations:

$$\frac{e}{\sigma_s}\frac{\partial J_s(z)}{\partial z} = \frac{\bar{\mu}_s(z) - \bar{\mu}_{-s}(z)}{l_s^2} \tag{1}$$

$$J_s(z) = \frac{\sigma_s}{e}\frac{\partial \bar{\mu}_s(z)}{\partial z} \tag{2}$$

where e is the electron charge ($e > 0$), σ_s and $J_s(z)$ are the conductivity and current density for the spin s, respectively, whereas $\bar{\mu}_s = \mu_s(z) - eV(z)$ is the electrochemical potential. As the local spin quantization axis we assume, following Ref. [4], the one determined by the local spin polarization (opposite to the local magnetization), with $s = \uparrow$ corresponding to the spin-majority electrons and $s = \downarrow$ corresponding to the spin-minority ones. Spin projection onto the global quantization axis will be denoted as $s = +$ and $s = –$. When the local and global axes coincide, then $s = \uparrow$ ($s = \downarrow$) is equivalent to $s = +$ ($s = –$).

The above equations may be rewritten in a more suitable form as:

$$\frac{e}{\sigma_\pm}\frac{\partial J_\pm(z)}{\partial z} = \pm 2\frac{\Delta\mu(z)}{l_\pm^2} \tag{3}$$

$$J_{\pm} = \sigma_{\pm}\left[F(z) \pm \frac{1}{e}\frac{\partial \Delta\mu(z)}{\partial z} \right] \tag{4}$$

where the spin accumulation $\Delta\mu(z)$ is introduced explicitly via the formula $\bar{\mu}_s(z) = \bar{\mu}(z) \pm \Delta\mu(z)$, and the driving electric field $F(z)$ is determined by the derivative of the spin-independent part of the electrochemical potential:

$$F(z) = \frac{1}{e}\frac{\partial \bar{\mu}(z)}{\partial z} \tag{5}$$

Equations (3) and (4) lead to the following two second-order differential equations:

$$\frac{\partial^2 \Delta\mu(z)}{\partial z^2} = \frac{\Delta\mu(z)}{l_{sf}^2} \tag{6}$$

$$\frac{\partial^2}{\partial z^2}\left[\sigma_+ \bar{\mu}_+(z) + \sigma_- \bar{\mu}_-(z)\right] = 0 \tag{7}$$

where l_{sf} is defined as $1/l_{sf}^2 = 1/l_+^2 + 1/l_-^2$. The general solutions of the above equations have the form:

$$\Delta\mu(z) = C_1 \exp(z/l_{sf}) + C_2 \exp(-z/l_{sf}) \tag{8}$$

$$[\sigma_+ \bar{\mu}_+(z) + \sigma_- \bar{\mu}_-(z)] = C_3 z + C_4 \tag{9}$$

where the constants C_1–C_4 are to be determined from the appropriate boundary conditions. From the solutions of (8) and (9) one can obtain the general expressions for the spin accumulation $\Delta\mu(z)$, electric field $F(z)$, and current density $J_s(z)$ inside each layer of any multilayer structure [4].

3. Ferromagnetic semi-infinite systems in direct contact

Consider a structure consisting of two equivalent semi-infinite parts, which are magnetized in opposite directions, e.g., the left one is magnetized along the positive axis x while the right one along the axis $-x$. Let the global spin quantization axis coincide with the axis x (it also coincides with the local spin quantization axis in the right part) and let the interface between the two semi-infinite systems be in the plane $z = 0$ (axis z is normal to the interface). It is convenient to introduce the bulk spin asymmetry coefficient β by writing the bulk resistivity of the ferromagnetic material in the form [4]:

$$\rho_{\uparrow(\downarrow)} = 1/\sigma_{\uparrow(\downarrow)} = 2\rho(1 \mp \beta) \tag{10}$$

where $\rho_\uparrow$ and $\rho_\downarrow$ denote bulk resistivities in the spin-majority and spin-minority channels, respectively, and the upper (lower) sign corresponds to ↑ (↓).

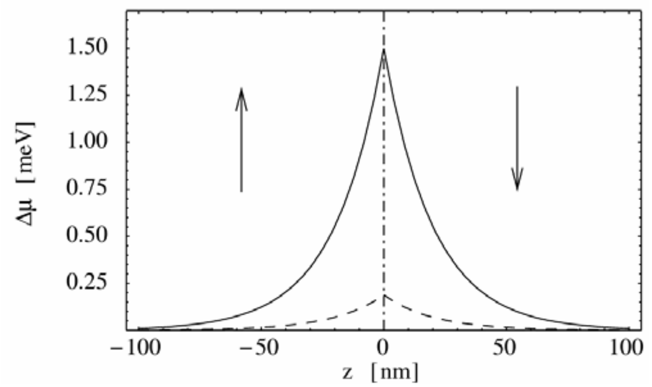

Fig. 1. Spin accumulation at the interface between two semi-infinite ferromagnets, calculated for $\rho = 100$ Ω·nm, $l_{sf} = 20$ nm, $\beta = 0.5$, $J = 1.5\times10^{-6}$A/nm^2, $R_{sf} = 0.5\times10^3$ Ω·nm^2 (dashed line), and $1/R_{sf} = 0$ (solid line)

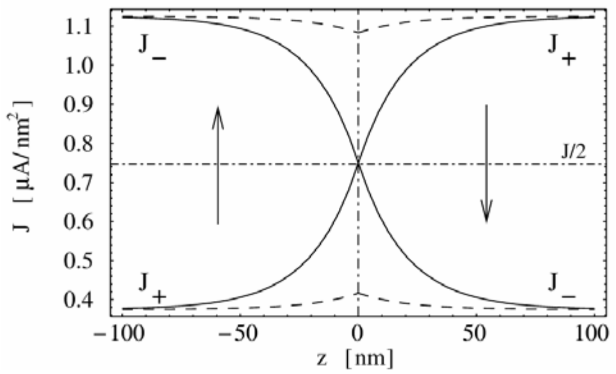

Fig. 2. Spin currents at the interface between two semi-infinite ferromagnets, calculated for the same situation as in Fig.1

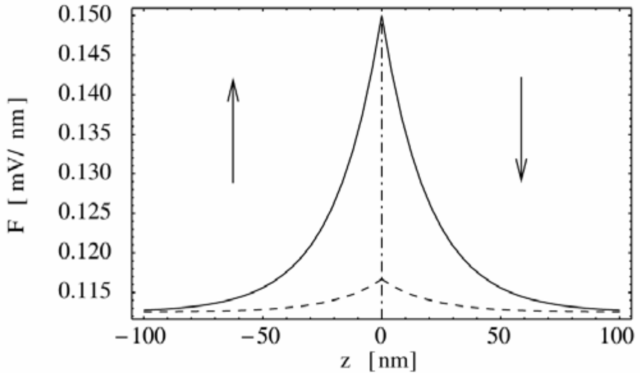

Fig. 3. Electric field at the interface between two semi-infinite ferromagnets, calculated for the same situation as in Fig.1. The dashed-dotted line represents the field E_0

In the limit of vanishing interface resistance and in the absence of spin-flip scattering at the interface, the solutions for spin accumulation, electric current, and effective field have been discussed in Ref. [4], and are presented in Figs. 1, 2, and 3 by solid lines. The main objective of this paper is to answer the question how interface spin -flip scattering modifies spin accumulation and spin currents. To answer this, we include interface spin-flip scattering effectively by a certain interfacial spin-mixing resistance R_{sf} per unit square. The interface boundary conditions are then given by the following expressions:

$$R_{sf}\left[J_+(z=0^-)-J_+(z=0^+)\right]=-\frac{1}{e}\left[\bar{\mu}_+(z=0^+)-\bar{\mu}_-(z=0^+)\right] \tag{11}$$

$$\bar{\mu}_+(z=0^+)-\bar{\mu}_+(z=0^-)=0 \tag{12}$$

$$\bar{\mu}_-(z=0^+)-\bar{\mu}_-(z=0^-)=0 \tag{13}$$

Since spin-flip processes allow spin transfer between the two spin channels, the spin current density is generally discontinuous across the boundary at $z = 0$. On the other hand, the electrochemical potentials are continuous across the interface in the absence of spin-conserving interface scattering.

Using the general solutions (8) and (9) together with the boundary conditions (11)–(13), one can obtain the exact solutions for spin accumulation, electric field, and current density in both the left and right parts of the structure. These solutions for the left part ($z < 0$) read:

$$\Delta\mu(z)=\beta J l_{sf} e\rho\frac{\tilde{R}_{sf}}{\tilde{R}_{sf}+1}\exp(z/l_{sf}) \tag{14}$$

$$J_\pm(z)=(1\mp\beta)\frac{J}{2}\pm\frac{\beta J}{2}\frac{\tilde{R}_{sf}}{\tilde{R}_{sf}+1}\exp(z/l_{sf}) \tag{15}$$

$$F(z)=J\rho(1-\beta^2)+\beta^2 J\rho\frac{\tilde{R}_{sf}}{\tilde{R}_{sf}+1}\exp(z/l_{sf}) \tag{16}$$

where $\tilde{R}_{sf}=R_{sf}/(2l_{sf}\rho)$ is a dimensionless spin-flip resistance, and J is the charge current density. The solutions for the right part ($z < 0$) are also given by Eqs. (14)–(16), but with $\exp(z/l_{sf})$ replaced by $\exp(-z/l_{sf})$, and β replaced by $-\beta$ in Eqs. (15) and (14).

As shown in Ref. [4], the interface gives rise to an additional interfacial resistance r_I due to the spin-bottle-neck effect. The additional voltage drop can be calculated as $V_I=\int_{-\infty}^{+\infty}(F(z)-E_0)dz$, where $E_0=J\rho(1-\beta^2)$ is the electric field far away from the interface (see Eq. (16)). This voltage drop can be related *via* Ohm's law to the additional interface resistance, finally yielding:

$$r_I = 2\beta^2 \rho l_{sf} J \frac{\tilde{R}_{sf}}{1+\tilde{R}_{sf}} \tag{17}$$

One should note that the absence of spin-flip processes corresponds to an infinite value of R_{sf}. The resistance r_I reduces then to the value $r_I = 2\beta^2 \rho l_{sf} J$, derived in Ref. [4]. It follows from the above formula that the presence of interfacial spin-flip scattering reduces the magnitude of r_I by a factor of $\tilde{R}_{sf}[1+\tilde{R}_{sf}]$.

The influence of interfacial spin-flip scattering on spin accumulation, electric current and electric field is shown in Figs. 1, 2, and 3 by dashed lines. Spin accumulation is significantly reduced in comparison to that in the case without spin-flip scattering (the solid line in Fig. 1). According to Eq. (14), the suppression is described by the factor $\tilde{R}_{sf}/[1+\tilde{R}_{sf}]$. The same factor also describes the suppression of the additional electric field, $F(z) - E_0$, near the interface. There is also a visible discontinuity of the spin currents at $z = 0$, $\Delta J_\sigma = J_\sigma(z = 0^+) - J_\sigma(z = 0^-)$, which follows from the presence of interfacial spin-flip processes (see Fig. 2). This discontinuity is equal to:

$$\Delta J_+ = -\Delta J_- = \beta J \frac{1}{1+\tilde{R}_{sf}} \tag{18}$$

and disappears in the absence of interfacial spin-flip scattering.

4. Magnetic/nonmagnetic superlattice structure

Let us now consider an infinite superlattice structure of nonmagnetic layers alternating with ferromagnetic ones. Two configurations are studied in detail – anti-parallel (AP) and parallel (P). The magnetic and nonmagnetic layers are characterized by the same parameters as before, but we attach indices *F* and *N* to distinguish parameters characterizing ferromagnetic (*F*) material from those describing nonmagnetic (*N*) material. Accordingly, the ferromagnetic layers are characterized by β, ρ_F, and l_{sf}^F, whereas the nonmagnetic ones by ρ_N and l_{sf}^N. Note that the spin asymmetry vanishes for nonmagnetic layers (the corresponding parameter β is equal to zero), hence $\rho_N = \rho_\uparrow/2 = \rho_\downarrow/2$ (we therefore did not attach the index *F* to the parameter β, as this makes no confusion).

Taking into account the superlattice periodicity and the boundary conditions (11)–(13), we calculated numerically the influence of the finite value of R_{sf} on spin accumulation, spin currents, and the electric field. Figure 4 shows spin accumulation in the AP configuration. The solid line there corresponds to the absence of interface spin-flip scattering, whereas the dashed line represents the solution with a finite spin-mixing interface resistance. As previously, the reduction of spin accumulation is clearly visible.

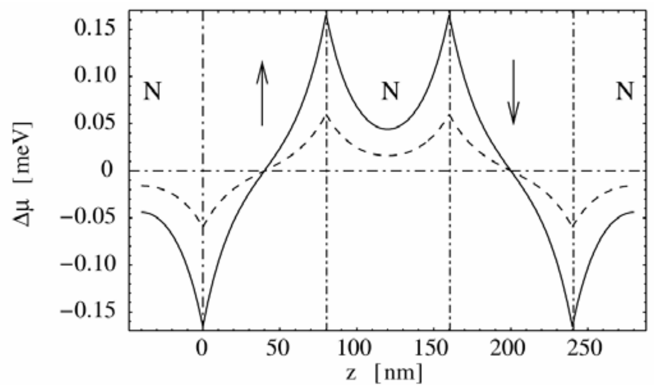

Fig. 4. Spin accumulation in a superlattice composed of magnetic and nonmagnetic metals in a antiparallel configuration. The parameters used for the numerical calculations were: ρ_F = 100 Ω·nm, l_{sf}^F = 20 nm, β = 0.5, nm (for the ferromagnetic metal), ρ_N = 12 Ω·nm, and l_{sf}^N = 20 nm (for the nonmagnetic metal). The other parameters were $J = 1.5\times10^{-6}$A/nm^2, $R_{sf} = 0.5\times10^3$ Ω·nm^2 (dashed line), and $1/R_{sf} = 0$ (solid line)

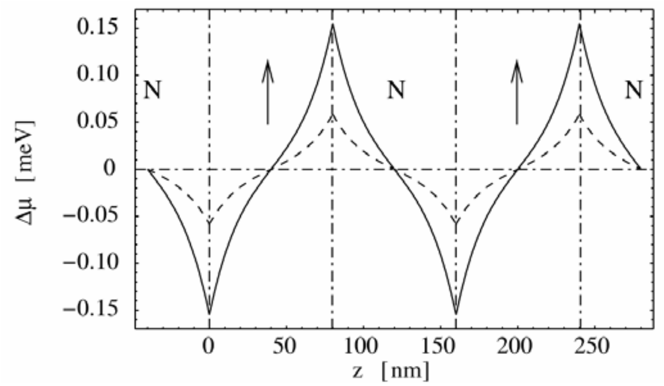

Fig. 5. The same as in Fig. 4, but for parallel magnetic configuration

Spin accumulation for the P configuration is shown in Fig. 5, where again the solid (dashed) line corresponds to the case with vanishing (non-vanishing) interface spin-flip scattering. The influence of spin-mixing resistance on the spin currents and electric field is qualitatively similar to that in the case of two semi-infinite systems in direct contact.

5. Conclusions

The presence of spin-flip scattering at the interfaces in a multilayer structure significantly reduces spin accumulation as well as other features that follow from spin accumulation. The suppression of spin accumulation is described by the factor

$\tilde{R}_{sf}/[1+\tilde{R}_{sf}]$. A finite spin-mixing interfacial resistance R_{sf} introduces sharp jumps in the spin current densities at the interfaces. Spin-memory loss at the interface has a significant impact on other transport characteristics, for instance on CPP GMR and spin switching phenomena. This is because these two phenomena rely on electron spin coherence at distances larger than the thickness of the nonmagnetic films separating the ferromagnetic ones. The loss of spin coherence at interfaces leads to a suppression of the CPP GMR and also to a suppression of the spin torque due to spin transfer.

Acknowledgements

The work was supported by the Polish State Committee for Scientific Research through the project PBZ/KBN/044/P03/2001.

References

[1] BAIBICH M.N., BROTO J.M., FERT A., NGUYEN VAN DAU F., PETROFF F., ETIENNE P., CREUZET G., FRIEDERICH A., CHAZELAS J., Phys. Rev. Letters, 61 (1988), 2472.

[2] BINASCH G., GRÜNBERG P., SAURENBACH F., ZINN W., Phys. Rev. B, 39 (1989), 4828. BARNAŚ J., FUSS A., CAMLEY R.E., GRÜNBERG P., ZINN W., Phys. Rev. B, 42 (1990), 8110.

[3] GIJS M.A.M., LENCZOWSKI S.K.J., GIESBERS J.B., Phys. Rev. Letters, 40 (1993), 7343.

[4] VALET T., FERT A., Phys. Rev. B, 48 (1993), 7099.

[5] BASS J., PRATT W.P., J. Magn. Magn. Materials, 200 (1999), 274.

[6] FERT A., PIRAUX L., J. Magn. Magn. Materials, 200 (1999), 338.

[7] DUVAIL J.L., FERT A., PEREIRA L.G., LOTTIS D.K., J. Appl. Phys., 75 (1994), 7070.

[8] FERT A., LEE S.F., Phys. Rev. B, 53 (1996), 6554.

Received 20 September 2004
Revised 2 November 2004

Materials Science-Poland, Vol. 22, No. 4, 2004

On the localization of electrons in disordered molecular wires

MACIEJ WOŁOSZYN[*], BARTŁOMIEJ J. SPISAK

Faculty of Physics and Applied Computer Science, AGH University of Science and Technology,
al. Mickiewicza 30, 30-059 Cracow, Poland

The aim of this report is to investigate electronic properties of a chain of atoms when its translational symmetry is broken by a topological disorder. The study uses the inverse participant ratio to obtain information on the localization of electrons in phase space.

Key words: *disorder; localization; inverse participant ratio; Husimi function*

1. Introduction

It is well established that electronic processes in low-dimensional systems, such as molecular wires, are determined by the quantum phenomena. One of the most intriguing problems of modern physics is the localization of conduction electrons in low-dimensional topologically disordered systems in the presence of various perturbations, such as magnetic field, temperature, spin-orbit scattering or electron–electron interaction. Localization in low-dimensional disordered systems has been subject to numerous theoretical papers, and we know that all eigenstates in such systems are localized by an arbitrary weak disorder [1–3] for uncorrelated random potentials [4]. On the other hand, localized states play a key role in the optical and transport properties of disordered systems.

In this paper, we use a method based on the phase space representation of quantum mechanics [5–8] to investigate localization. We applied this method to non-interacting electrons in a molecular wire using a one-electron liquid Kronig–Penney model [9, 10] and the Husimi function [11, 12]. The inverse participant ratio in phase space is calculated as a function of the disorder parameter for various wire lengths.

---

[*] Corresponding author, e-mail: woloszyn@novell.ftj.agh.edu.pl.

2. Theoretical model

A one-dimensional wire with topological disorder is described by the liquid Kronig–Penney model [9, 10]. We consider the time-independent Schrödinger equation for a system of non-interacting electrons with effective mass m, moving in a random potential $V(x)$, namely

$$\left[-\frac{\hbar^2}{2m}\frac{d^2}{dx^2}+V(x)\right]\psi(x)=\varepsilon\psi(x) \tag{1}$$

where ε and $\hbar$ have their usual meanings.

In fact, the potential $V(x)$ represents a collection of N elements, e.g. atoms or much more complex structures placed in a chain of the length $L = x_N - x_1$. The scattering potentials are assumed to be well located at random positions x_i

$$V(x)=\sum_{i=1}^{N}F_0\frac{\hbar^2}{m}\delta(x-x_i) \tag{2}$$

where $F_0 = mV_0b/\hbar^2$, and the parameter b is defined as the width of the square interatomic barriers, with V_0 being their height.

In the case of a system originating from a simple regular lattice (one-dimensional crystal), the locations x_i of the scattering centres in the chain are determined by the formula

$$x_i=(i+\eta r_i)a, \quad i=1, 2, ..., N \tag{3}$$

Equation (3) includes a random number r_i from the range (–1,1); a is the average distance between neighbouring sites, and η is a measure of the strength of disorder. This choice assures a fully periodic situation for $\eta = 0$ and an internal disorder proportional to η when we pass from a perfect lattice to a disordered system.

The limit of $V_0 \to 0$ and $b \to 0$ allows us to define a constant strength of the scattering potential, i.e. V_0b = const. Even in the case of a disordered chain we can construct a wave function for electrons that satisfies equation (1) by using the analytical expression for the wave function $\chi_i(x)$ inside the i-th square well

$$\chi_i(x)=C_i\cos(kx+\varphi_i) \tag{4}$$

where C_i is the amplitude, $k=\sqrt{2m\varepsilon}/\hbar$, and φ_i is the phase.

Joining the solutions (4) found at the consecutive ranges gives the wave function $\psi(x)$ which must satisfy the following conditions:

$$\psi(x_i^+)=\psi(x_i^-) \tag{5}$$

$$\left.\frac{d}{dx}\psi(x)\right|_{x_i^+}-\left.\frac{d}{dx}\psi(x)\right|_{x_i^-}=2F_0\psi(x_i) \tag{6}$$

where the finite discontinuity at the step results from integrating Eq. (1).

Knowledge of the exact form of $\psi(x)$ allows us to construct the Husimi function as follows

$$\rho_H(x,k)=\left(\frac{1}{2\pi\sigma^2}\right)^{1/2}\left|\int dx'\exp\left[-\frac{(x-x')^2}{4\sigma^2}+ikx'\right]\psi(x')\right|^2 \tag{7}$$

where σ^2 is chosen as La/π^2.

3. Results and discussion

In disordered systems, the phase and amplitude of the electronic wave function is changed by spatial fluctuations of potentials. In consequence, the envelope of the wave function decays exponentially from a localization centre ξ. This means that the electronic density $|\psi_n(x)|^2$ will not spread over the entire system, but will remain localized around ξ. This result can be described by the expression [15]

$$\psi_n(x)\propto A(x)\exp\left(-\frac{|x-\xi|}{\ell}\right) \tag{8}$$

where $A(x)$ is a randomly varying function describing the fluctuations in the amplitude of the wave function $\psi_n(x)$, and ℓ is the localization length, which can be defined as the asymptotic decay length of the envelope.

For a simple regular lattice, the electronic states can be extended over the whole system. As the disorder becomes larger, the localized states get more compressed. More information on the compression of the wave function can be extracted from the inverse participation ratio. This quantity is defined as the second moment of the electronic density and is given in real space by the formula

$$P_x(E_n)=\int dx|\psi_n(x)|^4 \tag{9}$$

and in momentum space by

$$P_k(E_n)=\int dk|\phi_n(k)|^4 \tag{10}$$

where the function $\phi_n(k)$ is the Fourier transform of $\psi_n(x)$.

The inverse participant ratio is inversely proportional to the volume of the part of the system that contributes effectively to eigenfunction normalization [16]. Our calculations indicate that this quantity has a monotonic character and strongly depends on the realization of disorder. In real space, the inverse participant number increases with increasing disorder strength. Simultaneously, in momentum space, the inverse participant ratio decreases as the strength of disorder increases and we observe a delocalisation of the wave function [17]. One of the possible phase space representations of the quantum states $|\phi_n\rangle$ is given by the Husimi function ρ_H, defined as in [11, 12]

$$\rho_H(x,k) = \left|\langle x_0, k_0 | \phi_n \rangle\right|^2 \tag{11}$$

where $\langle x_0, k_0|$ corresponds to a state whose uncertainty is minimal around x_0 and k_0 in real and momentum space [7], respectively. The implicit form of the Husimi function when the Gaussian form [8] for $\langle x_0, k_0|$ is used is given by formula (7).

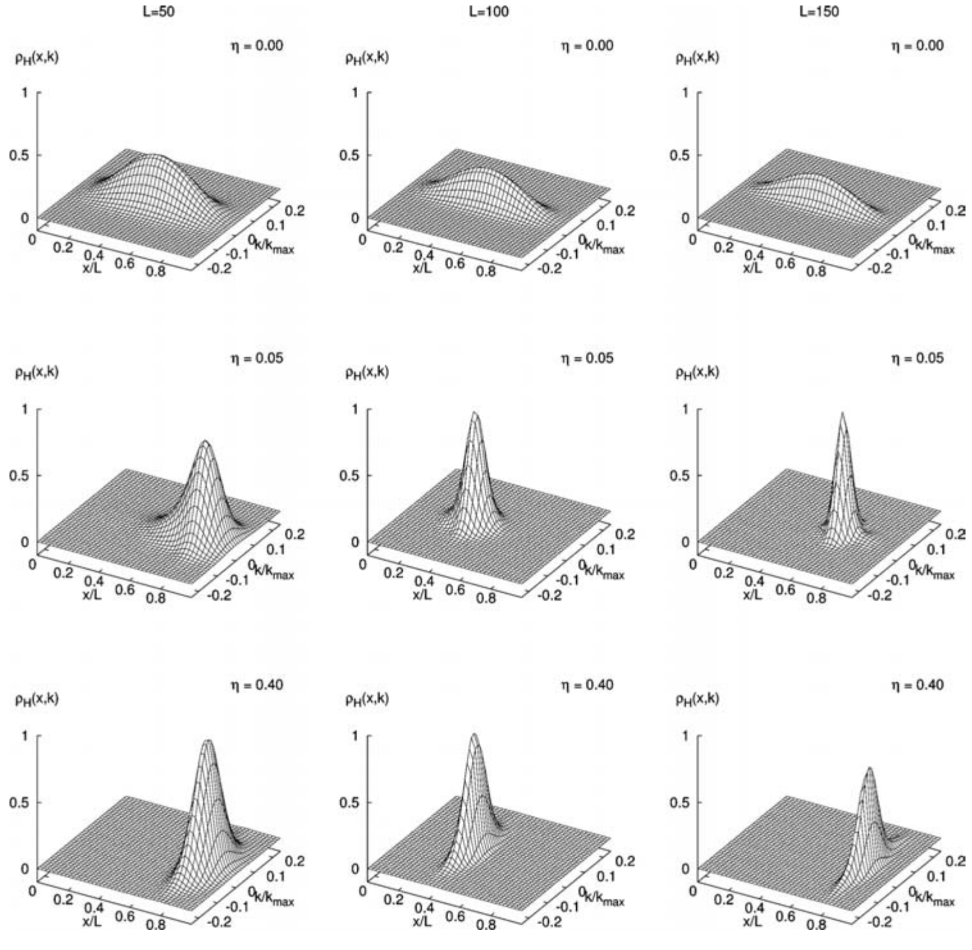

Fig. 1. The Husimi function for a disorder parameter $\eta = 0, 0.05, 0.4$
and wire length $L = 50, 100, 150$; $k_{\max} = 2\pi/a$

Figure 1 presents the Husimi functions corresponding to the ground state wave functions for some arbitrarily chosen values of disorder and for different numbers of atoms: N = 50, 100, and 150. In all cases, the average distance between neighbouring atoms is equal and taken as the unit length for molecular wires. Therefore, the results presented in Fig. 1 correspond to the lengths L = 50, 100 and 150.

We can see that for a medium strength of disorder the Husimi function in phase space has the most localized form. Quantitative information on the degree of localization of the Husimi function in phase space can be extracted from the phase space inverse participant number, which is given by the formula

$$P_{xk} = \frac{1}{2\pi} \int dx dk \rho_H^2 (x,k) \tag{12}$$

This quantity represents the effective volume occupied by the Husimi function in phase space, in analogy with the inverse participant ratio in real or momentum space.

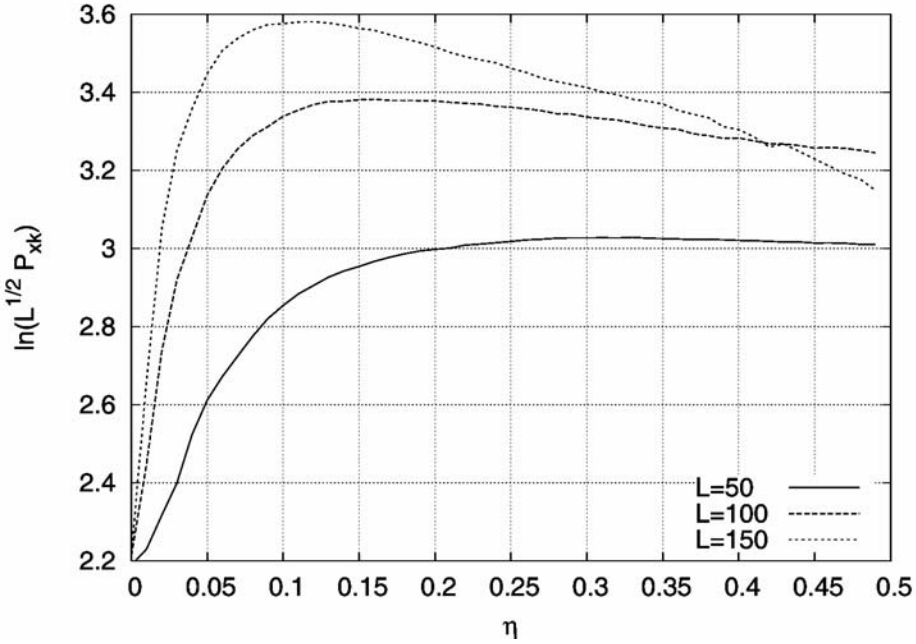

Fig. 2. The inverse participant ratio P_{xk} in phase space scaled with the chain length for L = 50, 100, and 150

The dependence of the inverse participant ratio in phase space on the disorder parameter, as a function of length L, is presented in Fig. 2. For the shortest wires (L = 50), we observe a plateau for moderate and strong disorder. In the remaining cases, a broad maximum is formed in the limit of weak disorder. The electronic wave function for such systems is non-vanishing only for a finite number of atoms. All these results suggest that we should get a peak corresponding to the most squeezed quantum state in the limit of very long wires. We expect that this hypothesis can be confirmed by numerical calculations based on high performance computing.

4. Numerical procedure

Each wave function of the ground state $\psi_0(x)$ is calculated from the Schrödinger equation for the ground state energy, which has to be determined using the shooting method and assuming the boundary conditions

$$\psi_0\left(x=0\right)=\psi_0\left(x=L\right)=0 \tag{13}$$

The relations between the median values of the inverse participant ratio and η parameters presented in Fig. 2 have been calculated for sets of 200 chains by repeating this procedure for each chain in our input data. From the numerical point of view, we find the P_{xk} parameters and Husimi functions this way mainly by performing simple one- and two-dimensional integrations.

All results included in this paper have been computed for chains consisting of N = 50, 100, or 150 sites, with an average inter-atomic distance of a = 1 in all wires.

5. Conclusion

In conclusion, we have used a one-dimensional version of the liquid Kronig –Penney model to investigate the process of electron localization in molecular wires when the strength of disorder η and wire length L are increased. We calculated the inverse participant ratio in phase space as one of the possible measures of particle localization in disordered media. Additionally, we demonstrate the influence of disorder on the ground state of the system, which is represented by the Husimi function in phase space.

References

[1] BORLAND R.E., Proc. Phys. Soc., 77 (1961), 705.
[2] BORLAND R.E., Proc. Phys. Soc., 78 (1961), 926.
[3] MAKINSON R.E.B., ROBERTS A.D., Proc. Phys. Soc., 79 (1962), 222.
[4] HILKE M., FLORES J.C., Phys. Rev. B, 55 (1997), 10625.
[5] INGOLD G.-L., WOBST A., AULBACH C., HÄNGGI P., Eur. Phys. J. B., 30 (2002), 175.
[6] WOBST A., INGOLD G.-L., HÄNGGI P., WEINMANN D., Phys. Rev. B, 68 (2003), 085103.
[7] WEINMANN D., KOHLER S., INGOLD G.-L., HÄNGGI P., Ann. Phys. (Leipzig), 8 (1999), SI277.
[8] VARGA I., PIPEK J., Phys. Rev. E, 68 (2003), 026202.
[9] KRONIG R. DE L., PENNEY W.G., Proc. Roy. Soc., A130 (1930), 499.
[10] ZIMAN J.M., *Models of Disorder*, Cambridge University Press, Cambridge, 1979.
[11] LEE H.-W., Phys. Rep. 259 (1995), 147.
[12] HILLERY M., O'CONNEL R.F., SCULLY M.O., WIGNER E.P., Phys. Rep., 106 (1984), 121.

[13] THOULESS D.J., Phys. Rep., 13 (1974), 93.
[14] WEGNER F.J., Z. Phys. B, 36 (1980), 209.
[15] MOTT N.F., TWOSE W.D., Adv. Phys., 10 (1961), 107.
[16] FYODOROV Y.V., MIRLIN A.D., Phys. Rev. B, 51 (1995), 13403.
[17] WOŁOSZYN M., *The electronic structure of low-dimensional disordered systems*, Thesis, Kraków, 2004 (in Polish).

Received 14 September 2004
Revised 30 September 2004

Materials Science-Poland, Vol. 22, No. 4, 2004

Quantum networks in the presence of the Rashba effect and a magnetic field

DARIO BERCIOUX[1*], MICHELE GOVERNALE[2],
VITTORIO CATAUDELLA[1], VINCENZO MARIGLIANO RAMAGLIA[1]

[1]Coherentia-INFM and Dipartimento di Scienze Fisiche Università degli studi Federico II,
I-80126 Napoli, Italy

[2]NEST-INFM and Scuola Normale Superiore, Piazza dei Cavalieri 7, I-56126 Pisa, Italy

We use a simple formalism to calculate the conductance of any quantum network consisting of single-channel one-dimensional quantum wires in the presence of Rashba spin-orbit coupling and a coupling magnetic field. We show that the Rashba effect may give rise to an electron localization phenomenon similar to the Aharonov–Bohm effect. This localization effect can be attributed to spin precession due to the Rashba effect. We present results for linear transport through a finite-size chain connected to leads, taking also the effect of disorder into account. The effects of applying a magnetic field and Rashba spin-orbit coupling are studied in two-dimensional networks, showing that their interplay can lead the system to a transition between localized and anti-localized behaviour.

Key words: *Rashba effect; quantum networks; Aharonov–Bohm effect; localization*

1. Introduction

In the recent years, a new effect of extreme localization in a large class of rhombus tiling networks has been discussed [1]. This effect is related to an interplay between the Aharonov–Bohm (AB) effect [2] and geometry of the network. Actually, for particular values of the magnetic field, the set of sites visited by an initially localized wave packet is bound by the AB destructive interference. This set of sites is referred to as the AB cage. Such a localization does not rely on disorder [3], but only on quantum-interference and on the geometry of the lattice. There have been several theoretical papers addressing different aspects of AB cages, such as the effect of disorder and electron–electron interaction [4], interaction-induced delocalisation [5], and trans-

---

[*] Corresponding author, e-mail: dario.bercioux@na.infn.it. Present address: Institut für Theoretische Physik, Universität Regensburg, D-93040, Germany.

port [6]. From the experimental point of view, the AB-cage effect has been demonstrated for superconducting [7] and metallic networks [8] in the so-called T_3 lattice.

It is known that the wave function on an electron moving in the presence of spin-orbit (SO) coupling acquires quantum phases due to the Aharonov–Casher effect [9–14]. We focus on the Rashba SO coupling [15, 16], present in semiconductor heterostructures due to the lack of inversion symmetry in the growth direction. It is usually important in small-gap zinc-blende type semiconductors, and its strength can be tuned by external gate voltages. This has been demonstrated experimentally by measuring Shubnikov–de Haas oscillations in two-dimensional electron gas (2DEG) [17–19].

In the recent letter [20], we have shown that it is possible to obtain a localization of the electron wave function by means of the Rashba effect in quantum networks with a particular bipartite geometry containing nodes with different coordination numbers. This phenomenon has been demonstrated for a linear chain of square loops connected at one vertex (Fig. 1), which has been termed the diamond chain.

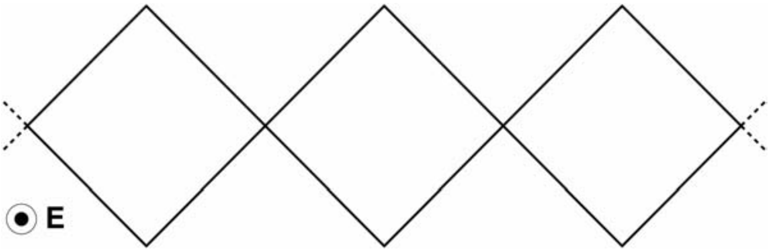

Fig. 1. Schematic view of the diamond chain

In this paper, the formalism introduced in our previous work [20] is improved in order to take into account the phase factor due to the magnetic field. The mechanism of electron localization owing to Rashba an SO coupling is analysed and compared in detail with the AB effect. It is shown that electron localization caused by the Rashba SO coupling is achieved only in geometrical structures that satisfy particular restrictions. Furthermore, we study the effect of applying SO coupling and a magnetic field on the transport properties of two different two-dimensional structures, the T_3 and square networks. One of the main results shown here is that a combination of both effects induces the phenomenon of electron anti-localization.

The paper is organized in the following way. In the Section 2 we introduce a very general formalism for studying quantum networks, realized with single-channel quantum wires in the presence of Rashba SO coupling and an external magnetic field. Section 3 is devoted to the transport properties of the diamond chain in presence of Rashba SO coupling alone. A physical interpretation of the localization phenomena due to Rashba SO coupling and a magnetic field is presented in Section 4. Section 5 is devoted to two different kinds of two-dimensional quantum networks in presence of Rashba SO coupling and a magnetic field. The paper ends with short conclusions of the presented results.

2. Model and formalism

We consider a single-channel quantum wire in a generic direction $\hat{\gamma}$ in the plane (x,y). The system is in the presence of a magnetic field B perpendicular to the plane (x,y) and Rashba SO coupling. The Hamiltonian for the single-channel quantum wire is:

$$H = \frac{\left(\vec{p} + q\vec{A}\right)^2}{2m} + \frac{\hbar k_{\mathrm{SO}}}{m}\left[\vec{\sigma} \times \left(\vec{p} + q\vec{A}\right)\right] \cdot \hat{z} + V(\hat{\gamma}) \qquad (1)$$

where m is the electron mass, $\vec{A}$ is the vector potential relative to the magnetic field ($\vec{B} = \vec{\nabla} \times \vec{A}$), k_{SO} is the SO coupling strength and $V(\hat{\gamma})$ is the wire confining potential. The SO coupling strength k_{SO} is related to the spin precession length L_{SO} by the relation $L_{\mathrm{SO}} = \pi/k_{\mathrm{SO}}$. For InAs quantum wells, the spin-precession length ranges from 0.2 to 1 μm [17–19]. The wave function on a bond (quantum wire) connecting nodes α and β, in the direction $\hat{\gamma}_{\alpha\beta}$, which takes into account SO coupling and the magnetic field, is

$$\Psi_{\alpha\beta}(r) = \frac{\mathrm{e}^{-if_{\alpha r}}\mathrm{e}^{i(\vec{\sigma}\times\hat{z})\cdot\hat{\gamma}_{\alpha\beta}k_{\mathrm{SO}}r}}{\sin(kl_{\alpha\beta})}\left\{\sin\left[k(l_{\alpha\beta} - r)\right]\Psi_{\alpha} + \sin(kr)\mathrm{e}^{if_{\alpha\beta}}\mathrm{e}^{-i(\vec{\sigma}\times\hat{z})\cdot\hat{\gamma}_{\alpha\beta}k_{\mathrm{SO}}l_{\alpha\beta}}\Psi_{\beta}\right\} \qquad (2)$$

where k is related to the eigenenergy by $\varepsilon = \left(\hbar^2/2m\right)(k^2 - k_{\mathrm{SO}}^2)$ [*], r is the coordinate along the bond, and $l_{\alpha,\beta}$ is the length of the bond. The spinors Ψ_{α} and Ψ_{β} are the values of the wave function at the nodes α and β, respectively. Spin precession due to the Rashba effect is described by the exponentials containing Pauli matrices in Eq. (2). The magnetic field contributes through the phase factor of the wave function (2)

$$\exp\left\{-if_{\alpha,r}\right\} = \exp\left\{-i\frac{2\pi}{\phi_0}\int_{\alpha}^{r}\vec{A}\cdot d\vec{l}\right\} \qquad (3)$$

where $\phi_0 = h/e$ is the flux quantum.

The wave function of the whole network [6, 20, 21] is obtained by imposing the continuity of probability current at the nodes. For a generic node α, it reads:

$$\mathbf{M}_{\alpha\alpha}\Psi_{\alpha} + \sum_{<\alpha,\beta>}\mathbf{M}_{\alpha\beta}\Psi_{\beta} = 0 \qquad (4)$$

where

$$\mathbf{M}_{\alpha\alpha} = \sum_{<\alpha,\beta>}\cot kl_{\alpha\beta} \quad \text{and} \quad \mathbf{M}_{\alpha\beta} = -\frac{\mathrm{e}^{-if_{\alpha\beta}}\mathrm{e}^{-i(\vec{\sigma}\times\hat{z})\cdot\hat{\gamma}_{\alpha\beta}k_{\mathrm{SO}}l_{\alpha\beta}}}{\sin kl_{\alpha\beta}} \qquad (5)$$

In Eqs. (4), (5), the sum $\sum_{<\alpha,\beta>}$ runs over all nodes β connected by bonds tothe node α.

---

[*] The term in k_{SO}^2 can be neglected in realistic situations.

3. The one-dimensional case

The one-dimensional analysis takes into account the case where only SO coupling is present, that is the magnetic field is zero ($B = 0$) [20].

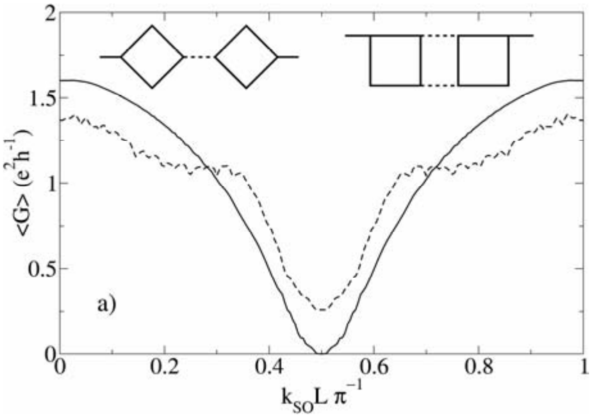

Fig. 2. Conductance (averaged over k_{in}) as a function of spin-orbit coupling strength for the diamond chain (continuous line) and for the ladder (dashed line). The two finite-size systems connected to input/output leads are shown in the inset. The parameters used for the calculation are: 50-elementary loops, k_{in} uniformly distributed in $[0, \pi/L]$

In the case of the AB cage, the first experimental verification came from transport measurements [7, 8]. To propose a possible experimental verification of the Rashba -cage effect, we evaluate the linear conductance of a diamond chain of finite length. To show that the localization effect is due to the peculiar bipartite geometry of the lattice, containing nodes with different coordination numbers, we contrast the diamond chain with a square ladder, i.e. a chain of square loops connected at two vertices, (the inset of Fig. 2). In the following, we will also refer to the latter topology simply as the ladder. The formalism to study the transport properties in the ladder has been introduced in the Ref. [20].

For a given k_{in}, the conductance has a rich structure, which takes into account the complexity of the associated energy spectrum [20]. In particular, on increasing k_{SO} gaps open and the energy of the incoming electrons ($\varepsilon_{\mathrm{in}} = (\hbar^2 k_{\mathrm{in}}^2 / 2m)$) can enter one of these gaps, leading to a vanishing conductance but not to a localization [20]. In fact, in this case the insulating behaviour is due to the absence of available states at the injection energy and not to the localization of the electron wave function in space. This effect is not present in $< G(k_{\mathrm{SO}}\, L) > k_{\mathrm{in}}$, since integration over k_{in} is equivalent to an average over energy. The dependence of the average conductance $< G(k_{\mathrm{SO}}\, L) >_{k_{\mathrm{in}}}$ on k_{SO} is shown in Fig. 2 for both the diamond chain and the square ladder. The conductance for both kinds of chains has a minimum for $k_{\mathrm{SO}}L = \pi/2$, caused by phase differences induced by the Rashba effect. Due to the existence of the Rashba cages, however, this minimum reaches zero only for the diamond chain.

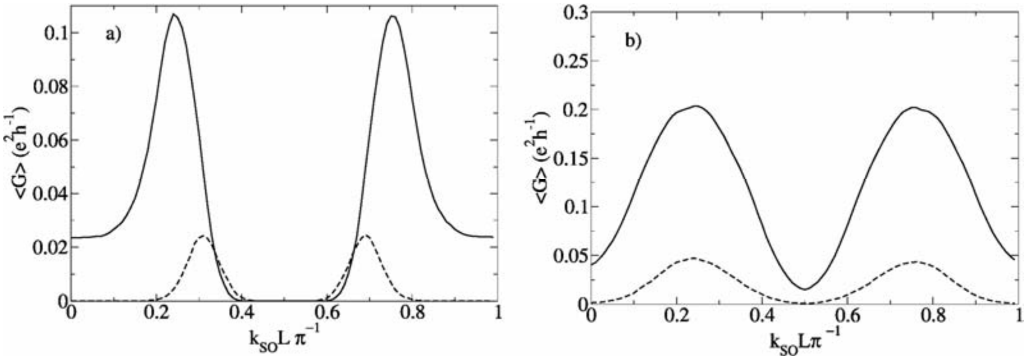

Fig. 3. Conductance (averaged over disorder configurations and over k_{in}) plotted as a function of spin-orbit coupling strength for the diamond chain (a) and the ladder (b). The two values of disorder strength used in the calculation were: $\Delta L = 0.01L$ (solid line) and $\Delta L = 0.02L$ (dashed line). Disorder averaging is done over 50 configurations, and k_{in} is uniformly distributed in $[k_F - \pi/2, k_F + \pi/2]$, with $k_F L = 100$. Both systems are composed of 50 elementary loops

From studies on AB cages, we expect the localization induced by the Rashba effect to be robust against disorder only in the bipartite structure that contains nodes with different coordination numbers (the diamond chain). A disorder that is more dangerous for the Rashba-cage effect is random fluctuation in the length of the bonds [6, 20], as such length fluctuations induce fluctuations in the phase shifts due to spin -precession. Hence, we consider a model where the length of each bond is randomly distributed in the interval $[L - \Delta L, L + \Delta L]$. The half width of the distribution ΔL gives the strength of the disorder.

In order to clarify if disorder affects the conductance, we average over disorder configurations. This is relevant to experiments, as in a real sample averaging is introduced by a finite phase-coherence length. For intermediate values of disorder ($k_F \Delta L \approx 1$), we find that the Rashba-cage effect is still present for the diamond chain, whereas the periodicity in k_{SO} is halved for the ladder, as shown in Fig. 3. The latter result can be interpreted as an analogue of the Altshuler–Aharonov–Spivak (AAS) effect [22] induced by the SO coupling. At higher values of disorder, the AAS effect also prevails in the diamond chain.

4. Physical interpretation

Let us consider the closed path in Fig. 4a, in which the four arms have the same length. An electron injected at the point A can reach the point D by moving through the upper path or though the lower path. The electron wave function gains a phase that depends on the Hamiltonian describing the travelled path. This corresponds to introducing a phase operator R_{pq} that relates the wave function at the starting point p with the its value in the end point q:

$$\psi(q) = R_{pq}\psi(p) \tag{6}$$

In this simple picture, the condition for having localization in this closed path is that an electron injected at the point A undergoes a destructive interference at D. This condition, in the mathematical form, corresponds to

$$(R_{BD}\cdot R_{AB} + R_{CD}\cdot R_{AC})\psi = 0, \quad \forall\,\psi \tag{7}$$

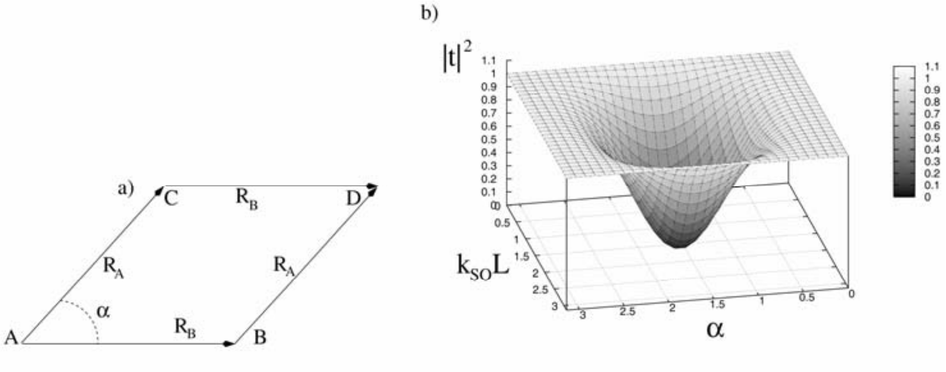

Fig. 4. Closed path between the points A and D (a). This is parameterised as a function of the angle α. Three-dimensional plot of the transmission probability as a function of the angle α between the paths AB and AC and spin-orbit coupling $k_{\mathrm{SO}}L$ (b)

When Rashba SO coupling is present and the magnetic field is zero, the phase operator takes the spin precession into account being of the form

$$R_{pq} = \exp\left\{-i\int_p^q \vec{\sigma}\cdot\left(\hat{z}\times d\vec{l}\,\right)k_{\mathrm{SO}}\right\} \tag{8}$$

i.e., this is a spin-dependent operator. From Eq. (7) it is possible to retrieve information about the transmission probability through the relation

$$|t|^2 = \mathrm{Tr}\left[\Gamma\Gamma^\dagger\right] \tag{9}$$

where $\Gamma = R_{BD}\cdot R_{AB} + R_{CD}\cdot R_{AC}$. In Figure 4b, the behaviour of the transmission probability (11) is shown as function of the angle α and of the SO coupling $k_{\mathrm{SO}}L$. It is clear that the transmission probability goes to zero if and only if the angle between the path is equal to $\pi/2$ and SO coupling is equal to $\pi/2$. This implies that we can achieve a complete localization only in a linear chain of square loops connected at one vertex and not in a chain of rhombi.

When the magnetic field *B* is present and Rashba SO coupling is zero, the phase operator has the form

$$R_{pq} = \exp\left\{ -i\frac{2\pi}{\phi_0}\int_p^q \vec{A}d\vec{l} \right\} \tag{10}$$

This operator is strongly dependent on the path along which the electron travels and it does not depend on spin. If we replace this phase operator in Eq. (7), the solution of the localization problem is given by

$$B = \left(n + \frac{1}{2} \right) \frac{\phi_0}{\sin(\alpha) L^2} \tag{11}$$

This equation relates the magnetic field inversely to the area of the closed path and tells us that for each area it is possible to apply a magnetic field that induces electron localization [2].

5. The two-dimensional case

We now concentrate on a periodic tiling with the hexagonal symmetry, called T_3 (Fig 5a). This is a periodic hexagonal structure with three sites per a unit cell, one sixfold coordinated and two threefold coordinated. It is also an example of a two-dimensional regular bipartite lattice containing nodes with different coordination numbers.

In Figure 5b, the behaviour of the averaged conductance for a finite piece of the T_3 lattice is shown as a function of reduced flux with zero SO coupling and SO coupling with zero magnetic field. In the case of the magnetic field, we observe a suppression of conductance due to the existence of the AB cage. The value of the averaged conductance minimum is not exactly zero. This is due to the existence of dispersive edge states [6], which are able to carry current even for $\phi/\phi_0 = 1/2$. This value is independent of the number of injection channels.

In the case of SO coupling, we do not observe a strong suppression of the averaged conductance as in the case of the magnetic field. A minimum is present, but it is due to interference phenomena that do not induce complete localization. Furthermore, this minimum cannot be caused by the existence of edge states, because it depends on the number of injection channels.

In Figure 5c, the behaviour of the averaged conductance is shown as function of SO coupling with $\phi/\phi_0 = 1/2$ and the magnetic field with $k_{SO}L\pi^{-1} = 0.5$. In the first case, the averaged conductance starts out from a point of maximum localization due to the AB effect, in the second case the averaged conductance starts out from a point of maximum localization due to the Rashba SO coupling. The main feature of these two curves is that the general behaviour is similar in the case of fixed SO coupling as in the case without it. A well-defined minimum for $\phi/\phi_0 = 0.5$ is still observed. On the contrary, in the case of a fixed magnetic field we observe as the SO coupling suppress the destructive interference due to the AB effect and an anti-localization peak appears.

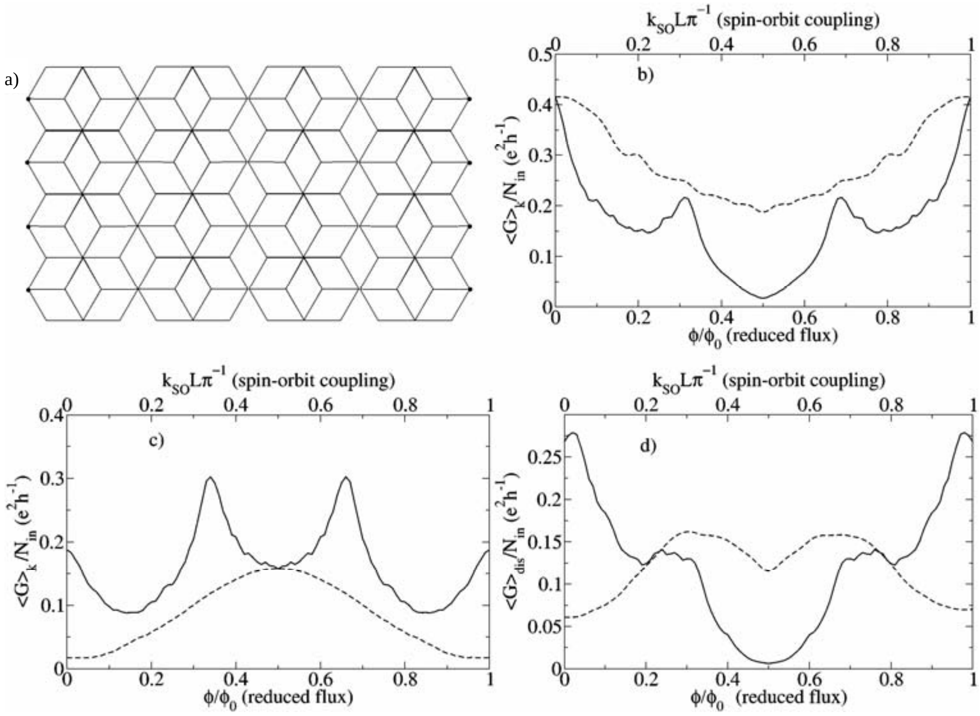

Fig. 5. A piece of the T network (a). Black dots on the left right) represent connections to the input (output) channels. Averaged conductance $<G>_{\boldsymbol{k}}/N_{\text{in}}$ as a function of reduced flux (solid curve) and spin-orbit coupling (dashed curve) for a T_3 lattice with 200 quantum wires (b). Averaged conductance $<G>_{\boldsymbol{k}}/N_{\text{in}}$ as a function of reduced flux evaluated at $k_{\text{SO}}L\pi^{-1} = 0.5$ (solid curve) and spin-orbit coupling evaluated at $\phi/\phi_0 = 0.5$ (dashed curve) for a T_3 lattice with 200 quantum wires (c). Averaged conductance $<G>_{\text{dis}}/N_{\text{in}}$ as function of reduced flux (solid curve) and spin-orbit coupling (dashed curve) for a T_3 lattice with 200 quantum wires in the disordered case (d)

In Figure 5d, the behaviour of the averaged conductance with respect to the disorder is shown as a function of reduced flux and SO coupling for a fixed disorder strength. It is clear that for the averaged conductance as a function of SO coupling the periodicity is no longer $k_{\text{SO}}L$, but $k_{\text{SO}}L/2$ according to the weak localization picture [22]. The averaged conductance as a function of reduced flux remains ϕ_0 periodic with a large amplitude. This strongly suggests that the AB cage effect survives for this strength of disorder.

We now consider transport through a finite square lattice (Fig. 6a). This network, unlike the T_3 lattice, does not present a bipartite structure containing nodes with different coordination numbers. Accordingly, we do not expect any electron localization phenomenon due to the AB effect or SO coupling. On the other hand, as we have shown in Section 4, the square network is composed of elementary cells (squares) that, as single elements, permit electron localization with both a magnetic field and SO coupling.

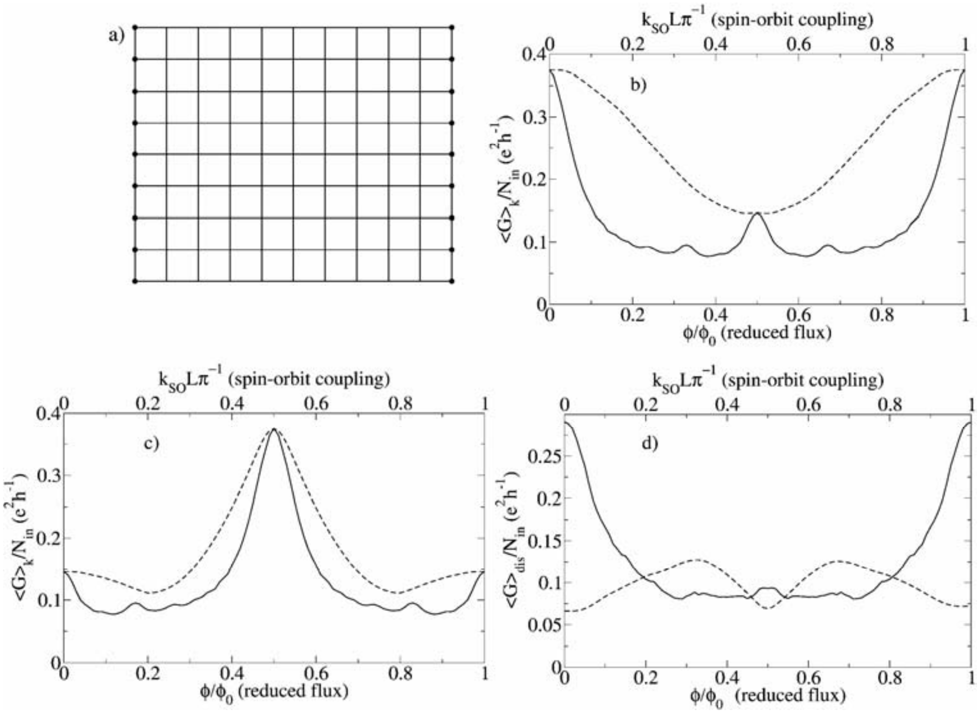

Fig. 6. A piece of the square lattice (a). Black dots on the left (right) represent the connections to the input (output) channels. Averaged conductance $<G>_{\boldsymbol{k}}/N_{\mathrm{in}}$ as a function of reduced flux (solid curve) and spin-orbit coupling (dashed curve) for the square lattice with 178 quantum wires (b). Averaged conductance $<G>_{\boldsymbol{k}}/N_{\mathrm{in}}$ as a function of reduced flux evaluated at $k_{\mathrm{SO}}L\pi^{-1} = 0.5$ (solid curve) and spin-orbit coupling evaluated at $\phi/\phi_0 = 0.5$ (dashed curve) for the square lattice with 178 quantum wires (c). Averaged conductance $<G>_{\mathrm{dis}}/N_{\mathrm{in}}$ as a function of reduced flux (solid curve) and spin-orbit coupling (dashed curve) for the square lattice in the disordered case (d)

In Figure 6b, the behaviour of the averaged conductance for a finite piece of the square lattice is shown as a function of reduced flux with zero SO coupling and SO coupling with zero magnetic field. The behaviour of the averaged conductance in the case of SO coupling is completely different from that of the magnetic field. Both, however, reach the same value, the former for $k_{\mathrm{SO}}L\pi^{-1} = 1/2$ and the latter for $\phi/\phi_0 = 1/2$. According to Section 4, both the AB effect and SO coupling induce electron localization in the elementary cell of the square network for these values, that is for these two critical values the system behaves the same way. If we now export this simple idea to the case of a square network, we infer that the conductance evaluated for $k_{SO}L\pi^{-1} = 1/2$ or $\phi/\phi_0 = 1/2$ has to show the same value.

It is interesting to analyse what happens when both the magnetic field and SO coupling are present. In Figure 6c, the behaviour of the averaged conductance is shown as a function of SO coupling with $\phi/\phi_0 = 1/2$ and the magnetic field with $k_{SO}L\pi^{-1} = 1/2$. The behaviour of both curves is very similar. The results of Section 4 tell us that these two localization phenomena manifest the same effect but as consequence of different physical aspects. In the case of SO coupling, we have a destructive interference between electrons undergoing spin-precession, instead of a spin-independent destructive interference process as in the case of the AB effect. When both localization phenomena are present at the maximum intensities, the destructive interference is completely lost. We then observe anti-localization rather than localization. The averaged conductance goes to the same value observed for zero magnetic field and zero SO coupling (Fig. 6b).

In Figure 6d, the behaviour of the averaged conductance is shown as a function of reduced flux and SO coupling in the case of a disordered system. It is also manifested in this case that the periodicity with respect to the magnetic flux and SO coupling is no longer ϕ_0 and $k_{SO}L$, but $\phi_0/2$ and $k_{SO}L/2$, respectively.

6. Conclusion

We have shown that in a quantum network with a particular bipartite geometry and containing nodes with different connectivities (a diamond chain), it is possible to obtain localization of the electron wave function by means of the Rashba effect. This localization shows up in the transport properties of a finite-size chain connected to leads. Furthermore, transport calculations in the presence of disorder show that this Rashba-cage effect is robust against disorder in the diamond chain. The effect of localization is not verified in two-dimensional networks with a bipartite structure and containing nodes with different coordination numbers, such as the T_3 lattice. We have shown, however, that the effect of applying Rashba SO coupling and a magnetic field can induce a strong anti-localization phenomena in those structures.

Acknowledgements

Fruitful discussion with C. Cacciapuoti, G. De Filippis, P. Lucignano and C.A. Perroni (Federico II University of Naples, Italy) and with R. Fazio, D. Frustaglia and M. Rizzi (Scuola Normale Superiore of Pisa, Italy) are gratefully acknowledged. Finally, DB wishes to acknowledge A. Ceré (Hippos Campi Flegrei of Naples, Italy).

References

[1] VIDAL J., MOSSERI R., DOUÇOT B., Phys. Rev. Lett., 81 (1998), 5888.
[2] AHARONOV Y., BOHM D., Phys. Rev., 115 (1959), 485.

[3] ANDERSON P.W., Phys. Rev., 109 (1958), 1492.
[4] VIDAL J., BUTAUD P., DOUÇOT B., MOSSERI R., Phys. Rev. B, 64 (2001), 155306.
[5] VIDAL J., DOUÇOT B., MOSSERI R., BUTAUD P., Phys. Rev. Lett., 85 (2000), 3906.
[6] VIDAL J., MONTAMBAUX G., DOUÇOT B., Phys. Rev. B, 62, R16294 (2000).
[7] ABILIO C.C., BUTAUD P., FOURNIER T., PANNETIER B., VIDAL J., TEDESCO S., DALZOTTO B., Phys. Rev. Lett., 83 (1999), 5102.
[8] NAUD C., FAINI G., MAILLY D., Phys. Rev. Lett., 86 (2001), 5104.
[9] AHARONOV Y., CASHER A., Phys. Rev. Lett., 53 (1984), 319.
[10] MATHUR H., DOUGLAS STONE A., Phys. Rev. Lett., 68 (1992), 2964.
[11] BALATSKY A.V., ALTSHULER B.L., Phys. Rev. Lett., 70 (1993), 1678.
[12] ARONOV A.G., LYANDA-GELLER Y.B., Phys. Rev. Lett., 70 (1993), 343.
[13] SPLETTSTÖßER J., GOVERNALE M., ZÜLICKE U., Phys. Rev. B, 68 (2003), 165341.
[14] FRUSTAGLIA D., RICHTER K., Phys. Rev. B, 69 (2004), 235310.
[15] RASHBA E.I., Fiz. Tverd. Tela (Leningrad), 2 (1960), 1224 (Sov. Phys. Solid State 2, 1109 (1960)).
[16] BYCHKOV Y.A., RASHBA E.I., J. Phys., C 17 (1984), 6039.
[17] NITTA J., AKAZAKI T., TAKAYANAGI H., ENOKI T., Phys. Rev. Lett., 78 (1997), 1335.
[18] SCHÄPERS T., ENGELS J., KLOCKE T., HOLLFELDER M., LÜTH H., J. Appl. Phys., 83 (1998), 4324.
[19] GRUNDLER D., Phys. Rev. Lett., 84 (2000), 2000.
[20] BERCIOUX D., GOVERNALE M., CATAUDELLA V., MARIGLIANO RAMAGLIA V., Phys. Rev. Lett., 93 (2004), 56802.
[21] KOTTOS T., SMILANSKY U., Ann. Phys. (N.Y.), 274 (1999), 76.
[22] ALTSHULER B., AHARONOV A., SPIVAK B., Pisma Zh. Eksp. Teor. Fiz., 33 (1981), 101, (JETP Lett., 33, 94, (1981)).

Received 12 October 2004
Revised 25 October 2004

Materials Science-Poland, Vol. 22, No. 4, 2004

A new organic metal with thedithiooxalato-bridged anion network, β''-ET)$_2${[NMe$_3$Ph]NaCr(C$_2$S$_2$O$_2$)$_3$(MeCN)}

E.I. ZHILYAEVA[1*], G.V. SHILOV[1], O.A. BOGDANOVA[1], R.N. LYUBOVSKAYA[1],
R.B. LYUBOVSKII[1], N.S. OVANESYAN[1], S.M. ALDOSHIN[1], C. TRAIN[2], M. GRUSELLE[2]

[1]Institute of Problems of Chemical Physics, Russian Academy of Sciences,
Chernogolovka, MD, 142432, Russia

[2]Laboratoire de Chimie Inorganique et Materiaux Moleculaires Unite C.N.R.S. 7071, Case 42, Bt F74,
Universite Pierre et Marie Curie, 4 place Jussieu, F-75252 Paris Cedex 05, France

The synthesis, crystal structure, and conductivity of a new bis(ethylenedithio)tetrathiafulvalene (ET)-based cation radical salt with a β''-(ET)$_2${[NMe$_3$Ph]NaCr(C$_2$S$_2$O$_2$)$_3$(MeCN)} composition is described. The compound is metallic down to 60 K. In the structure, conducting donor layers with a β''-type packing alternate with {[NaCr(C$_2$S$_2$O$_2$)$_3$]$^{2-}$}$_\infty$ anionic networks and [NMe$_3$Ph]$^+$organic cation layers.

Key words: *organic conductors; cation radical salt; electrical conductivity; X-ray diffraction*

1. Introduction

The properties of organic conductors based on cation radical salts are essentially defined by the nature of the counter-ions. Small changes in their structure affect the properties of the resulting compounds. Recently, organic conductors of the ET$_4$M$^{\mathrm{I}}$M$^{\mathrm{III}}$(C$_2$O$_4$)$_3$(solvent) family (ET – bis(ethylenedithio)tetrathiafulvalene) have been extensively studied [1–7]. Depending on the single charged cation M$^{\mathrm{I}}$, solvent, and trivalent metal M$^{\mathrm{III}}$, the compounds of this family exhibit phase transitions to a superconducting (M$^{\mathrm{I}}$ = H$_3$O, M$^{\mathrm{III}}$ = Fe, Cr, Ga) [1–5] or insulating state (M$^{\mathrm{I}}$ = H$_3$O, M$^{\mathrm{III}}$ = Fe, solvent – pyridine) [6], or reveal semiconducting (M$^{\mathrm{I}}$ = K, NH$_4$, M$^{\mathrm{III}}$ = Fe, Cr, Co, Al; solvent – PhCN) [4] or metallic behaviour (M$^{\mathrm{I}}$ = K, NH$_4$, M$^{\mathrm{III}}$ = Fe, Cr, solvent – DMF) [7] with decreasing temperature.

---

[*] Corresponding author, e-mail: zhilya@icp.ac.ru.

In organic conductors of this family, M^{III}, M^{I}, and the solvent were varied while retaining a honeycomb structure of the anionic oxalato-based sheets. It is of interest to study the effect of substituting an oxalate ligand (ox) for a dithiooxalate one (dto) in the $[M^{III}(ox)_3]^{3-}$ anion on the stoichiometry, structure, and properties of the resulting ET compound. In this work, we report on the synthesis, crystal structure and conductivity of a new conducting ET-based cation radical salt containing a dithiooxalato-bridged honeycomb anion network with a β″-$(ET)_2[(NMe_3Ph)NaCr(dto)_3(MeCN)]$ composition.

2. Experimental

$[NMe_3Ph]_2NaCr(dto)_3$ was synthesized according to the procedure described in [8]. Single crystals of $(ET)_2\{[NMe_3Ph]NaCr(dto)_3(MeCN)\}$ (**1**) were obtained by the electrochemical oxidation of ET (7.6 mg, 2 mmol) at 16 °C in the presence of 30 mg of $[NMe_3Ph]_2NaCr(dto)_3$ under an argon atmosphere and at a current of 0.1 μA. Thick shiny plates were collected after two weeks.

The resistivity of single crystals was measured down to 4 K by a standard dc four -probe technique with graphite paste.

The main crystallographic data for β″-$(ET)_2[(PhMe_3N)NaCr(dto)_3(MeCN)]$ are: $C_{37}H_{33}CrN_2NaO_6S_{22}$, the triclinic centro-symmetrical space group, $P\bar{1}$, $a = 10.335(2)$, $b = 11.211(2)$, $c = 26.016(5)$ Å, $\alpha = 82.79°$, $\beta = 86.63°$, $\gamma = 62.64°$, $V = 2656(1)$ Å^3, $d_{calcd} = 1.728$ g/cm^3, and $Z = 2$. The structure was solved by direct methods using the SHELXL-97 program suite [9]. The final refinement parameters were $R = 0.0957$, and GOOF = 0.964.

3. Results and discussion

The compound **1** was precipitated by the electrochemical oxidation of ET from a constant-current electrocrystallisation cell using a low concentration solution of $[NMe_3Ph]_2NaCr(dto)_3$ in MeCN. The crystals of **1** form shiny and thick elongated plates. The compound loses the solvent during storage, the crystal surface losing its lustre and becoming rough.

1 has a layered structure. The crystal structure is characterized by four alternating layers along the *c* direction in the sequence: ET, $[NaCr(dto)_{3]}\}_\infty$, $[NMe_3Ph]^+$ cations together with CH_3CN molecules, and $[NaCr(dto)_3]_\infty$. The ET molecules are aligned side-by-side and form a 2D array within the *ab* plane shown in Fig. 1, in which a view of the ET cation layer along the longer axis of the donor molecule is presented. Numerous shortened S…S intermolecular contacts exist between molecules within the donor cation layer, giving the material a two-dimensional electronic character. The overall donor ion packing exhibits the so-called *β''* type [10] donor arrangement, which often occurs in conducting ET salts.

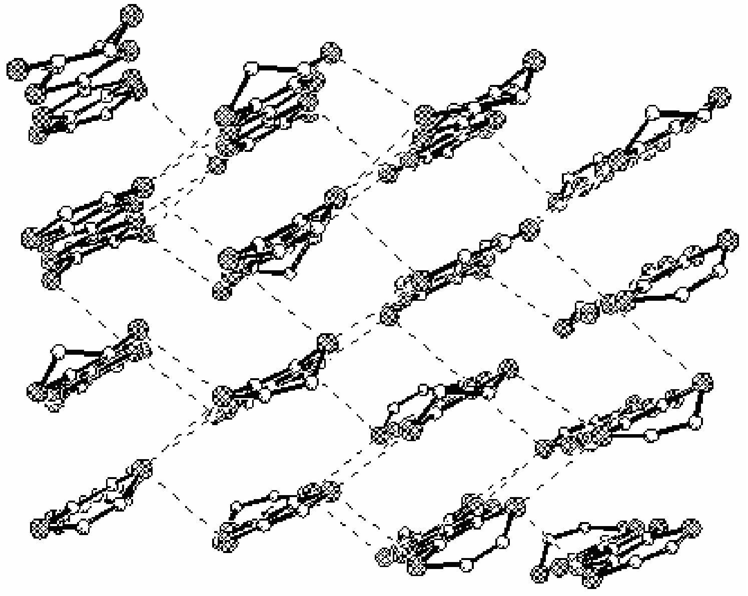

Fig. 1. View of the ET cation layer along the longer molecular axis

Each $[NaCr(dto)_3]_\infty$ sheet has a honeycomb arrangement, in which Na and Cr alternate to form an approximately hexagonal network. Organic $[NMe_3Ph]^+$ cations are enclosed between the two $[NaCr(dto)_3]_\infty$ sheets. Half of the cations are intercalated in the first network and the other half are intercalated in the other.

No short interatomic S…S contacts were found between the ET donor layers and anionic ones. The shortest distance from the S dto atom to the S atom of ET (S1…S13) was 3.74 Å. This value exceeds that of a normal van der Waals S…S contact, namely 3.60 Å [11].

Of the ET cation-radical salts usually comprising a donor and one anion, the salt **1** has both an unusual composition and structure. Apart from the donor, it contains the $[Cr(dto)_3]^{3-}$ anion, two different cations and a solvent molecule, and can be said to be a four(multi)-component system, similarly to the so-called three-component $ET_nM^IHg(SCN)_4$ family [12, 13]. In the three-component $ET_nM^IHg(SCN)_4$ system, as well as in β''-$ET_4[M^IM^{III}(ox)_3]\cdot$(solvent), there is a third component M (alkali metal, ammonium, or hydroxonium cations) which participates during the formation of the polymeric network of an insulating layer. In contrast to the above-mentioned families, whose structures involve only two alternating layers (ET and a polymeric network), the polymeric anion networks in the title compound alternate with either ET or $[NMe_3Ph]^+$ layers. In fact, the packing motifs of two structures are combined in one structure: β''-$ET_4[M^IM^{III}(ox)_3]\cdot$(solvent) [1–7] and the molecular ferromagnet $[Bu_4N]$

[MnCr(ox)$_3$] [14]. The most important difference between the crystal structures of **1** and the molecular ferromagnet [Bu$_4$N][MnCr(ox)$_3$] is that the number of [NMe$_3$Ph]$^+$ cations in the cation layer of **1** is twice as large as the number of [Bu$_4$N]$^+$ cations in [Bu$_4$N][MnCr(ox)$_3$] Also, in **1** they are intercalated in both of the nearest networks, while the organic cations in [Bu$_4$N][MnCr(ox)$_3$] are intercalated only in one network [14].

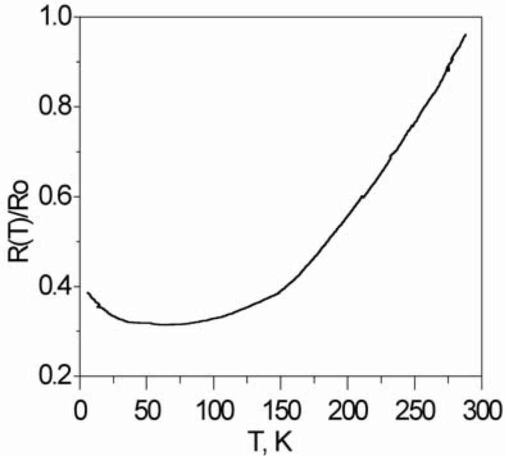

Fig. 2. Temperature dependence of relative electrical resistance for a single crystal of β″-(ET)$_2${[NMe$_3$Ph]NaCr(dto)$_3$(MeCN)}

Conductivity data for **1** are shown in Fig. 2. (ET)$_2${[NMe$_3$Ph]NaCr(dto)$_3$(MeCN)} is metallic at room temperature, with σ_{298K} = 120 S·cm^{-1}. With decreasing temperature, the complex remains metallic down to 60 K. At lower temperatures, its resistance smoothly rises, being lower than the room-temperature value. In this case, a gradual localization of conduction electrons appears to be caused by the quality of the crystal and impurities.

4. Conclusion

A new metallic ET cation radical salt with a dithiooxalato-bridged honeycomb anion network, namely (ET)$_2${[NMe$_3$Ph]NaCr(C$_2$S$_2$O$_2$)$_3$(MeCN)}, has been synthesized and characterized. The conducting layers in this cation radical salt alternate with three insulating layers and adopt the β″-packing motif found in other ET cation radical salts. In fact, the crystal structure of this compound combines the features characteristic of both β″-ET-oxalatometallates and the molecular ferromagnet [Bu$_4$N][MnCr(ox)$_3$]. The title compound is metallic with the room temperature conductivity of 120 S·cm^{-1}. Below 60 K, its resistance smoothly increases on decreasing temperature, not attaining, however, the room-temperature value.

Acknowledgements

The project was supported by the RFBR grants 02-03-33283 and 04-03-32296.

References

[1] KURMOO M., GRAHAM A.W., DAY P., COLES C.J., HURSTHOUSE M.B., CAULFIELD J.L., SINGLETON J., PRATT F.L., HAYES W., DUCASSE L., GUIONNEAU P., J. Am. Chem. Soc., 117 (1995), 12209.

[2] MARTIN L., TURNER S.S., DAY P., GUIONNEAU P., HOWARD J.A.K., HIBBS D.E., LIGHT M.E., HURSTHOUSE M.B., URUICHI M., YAKUSHI K., Inorg. Chem., 40 (2001), 1363.

[3] MARTIN L., TURNER S.S., DAY P., MABBS F.E., MCINNES E.J.L., J. Chem. Soc., Chem. Commun., (1997), 1367.

[4] RASHID S., TURNER S.S., DAY P., LIGHT M.E., HURSTHOUSE M.B., GUIONNEAU P., Synth. Met., 120 (2001), 985.

[5] AKUTSU H., AKUTSU-SATO A., TURNET S.S., PELEVEN D.L., DAY P., LAUKHIN V., KLEHE A.-K., SINGLETON J., TOCHER D.A., PROBERT M.R., HOWARD J.A.K., J. Am. Chem. Soc., 124 (2002), 12430.

[6] TURNER S.S., DAY P., MALIK K.M.A., HURSTHOUSE M.B., TEAT S.J., MACLEAN E.J., MARTIN L., FRENCH S.A., Inorg. Chem., 38 (1999), 3543.

[7] PROKHOROVA T.G., KHASANOV S.S., ZORINA L.V., BURAVOV L.I., TKACHEVA V.A., BASKAKOV A.A., MORGUNOV R.B., GENER M., CANADELL E., SHIBAEVA R.P., YAGUBSKII E.B., Adv. Funct. Mater., 13 (2003), 1.

[8] COUCOUVANIS D., PILTINGSRUD D., J. Am. Chem. Soc., 95 (1973), 5556.

[9] SHELDRICK G.M., SHELXL-97, University of Göttingen, Göttingen, Germany, 1997.

[10] MORI T., Bull. Chem. Soc. Jpn., 71 (1998), 2509.

[11] BONDI A., J. Phys. Chem., 68 (1964), 441.

[12] OSHIMA M., MORI H., SAITO G., OSHIMA K., Chem. Lett. (1989), 1159.

[13] MORI H., TANAKA S., MORI T., MARUYAMA Y., INOKUCHI H., SAITO G., Solid State Commun., 78 (1991), 49.

[14] ATOVMYAN L.O., SHILOV G.V., LYUBOVSKAYA R.N., ZHILYAEVA E.I., OVANESYAN N.S., MOROZOV YU.G., PIRUMOVA S.I., GUSAKOVSKAYA I.G., Pisma v ZhETF, 58 (1993), 818.

Received 14 October 2004
Revised 22 November 2004

Materials Science-Poland, Vol. 22, No. 4, 2004

New organic electroluminescent materials

M.G. KAPLUNOV[1*], S.S. KRASNIKOVA[1],
I.K. YAKUSHCHENKO[1], O.N. ERMAKOV[2], S.A. STAKHARNY[2]

[1]Institute of Problems of Chemical Physics, Russian Academy of Sciences,
142432, Chernogolovka, Moscow Region, Russia

[2]Joint-Stock Scientific and Technological Co "Sapfir", Moscow, Russia

Spectral and electric properties of six new materials for electroluminescent devices are described, including materials for emitting layers based on triazole derivatives and zinc chelate complexes, and a high-T_g hole-transporting material based on triphenylamine.

Key words: *organic electroluminescence; photoluminescence; new materials*

1. Introduction

The study of organic electroluminescent (EL) materials is now a rapidly developing field of science due to promising practical applications [1, 2]. In spite of the impressing achievements of the last decade, the problem of searching for new effective luminescent materials of different emission colours is still topical. Another important task in the design of organic EL devices is improving their thermal stability in order to prevent degradation due to morphological changes in amorphous organic layers near the glass transition temperature (T_g). Therefore, materials with high T_g are required for organic EL devices.

In the present work, we report a study of spectral and electroluminescent properties for some new materials. The chemical structures of the materials studied are shown in Fig. 1.

---

[*]Corresponding author, e-mail:kaplunov@icp.ac.ru.

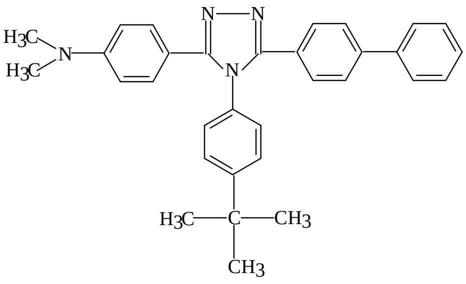

DA-BuTAZ

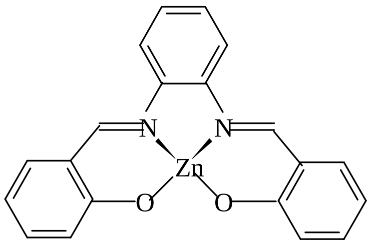

Zn(OB-PDA)

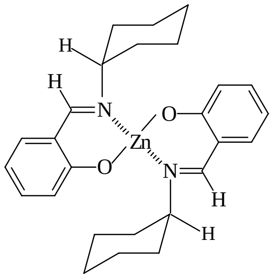

Zn(OBCG)$_2$

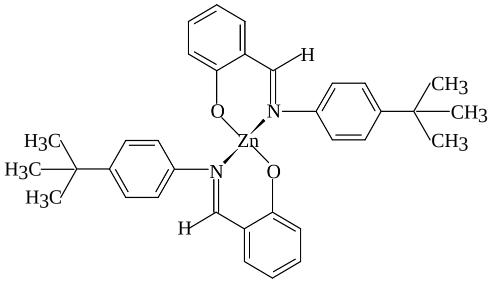

Zn(OBBA)$_2$

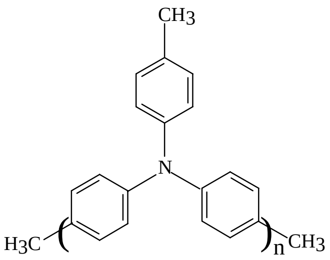

PTA

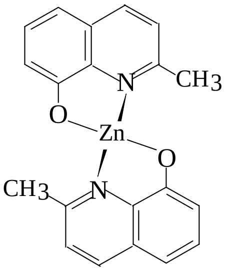

Zn(CH$_3$Q)$_2$

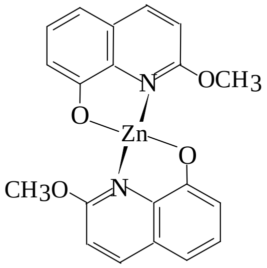

Zn(MeQ)$_2$

Fig. 1. Chemical structures of the materials studied

3-(4-dimethylaminophenyl)-4-(4′-*tert*-butylphenyl)-5-diphenyl-1,2,4-triazole or DA-Bu TAZ, is a promising 1,2,4-triazole derivative for blue emitting layer [3].

Zinc complexes containing the azomethine group –CH=N–R (R is an alkyl group) and characterized by blue electroluminescence have been recently proposed [4]. We have synthesized three new electroluminescent materials based on zinc chelate complexes with azomethine groups, which are characterized by electroluminescence in the blue and green spectral regions: bis(N-(2-oxybenzylidene)cyclohexylamine)-zinc, ($Zn(OBCG)_2$), N,N′-bis(2′-oxybenzylidene)-1,2-phenylenediamine-zinc, (Zn(OB-PDA)), and bis(N-2-oxybenzylidene)-4-*tert*-butylanyline)-zinc ($Zn(OBBA)_2$) [5]. The addition of various substituents at the nitrogen atoms or bridges between them enables changing the position of the absorption and luminescence spectral maxima due to changes in the electron density and conjugation length. Also, new Zn complexes with quinoline derivatives, bis(2-methoxy-8-oxyquinoline)zinc ($Zn(MeQ)_2$) and bis(2-methyl-8-oxyquinoline)zinc ($Zn(CH_3Q)_2$) were synthesized and studied.

We have also proposed a novel high-T_g oligomeric material (PTA) for hole-transporting layers (HTL) in EL devices based on triphenylamine. Dimeric triphenylamine, or N,N′-diphenyl-N′N′-bis(3-metylphenyl)-1,1′-biphenyl-4,4′-diamine (TPD), is a well-known hole-transporting material exhibiting excellent hole injection and transport capability with good electron-blocking capability at the HTL boundary. It is not very stable, however, due to its low T_g value [6]. Oligomers of triphenylamine with an oligomerisation number n in the range of 2–5 have been shown to have good hole-transporting characteristics, and the T_g for these materials is shown to increase with increasing n – from 60 °C for TPD to 140 °C for the oligomer with $n = 5$ [6]. PTA is a mixture of triphenylamine oligomers of a general formula shown above with oligomerisation numbers n from 7 to 11, characterized by the T_g as high as 185 °C [3].

2. Experimental

The synthesis of the materials was described elsewhere [3, 5]. TPD was an Aldrich commercial product. The electroluminescent devices in our study were of the four-layered structure ITO/HTL/EML/M, where ITO is a transparent anode of $In_2O_3:SnO_2$ on a glass substrate, HTL is a hole-transporting layer, EML is an emitting layer, and M is a metallic cathode of Al or Mg:Ag alloy. The HTLs were prepared by the spin casting of PTA or by the vacuum evaporation of TPD. EMLs and metal cathodes were prepared by vacuum evaporation at a base pressure of about $5\cdot10^{-6}$ Torr.

The current–voltage and brightness–voltage characteristics of the EL devices were recorded simultaneously with a computer-controlled potentiostat PI-50 and a calibrated photomultiplier, or with a Hewlett-Packard semiconductor parameter analyser HP4155A and Si photodiode. The technique for measuring the absorption and photoluminescence (PL) spectra and PL quantum yields is described elsewhere [7].

3. Results and discussion

Figure 2 shows the absorption and photoluminescence (PL) spectra for the evaporated films of the studied materials. For the zinc chelate complexes, the maximum with the longest wavelength absorption band shifts to longer wavelengths in the order: Zn(OBCG)$_2$, Zn(OBBA)$_2$, Zn(OBPDA). In the PL spectra, the broad bands (a half -width of about 100 nm) with maxima at 453, 510, and 565 nm, correspondingly, are observed shifting to longer wavelengths in the same sequence. For DA-BuTAZ films, the PL maximum is observed at about 430 nm. We have measured the PL quantum yield for DA-BuTAZ and PTA in benzene solutions, being estimated at about 90% and 70%, respectively. We have estimated the PL quantum yields of evaporated films of zinc complexes at 20–25% for Zn(OBCG)$_2$, 7–10% for Zn(OBBA)$_2$, and 1–2% for Zn(OBPDA). With the exception of the last complex, these quantum yields are comparable or higher than that of the well-known tris-8-oxiquinolate aluminium Alq$_3$, for which the PL quantum yield is reported to vary from 8–10 to 32% depending on the source of data [8]. The film containing 0.5% of Nile Red (NR) in Zn(OBBA)$_2$ is characterized by a PL band in the red spectral region, with a maximum at 625 nm and a quantum yield of about 100%, which is due to electron excitation energy transfer from Zn(OBBA)$_2$ molecules to NR molecules [7, 9]. Spectral properties of the materials studied are summarized in Table 1.

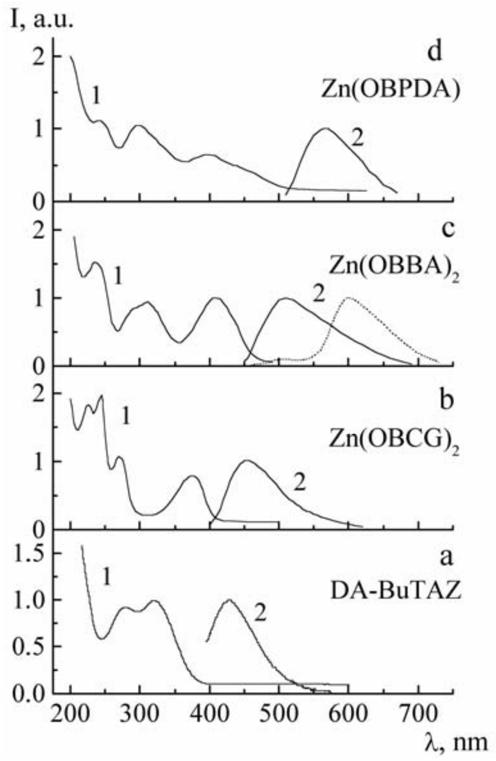

Fig. 2. Absorption (1) and photoluminescence (2) spectra of the materials: a) DA-BuTAZ, b) Zn(OBCG)$_2$, c) Zn(OBBA)$_2$ (dashed curve – PL of the film containing 0.5% of Nile Red), d) Zn(OBPDA)

Typical current–voltage and brightness–voltage characteristics of the studied devices with a ITO/TPD/DA-BuTAZ/Al structure are shown in Fig. 3a. Exchanging TPD with PTA does not principally change the electric and luminous properties, but systems with PTA are more stable at high currents. Exchanging the Al cathode with a Mg:Ag alloy gives a sufficient increase in luminosity (about two orders of magnitude) and a shift of the light appearance threshold to lower voltages (down to 8–10 V for DA-BuTAZ). The EL properties of the materials with a ITO/PTA/EML/Mg:Ag structure are given in Table 1.

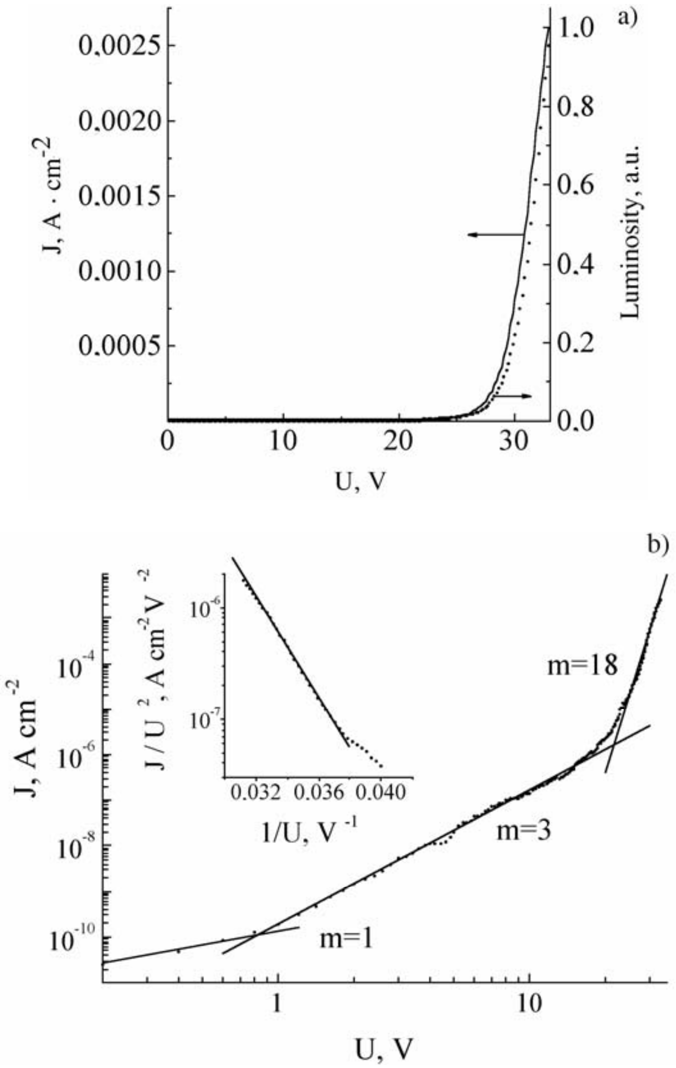

Fig. 3. Typical current–voltage and brightness–voltage characteristics of the EL device ITO/TPD/DA-BuTAZ/Al (a) and the current-voltage curve of the same device in a double logarithmic scale (b); the insert shows a part of this curve in the Fowler–Nordheim coordinates: J/U^2 vs. $1/U$

Table 1. Absorption, photoluminescence (PL), end electroluminescence (EL) of the materials studied

Compound	Colour	Absorption λ_{max}, nm	PL λ_{max} ($\Delta\lambda$) nm	PL QY, %	EL λ_{max} ($\Delta\lambda$) nm	Brightness, cd/m^2 (at voltage, V)	EL efficiency, cd/A
DA-BuTAZ	blue	320	430 (70)	>90	451 (70)	120 (12.8)	24
Zn(OBCG)$_2$	blue	376	453 (87)	20–25	450 (75)	120 (8.4)	1,4
Zn(OBBA)$_2$	green	406	510 (115)	7–10	520 (112)	360 (12.7)	15
Zn(CH$_3$Q)$_2$	green	374	514 (100)	–	–	10 (50)	0.05
Zn(MEQ)$_2$	green	386	520 (100)	–	–	140 (14.8)	2.8
Zn(OBPDA)	yellow -green	387–415	565 (95)	1–2	560–580	360 (8.5)	1,7
Zn(OBBA)$_2$+NR	red	406; 525	625 (50)	~100	625–650	280 (20)	0.1
PTA	blue	370	420 (120) 480 (sh)	~70	–	–	–

Figure 3b shows the dependence of the current density J on voltage U in the double logarithmic scale. Three regions can be seen in the current–voltage curve. At low voltages (less than 1 V), the current is proportional to voltage, which is the usual Ohmic behaviour. Beyond the Ohmic region up to the electroluminescence threshold, the dependence of the current on voltage follows a power law (J~U^m). Such a behaviour is characteristic of trap-controlled space charge-limited currents, and indeed it has been observed in EL devices based on Alq$_3$ and polymers with m changing from 2 to about 10 [10, 11]. The third region (beyond the light appearance threshold) may be characterized by a power low with a very high power index m (18–30), much higher than usually observed [10, 11]. An alternative explanation for this region is the injection limitation of current, for example by the Fowler–Nordheim tunnelling mechanism, which has been shown to be appropriate for some polymer based EL devises [12]. This is illustrated in the inset in Fig. 3b, which demonstrates a linear dependence of $\log(J/U^2)$ vs. $1/U$. This corresponds to the Fowler–Nordheim law: $J \sim U^2 \exp(-C/U)$ (C is a parameter depending on the shape of the potential barrier at the layer interface). Another confirmation of the tunnelling mechanism is the experimental fact that changing the metallic cathode significantly changes the electric properties, possibly due to changes in the metal work function [12].

Acknowledgement

This work was supported by the Russian Foundation for Basic Research, grant N 03-03-32199.

References

[1] MITSCHKE U., BAUERLE P., J. Mater. Chem., 10 (2000), 1471.
[2] BRAUN D., Materials Today, June 2002, 32.

[3] YAKUSHCHENKO I.K., KAPLUNOV M.G., EFIMOV O.N., BELOV M.YU., SHAMAEV S.N., Phys. Chem. Chem. Phys., 1 (1999), 1783.

[4] SANO T., NISHIO Y., HAMADA Y., TAKAHASHI H., UZUKI T., SHIBATA K., J. Mater. Chem., 10 (2000), 157.

[5] KAPLUNOV M.G., YAKUSHCHENKO I.K., KRASNIKOVA S.S., SHAMAEV S.N., PIVOVAROV A.P., EFIMOV O.N., Russ. Chem. Bull., in press.

[6] TANAKA H., TOKITO SH., TAGA Y., OKADA A., Chem. Commun. (1996) 2175.

[7] PIVOVAROV A.P., KAPLUNOV M.G., YAKUSHCHENKO I.K., BELOV M.YU., NIKOLAEVA G.V., EFIMOV O.N., Russ. Chem. Bull. 51 (2002) 67.

[8] GIRO G., COCCHI M., DI MARKO P., FATTORI V., DEMBECH P., RIZZOLI S., Synth. Met., 123 (2001), 529.

[9] PIVOVAROV A.P., KAPLUNOV M.G., EFIMOV O.N., YAKUSHCHENKO I.K., BELOV M.YU., Mol. Cryst. Liq. Cryst., 361 (2001), 263.

[10] IOANNIDIS A., FORSYTHE E., GAO Y., WU M.W., CONWELL E.M., Appl. Phys. Lett., 72 (1998), 3038.

[11] MARAI F., ROMDHANE S., HASSINE L., MAJDUB M., BOUCHRIHA H., Synth.Met., 132 (2003), 117.

[12] PARKER I.D., J. Appl. Phys., 75 (1994), 1656.

Received 14 October 2004
Revised 22 November 2004